

GEOLOGY AND MINERALOGY RESEARCH DEVELOPMENTS

CRYSTAL GROWTH

**CONCEPTS, MECHANISMS
AND APPLICATIONS**

Nova Science Publishing, Inc.

**GEOLOGY AND MINERALOGY
RESEARCH DEVELOPMENTS**

Additional books in this series can be found on Nova's website
under the Series tab.

Additional e-books in this series can be found on Nova's website
under the e-book tab.

Nova Science Publishing, Inc.

GEOLOGY AND MINERALOGY RESEARCH DEVELOPMENTS

**CRYSTAL GROWTH
CONCEPTS, MECHANISMS
AND APPLICATIONS**

**JINJIN LI,
JIANWEI LI
AND
YANHUI CHU
EDITORS**



Copyright © 2017 by Nova Science Publishers, Inc.

All rights reserved. No part of this book may be reproduced, stored in a retrieval system or transmitted in any form or by any means: electronic, electrostatic, magnetic, tape, mechanical photocopying, recording or otherwise without the written permission of the Publisher.

We have partnered with Copyright Clearance Center to make it easy for you to obtain permissions to reuse content from this publication. Simply navigate to this publication's page on Nova's website and locate the "Get Permission" button below the title description. This button is linked directly to the title's permission page on copyright.com. Alternatively, you can visit copyright.com and search by title, ISBN, or ISSN.

For further questions about using the service on copyright.com, please contact:

Copyright Clearance Center

Phone: +1-(978) 750-8400

Fax: +1-(978) 750-4470

E-mail: info@copyright.com.

NOTICE TO THE READER

The Publisher has taken reasonable care in the preparation of this book, but makes no expressed or implied warranty of any kind and assumes no responsibility for any errors or omissions. No liability is assumed for incidental or consequential damages in connection with or arising out of information contained in this book. The Publisher shall not be liable for any special, consequential, or exemplary damages resulting, in whole or in part, from the readers' use of, or reliance upon, this material. Any parts of this book based on government reports are so indicated and copyright is claimed for those parts to the extent applicable to compilations of such works.

Independent verification should be sought for any data, advice or recommendations contained in this book. In addition, no responsibility is assumed by the publisher for any injury and/or damage to persons or property arising from any methods, products, instructions, ideas or otherwise contained in this publication.

This publication is designed to provide accurate and authoritative information with regard to the subject matter covered herein. It is sold with the clear understanding that the Publisher is not engaged in rendering legal or any other professional services. If legal or any other expert assistance is required, the services of a competent person should be sought. FROM A DECLARATION OF PARTICIPANTS JOINTLY ADOPTED BY A COMMITTEE OF THE AMERICAN BAR ASSOCIATION AND A COMMITTEE OF PUBLISHERS.

Additional color graphics may be available in the e-book version of this book.

Library of Congress Cataloging-in-Publication Data

ISBN: 978-1-53612-203-9

Published by Nova Science Publishers, Inc. † New York

CONTENTS

Preface		vii
Chapter 1	Single Crystal Growth by a Slow Evaporation Technique: Concept, Mechanisms and Applications <i>Sahajkumar A. Gandhi</i>	1
Chapter 2	Targeted Synthesis of Metastable Compounds and Intergrowths: The Modulated Elemental Reactants Method <i>Marco Esters and David C. Johnson</i>	35
Chapter 3	Analysis for the Morphology Prediction of Materials from First Principles Calculations <i>Marisa Carvalho de Oliveira, Thiago Marinho Duarte, Lourdes Gracia, Elson Longo and Juan Andres</i>	119
Chapter 4	Growth Behaviors of CaCO ₃ Polymorphs under Various Environmental Conditions <i>Clifford Y. Tai, Meng-Chieh Lin, Su-Chun How, Yu-Hong Cheng and Steven S.-S. Wang</i>	165

Chapter 5	Weak Nonlinear Three-Dimensional Convective Flow during the Solidification of Binary Alloys <i>Dambaru Bhatta and Daniel N. Riahi</i>	199
Chapter 6	Metal–Organic Frameworks: Design and Applications <i>Yue Liang, Xia Zhang and Da-Bin Qin</i>	227
Chapter 7	Concept, Property and Applicability of Liquid Crystals <i>Saswati Roy</i>	251
Chapter 8	The Correlation of Density, Refractive Index and Dielectric Studies on Two Peculiar Liquid Crystals <i>Debanjan Bhattacharjee and Ayon Bhattacharjee</i>	265
Chapter 9	X-Ray, Spectroscopic and Computational Studies of [N'-(2-Hydroxy-3-ethoxybenzylidene)-4-Methylbenzenesulfonhydrazide] Copper(II) <i>Çiğdem Yüksektepe Ataoğlu, Nuray Şenyüz, Feyizan Güntepe, Murat Taş and Hümeýra Bati</i>	285
Chapter 10	Fenamate Crystals and Cocrystals: Structural and Thermodynamic Aspects <i>German L. Perlovich and Artem O. Surov</i>	317
	About the Editors	365
	Index	369

PREFACE

Crystals are a kind of solid materials that can be easily found in our daily life such as snowflakes, table salt and diamonds. However, not all solid materials are crystals. Their structures are strictly defined based on a periodic arrangement of constituent atoms forming a crystal lattice that extends in all directions. During the past decades, we have witnessed that crystalline materials are playing significant roles in the development of science and technology. For instance, they have greatly contributed to the field of semiconductors for electronic devices, lasers and solar cells. As most colleagues working in the field have noticed, many future applications require materials with high degree of crystallinity. Unfortunately, there is not a general approach or technology that can meet this need. Thus, it is time to look back the fundamentals of crystals that may trigger insights into the future applications.

In this book, we will mainly target at introducing crystal growth from three aspects ranging from basic concepts, detailed mechanisms to advanced applications in hot areas of materials science. Although some of these topics may have been reviews in other books, it is still an advantage of providing a compendium where the frontier of the three aspects are all extensively reviewed from the first-hand research discoveries of active researchers in the area of crystal growth.

The book will start with a detailed discussion of various experimental techniques that may give rise to single crystals with high quality in Chapter 1. Apart from this, some unexpected cases we may encounter in practical experiments and their effects on single crystals will also be discussed. It is known that the crystallization process should be spontaneous, suggesting that it is a challenge to control the synthesis of the targeted crystal materials. In Chapter 2, modulated elemental reactants method will be introduced as a powerful approach for the synthesis of new metastable compounds and heterostructures of designed nanoarchitectures by kinetic control of the reactions. Subsequently, in Chapter 3, the interfaces between surfaces will be examined and their effects on morphology of the target (nano)crystal will be reviewed. More interestingly, we will even be able to predict the morphology of the resulting crystals from first principles calculations. In Chapter 4, the crystal growth rates of CaCO_3 polymorphs, i.e., calcite and aragonite, were measured at different environments by conducting the growth experiment in the metastable region, using the constant-composition technique. In recent years, the qualitative features of three-dimensional convective flow have been determined by investigating the weakly nonlinear analysis of the flow during solidification of binary alloys. Chapter 5 will provide a very detailed discussion on this topic. Metal-organic frameworks (MOFs) are crystalline and porous polymers formed by the coordination between metal ions or clusters and organic ligands. They have achieved wide applications in catalysis, gas storage, drug delivery and sensing due to their advantages of simple synthetic method, robust porosity, adjustable structure and high stability. Such well-studied materials are also attracted our attention. Thus, Chapter 6 will describe the synthetic strategies, structure, properties and applications of MOFs with a number of selected examples. Besides of crystalline materials at solid phase, liquid crystals have properties that are intermediate between the solid and liquid states. In the liquid crystalline state, the three-dimensional translational ordering of the centre of mass of the molecules is partially or entirely broken. The type of order retained characterises the type of liquid crystalline phase, representing many interesting properties. Then, an over-review of this unique materials on its concept, property and

applicability are given in Chapter 7 and a typical example of optical and electrical properties of liquid crystals will be presented in Chapter 8. Chapter 9 will show experimental and theoretical studies of single crystals from a metal-organic complex, where the $C_{30}H_{30}CuN_4O_8S_2$ complex is investigated and characterized by single crystal X-ray diffraction. The last chapter study and find the relationship of crystal structures between different polymorphic forms of nonsteroidal anti-inflammatory drug fenamates and structurally related compounds, including conformational features, packing arrangements and hydrogen bonds.

From these carefully selected contents, readers will not only can learn the basic knowledge, but also keep abreast of both state-of-the-art of crystal growth and its overlaps with other subjects. Therefore, we recommend this book as a primer for students or beginners of natural sciences, materials science, and engineering. It will also work as a handbook for experienced researchers and engineers in materials, crystal growers, engineers and solid state physicists.

Nova Science Publishing, Inc.

In: Crystal Growth
Editors: J. Li, J. Li and Y. Chu

ISBN: 978-1-53612-203-9
© 2017 Nova Science Publishers, Inc.

Chapter 1

**SINGLE CRYSTAL GROWTH BY A SLOW
EVAPORATION TECHNIQUE: CONCEPT,
MECHANISMS AND APPLICATIONS**

*Sahajkumar A. Gandhi**

Physics Department, Bhavan's Shri I. L. Pandya Arts –
Science and Smt. J. M. Shah Commerce College,
Sardar Patel University, Dakor, Gujarat, India

ABSTRACT

This chapter discusses in detail various experimental techniques with its concept, mechanisms and applications of a single crystal. Growing good single crystals is an art. Single crystal is a material in which the crystal lattice of the entire sample is continuous and unbroken to the edges of the sample, with no grain boundaries. i.e., atomic arrays which are periodic in three dimension, with repeated distances are outstanding advantages of a single crystal. A good quality of single crystal is prerequisite for crystal structure determination by X-ray diffraction technique. Growth of crystal ranges from a small inexpensive technique to a

* Corresponding Author address Bhavan's Shri I. L. Pandya Arts –Science and Smt. J. M. Shah Commerce College, Dakor. Email: sahaj7@gmail.com.

complex sophisticated expensive process and the crystallization time ranges from minutes, hours, days to months. Single crystal may be produced by the transport of crystal constituents in the solid, liquid or vapor phase. Crystal growth techniques are classified into solid growth, vapor growth, melt growth and solution growth based on the phase transformation process. There are two methods in solution growth depending on the solvents and the solubility of the solute. Water is a popular solvent for the growth of a variety of inorganic and organic compounds. Crystals of nonpolar organic compounds can be grown easily from nonpolar organic solvents. Organic solvents such as acetone, acetonitrile, hexane, toluene and acetic acid and alcohols such as ethanol, methanol and propanol are also used as solvent. A solvent can also play an indirect role in changing the morphology of a crystal. Also discusses in this chapter are the factors influencing of the crystal growth. There are number of variables which influence crystallization of materials, like sample purity, selection of a proper solvent, temperature etc. In the last part of this chapter, we discusses slow evaporation method in detail with examples and applications of a single crystal.

Keywords: crystal growth, single crystal, X-ray diffractions

1. INTRODUCTION

This chapter is intended for beginners who have been working in the area of crystal growth by slow evaporation method. It is divided into three sections. The first section, starts with "Principles" which begins with this introduction, which enumerates the historical development of the field of crystal growth, nucleation and growth mechanism. The second section, deals with the preliminary idea about experimental techniques falling under solid, liquid, vapor, gel and solution growths have been discussed. In the last section, especially on details of single crystal growth of slow evaporation techniques, along with examples, results and discussions. Towards the end of the section, essentials to measure the quality of the grown crystals and applications have discussed.

1.1. Background of Crystal Growth

Crystal growth is a very old subject. Crystal growth is an interdisciplinary subject covering physics, chemistry, material science, chemical engineering, metallurgy, crystallography and mineralogy. The historical development of this subject is attractive and gorgeous. Crystals have fascinated human civilization from prehistoric times, likely because of their attractiveness, clarity and rarity. In initial times, crystallization of salt from seawater and from salt solutions must have been practiced to get cooked salt. Normally, crystallization of salt was achieved by the evaporation of water from the solution, which in modern times is called the solvent evaporation method. In the past, particularly in view of the increasing demand of materials for technological applications, interested how to grow single crystals [1]. Atomic arrays that are periodic in three dimensions, with repeated distances are called single crystals. It is clearly more difficult to prepare single crystal than poly-crystalline material and extra effort is justified because of the outstanding advantages of single crystals. Due the effect of grain boundaries, it is a very difficult to grow the single crystals from the polycrystalline materials [2-3]. In the twentieth century, the progress of crystal growth technology had been very remarkable. Various physical properties like piezoelectricity, pyroelectricity, ferroelectricity, optoelectronic were exploited in sensor, detector applications and also in semiconductor material properties. With the discovery of lasing action in ruby, crystals became amplifiers of coherent radiation also progressed rapidly. Much of this progress was initially propelled by World War II, in which the potential of crystals in a variety of applications was exploited for military purposes. A major input to the understanding of crystal growth phenomena came from the understanding of crystal structure, which was facilitated by X-ray diffraction, for which foundations were laid by Laue and Bragg [4-6]. With the knowledge of crystal structure it also became easy to predict various defect structures, which greatly influence a number of physical properties of the crystal. Electronic manufacturing, photonic industry, fiber optic communications, computer industries and pharmaceuticals depend on

materials or crystals such as semiconductors, superconductors, polarizers, transducers, radiation detectors, ultrasonic amplifiers, ferrites, magnetic garnets, solid state lasers, non-linear optics, piezo-electric, electro-optic, acousto-optic, photosensitive, refractory of different grades and crystalline films. The availability of high quality single crystals is vital for many diverse applications in solid state and quantum electronics as well as for the detailed study of the intrinsic physical properties of materials. Single crystals find important uses in research and development. To synthesize and grow single crystals of increasingly complex materials with the appropriate properties, crystal quality and homogeneity, growth conditions have to be precisely controlled while growth mechanisms need to be understood at an atomic level. This may be achieved by improving or adapting existing techniques or the development of entirely new methods.

New materials are the essence of solid state research and device technology. They are mostly discovered by crystal chemists who are crystal growers. Thus the crystallographer, especially if he develops a proficiency in relating structure, bonding and other chemo-physical considerations to properties of interest, is in a key position in determining the direction and success of solid state research and technology [7]. The perfect crystalline solid is a mathematical abstraction often useful in discussion of crystals. There is no ideal atomic lattice in nature, and it would be not very useful either. Certain imperfections of the chemical and structural atomic arrangement are essential for the usefulness and value of crystals. The high structural perfection of the crystals allows investigating intrinsic properties of the materials. That leads to more deep understanding of solid state physics and prediction of the possible applications of various substances in electronics, optics and other related areas. In research and technology many artificial crystals are required with chemical compositions from all parts of the periodic system with high chemical and in special cases even isotopic purity.

The surface layers play a very important role in the growth of crystals because they act as collectors of fresh material. Number of techniques such as electron microscopy, phasecontrast microscopy and multiple-beam interferometry are developed to study the surface of crystals. The

knowledge gained by such studies has provided valuable information concerning the way in which single crystals grow.

1.2. Single Crystal

Matter exists in three states—(i) gaseous (ii) liquid and (iii) solid. In the gaseous state, the molecules are in constant, vigorous, and random motion, freely compressible, and exhibits very low viscosity. In the liquid state, the random molecular motion is much more restricted. Unlike a gas, the volume occupied by a liquid is limited. A liquid shows a much higher viscosity than a gas and is less easily compressed. In the solid state, however, molecular motion is confined to an oscillation about a fixed position, and the structure is elastically deformable only to a small extent. Solids may be crystalline or amorphous, and the crystalline state differs from the amorphous state in the regular arrangement of constituent molecules, atoms, or ions into some fixed and rigid pattern known as a lattice. As we know, polycrystals contain grain boundaries. The grain boundaries play a vital role for measurement of property on a polycrystalline specimen. A notable example of a property where single crystals are essential is electrical conductivity, which is particularly impurity sensitive. Impurities tend to segregate at grain boundaries, thereby obstructing the passage of current. Hence, single crystals are almost always required for determining any conductivity-dependent property. Another common effect of grain boundaries and associated voids is light scattering and, hence, single crystals are required in optical studies as well. The X-ray diffraction technique involves recording of the intensity of the diffraction pattern, so the good single crystal, better the data and more accurate the structure exploring to the informations down to atomic level. Natural crystals have often been formed at relatively low temperatures by crystallization from solutions, sometimes in the course of hundreds and thousands of years.

1.3. Nucleation

All natural and artificial crystallization processes start with a nucleation. Most nucleation processes are physical, rather than chemical. Nucleation normally occurs at nucleation sites on surfaces contacting the liquid or vapor. Nucleation is one of the major mechanisms of first order phase transitions that involve a latent heat. Here, a new phase emerges from the old phase whose free energy becomes higher than the generated new phase. Nucleation of the new phase, which is an extremely localized phenomenon that bring a sufficient number of atoms or molecules together to form a stable size. Many natural processes happen due to nucleation, the most common among them being the formation of raindrops. Suspended particles also provide nucleation sites. This is called heterogeneous nucleation. Nucleation without preferential nucleation sites is called homogeneous nucleation. Homogeneous nucleation occurs spontaneously and randomly. The formation of a solid crystalline phase from liquid and gaseous solutions can occur only if some degree of supersaturation or supercooling has been achieved first in the system. The attainment of the supersaturated state is essential for any crystallization process, and the degree of supersaturation is the prime factor controlling the process. Any crystallization process can be considered to contain three basic steps:

1. Supersaturation
2. Critical nucleiation
3. Growth of crystals

In practice, all three processes may be occurring simultaneously in different regions of the same crystallization vessel. The ideal crystallization, of course, would consist of a strictly controlled sequential procedure, but the complete cessation of nucleation cannot normally be guaranteed in a growth vessel where a suspended crystal is growing. The supersaturation of a system may be achieved by cooling, evaporation, the addition of a precipitant or diluting agent, or as a result of a chemical reaction between two homogeneous phases. However, the condition of

supersaturation alone is not sufficient for crystal growth. Before crystals can grow, there must exist in the solution a number of minute solid bodies known as centers of crystallization, seeds, embryos, or nuclei. Nucleation may occur spontaneously (homogeneous), or it may be induced artificially (heterogeneous). It is not always possible, however, to decide whether a system has nucleated on its own or under the influence of some external stimulus [8-10].

To facilitate growth of crystals with diverse physicochemical properties, various crystal growth techniques were developed that were suited to obtain crystals from solid–solid, liquid–solid, and vapor–solid transitions.

2. CRYSTAL GROWTH TECHNIQUE

To synthesize and grow single crystals of increasingly complex materials with the appropriate properties, crystal quality and homogeneity, growth conditions have to be precisely controlled while growth mechanisms need to be understood at an atomic level. This may be achieved by improving or adapting existing techniques or the development of entirely new methods. A large number of crystal growth techniques are established now days and all of these techniques have its own importance and applications. Growth of crystal ranges from a small inexpensive technique to a complex sophisticated expensive process and the crystallization time ranges from minutes, hours, days and to months. Growing good single crystals is an art [11-13]. Single crystals may be produced by the transport of crystal constituents in the solid, liquid or vapour phase. In the literature, the growth techniques have been classified in a number of ways, and there is no unique way of classifying them. Classification based on the technique in manufacturing bulk crystals to thin films are also found in the literature. The growth techniques are categorized as single (mono)-component and multi (poly)-component techniques depending on the number of components present in the growing medium. For example, melt growth techniques are essentially single-

component techniques in the sense that here the material to be grown as a single crystal itself is the pioneer. However, solid-state precipitation or exsolution is an example of polycomponent solid–solid growth. Growth from a liquid solution invariably has more than one component; hence, these are polycomponent growth methods. Materials, which have high solubility and have variation in solubility with temperature, can be grown easily by solution method. They are (i) High temperature solution growth and (ii) Low temperature solution growth. The solution growth also depending on the solvents and the solubility of the solute. Crystal growth from a vapor phase may involve either monocomponent or polycomponent techniques. Based on the phase transformation process, crystal growth techniques are classified as solid growth, vapour growth, melt growth and solution growth [14]. On the basis of these, few single crystal growth techniques are discussed here in brief.

2.1. Growth from Solid

The greatest advantage of the solid–solid growth method is, it is simple to grow and possibility of contamination is minimum. The shape of the grown crystal can be predetermined and distribution of impurities can be fixed before growth. The principle of solid–solid growth methods is that the sample is simply annealed because the starting material is a solid. The main disadvantage, however, is that it is difficult to control nucleation in the solid phase and hence difficult to obtain large single crystals. Also, achieving a high degree of structural perfection is difficult. Even under ideal growth conditions, some crystallographic defects will always be present in the grown crystals. Lack of reproducibility is another problem with these techniques. Nevertheless, solid–solid growth methods are useful to grow single crystals or, more often, materials that are predominantly single crystalline and hence are being practiced. There are many techniques available under this category like- grain growth, strain annealing and solid-state transformation techniques are quite popular [15].

Grain Growth

In grain growth technique [16-17], the size of crystalline grain increases when a finely grained material is kept at high temperature for a certain duration. This grain growth occurs after the completion of recovery and recrystallization processes that bring down the internal energy of the system. Recrystallization is a process by which deformed grains are entirely replaced by a new set of undeformed grains that nucleate and grow in the matrix. Any further reduction in the internal energy would be possible only by reducing the total area of the grain boundary. It is well established that amorphous solids have excess free energy with respect to their crystalline phases, and this excess free energy is the driving force in the case of crystal growth from amorphous solids. Likewise, polycrystalline materials also have higher free energy with respect to their single crystalline counterparts.

Strain-Annealing Technique

When a body is stressed beyond its elastic limit, withdrawal of the applied stress would not lead to removal of complete strain but the body will get permanently deformed (i.e., plastically deformed). Plastically deformed bodies contain a large amount of strain energy. This stored energy is the main driving force for recrystallization in the strain-annealing technique [18-19]. In this method one generally starts with fine-grained matrix that is subjected to a minimal strain just sufficient to cause the formation of one or at most a few new grains during annealing. In principle, a single crystal can be obtained by annealing a polycrystalline specimen that has been given a critical amount of strain. If less than critical strain is applied, no grain growth will occur during annealing. For larger strains, several crystallites will result in the same specimen. Critical strain varies from material to material and is in the range of 1 to 10%. The critical strain is usually determined by straining a tapered specimen by applying suitable stress and thereby producing a strain gradient in the specimen. The strain-annealing technique has been applied extensively to iron and its alloys. It has also been used to grow crystals of several metals like tantalum, niobium and titanium [20-22].

Solid-State Phase Transformation

In growth by solid-state transformation, one initiates the process with a poly or single crystalline specimen of an undesired polymorph (usually a high temperature phase) and transforms it to the required polymorph through a structural transition. To effect the desired phase change, one may have to apply pressure, vary the temperature, or both. A classic example of these two variables being simultaneously applied is the growth of diamond through polymorphic transformation of graphite. In the case of materials undergoing phase transition, the grains of high-temperature phase are completely replaced by a new set of grains belonging to the low-temperature phase. If now the phase change takes place by continuous growth of the nuclei of the low-temperature polymorph, it is possible to produce a single crystal by allowing the specimen to cool to the transformation temperature progressively along the specimen. The usual requirement is to produce single crystals of the phase that is stable at room temperature. Retention of high-temperature phase is sometimes possible, usually by alloying, which means the phase is no longer pure and hence is not a preferred option. Low-temperature phases of refractory metals such as zirconium [23] and titanium [24] have been produced in single crystalline form by this method.

In crystal growth by phase transformation, there is a transformation front that separates the high and low temperature phases, and it is the movement of this front that leads to crystal growth. Phase transitions are usually accompanied by structural change and therefore may involve change in volume and many other properties that are relevant to crystal growth.

The solid–solid growth methods have largely been applied to refractory metals and alloys and certain ceramics. Although many advantages are attributed to solid–solid growth, because of several disadvantages associated with it, the use of these solid–solid growth methods is limited. Principal among them is the control over orientation of the grown crystal. Cross section of the specimen is often limited. Growth resulting in twinned crystals is also a problem, particularly in face-centered

cubic structures. Consequently, these techniques are not exploited extensively by the industry.

2.2. Growth from the Melts

Crystal growth from melt in essence is a mono-component liquid–solid growth. Any material that is melting congruently or near congruently can be grown by melt techniques. Ideally, in mono-component liquid–solid growth, since the rate of growth is not diffusion controlled, growth as such can be quite rapid and the purity of the resultant crystals can be quite high. It is essentially growth by controlled freezing; consequently, in comparison to other growth techniques, it is readily controllable. Except for the growth from aqueous solution, it is perhaps the earliest studied technique. Also, in all probability, it is the most exploited commercial process for single crystal growth and because of this, sophistication and automation have been introduced into the process. The simplest method of forming crystals by melt–solid equilibrium is by uncontrolled freezing of a melt. In this process, the initial nucleation is random, and the resultant product is generally a fine-grained polycrystalline ingot. Sometimes, however, single crystal grains of appreciable sizes can be identified in the solid matrix. When such large-sized grains are seen, one can infer that single crystal growth of that material can be achieved with relative ease. The noticeable techniques that fall under mono-component liquid–solid growth are as follows:

1. Bridgman technique
2. Czochralski technique
3. Zone-melting technique
4. Verneuil flame fusion technique
5. Arc fusion growth
6. Growth by skull-melting

Bridgman Technique

This technique was originally developed by Bridgman in 1925 to grow single crystals of certain metals such as tungsten, antimony, and bismuth [25], and later the method was exploited by Stock Barger to grow large crystals of lithium fluoride [26] and hence the name. However, in recent years, it is named after of its original inventor. As with all the growth techniques, since the design of the growth apparatus is material specific, the basic technique has been modified by various workers depending on the specific conditions required to grow the chosen crystals. The range of materials grown by the Bridgman technique is so broad [27-28]. The main problems in Bridgman growth is that the growth occurs by self-nucleation. As a result, the crystallographic orientation of the grown crystal is not known. However, if the crystal has an easy growth axis, this axis might coincide with the ampoule axis. Although some efforts have been made to use seed crystals in Bridgman growth, this is not very common, mainly because the seed melt interface is not visible. Hence, in most cases, the orientation of the crystal has to be determined after each growth.

Czochralski Techniques

The method that has been used to grow a wide range of materials from low melting point metal such as Ga (29.8°C) to high melting point oxide spinel, (2135°C) which is the pulling technique due originally to Czochralski [29]. This method has become very popular largely because of the rapidity with which it can produce relatively large crystals that are highly perfect. The principal advantage of crystal pulling is that the growth can be initiated on a seed under controlled conditions which arises because both the seed and the crystal are visible during growth and the crystal grower can use this facility to guide him or her to adjust various process parameters to obtain crystals with a high degree of perfection. In addition, growth in any direction can be performed when oriented seeds are available. The method also permits the addition of suitable dopants during growth. Even though it is necessary to have a crucible to melt and hold the charge that may often contaminate the charge and hence the crystal, the growing crystal is free from physical constraints imposed by the crucible.

This is mainly because the growing crystal is not in contact with the crucible.

In principle, any material with a congruent melting point can be grown by the pulling technique. Other desirable properties are high thermal conductivity, low vapor pressure, low viscosity, suitable growth habit, absence of easy cleavage, and no phase changes between the melting point of the material and room temperature. A material without the congruent melting point will have to be grown by some other method. However, lack of any of the other properties mentioned earlier can usually be overcome by some ingenious methods. By automating the growth system, the weight, shape, and quality of the crystals can be constantly monitored [30].

Zone-Melting Techniques

The zone-melting technique was first invented by Kapitza [31] to grow high-purity bismuth crystals in glass tubes to study their electrical resistivity at very low temperatures under high magnetic fields. Later, in the early 1950s, it was developed as a refining technique by Pfann [32] at Bell Telephone Laboratories in response to the demand for extremely pure germanium (melting point: 958.5°C). Purification of germanium was essential for the development of transistor, which in turn led to the revolution in electronics. Subsequently, it was applied to silicon (melting point: 1420°C) [33] and then to many more substances. In fact, zone refining can be applied to the purification of any material that melts congruently. The technique has also been used to control the discontinuities in impurity in p-n or n-p junction. Actually, zone refining is one of the several techniques grouped under the general class "zone-melting." Other techniques in this class are zone freezing, zone leveling, zone separation, float zone technique, traveling solvent method, and so on. Although developed by Pfann for the purpose of purification, it could be easily adapted to growing crystals and hence has now become an established method of growing high-purity single crystals.

Flame Fusion Technique

The flame fusion technique is a well-established technique for the growth of refractory oxide crystals. The process was developed by the French chemist Verneuil in 1902 [34] and became the first commercially successful method of manufacturing synthetic gemstones. In this technique, a flame produced by an oxy-hydrogen torch melts the powder, which rains down into a shallow pool of liquid on the top of a seed crystal; this is slowly lowered down into an after heater to produce a cylindrical crystal. The technique has the advantage of being crucible-less. In a typical growth run, finely powdered starting material is placed in a container within a Verneuil system, with a sieve at the bottom through which the powder can rain down when the container is tapped or vibrated. While the powder is being released, oxygen is supplied into the furnace and travels with the powder down a narrow tube. This tube is surrounded by a larger tube, into which hydrogen is supplied. At the point where the narrow tube opens into the larger one, a flame is formed due to combustion with a temperature of more than 2000°C at its core. As the powder passes through the flame, it melts into small droplets, which fall onto a pedestal placed below, forming a shallow pool of melt. As more droplets fall onto it, the pedestal is slowly moved downward, allowing the lower portion of the liquid to crystallize, while its cap always remains liquid. The crystal is formed in the shape of a tapered cylinder, with its diameter broadening slowly from the base and eventually remaining more or less constant. With a constant supply of powder and withdrawal of the pedestal, very long cylindrical boules can be obtained.

Arc Fusion Technique

This method is useful to produce low-cost crystals of high melting point materials. Since there is not much control on this technique, the resulting crystals are poor in quality. The method basically involves striking an arc in a large quantity of charge in the form of compacted powder taken in a water-cooled steel closure [35-36]. Graphite electrodes are used. Once a pool of molten material is formed due to arcing, the power is slowly reduced to stop the arc, and the melt is left to solidify. The

solidified mass, which contains many crystals, is broken to harvest the crystals. Crystals weighing up to half a kilogram have been grown. Since the melt is in contact with its own solid, there is no contamination due to crucible material. The shell left by taking out the crystals may be reused by refilling it with fresh material, thereby economizing the process. Introduction of certain gases sometimes improves the quality of the grown crystals. For example, it is found that by introducing argon through the hollow electrode, one could obtain much clearer MgO crystals. The number of electrodes are used for improvement. Other crystals grown by the arc fusion method are CaO, SrO, BaO, and ZrO₂.

Skull-Melting Technique

The skull-melting technique is also called the cold crucible technique. The technique allows the melt to sustain at very high temperatures (3000°C or even above). Actually, skull-melting as a crystal growth process must have evolved from growth of crystals in water-cooled crucibles using the Czochralski method [37-38]. Keeping the melt in a solid shell (skull) with a chemical composition identical to that of melt and using a contact-free method of heating the material are the two special features of this technique. Since melting is carried out through radio frequency heating using an induction furnace, superficially it looks as if the method is useful only to grow such materials which are conducting. However, most materials become conducting when hot and hence couple to the radio frequency source which eventually melt. Normally, metal of the same oxide that is to be melted to obtain crystals is used for initial coupling. Alternately, conducting cylinder-like graphite can be inserted into the insulating charge, which can be removed once the charge becomes hot and starts melting. The cold crucible usually consists of interconnected hollow sections with gaps, fabricated in the form of a cylindrical crucible. The crucible is kept cold by flowing water. The leakage of the molten charge is prevented by surface tension and wetting property of the melt as well as the size of the gaps. Materials used for water-cooled crucible are copper, brass, chromium plated brass, nickel, platinum-plated nickel, stainless

steel, rhodium-plated stainless steel, and so on. In a typical experiment, the charge is loaded into the crucible.

2.3. Crystal Growth from the Vapor Phase

Vapor growth techniques were mainly used to obtain bulk crystals. Vapor growth can either be mono-component or poly-component. Crystals grown from mono-component techniques have less contamination, but the growth will occur at higher temperature. On the other hand in poly-component techniques, the growth occurs at lower temperature, but the techniques have the disadvantage of contamination and diffusion-related problems due to presence of additional components. Basically, material transport in the vapor form is the essence of all bulk growth techniques. Crystal growth from vapor phase techniques have classified in two ways; 1. Direct Vapor Transport and 2. Chemical vapor transport.

Direct Vapor Transport

In direct vapor transport, the growth is carried out either in a closed-tube or in an open-tube system. In a closed-tube system, the material on sublimation is transported directly, the driving force being the temperature gradient. In an open-tube system, a carrier gas is additionally used to transport the species from the source region to the growth region. Here, the source material is kept at one end of the sealed tube and heated to a temperature so that it sublimes. The vapor is transported to the other end of the tube, which is at a lower temperature where it condenses to form crystallites. The transport is initiated by a difference in the partial pressures of the species to be transported. The movement is from higher to lower partial pressure, which for a sublimation reaction is from higher temperature region to lower temperature region. This method was first used by Pizzarello [39] for the growth of lead sulfide crystals. In the open tube system, the source material is vaporized at the hot end of the tube, and an inert gas flows through the tube causing transport of the vapor molecules from the higher temperature to the lower temperature side where

they deposit. If volatile components are used as starting materials and the desired compound is formed at a higher temperature, the source zone may be at a lower temperature than the crystallization zone.

Chemical Vapor Transport

The chemical vapor reactions may be reversible or irreversible. They may be simple or complex. But owing to chemical reaction, the concentration of the substances transported in the vapor phase increases sharply; hence, it is possible to crystallize even those materials that have negligible vapor pressure at crystallization temperatures. In fact, the introduction of vapor transport aided by chemical reaction is considered as one of the most important contributions to the field of crystal growth, which has tremendously enhanced the scope of vapor phase growth. Consequently, literature pertaining to chemical vapor transport is prolific.

2.4. Growth from Silica Gel

Growing crystals in gels has been known since the end of the nineteenth century. The method was initially used to grow only those crystals that had very low solubility in water. Since then, various modifications have been introduced to the basic gel method, and different types of crystals, including the ones soluble in water, have been grown with a high degree of perfection. Although the size of the crystals that could be grown by the gel method is limited, its ability to grow practically insoluble materials (in water) at room temperatures with exceedingly simple and inexpensive equipment makes the technique attractive. Also, since gel medium is almost transparent, the growing crystals can be viewed during the entire growth period. Further, since the growth occurs at room temperature, one can expect them to contain a lower concentration of equilibrium defects than those grown by high-temperature techniques. In this method, one reagent is incorporated in the gelling mixture, and the other is later diffused into the gel leading to a very high super saturation of the main product and in due course to nucleation and crystal growth. This

is, of course, growth from solution but without convection currents. This is because the gel medium prevents turbulence and provides a three-dimensional structure that permits the reagents to diffuse at a rate that can be controlled by varying the gel parameters. Further, since the gel is soft and isotropic, it exerts low and uniform constraining forces upon the growing crystals, promoting orderly growth. Also, the gel medium is chemically inert to most of the reactants and products. The other advantage is that the growing crystals are spatially separated, thereby preventing the interactions between them to a certain extent. The recent interest in gel growth has been on account of its suitability to grow crystals of biological macromolecules and studies related to bio mineralization [40]. Gels can be prepared from a variety of materials. The most commonly used ones for growing crystals are those prepared from agar, gelatin, silica, tetramethoxysilane (TMOS), and polyacrylamide. Silica gel is prepared by neutralizing the aqueous solution of sodium metasilicate with mineral or organic acids. One of the most important factors affecting the hardness of the gel medium is the density of the sodium metasilicate solution. In almost all cases, dense and hard gels have produced poor-quality crystals. On the other hand, if the gel density is too low, it will take a very long time to set, and the resulting gel will be mechanically fragile and hence unstable. Silica gel can be set by adding either acid to sodium metasilicate or sodium metasilicate to the acid. The two routes are not the same because in one case the gelation pH is approached from the acid side (pH 0.5–4.0) and in the other it is from the alkaline side (pH ~12). The gel may be allowed to set in a simple test tube with one of the reactants already added to it. Once the gel is set, the other reactant may be poured over the gel without damaging its surface. A 'U' tube may be used with the gel set at the bottom and the reactants added to the two arms of the 'U' tube. To grow copper crystals, a suitably set gel with CuSO_4 as an inner reactant is taken in a test tube. Afterward, a reducing agent such as hydroxylamine hydrochloride or hypophosphoric acid is added on the top as an outer reactant. The chemical reduction of the CuSO_4 gives the desired copper crystal inside the gel. The solubility reduction method is mainly applicable to water-soluble materials. Glocker and Soest [41] used this technique to

grow ADP (ammonium di phosphate) crystals. They diffused alcohol into a gel containing the crystal salt solution. The alcohol reduced the solubility of the compound and thereby created the nucleation, leading to the formation of the crystals. Utilizing this technique, KDP (potassium di phosphate) crystals of reasonable size have been grown [42].

2.5. Hydrothermal Growth

Hydrothermal growth is normally carried out in a sealed vertical autoclave with a temperature gradient established between the top and bottom of the vessel. Usually, the nutrient is placed in the lower, hotter part of the autoclave, and the seeds are mounted in the cooler, upper part. The seeds are single crystal plates properly oriented and mounted on a suitable wire frame. A perforated metal disc called the baffle is often placed to separate the dissolution and growth regions so that the temperature gradient is localized. Transport of hot solution from the dissolution region to the growth region containing the seeds is by convection. Once the solution reaches the growth region, it becomes supersaturated with respect to the temperature of that region and the material is deposited on the seeds. The cooler depleted solution then returns to the hotter zone by convection and dissolves more nutrients, and the cycle repeats. Because hydrothermal growth is quite involved in terms of both equipment and procedure, not many laboratories practice this technique. However, in recent years, low-pressure and moderate-temperature hydrothermal synthesis has gained prominence particularly in the preparation of nanoparticles. The success of the hydrothermal crystal growth experiments depends mainly on the quality of the autoclaves, which contain corrosive aqueous solution at high temperature and pressure. Therefore, the first consideration in the fabrication of an autoclave is the material of construction. For temperature in the range of 250°C–300°C, sealed glass or vitreous silica tubes have been used fairly successfully up to 6 atm. The use of glass in hydrothermal growth has not been explored fully because early works were mainly on the growth of materials that could not be dissolved readily in the pressure-

temperature (P-T) range attainable in glass autoclaves. Many designs have been developed for the fabrication of autoclaves. Different designs have different pressure-holding capabilities. Proper selection of the autoclave is necessary to prevent failures [43-45].

2.6. Flux Growth

The solution growth methods have been extended by the use of molten salt solvents, the technique being called flux growth. Here, the crystallization is carried out using molten inorganic compounds at elevated temperatures as a solvent and hence is actually a high-temperature solution growth process. It is also sometimes referred to as molten salt solvent growth technique. The solvents are usually called fluxes. Because there are innumerable chemical compounds available that can be used as fluxes for growing crystals, it is probably true that any material can be grown by this technique. A good compilation of phase equilibrium data is helpful in selecting a proper solvent. Temperature control is one of the most important aspects of flux growth. In the case of growth by slow cooling, it is necessary to reduce the temperature according to a predetermined program. Crystals usually nucleate first in the coolest region of the crucible. Even where great effort has been made to keep the crucible isothermal, some regions remain slightly cooler than the rest and the nucleation begins. Nucleation in flux growth is usually heterogeneous at the walls of the crucible, although spontaneous nucleation cannot be completely ruled out. If a small gradient is established between the top and bottom of the crucible, with the bottom being at a lower temperature, crystals grow at the bottom or lower side wall of the crucible. This method [46-47] has been extensively used to grow hundreds of crystals of scientific and technological importance. After the small introduction of few single crystal growth techniques detailed analysis with examples are available in the book written by H. L. Bhatt [14].

3. CRYSTAL GROWTH FROM SLOW EVAPORATION TECHNIQUE

Different techniques are well known to grow the single crystal of organic compounds viz., slow evaporation, slow cooling, vapor diffusion, liquid diffusion, sublimation etc. Slow cooling is the simplest method for single crystal growth in which the saturated solution of the compound is heated to just its boiling point or just below it and allow it to cool to room temperature. It is the most widely used method for the growth of single crystals, when the starting materials are unstable at high temperatures [48] and also which undergo phase transformations below melting point [49]. In vapor diffusion and liquid diffusion method, one solvent diffuse into the other while precipitating the product that results into depositing crystals. Sublimation is different than above listed methods of crystal growth. In this method compound is heated under vacuum and crystals are collected on cold-finger. Slow evaporation technique is used to grow the single crystals of these heterocyclic compounds from different solvents like water, methanol, chloroform, ethanol, ethyl acetate.

3.1. Slow Evaporation Technique

In the Slow evaporation method, crystals are grown from the saturated or nearly saturated solution of the compound, prepared using different solvents like methanol, ethanol, acetonitrile, ethyl acetate or mixture of any two solvents with varying proportions and is allowed to stand without disturbance as shown in Figure 1. Solvent evaporates slowly resulting in the precipitation of the compound in the form of single crystal. It is the best way to grow single crystals by solution technique. Growth of good quality single crystals by slow evaporation techniques require optimized conditions. The use of a range of temperatures may not be desirable because the properties of the grown material may vary with temperature. There are so many factors affecting on the mechanism of crystallization

like, the interaction of ions/molecules of the solute, the solubility of substance and thermodynamic parameters of the process; temperature, pressure and solvent concentration. The choice of the solvent is very important because it can greatly influence the mechanism of crystal.

3.2. Choice of Solvent and Solubility

Water is a popular solvent for the growth of a variety of inorganic and organic compounds. A simple thumb rule in proper selection of a solvent is chemical similarity between the solvent and the compound to be grown. For example, crystals of nonpolar organic compounds can be grown easily from nonpolar organic solvents. Chemical similarity also determines solute solubility in the solvent. Various experiments reveal that a solvent in which the compound has solubility between 10 and 60% at a given temperature is economically suitable for crystal growth. Very low and very high solubility of a solute provide low growth rates due to low solute concentration and increased viscosity, respectively. Organic solvents such as acetone, acetonitrile, hexane, toluene and acetic acid and alcohols such as ethanol, methanol and propanol are also used as solvent [50]. A solvent can also play an indirect role in changing the morphology of a crystal. The solvent changes the structure of the solute molecules, which subsequently adsorb on several faces of the crystal, thereby blocking their normal growth. The solvent has a strong influence on the habit of crystalline materials because solvent molecules affect the growth rates of different faces appearing in the crystal morphology differently. Solution is a homogeneous mixture of a solute in a solvent. Solute is the component, which is present in a smaller quantity. If the solubility is too high, it is difficult to grow bulk single crystals and too small a solubility restrict the size and growth rate of the crystals. Solubility gradient is another parameter, which dictates the growth procedure.



Figure 1. Slow evaporation method: Beaker and test tubes are used for allowed to stand without disturbance.

3.3. Factors That Influence the Crystal Growth

There are number of variables which influence on crystallization of organic materials.

- *Sample purity*: The poor purity is one of the most common cause of unsuccessful crystallization and at the same time, the selection of a proper solvent for a given crystallization is difficult to predict.

- *Selection of a proper solvent:* A mixture of two or more solvents is occasionally found to possess the best properties for a particular crystallization purpose. To reduce the solubility of the solute, another solvent is added to a solution causing its precipitation and maximize the yield of the product. However it is expected that both the liquids must completely mix with one another.
- *Temperature:* Other environmental variables which influence crystallization include the rates of change of temperature and concentration of solution.
- *Viscosity of solvent:* The viscosity of the solvent directly affects the rate of crystal growth through its influence on the solute flux. Increased volatility of the solvent raises the rate of increase in concentration of the solution, speeding up both nucleation and growth.
- *Chemical nature of solution:* The chemical nature of the solution also plays a leading role in the crystallization process. The nature of solute-solvent interactions influences the balance in stabilities of solid and solution and therefore affects the energy of crystallization. If these interactions are strong, they may also act as a retarding force on nucleation and growth rates.

3.4. Results and Discussion

The compounds picked up for the present study are chalcones. Chalcone is an aromatic ketone and an enone that forms the central core for a variety of important biological compounds, which are known collectively as chalcones or chalconoids. Benzylidene acetophenone is the parent member of the chalcone series. The alternative names given to chalcone are phenyl styryl ketone, benzalacetophenone, β -phenylacrylophenone and α -phenyl- β -benzoyl ethylene. In the chemical structure, three carbon $\alpha - \beta$ unsaturated carbonyl system, the backbone of the open chain flavonoid, joins two aromatic rings. The chemical structure with physical properties of chalcone is shown in Table 1. Chalcone can be

prepared by an aldol condensation between a benzaldehyde and acetophenone in the presence of sodium hydroxide as a catalyst (Figure 2). Kinetic studies have been reported for the base-catalyzed formation of chalcone and its derivatives [51-52].

Table 1. Chemical structure and physical properties of chalcone

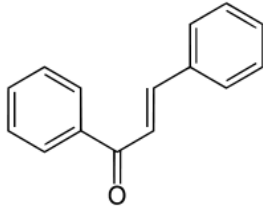
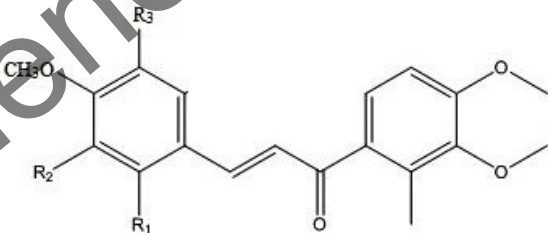
	
<i>Physical Properties</i>	
Molecular formula	C ₁₅ H ₁₂ O
Molar mass	208.26 g mol ⁻¹
Density	1.071 g/cm ³
Melting point	55–57 °C
Boiling point	345–348 °C

Table 2. Three different chalcone derivative

				
No.	R ₁	R ₂	R ₃	
1.	H	Cl	OCH ₃	
2.	H	Cl	H	
3.	Cl	OH	H	

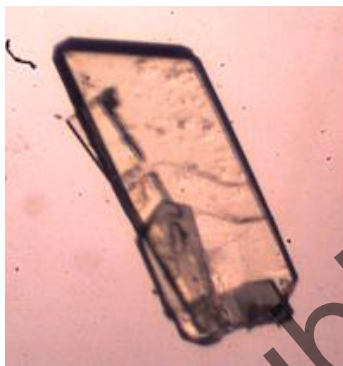
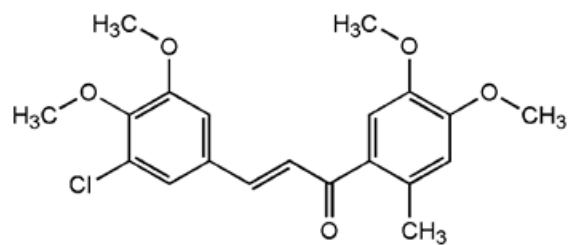


Figure 2. Chemical structure & single crystal Photograph of the molecule 1.

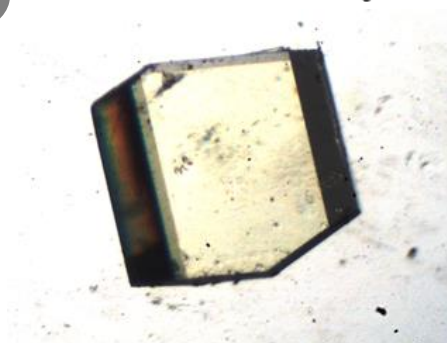
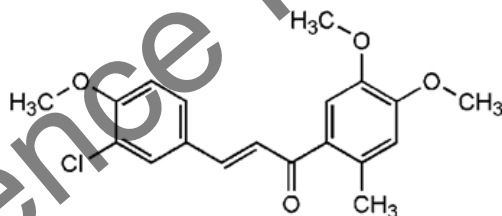


Figure 3. Chemical structure & single crystal Photograph of the molecule 2.

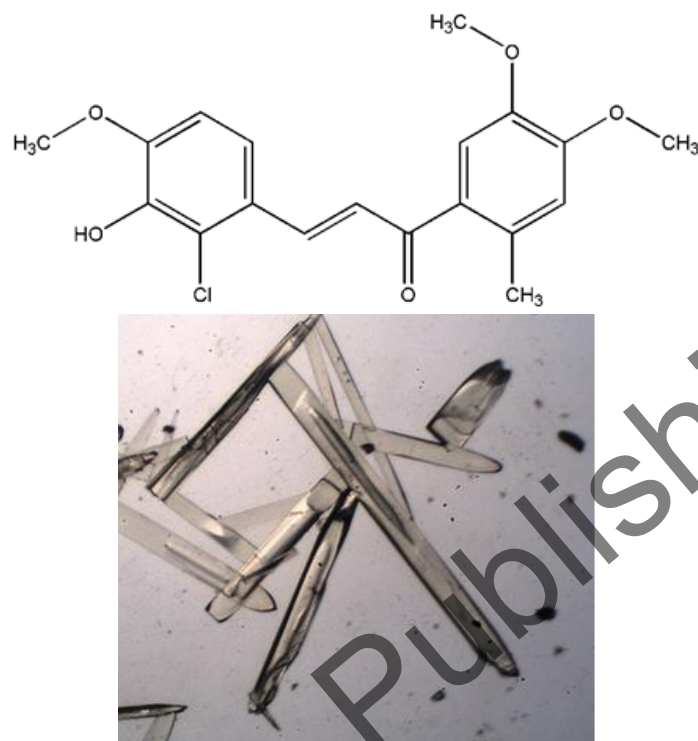


Figure 4. Chemical structure & single crystal Photograph of the molecule 3.

The chalcone (1, 3-diaryl-2-propenones), belongs to a flavonoid family, and their derivatives are important intermediates in organic synthesis [53]. The derivatives of chalcone, synthesized or the natural one, display many interesting properties like anti-inflammatory [54], antifungal [55], antioxidant [56], antimalarial [57], antituberculosis [58], analgesic [59], anti HIV [60] and anticancer [61] activities. These groups of compound constitute an important class of natural products and its derivatives have attracted particular interest in medicine during the last few decades. In view of the pharmacological importance of chalcone, author has determined crystal structures of three novel chalcone derivatives with halogen, hydroxy and methoxy moieties substituted at different sites at (4, 5-dimethoxy-2-methyl-phenyl) prop-2-en-1-one (as shown in Table 2).



Figure 5. Bruker AXS Kappa Apex II diffractometer.

Table 3. X-ray crystallographic data

	Mol. 1 R₁ = H, R₂ = Cl, R₃ = OCH₃	Mol. 2 R₁ = H, R₂ = Cl, R₃ = H	Mol. 3 R₁ = Cl, R₂ = OH, R₃ = H
Crystal System	Monoclinic	Triclinic	Orthorhombic
a	23.540(11) Å	7.0992(2) Å	14.2134 (4) Å
b	9.738(4) Å	9.3464(3) Å	10.2802 (2) Å
c	17.305(7) Å	13.2331(4) Å	24.2786 (7) Å
α	90.00 (0)°	79.954(2)°	90.00 (0)°
β	106.37(3)°	82.4490(10)°	90.00(0)°
γ	90.00 (0)°	80.6030(10)°	90.00 (0)°
Space group	C2/c	P1—	Pbcn
Density (gm/cm³)	1.314	1.358	1.359
Z	8	2	8
R[F² > 2σ(F²)]	0.0612	0.0431	0.0395
Goodness of fit (S)	1.048	1.041	1.017

As a part of collaborative research with Dr. V. M. Barot, P. G. Center in Chemistry, Smt. S. M. Panchal Science College, Talod, Gujarat, the synthesis of the title compounds have been carried out. The pure powder of the compound is soluble in methanol, ethanol and ethyl acetate. The chemical structures are confirmed by ^1H NMR, ^{13}C NMR and IR data. Transparent and diffraction quality single crystals of the all three chalcone compounds are grown by slow evaporation technique using ethanol as the solvent at room temperature. The chemical structure of the compounds 1, 2 and 3 with their single crystal photographs are shown in Figure 2, 3 and 4, respectively.

A suitable sample of single crystal is selected for crystallographic study. All diffraction measurements are performed at room temperature 293(2) K using graphite monochromated $\text{MoK}\alpha$ radiation of wavelength 0.71073 Å. The three dimensional X-ray intensity data are collected from a crystal using φ and ω scans mode on a KAPPA APEX II CCD diffractometer (Figure 5) at Department of Physics, Sardar Patel University, Vallabh Vidyanagar. The cell refinement and data reductions are obtained using Bruker SAINT programme. Preliminary crystallographic data and details of the data collection and structure refinements are listed in Table 3 for all three chalcone derivatives.

CONCLUSION

Looking towards the importance of the chalcone compounds, we have picked up three important chalcone derivatives for growing single crystal using slow evaporation method. X-ray Crystallographic investigations has been done for these three chalcone derivatives. Crystal system of mol. 1, mol. 2 and mol. 3 are monoclinic, triclinic and orthorhombic system, respectively.

REFERENCES

- [1] Brice, J. C. (1986). Crystal growth processes. Glasgow, UK: Blackie.
- [2] Laudise, R. A. and J. W. Nielsen (1961). Hydrothermal crystal growth. In Solid state physics, Vol. 12, edited by F. Seitz and D. Turnbull. New York: Academic Press, pp. 149–222.
- [3] Ballman, A. A., and R. A. Laudise. 1963. Hydrothermal growth. In The art and science of growing crystals, edited by J. J. Gilman. New York, NY: John Wiley, pp. 231–251.
- [4] Laue, M. (1912). Eine Quantitative Prufung der Theorie fur die Interferenz-Erscheinungen bei Rontgenstrahlen. *Sitz. ber. Bayer. Akademie d. Wiss* 8, 363–373.
- [5] Bragg, W. L. (1912). X-rays and crystals. *Nature* 90, 219.
- [6] Bragg, W. L. (1912). The diffraction of short electromagnetic waves by a crystal. Proceedings of the Cambridge Philosophical Society 17, 43–57.
- [7] Van Bueren, H. G. (1960). Imperfection in crystals, North-Holland, Amsterdam.
- [8] Fahrenheit, D. B. (1724). Experimentaet Observationes de Congelatione aquae in vacuo factae. *Philosophical Transactions of the Royal Society* 33, 381–391.
- [9] Gibbs, J. W. (1876). On the equilibrium of heterogeneous substances. *Transactions of the Connecticut Academy of Arts and Sciences* 3, 108–248.
- [10] Mullin, J. W. (1961). Crystallization. London: Butterworths, p. 104.
- [11] Robert, A. L. (1970). The Growth of Single Crystals, Prentice-Hall.
- [12] Pamplin, B. R. (1980). Crystal Growth, 2nd edition, Pergamon Press, New York.
- [13] James, J. A. and Kell R. C. (1975). Crystal Growth, Pergamon Press, New York.
- [14] H. L Bhat (2015). Introduction to Crystal Growth Principles and Practice, CRC Press Taylor & Francis Group.
- [15] Humphreys, F. J. and Hatherly M. (1995). Recrystallization and related annealing phenomena. Oxford, UK: Elsevier.

- [16] Aust, K. T. (1963). Large crystals grown by recrystallization. In *Art and science of growing crystals*, edited by J. J. Gilman. New York, NY: John Wiley, pp. 452–478.
- [17] In-Kwon, J., K. Doh-Yeon, Z. G. Khim, and S. J. Kwon. (1989). Exaggerated grain growth during the sintering of Y·Ba·Cu·O superconducting ceramics. *Materials Letters* 8, 91–94.
- [18] Laudise, R. A. (1970). *The growth of single crystals*. New York, NY: Prentice Hall.
- [19] Bailey, D. J., and Brewer, E. G. (1975). Improved strain-anneal crystal growth technique. *Metallurgical Transactions A* 6, 403–408.
- [20] Seraphim, D. P., J. I. Budnick, and N. B. Ittner (1960). Extractive metallurgy division Single-crystal growth and purification of tantalum. *Transactions of the Metallurgical Society of AIME* 218, 527–534.
- [21] Digges, T. G., and M. R. Achter. (1964). Growing large single crystals of niobium by the strain-anneal method. *Transactions of the Metallurgical Society of AIME* 230, 1737–1737.
- [22] Churchman, A. T. (1954). The slip modes of titanium and the effect of purity on their occurrence during tensile deformation of single crystals. *Proceedings of the Royal Society of London A* 226, 216–226.
- [23] Mills, D., and G. Craig. (1966). Etching dislocations in zirconium. *Journal of Electrochemical Technology* 4, 300.
- [24] Cass, T. R., R. W. Quinn, and Spencer, W. R. (1968). Growth of hexagonal titanium and titanium-aluminum single crystals. *Journal of Crystal Growth* 2, 413–416.
- [25] Bridgman, P. W. (1925). Certain physical properties of single crystals of Tungsten, Antimony, Bismuth, Tellurium, Cadmium, Zinc, and Tin. *Proceedings of the American Academy of Arts and Sciences* 60: 305–383.
- [26] Stockbarger, D. C. (1936). The production of large single crystals of lithium fluoride. *Review of Science Instruments* 7: 133–136.
- [27] Brice, J. C. (1986). *Crystal growth processes*. Glasgow, UK: Blackie.

- [28] Hurle, D. T. J. (1994). Hand book of crystal growth. Amsterdam: North Holland.
- [29] Czochralski, J. (1917). Ein neu es Verfahren zur Messung der Kristallisationsgeschwindigkeit der Metalle [A new method for the measurement of the crystallization rate of metals]. *Zeitschrift fur Physikalische Chemie* 92, 219–221.
- [30] Tatarchenko, V. A. (1994). Shaped crystal growth. In *Handbook of crystal growth*, Vol. 2, edited by D. T. J. Hurle. Amsterdam: North Holland, pp. 1015–1110.
- [31] Kapitza, P. (1928). The study of the specific resistance of bismuth crystals and its change in strong magnetic fields and some allied problems. *Proceedings of the Royal Society of London A* 119, 358–443.
- [32] Pfann, W. G. (1952). Principles of zone melting. *Transactions of the American Institute of Mining and Metallurgical Engineers* 194, 747–753.
- [33] Keck, P. H., and M. J. E. Golay. 1953. Crystallization of silicon from a floating liquid zone. *Physical Review* 89, 1297–1297.
- [34] Verneuil, A. (1902). Production artificielle du rubis par fusion. *Comptus Rendus* 135, 791–794.
- [35] Falckenberg, R. (1978). The Verneuil process. In *Crystal growth: Theory and techniques*, Vol. 2, edited by C. H. L. Goodman. New York, NY: Plenum Press, pp. 109–184.
- [36] Schupp, L. J. (1968). Magnesia crystals grown in carbon arc furnace. *Electrochemical Technology* 6, 219–221.
- [37] Osiko, V. V., M. A. Borik, and E. E. Lomonova (2010). Synthesis of refractory materials by skull melting techniques. In *Springer handbook of crystal growth*, edited by G. Dhanaraj et al. New York, NY: Springer, pp. 443–477.
- [38] Kuzminov, Y. S., E. E. Lomonova, and V. V. Osiko. (2008). *Cubic Zirconia and skull melting*. Cambridge, UK: Cambridge International Science.
- [39] Pizzarello, F. (1954). Vapor phase crystal growth of lead sulfide crystals. *Journal of Applied Physics* 25, 804–805.

- [40] Kalkura, S. N., and S. Natarajan. (2010). Crystallization from gels. In Springer handbook of crystal growth, edited by G. Dhanaraj et al. New York, NY: Springer, pp. 1607–1636.
- [41] Glocker, D. A., and I. F. Soest. 1969. Growth of single crystals of monobasic ammonium phosphate in gel. *Journal of Chemical Physics* 51, 3143–3143.
- [42] Brezina, B., and M. Havrankova. 1971. Growth of KH_2PO_4 single crystals in gel. *Materials Research Bulletin* 6, 537–543.
- [43] Byrappa, K. (1994). Hydrothermal growth crystals. In Handbook of crystal growth, edited by D. T. J. Hurle. Amsterdam: North Holland, pp. 465–562.
- [44] Byrappa, K. (2010). Hydrothermal growth of polyscale crystals. In Springer handbook of crystal growth, edited by G. Dhanaraj et al. New York, NY: Springer, pp. 599–653.
- [45] Laudise, R. A., and J. W. Nielsen. (1961). Hydrothermal crystal growth. In Solid state physics, Vol. 12, edited by F. Seitz and D. Turnbull. New York: Academic Press, pp. 149–222.
- [46] Elwell, D., and H. J. Scheel. (1975). Crystal growth from high temperature solution. London, UK: Academic Press.
- [47] White, E. A. D. (1965). Growth of single crystals from the fluxed melt. In Techniques of inorganic chemistry, Vol. 4, edited by H. B. Jonassen and A. Weissberger. New York: John Wiley, pp. 31–63.
- [48] Chernov, A. A. (1984). 'Modern Crystallography,' III-Crystal Growth, Springer Series, Solid State, 36, Berlin.
- [49] Buckley, H. E. (1951). 'Crystal Growth,' John Wiley and Sons, New York.
- [50] Algra R. E., Graswinckel W. S., Enkevort W. J. P and Vlieg E. (2005). 'Alizarin crystals: An extreme case of solvent induced morphology change,' *J. Crystal Growth*, Vol. 285, pp. 168-177.
- [51] Boydston, A. J., Williams K. A. and Bielawski, C. W. (2005). *Journal of the American Chemical Society*, 127, 12496.
- [52] P. L. Nayak and M. K. Rout (1975). *Journal of the Indian Chemical Society*, 52, 809.

-
- [53] E. Coombs and D. P. Evans (1940). *Journal of Chemical Society*, 1295.
- [54] Straub, T. S. (1995). *Tetrahedron Letter*, 36, 663.
- [55] Ballesteros, J. F., Sanz, M. J., Ubeda, A, Miranda, M. A., Iborra, S., Paya, M. and Alcaraz, M. (1995). *Journal of Medicinal Chemistry* 38, 2794.
- [56] Go, M. L., Wu X. and Liu, X. L. (2005). *Current Medicinal Chemistry* 12, 483.
- [57] Sivakumar, P. M., Prabhakar, P. K. and Doble, M. (2010). *Medicinal Chemistry Research*, 19, 1-17.
- [58] Awasthi, S. K., Mishra, N., Kumar, B., Sharma, M., Bhattacharya, A., Mishra, L. C. and Bhasin, V. K. (2009) *Medicinal Chemistry Research* 18, 407-420.
- [59] Sivakumar, P. M., Geetha Babu, S. K. and Mukesh, D. (2007). *Chemical and Pharmaceutical Bulletin* 55, 44.
- [60] Viana, G. S., Bandeira, M. A. and Mantos, F. J. (2003) *Phytomedicine* 10, 189.
- [61] Achanta, G., Modzelewska, A., Feng, L., Khan, S. R. and Huang, P. (2006) *Molecular Pharmacology* 70, 426-433.

In: Crystal Growth
Editors: J. Li, J. Li and Y. Chu

ISBN: 978-1-53612-203-9
© 2017 Nova Science Publishers, Inc.

Chapter 2

**TARGETED SYNTHESIS OF METASTABLE
COMPOUNDS AND INTERGROWTHS:
THE MODULATED ELEMENTAL
REACTANTS METHOD**

*Marco Esters and David C. Johnson**

Department of Chemistry, University of Oregon, Eugene, OR, US

ABSTRACT

The controlled and targeted synthesis of new solid materials is still a challenge difficult to overcome. Slow diffusion rates and long diffusion lengths require long reaction times and high synthesis temperatures, resulting in a loss of control over the reaction pathway. The Modulated Elemental Reactants (MER) method uses compositionally modulated precursors with atomically thin elemental layers that form amorphous alloys upon annealing, but can maintain composition modulation. In this amorphous intermediate, nucleation and not diffusion control the formation of the product, which enables kinetic control of the reaction,

* Corresponding Author: davej@uoregon.edu.

and the synthesis of new metastable compounds and heterostructures with designed nanoarchitecture.

Keywords: thin films, kinetic control, metastability, heterostructures, designed materials

INTRODUCTION - RETHINKING SOLID STATE SYNTHESIS

Throughout history, the search and discovery of new materials and compounds has been an important driving force for innovation and transformation of human society. From early metallurgy to complex nanomaterials, and from the extraction of herbal medical ingredients to the targeted synthesis of potent drugs, the emergence of new materials and compounds has continuously changed the way humans lived. While many materials have already been discovered, it is predicted that they still make up only the tip of the iceberg [1]. Using a purely combinatorial approach, the total number of possible systems N , i.e., without taking different compositions and polymorphs into account, increases exponentially:

$$N = \sum_{k=1}^n \frac{n!}{k!(n-k)!} = 2^n - 1 \quad (1)$$

where k is the number of elements in a compound and n is the number of elements that can form a compound. Using $n = 95$ (the number of elements of which compounds are known), the maximum number of combinations is approximately 4×10^{28} . The numbers of element combinations for each individual k are displayed in Figure 1a. Including different possible compositions and structures, this number easily increases to 10^{90} , making this parameter space impossible to explore in an unrestricted manner [1]. The number of known structures is significantly smaller as it is more challenging to include an increasing number of elements (Figure 1b).

For solids, significant effort has been expended to develop computational algorithms dedicated to finding stable structures. Notable

examples are genetic algorithms and explorations of energy landscapes [2, 3]. However, even when a material is predicted to be thermodynamically stable, i.e., it lies in the global minimum in the parameter space, finding the synthesis route to obtain it, ideally while using as little energy and time as possible, is one of the biggest challenges in chemical synthesis. Such a synthesis should ideally have a controllable reaction pathway that yields exactly the desired product and nothing but the desired product. The difficulty to meet these goals is even further amplified when trying to synthesize compounds that lie in local minima of the parameter space.

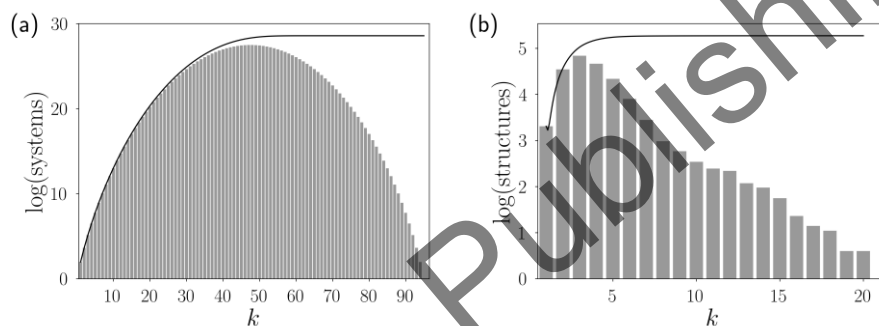


Figure 1. (a) Number of possible element combinations as a function of components in the system k . (b) Number of entries for structures in the International Crystal Structure Database (ICSD) as a function of elements in the structure k as of January 2017. The lines represent the cumulative sums.

Significant strides to control this reaction pathway have been made in the synthesis of organic compounds where different pathways with different activation energies can be accessed to end in a local minimum instead of a global minimum (Figure 2a). The simplest way is reducing the temperature below the activation energy required to synthesize the thermodynamic product, but high enough to overcome the activation energy to another reaction pathway that leads to a kinetic product. Other methods to open new reaction pathways are to change the energy landscape by functionalizing molecules with electron donating and electron withdrawing groups as it is done in electrophilic substitutions, or by stabilizing a byproduct/leaving group. A different approach is to block

certain reaction pathways by employing protective groups. These protective groups can also be used to limit diffusion access to certain sites of the molecule through steric hindrance.

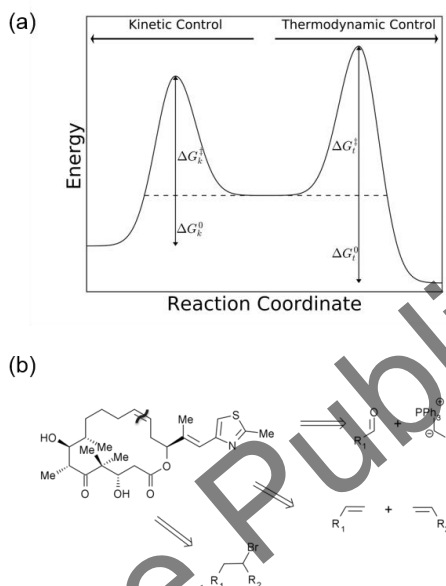


Figure 2. (a) Schematic reaction pathway for kinetically and thermodynamically controlled reactions. ΔG_k^\ddagger and ΔG_t^\ddagger are the activation energies, and ΔG_k^0 and ΔG_t^0 are the Gibbs free enthalpies for the kinetically and thermodynamically controlled reactions, respectively. (b) Retrosynthesis of Epothilone C with three possible reactions to form the double bond.

Moreover, many reaction mechanisms and many reactions that manipulate specific functional groups or sites are well known for organic reactions. As a result, design principles could be established that allowed the development of viable synthesis routes based on the target molecule alone. An example of such an analysis is shown in Figure 2b. This retrosynthetic approach proved to be so impactful that it earned Elias J. Corey the Nobel prize in chemistry in 1990, and nowadays, even software to perform retrosynthetic analysis exists [4, 5].

For the synthesis of solids, however, kinetic control and systematic synthesis approaches have not been realized yet to the degree that exists in organic chemistry. Solid state reactions can only occur at interfaces, which adds significant challenges that do not exist in the reactions of discrete molecules in a homogeneous solution.

Since powders are inherently inhomogeneous, the ratio of interface to bulk is very low. This makes observing the processes at the interfaces, and thus determining the reaction mechanisms, extremely challenging because not only is the volume of interest very small, but it also needs to be selectively probed. Moreover, the reaction is limited by diffusion, which follows the Arrhenius equation in solids:

$$D = D_0 e^{-\frac{E_A}{kT}} \quad (2)$$

where D is the diffusion coefficient, D_0 is the diffusion coefficient at infinite temperature, E_A is the activation energy for diffusion, T the temperature, and k the Boltzmann constant. D is extremely small for solids, so very high temperatures and long reaction times are typically required for solid state syntheses. Consequently, many reaction pathways that could lead to local minima are either not available, or the product does not remain inside these minima and instead converges to the most stable product or products.

Further complications arise when compounds with three or more different elements are being synthesized from three or more reactants. Since it is very unlikely that all three reactants meet at the same interface, intermediates need to form. These intermediates may be thermodynamically more stable than the desired product, leading to a dead end. Kinetic control in solid state synthesis is thus extremely challenging and in many cases not possible yet.

Many approaches have been devised to overcome these drawbacks. Most of them are focused on increasing diffusion rates by introducing a fluid phase. One method, hydrothermal synthesis, uses aqueous solutions at high temperatures and high vapor pressures, so crystals that are unstable at high temperatures can be grown. While this method gave access to a wide

variety of metastable aluminosilicates (zeolites) and phosphates, controlling and observing the reaction is very difficult [6]. Similar approaches using liquid metals, low temperature eutectic mixtures or polychalcogenide fluxes provide access to new compounds, but the reaction mechanisms are not known.

Another common approach is to use starting materials that are structurally similar to the desired product, which can even be applied to traditional solid state synthesis. One example of such a reaction is the synthesis of the Zintl phases Rb_7NaSi_8 and Cs_7NaSi_8 from Na_4Si_4 and Rb_4Si_4 and Cs_4Si_4 , respectively [7, 8]. Various *chimie douce* methods also use precursors that undergo low-temperature reactions such as intercalation/deintercalation, ion exchanges, dehydration, etc. Sol-gel methods and co-precipitation reactions use solutions as the starting materials instead of solids [9, 10]. All of these methods have the disadvantage that the selection of precursors is limited either due to a lack of structurally similar materials or because there are no soluble precursors available.

This chapter will introduce another precursor-based approach, the Modulated Elemental Reactants method (MER) [11]. MER uses compositionally modulated, atomically thin, elemental precursors prepared with physical vapor deposition to control the starting local composition and structure to increase the total interfacial area and significantly reduce diffusion lengths. As a result, synthesis times and temperatures are greatly reduced, resulting in kinetically controlled reactions.

First, a description of the MER technique and the rationale behind it will be provided, followed by case studies of the Nb-Se and the Fe-Si systems to demonstrate how MER precursors can be used to provide insights into the mechanisms of solid state reactions. It will further be demonstrated that these insights can be exploited to synthesize ternary compounds without binary intermediates ($\text{Cu}_x\text{Mo}_6\text{Se}_8$) and metastable compounds such as FeSb_3 , and to control the crystallographic alignment of the final structure such as in highly textured CuCr_2Se_4 films.

The last part of this chapter will present the synthesis of the intergrowths of main group element monochalcogenides and transition

metal dichalcogenides with the general formula $[(MX)_{1+\delta}]_m[(TX_2)]_n$ (M: Sn, Pb, Bi, rare earth metal; T: transition metal; X: S, Se, Te; m, n : integer; $\delta < 1$). Similar compounds can be synthesized as misfit layer compounds using thermodynamic methods where m and n are typically limited to 1. With the kinetic control MER offers, m, n , and the sequence of layers can be varied at will, enabling tens of thousands of these compounds to be prepared for each M and T. First, the synthesis and structure of these compounds will be presented, as well as the challenges these compounds pose to structure determination techniques. The versatility of this technique will be further demonstrated by introducing a new type of structural isomerism, and by presenting the synthesis of intergrowths with MX and TX_2 alloys, and intergrowth compounds of BiSe where the additional valence electron in BiSe causes interesting changes in the structure, namely the appearance of anti-phase boundaries.

THE MODULATED ELEMENTAL REACTANTS (MER) METHOD

Precursor Synthesis and Analysis

Solid state synthesis is challenged by low diffusion rates, long diffusion paths, and small interfacial areas, requiring high temperatures and long reaction times, which makes kinetic control of the reaction pathway very difficult. The Modulated Elemental Reactants (MER) method addresses two of these drawbacks, long diffusion paths and small interfacial areas, by using compositionally modulated, layered thin film precursors with individual layers being only a few Ångström thick. The individual layers are repeated a set number of times to achieve a desired total film thickness. The repeated set of atomic layers will be referred to as the *repeating unit* and its thickness, the modulation wavelength of the precursor, as the *repeat unit thickness* t_{repeat} .

A representation of such a precursor is shown in Figure 3. As the figure demonstrates, the number of atoms that are not close to an interface is very low, which greatly reduces the need for atoms to diffuse through the solid. Moreover, the distances an atom needs to travel to reach an interface are only a few Ångström, which is a very short diffusion length. Both factors do not require a large diffusion coefficient, which should greatly reduce reaction temperatures and reaction times, since the atoms that need to diffuse only need to travel very short distances.

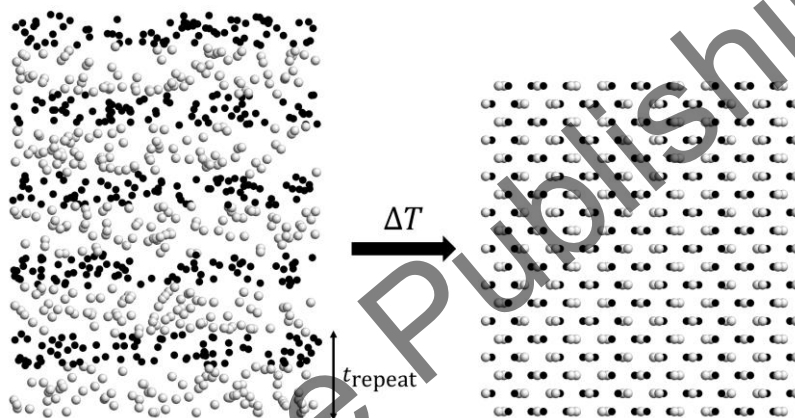


Figure 3. Schematic representation of an MER precursor of alternating atomic layers of Nb and Se that reacts to form Nb_5Se_4 . t_{repeat} is the repeat unit thickness of the Nb-Se repeating unit. Nb atoms are gray, Se atoms are black.

Precursors are synthesized using physical vapor deposition (PVD) in a custom-built vacuum chamber [12]. Chalcogens and antimony are evaporated using an effusion cell with resistive heaters whereas metals with very low vapor pressures are evaporated using electron beam guns. Deposition rates (typically less than 1 \AA s^{-1}) are controlled using quartz crystal microbalances (QCMs). Shutters are used to control the elements deposited onto the substrate. To control the thickness of the individual layers, the shutters can be opened for a specified time or the shutters can be controlled by the QCMs that close the shutters at a specified thickness is achieved.

Since the microbalances are typically situated below the substrate, neither the product of the time the shutters are opened times the deposition rate, nor the thickness measured with the QCMs directly, corresponds to the thickness of the layer on the substrate. The deposition parameters thus need to be calibrated for composition and thickness. For this, the parameters of one element will be held constant while the parameters of the other element are systematically varied.

The composition of the precursors can be determined using electron probe microanalysis (EPMA) and x-ray fluorescence spectroscopy (XRF) [13, 14]. The repeat unit thickness of the precursor can be determined using x-ray diffraction (XRD) and Bragg's law of diffraction. X-ray reflectivity (XRR) can be used to determine the total thickness of the precursor using a modified version of Bragg's law:

$$\left(n + \frac{1}{2}\right) \lambda = 2d(\sin \theta - \sin \theta_c)^2 \quad (3)$$

where n is a positive integer, λ the wavelength, d is the total thickness of the layer, θ the angle between the x-ray source and the sample, and θ_c is the critical angle of reflection.

Figure 4 shows representative XRR patterns of a precursor with 42 Ti-Se bilayers. The thickness read on the QCM for the Se layers was kept constant while the thickness of the Ti layer, t_{Ti} , was systematically increased to create the different samples.

The maxima of the oscillations in the XRR pattern, the Kiessig fringes, shift systematically to lower 2θ with increasing t_{Ti} because of an increased total film thickness. Above $5^\circ 2\theta$, a broad maximum with higher intensity than the Kiessig fringes can be observed, which can be described with Bragg's law of diffraction. The repeating electron density that is responsible for diffraction comes from the modulated nature of the precursors, and the d -spacing corresponds to its repeat unit thickness t_{repeat} .

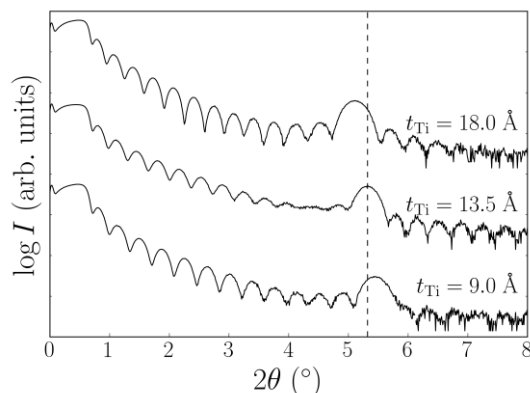


Figure 4. XRR patterns for Ti-Se precursors. The Se thickness read by the QCM was kept constant at 54.9 \AA , and the thickness of Ti (t_{Ti}) was varied. The vertical line corresponds to the Bragg reflection maximum for $t_{Ti} = 13.5 \text{ \AA}$. Offset added for clarity.

If the sticking coefficients of the elements are constant and if depositions are consistent, a linear increase in t_{Ti} should result in a linear increase in the Ti:Se ratio and in t_{repeat} . Systematically varying t_{Ti} can then be used as a calibration procedure to find the parameters for the desired t_{repeat} and the desired precursor composition. Figure 5 shows such calibration curves. The slopes show the change in the Ti:Se ratio and the repeat unit thickness per Angström of Ti read by the QCM. The intercept in Figure 5b, 15.25 \AA , is the actual thickness of the Se layer in the film. The thickness read by the QCM was 59.4 \AA , so only 25% of the Se deposited onto the QCM is actually deposited onto the substrate, emphasizing the importance of this calibration procedure. Assuming that no excess Se is added to the precursor, t_{Ti} for a precursor for $TiSe_2$ should have a value of:

$$t_{Ti} = \frac{1}{2} \cdot \frac{1}{0.022} \text{ \AA} = 22.7 \text{ \AA} \quad (4)$$

This would result in a repeat unit thickness of:

$$t_{repeat} = 0.103 \cdot 22.7 \text{ \AA} + 15.254 \text{ \AA} = 17.6 \text{ \AA} \quad (5)$$

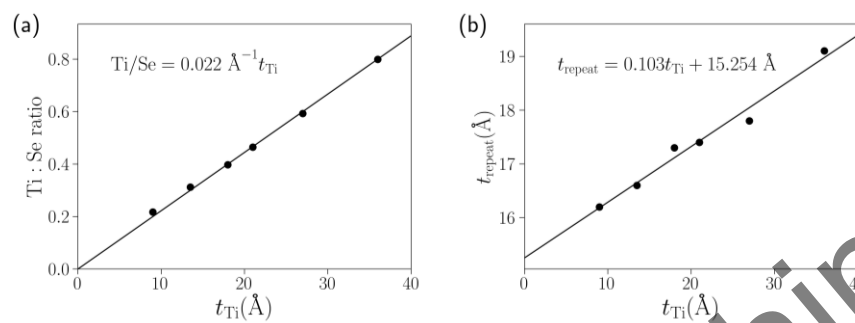


Figure 5. Calibration data for a Ti-Se precursor. The Se thickness read by the quartz crystal microbalance was kept constant at 54.9 Å, and the thickness of Ti (t_{Ti}) was varied. (a) Composition calibration. (b) Repeat unit thickness (t_{repeat}) calibration. The insets show the results of the linear fits through the data.

Kinetic and Thermodynamic Control in Solid State Reactions

The thickness of the repeating unit in the precursor plays an important role in the MER synthesis method. Nb_5Se_4 , a thermodynamically stable compound, will be used to illustrate this phenomenon [15]. Figure 6a and b show the differential scanning calorimetry (DSC) scans of precursors with a repeat unit thickness of (a) above and (b) below 90 Å. Samples for DSC can be obtained by depositing the precursor onto silicon wafers that are coated with poly(methyl) methacrylate (PMMA), which is then dissolved in acetone, lifting off the precursor as a powder. The powder can be collected by filtration and transferred into the DSC sample container.

The DSC data shows two exothermal signals for both precursor types, but they appear at different temperatures. For the precursor with thick atomic layers, the exotherms appear at 125°C and 200°C. X-ray diffraction, however, shows that at these temperatures, the precursor structure is mostly preserved and the sample needs to be annealed further to crystallize completely into Nb_5Se_4 . The grain sizes are rather small with 40 nm or less. All of this is consistent with nucleation and growth along

the Nb-Se interfaces. For the precursor with thin atomic layers, the DSC data look significantly different: instead of two prominent exotherms at low temperatures, a very broad exotherm starts at approximately 100°C and lasts until about 400°C, and a sharp exotherm is present between 550°C and 600°C. The x-ray diffraction pattern (Figure 6c) of this precursor annealed at different temperatures shows that below 600°C, the sample is amorphous, and that it is fully crystalline at 600°C.

This indicates two different reaction pathways: for precursors with atomic layers above a certain thickness, the *critical thickness* [16], the crystallites that nucleate first form at the interface and by diffusion of the elements around them, they grow heterogeneously. Below the critical thickness, the precursor becomes completely amorphous first and needs to overcome a considerable nucleation barrier to homogeneously nucleate and grow into Nb₅Se₄. Figure 6d shows a schematic of the free energy of these different reaction pathways.

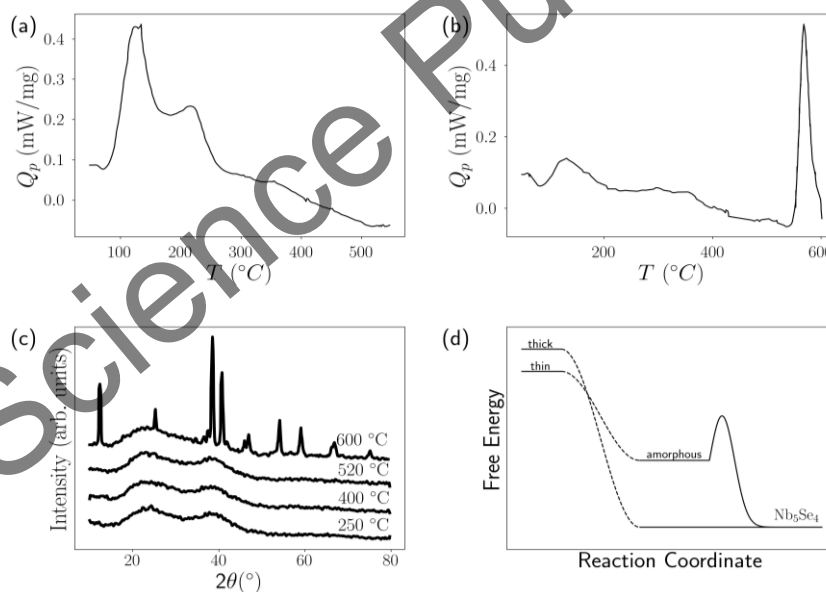


Figure 6. Differential scanning calorimetry data of a Nb₅Se₄ precursor with (a) thick and (b) thin atomic layers. (c) X-ray diffraction pattern of a Nb₅Se₄ precursor with thin atomic layers. (d) Schematic free energy vs. reaction coordinate plot for a Nb₅Se₄ precursor with different thicknesses of atomic layers [15].

Figure 7 provides an illustration on how the structures evolve during that process. Using thin atomic layers, the product of the reaction thus depends on the crystal phase that nucleates first, which is a kinetic parameter. Thus, if nucleation can be controlled, kinetic control of the reaction can be achieved.

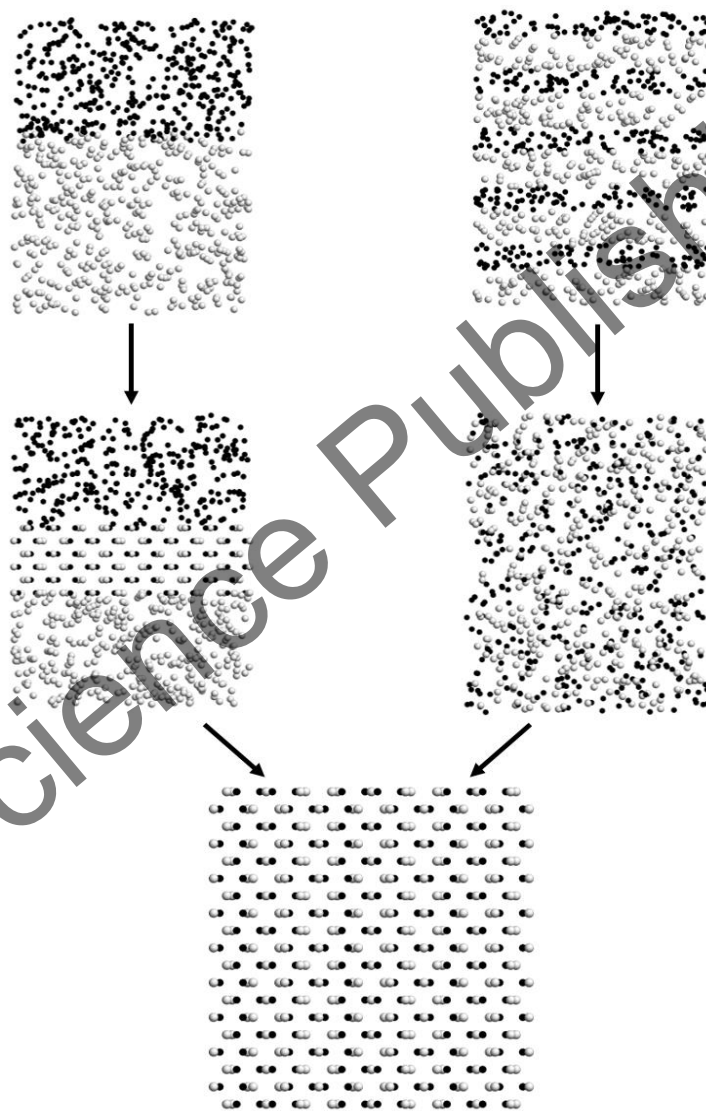


Figure 7. Reaction pathway for a Nb₅Se₄ precursor with thick and thin atomic layers.

The different reaction pathways have profound consequences for the phases that form. For thick atomic layers, the compound that forms at the interface can be determined by the “First Phase Rule” according to Walser and Bené: “The first compound nucleated in planar binary reaction couples is the most stable congruently melting compound adjacent to the lowest temperature eutectic on the bulk equilibrium phase diagram” [17]. For the Nb-Se system, this would be NbSe₂ and corresponds to the first exothermal peak in the DSC data. Due to the composition of the precursor, NbSe₂ then reacts to Nb₅Se₄. However, this can only be successful when the compounds are thermodynamically stable at the reaction temperatures.

The Fe-Si system provides an example for a system that contains a compound that is only stable at high temperatures, Fe₅Si₃ (see schematic phase diagram in Figure 8) [18]. The “First Phase Rule” predicts that the compound that forms first is FeSi, and the product(s) of the reaction depend on the overall stoichiometry of the precursor film and the reaction temperature. If the precursor contains Fe and Si in a 1:1 ratio, phase pure FeSi will form. If the precursor contains excess Si, the Si will react with FeSi to form FeSi₂ until one of the components is depleted. If the precursor contains excess Fe and if the temperature of the reaction is below 825°C, the excess Fe will react with FeSi to form Fe₃Si until one of the components is depleted. Above 825°C, however, Fe₅Si₃ will form first until Fe is depleted and the reaction stops, or until FeSi is depleted, in which case the remaining Fe will react with Fe₅Si₃ to form Fe₃Si. These processes are illustrated schematically in Figure 9.

Thus, using thick elemental layers, synthesizing Fe₅Si₃ should only be possible with temperatures above 825°C. Thin layers, however, amorphize quicker than components nucleate, so the first phase to crystallize cannot be predicted by the First Phase Rule anymore. In general, the nucleation energy depends on the change of free energy, the surface energy of the growing nucleus, internal stresses, and the energy required to rearrange the amorphous alloy to form the crystallite. While the first three terms are guided by the First Phase Rule, the rearrangement energy depends on the local structure of the amorphous alloy. It is reasonable to assume that the crystallite with a composition closest to the composition of the amorphous

alloy has the lowest rearrangement energy, so it should be possible to control which phase nucleates by controlling the composition of the precursor.

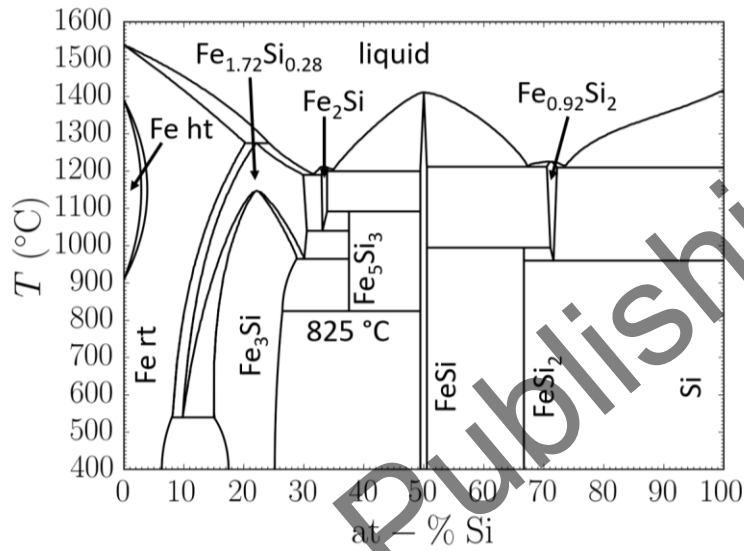


Figure 8. Schematic phase diagram of the Fe-Si system [18].

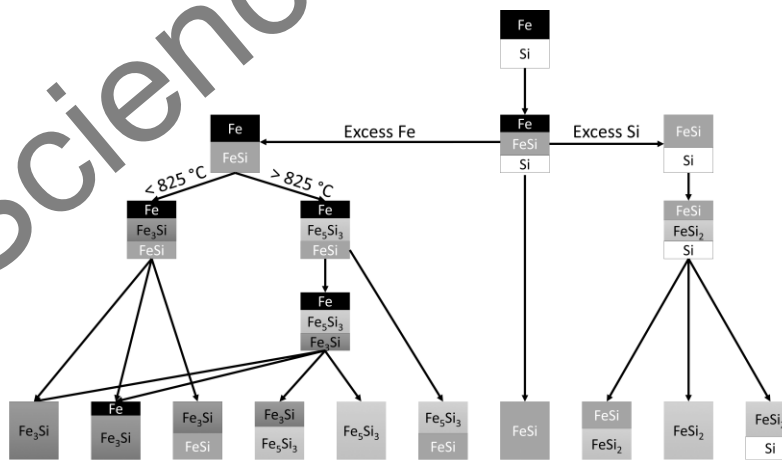


Figure 9. Schematic representation of the reaction pathways of a Fe-Si thin film diffusion couple for different Fe-Si ratios and temperatures.

A systematic test of this hypothesis was conducted by Novet and Johnson by conducting a DSC analysis on multi-layer precursors with different Fe:Si ratios [19, 20]. The main results of these experiments are displayed in Table 1. For every composition, a broad exotherm could be observed at 80°C, followed by a sharp exotherm at different temperatures for different compositions, except for precursors with a Fe:Si ratio of 2:1, which did not show an exothermal peak. The broad exotherm corresponds to the formation of an amorphous alloy, which shows that the amorphization reaction is independent of the sample composition and only depends on whether the layers are below or above the critical thickness. The mixing enthalpies, ΔH_{mixing} , however, do depend on the composition of the precursor with a minimum observed at a Fe:Si ratio of 2:1. X-ray diffraction of samples annealed above the amorphization temperature confirms that the samples are amorphous even when annealed for more than 12 hours.

Table 1. Thermodynamic data of the annealing of different Fe-Si multilayers from DSC [19.] $\Delta H_{\text{formation}}$ is taken from the literature [21–23]. No crystallization event occurs for multilayers with an Fe:Si ratio of 2:1 beneath 600°C

Fe:Si ratio	ΔH_{mixing} (kJ/mol/atom)	$\Delta H_{\text{crystallization}}$ (kJ/mol/atom)	ΔH_{total} (kJ/mol/atom)	$\Delta H_{\text{formation}}$ (kJ/mol/atom)	$T_{\text{crystallization}}^{\text{onset}}$ (°C)
1:2	-20(4)	-8(1)	28(4)	30.6[21]	485
1:1	-22(4)	-4(0.5)	26(4)	39.3[22]	290
5:3	-30(4)	-1(0.3)	31(4)	—	455
2:1	-37(4)	—	37(4)	—	—
3:1	-15(4)	-1(0.3)	16(4)	25.8[23]	540

The exotherm corresponds to the crystallization of the crystalline phases. X-ray diffraction shows that the phases are FeSi_2 , FeSi , Fe_5Si_3 and Fe_3Si for Fe:Si ratios of 1:2, 1:1, 5:3 and 3:1, respectively. For a precursor with an Fe:Si ratio of 2:1, no crystallization was observed below 600°C. The crystallization enthalpies, $\Delta H_{\text{crystallization}}$, are all very small, suggesting that only little rearrangement is required to transition from the amorphous

alloy to the crystalline phase. The extensive intermixing during annealing for these very thin layers results in a total change of heat, ΔH_{total} , that is lower than the formation energies found for bulk reactions [21–23]. The onset crystallization temperatures also depend on the composition of the precursor and increase with increasing deviation from an equimolar Fe:Si ratio, and are a measure for the energy required to nucleate the crystalline phase.

The data show that the rate limiting step in the formation of compounds with the MER method is nucleation, not diffusion, since the amorphization reaction occurs spontaneously. They also confirm that the composition of the precursor determines the phase that nucleates, and that the nucleated phase determines the final structure. This is especially notable for the precursors with Fe:Si ratios of 2:1 and 5:3. The former does not crystallize at all below 600°C because the energy barrier to form a Fe_2Si nucleus is too high. However, the phases that are the closest in composition, Fe_3Si and Fe_5Si_3 , do not crystallize either even though they have lower crystallization temperatures because the energy required to rearrange the local structure to form a nucleus of either compound is too large due to low diffusion rates in solids.

In other words, the farther the composition of the precursor deviates from the composition of a stable nucleus, the larger is the nucleation energy. Figure 10 shows such a relationship for a Se-In MER precursor that forms InSe [24]. The nucleation energy has a minimum near a Se:In ratio of 1:1 and increases the further the composition deviates from this ideal ratio. If the ratio deviates too far, other phases form alongside InSe: if it is 0.9 or smaller, In_4Se_3 forms, and if it is 1.12 or larger In_2Se_3 crystallizes.

The precursor with an Fe:Si ratio of 5:3 crystallizes into Fe_5Si_3 at 455°C, which, according to the phase diagram in Figure 8, is far below its decomposition temperature of 825°C. In an Fe-Si diffusion couple, Fe_5Si_3 should not form at these temperatures, but since the precursor has a Fe:Si ratio of 5:3, the nucleation energy of Fe_5Si_3 is lower than for the other silicides. *The MER method is thus able to synthesize metastable compounds if the energy required to nucleate them is lower than the*

energy required to rearrange the precursor and to nucleate thermodynamically more stable compounds.

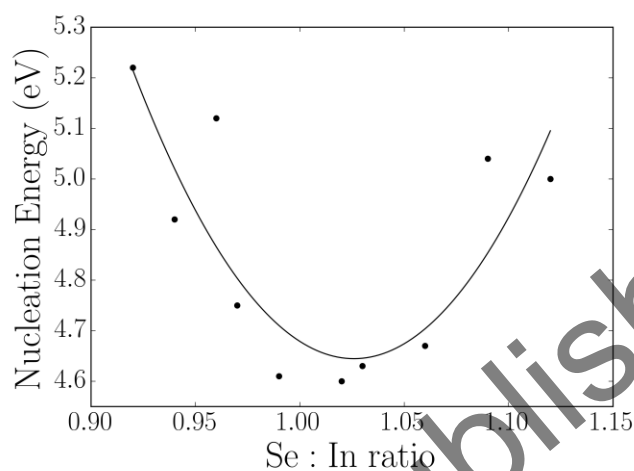


Figure 10. Nucleation energy as a function of MER precursor composition for InSe. A parabolic fit is added as a guide for the eye [24].

The examples demonstrated so far only contain compounds that can already be found in the phase diagram: while Fe_5Si_3 could be successfully synthesized below 825°C without decomposing into Fe_3Si and FeSi , this phase had already been known to exist. It is reasonable to assume that there are unknown phases that can nucleate easily from an amorphous intermediate which cannot be found on a given phase diagram because they are metastable. If one can nucleate any metastable phase by controlling the precursor composition and by keeping the repeat unit layer thickness below the critical thickness, these metastable compounds should be accessible with the MER technique.

Compounds that crystallize in the skutterudite structure, such as CoSb_3 , have been of great interest due to their promising thermoelectric properties [25–27]. The structure of CoSb_3 consists of cubic arrangements of cobalt where 75% of these cubes are filled with Sb_4 rectangles, and 25% are empty and can be filled with other atoms (Figure 11). In CoSb_3 , only large electropositive cations can occupy these vacancies and typically, only

partial occupancies site occupation factors of less than 0.25 can be achieved [28, 29].

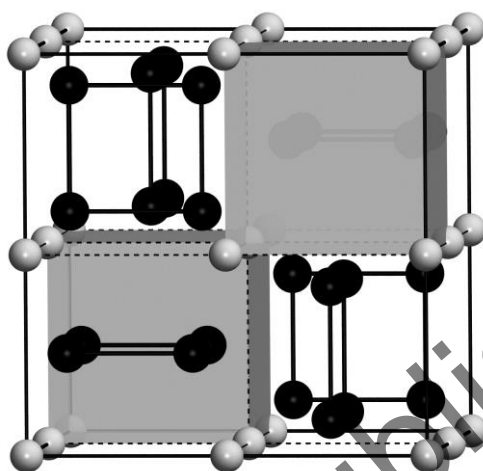


Figure 11. The crystal structure of skutterudite CoSb_3 . Co is gray and Sb is black. The shaded areas are vacancies that can be occupied by another atom.

Filled skutterudites with iron as the transition metal have a larger filling capacity due to its smaller ionic radius. FeSb_3 skutterudites with fully filled vacancies exist with a diverse range of atoms such as the alkali metals, earth alkaline metals, and rare earth metals [30–37]. However, while these filled skutterudites are thermodynamically stable, the unfilled compound is not [38]. The reason for this instability is the reduction of framework electrons since iron has one valence electron less than cobalt. Adding electropositive elements increases the number of electrons in the framework and stabilizes the structure. Using traditional solid state synthesis, unfilled iron skutterudites could only be synthesized as the ternary compounds $\text{Fe}_{0.5}\text{Ni}_{0.5}\text{Sb}_3$ and $\text{Fe}_{0.5}\text{Pd}_{0.5}\text{Sb}_3$, which are isoelectronic to CoSb_3 and thus thermodynamically stable [39, 40].

The existence of the filled FeSb_3 compounds suggests that FeSb_3 may form a stable nucleus, and thus should be accessible using the MER method. Annealing a precursor with a repeat layer thickness of less than 35 Å and more than 75% antimony indeed forms a compound that is

isostructural to CoSb_3 and confirms that FeSb_3 could be prepared using the MER method (Figure 12a) [41]. Precursors with a repeat unit thickness above 35 Å form FeSb_2 and Sb instead. Which phase nucleates also depends on the composition of the precursor as demonstrated in Figure 12b. Below compositions of about 25% Fe, FeSb_2 forms exclusively whereas above, FeSb_3 is the primary product of the reaction, regardless of how much excess Sb is present. For precursors with 25% Fe, the nucleation temperature and the phase that forms vary [42].

The lattice parameter of FeSb_3 ($a = 9.1763$ Å) is larger than for the rare-earth metal filled skutterudites (9.14 Å) because the reduction in electrons in the structure leads to an expansion of the lattice. $\text{NaFe}_4\text{Sb}_{12}$ ($a = 9.1759$ Å) has a comparable lattice parameter because Na cannot donate as much charge as rare earth or earth alkaline metals. Only $\text{BaFe}_4\text{Sb}_{12}$ ($a = 9.20$ Å) has a larger lattice parameter than unfilled FeSb_3 because of the large size of the Ba^{2+} ion [30–37]. Another unfilled skutterudite that was successfully synthesized using the MER method is NiSb_3 , which is isostructural to CoSb_3 as well [43].

Both compounds are metastable and decompose into FeSb_2 and Sb at 360°C, and into NiSb_2 and Sb at 250°C, respectively. These temperatures are significantly lower than the temperatures used in traditional solid state synthesis methods and explain why these compounds cannot be synthesized using traditional methods. On the other hand, the amorphization step in the MER method decreases the nucleation energy for FeSb_3 and NiSb_3 , so they can be crystallized at temperatures that are below their decomposition temperatures.

This is analogous to kinetic and thermodynamic control in organic reactions (see Figure 2a): in the amorphous precursor, the formation of the skutterudite nucleus has a ΔG^\ddagger smaller than the disproportionation reaction even though the latter has a larger ΔG^0 . By keeping the temperature above the nucleation temperature and below the decomposition temperature, the kinetically controlled reaction path and not the thermodynamically controlled path is followed. The MER technique is thus a method to achieve kinetic control in solid state reactions.

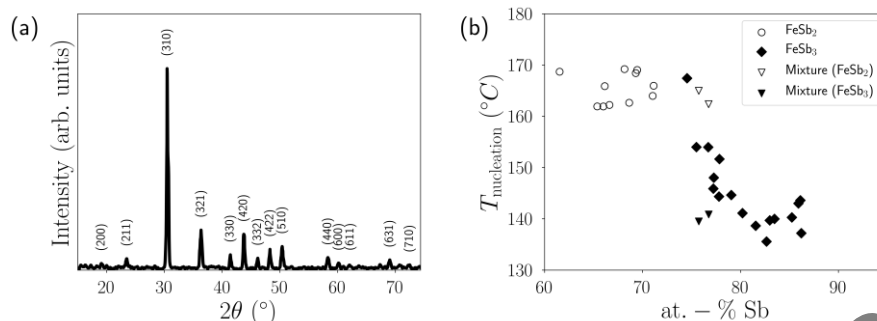


Figure 12. (a) XRD pattern of FeSb₃ synthesized by the MER method. The pattern is indexed with the CoSb₃ skutterudite structure. The (622) and (444) reflections were omitted for clarity (b) Nucleation temperature as a function of precursor composition. For mixtures, the open and closed triangles display the nucleation temperatures of FeSb₂ and FeSb₃, respectively [41].

Synthesis of Ternary Compounds with the MER Method

In this chapter, the MER method has so far only been demonstrated on the synthesis of binary compounds. Ternary compounds pose additional challenges, which will be demonstrated with the synthesis of Cu_xMo₆Se₈. In traditional solid state synthesis, Cu_xMo₆Se₈ is synthesized from the elements or from Mo, Se, and CuSe at 1200°C [44, 45]. As Figure 13 demonstrates, interfaces predominantly consist of only two components. Each interface will behave like diffusion couples and crystallize in a similar scheme as in Figure 9, so the first phases to form are the binary phases MoSe₂ and Cu_{2-x}Se. Over time, MoSe₂ and Cu_{2-x}Se will react at newly formed interfaces and nucleate Cu_xMo₆Se₈, but MoSe₂ also reacts with the remaining Mo to form Mo₃Se₄. For a complete reaction to Cu₂Mo₆Se₈, Mo₃Se₄ must react with other Cu-containing intermediates to finally form Cu₂Mo₆Se₈. Since the interfacial area compared to the bulk volume is small and diffusion is slow, the entire synthesis takes multiple days. Another drawback is that this reaction only works if the final product is thermodynamically more stable than the mixture of binary intermediates. If an intermediate mixture is more stable, the ternary compound will not form.

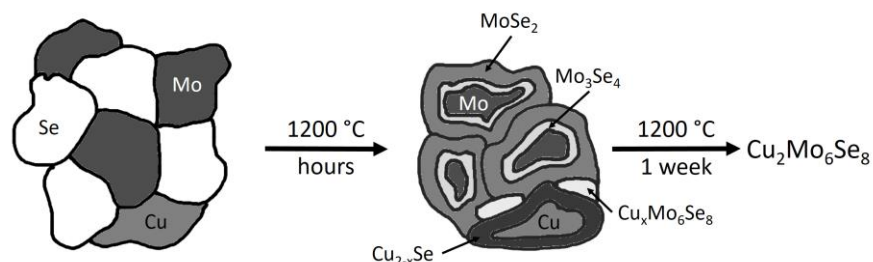


Figure 13. Cartoon of the processes during synthesis of $\text{Cu}_2\text{Mo}_6\text{Se}_8$ from the elements using classic solid state synthesis techniques.

The repeating unit of an MER precursor would consist of a Mo-Cu-Se multilayer. In this case, however, the high diffusion rates of copper in selenium leads to copper diffusing into the Se layer at room temperature so that the precursor actually consists of multilayers of molybdenum and an amorphous copper-selenium alloy [46].

Depending on the chosen Mo layer thickness, two different behaviors can be found. Above 12 \AA , MoSe_2 forms at the interface first. These MoSe_2 layers are crystallographically aligned along the c -axis so that in specular diffraction patterns, only $00l$ reflections can be found. This intermediate reacts with the remaining copper, molybdenum and selenium at $1200\text{ }^\circ\text{C}$ to $\text{Cu}_x\text{Mo}_6\text{Se}_8$. The precursor forms an amorphous ternary alloy at low temperatures, however, when the thickness of the Mo layer is kept at 12 \AA or below. Small reflections can already be found below $170\text{ }^\circ\text{C}$ that grow in intensity and become sharper with higher temperatures. $\text{Cu}_x\text{Mo}_6\text{Se}_8$ fully crystallizes at $912\text{ }^\circ\text{C}$ without forming MoSe_2 as a binary intermediate [46].

Interdiffusion plays an important role in the formation of the amorphous intermediate since MoSe_2 interfacially nucleates at temperatures as low as $200\text{ }^\circ\text{C}$ [47]. Forming a ternary molybdenum selenide would thus require rapid interdiffusion of the third component with the selenium layer. Elements that only poorly diffuse through selenium such as nickel cannot prevent the formation of interfacial MoSe_2 , and thus will not form an amorphous alloy. Instead, MoSe_2 will nucleate and nickel will then diffuse into the dichalcogenide to form Ni_xMoSe_2 [48].

Investigations on MER precursors of the composition $M_x\text{Mo}_{0.75}\text{Se}_1$ ($M = \text{Cu, In, Zn}$) showed very different behaviors for different metals and concentrations of the third component [48]. Samples with copper, which has a higher diffusion rate through selenium than the other metals, crystallized MoSe_2 for $x < 0.31$ and nanocrystalline $\text{Cu}_x\text{Mo}_6\text{Se}_8$ for higher concentrations above 250°C . At higher temperatures, MoSe_2 forms which then reacts to the Chevrel phase at 850°C . The higher the copper concentration is the more depressed is the formation of the dichalcogenide. Indium also diffuses rapidly through selenium and can prevent MoSe_2 from crystallizing when $x > 0.36$ to form an amorphous intermediate instead. Annealing the intermediate between 600 and 700°C results in the formation of $\text{In}_{3.3}\text{Mo}_{15}\text{Se}_{19}$. Zinc was only tested for $x > 0.37$, but could prevent the formation of MoSe_2 in all cases. It forms a Chevrel phase at 800°C , but MoSe_2 forms simultaneously as a second phase.

The general trend is that the higher the concentration of the ternary metal is the higher is the nucleation temperature of interfacial MoSe_2 . In order to form MoSe_2 , the precursor needs to rearrange in a way that expels the third component from the MoSe_2 nucleus. The higher the concentration of the ternary component, the more energy needs to be expended for this rearrangement. Once the local concentration of the third component is below a critical composition, MoSe_2 can form interfacially. This also explains why in some cases, such as in the zinc system, the formation of MoSe_2 cannot be prevented: as the Chevrel phase forms, the precursor will become increasingly Zn-poor until it reaches the critical composition. When the zinc concentration decreases further, MoSe_2 crystallites can form. In some cases, the nucleation barrier to form the ternary compound is too high and MoSe_2 forms regardless such as for Sn-Mo-Se precursors, which only form the Chevrel phase at 1250°C in a thermodynamically controlled reaction [48].

The challenge in the MER synthesis has thus shifted from preventing the binary compound that is thermodynamically more stable to form to preventing the binary compound that nucleates more easily to form. One way to achieve this is to use components that need higher nucleation temperatures to form binary compounds or that interdiffuse at temperatures

lower than the crystallization temperature of the binary compounds. The FeSb₃ skutterudite system is such a system where interdiffusion occurs more rapidly than crystallization. Many metastable filled FeSb₃ skutterudites have been synthesized with the MER method, many of which have not been accessible with classic solid state synthesis routes [41, 49, 50]. Their lattice parameters, and crystallization and decomposition temperatures are shown in Table 2. The effect that a ternary atom delays crystallization can be seen with this system as well except for In_xFe₄Sb₁₂, which is likely due to indium's high diffusion rates. In most cases, the FeSb₃ lattice is also stabilized by the additional constituent as the decomposition temperatures of the ternary skutterudites are higher than of FeSb₃.

Table 2. Lattice parameter a , crystallization temperature T_{cryst} , and decomposition temperature T_{decomp} of (partially) filled metastable $M_x\text{Fe}_4\text{Sb}_{12}$ with the skutterudite structure. FeSb₃ was added for comparison. No lattice parameter was published for $Y_x\text{Fe}_4\text{Sb}_{12}$

M	a (Å)	T_{cryst} (°C)	T_{decomp} (°C)
Al	9.177(1)	177	494
Ga	9.165(1)	181	362
In	9.201(1)	146	463
Zn	9.172(1)	161	416
Sn	9.186(1)	160	484
Y	—	205	550
Hf	9.17(1)	240	400
La	9.1957(8)	210	535
FeSb ₃	9.1762(3)	145	360

Another strategy to change the crystallization behavior is to change the layering sequence of the three constituents to avoid interfaces that could crystallize undesired phases. CuCr₂Se₄ is a ferromagnetic spinel that can be synthesized with the MER technique, but the precursor structure is important to avoid the formation of binary compounds [51]. As discussed

earlier, copper diffuses into selenium layers at room temperature, so an MER precursor with the sequence Cr-Se-Cu-Cr-Se will rapidly nucleate Cu_{2-x}Se ($0 < x \leq 1$). Upon annealing at higher temperatures, more Cu-Se binaries form before reacting with the remaining chromium and selenium to CuCr_2Se_4 at 600°C . Chromium obviously diffuses much slower through selenium than copper, which prevents the formation of a homogeneous amorphous intermediate. However, using the layering sequence Se-Cr-Cu-Cr-Se leads to the formation of an amorphous intermediate that crystallizes to CuCr_2Se_4 at 400°C in Se vapor without binary compounds as intermediates. The chromium layers act as a diffusion barrier for copper and can thus prevent the formation of amorphous Cu-Se layers that crystallize to Cu_{2-x}Se at room temperature.

The thin films exhibit strong crystallographic alignment as indicated by x-ray diffraction and precession electron diffraction (PED) experiments [52]. The specular (“out-of-plane”) diffraction patterns (Figure 14a) contain only (hhh) reflections, showing that the (111) planes must be parallel to the substrate. The intensity of the reflections decrease with annealing time, indicating that the crystallographic alignment is a kinetic effect. The off-specular (“in-plane”) diffraction patterns (Figure 14b) show the same trend in intensities and contain only the reflections that correspond to planes perpendicular to the (111) planes for the sample annealed for 24 hours ($hkl = 220, 311, 440, 622$). For longer annealing times, the (222) reflection appears in the in-plane pattern, showing that the degree of crystallographic alignment is decreased.

The PED image of a sample annealed for 24 h (Figure 14c) shows that the majority of the crystallites are oriented along the $\langle 111 \rangle$ directions. The pole figures confirm that most lattice planes along the z -axis are $\langle 111 \rangle$ -oriented whereas they are disordered within the xy -plane. The mild reaction conditions promote this crystallographic alignment since nucleation and subsequent Ostwald ripening are likely the driving forces in the formation of the crystal. The growing nuclei will try to minimize their surface energy, and for CuCr_2Se_4 , the surface with the lowest surface energy is along the (111) plane [53].

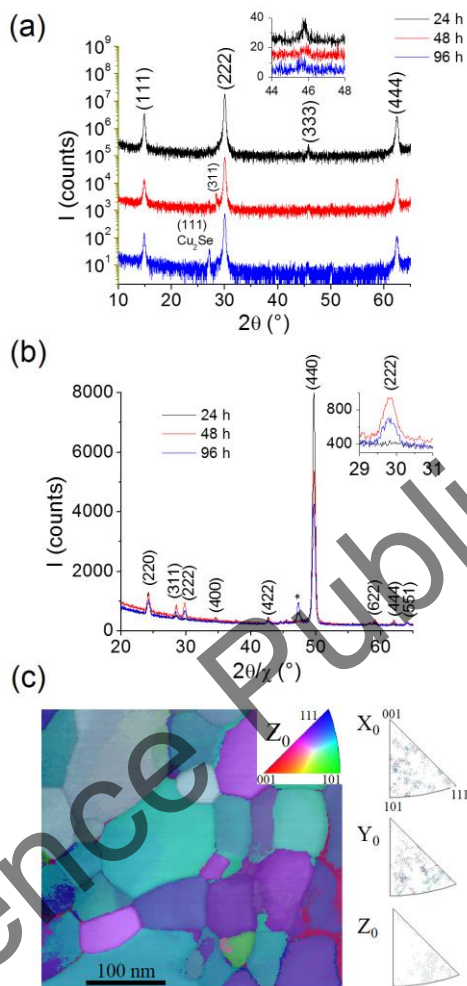


Figure 14. Specular (a) and in-plane (b) x-ray diffraction, and precession electron diffraction (c) on CuCr_2Se_4 films annealed in Se vapor for 24 h, 48 h, and 96 h. Offsets were added in the specular XRD pattern for clarity. The asterisk in the in-plane XRD is a Si substrate reflection. For PED, the samples were aligned so that the z -axis is perpendicular to the substrate surface.

Showing preferred orientation is not unique to spinels. The preferred orientation of MoSe_2 was briefly mentioned while discussing the synthesis of $\text{Cu}_x\text{Mo}_6\text{Se}_8$. Other transition metal dichalcogenides (TMDs) such as TiSe_2 , VSe_2 , and TaSe_2 show the same behavior [54, 55]. The specular

XRD pattern of TiSe_2 synthesized using the MER method is shown in Figure 15a and is representative of the other aforementioned TMDs. Only four reflections are visible, which can be indexed as $(00l)$. The sample thus shows strong texture with crystallographic alignment along the c -axis. Cross section transmission electron microscopy (TEM, Figure 15b) reveals that inside the ab -plane, different TMDs exhibit different degree of long-range order. Whereas VSe_2 , which crystallizes in the 1T structure, shows a high degree of order, TaSe_2 , which crystallizes in the 3R structure, is strongly disordered in the plane, similar to CuCr_2Se_4 . This suggests that a structure that has only one TMD layer inside its unit cell exhibits order whereas the TMDs with multiple layers inside the unit cell exhibit disorder along the c -axis, so-called *turbostratic disorder*. This suggests that each TMD monolayer nucleates independently even when less layers are present than the thermodynamically more stable structure requires. In other words, it should be possible to synthesize heterostructures with TMD monolayers even when the 1T-structure is not the thermodynamically stable structure. These types of heterostructures, misflit layer compounds and ferecrystals, will be discussed in the remainder of this chapter.

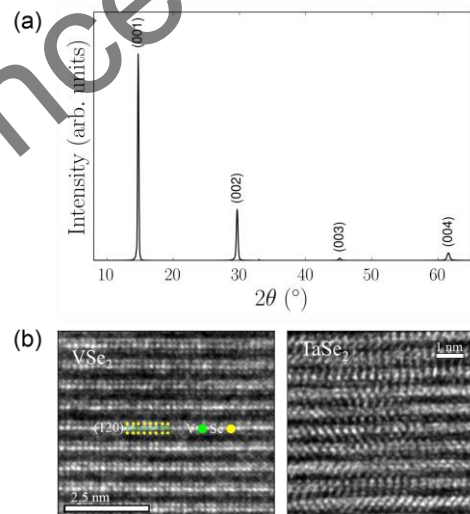


Figure 15. (a) Specular XRD pattern of TiSe_2 films. Reprinted from ref. [54]. (b) TEM cross sections of VSe_2 and TaSe_2 films. Reprinted from ref. [55].

Summary – The Modulated Elemental Reactants (MER) Method

The Modulated Elemental Reactants (MER) method was presented as a technique to achieve kinetic control in solid state reactions. It uses a compositionally modulated precursor that consists of atomically thin elemental layers which are synthesized using physical vapor deposition. The deposition parameters need to be calibrated for composition and repeat unit thickness.

Below a *critical thickness*, these layers interdiffuse rapidly to form an amorphous alloy, which changes the reaction kinetics from being diffusion-limited to being nucleation-limited. The final product is thus controlled by the phase that nucleates quicker and not by the phase that is thermodynamically more stable, i.e., the final product can be controlled with the composition of the precursor. This kinetic control has enabled the synthesis of known compounds at lower temperatures and of new, metastable compounds like FeSb₃ with the skutterudite structure.

The synthesis of ternary compounds is more complex and depends on the diffusivity of all three elements. If one element diffuses slower than a binary compound can interfacially nucleate, the amorphous intermediate cannot form. The amorphous intermediate can be formed with elements that diffuse rapidly into Se such as Cu or In, or by using the slower elements as diffusion barriers as in the synthesis of CuCr₂Se₄.

Finally, films synthesized by the MER method show preferred orientation in many cases, specifically in CuCr₂Se₄, which is oriented along the <111> axes, and transition metal dichalcogenides, which are oriented along the *c*-axis. Inside the *ab*-plane, they are often turbostratically disordered, which suggests independent nucleation of monolayers. This independent nucleation can potentially be used to synthesize crystallographically aligned heterostructures.

FERECRYSTALS – HETEROSTRUCTURES WITH DESIGNED NANOARCHITECTURE

Synthesis of Ferrecrystals

Ferrecrystals (from the Latin *ferre*: “almost”) are heterostructures that belong to the family of Misfit Layer Compounds (MLCs). MLCs are layered structures that are synthesized directly from the elements, and crystals are of them are grown using vapor transport methods. They consist of slabs of two subunits that are alternating along the c -axis as shown in Figure 16a. One subunit consists of an MX bilayer ($M = \text{Sn, Pb, Bi, Sb, rare earth; X = S, Se}$) in a pseudo-tetragonal structure. The atoms are ordered in a NaCl-like arrangement in the ab -plane, but the M atoms are distorted to the outside (Figure 16b). The other subunit is a trilayer that consists of a transition metal dichalcogenide TX_2 (Figure 16c). These subunits are aligned such that their a -lattice vectors are parallel to each other. To achieve this, the lattice vectors along the b -axes of the subunits distort, giving rise to a common b -lattice vector. The TX_2 lattice now needs to be described as an orthorhombic lattice with $a = a_{\text{TX}_2}$ and $b = \sqrt{3}a_{\text{TX}_2}$ where a_{TX_2} is the lattice parameter of the hexagonal TX_2 lattice (Figure 16d).

Since a_{MX} , the a -axis lattice parameter of the MX subunit, and a_{TX_2} are of different sizes, this alignment creates a lattice mismatch, which requires one subunit to be in excess, resulting in a general formula of $(\text{MX})_{1+\delta}\text{TX}_2$. The parameter $1+\delta$, the misfit parameter, describes the excess of MX that is needed to accommodate this lattice mismatch. It can be calculated as:

$$1 + \delta = \frac{\frac{Z_{\text{MX}}}{V_{\text{MX}}}}{\frac{Z_{\text{TX}_2}}{V_{\text{TX}_2}}} = \frac{4a_{\text{TX}_2}bc}{2a_{\text{MX}}bc} = \frac{2a_{\text{TX}_2}}{a_{\text{MX}}} \quad (6)$$

where Z_i represents the number of formula units in each subsystem, and V_i represents the volumes of each subsystem in the crystal. c represents the c -axis lattice parameter of the repeating unit of the MLC and b is lattice parameter of the common in-plane axis of both constituents. The misfit parameter thus describes the ratio of cation densities between both subsystems and typically assumes a value between 1.07 and 1.28.

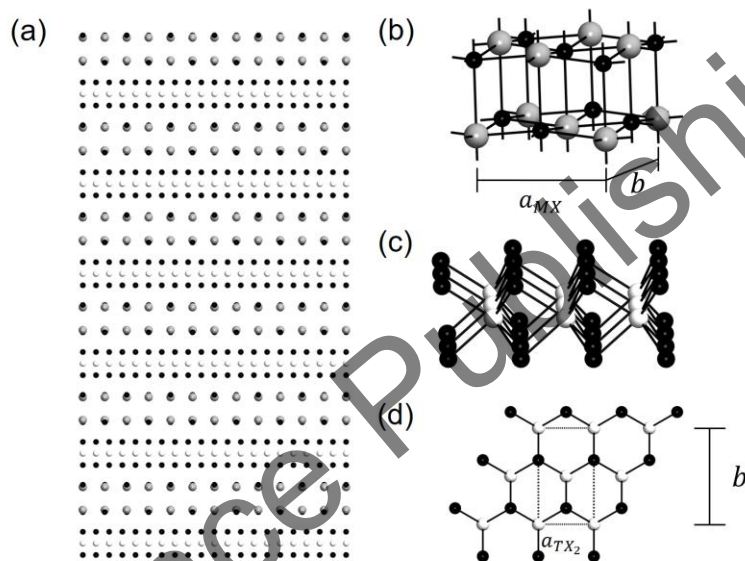


Figure 16. (a) A $(MX)_{1.6}TX_2$ misfit layered compound (MLC) viewed along the b -axis. (b) The unit cell of the MX subunit with its lattice parameters a_{MX} and b . M atoms are gray, X atoms are black. (c) The structure of the TX₂ subunit. T atoms are white, X atoms are black. (d) The transformation of the TX₂ structure into the MLC unit cell with the lattice parameters a_{TX_2} and $b = \sqrt{3}a_{TX_2}$.

MLCs have a variety of electrical, magnetic, and superconducting properties, depending on the metals that are used. The structures and properties have been extensively reviewed by Wiegiers and the interested reader is referred to ref. [56]. In Figure 16a, the structure shows alternating MX bilayers and TX₂ layers. However, since TX₂ layers have no dangling bonds and MX bilayers are stable in MLCs, it is reasonable to assume that a repeating unit consisting of more than one TX₂ layer or MX bilayer

might be stable, or at least be in a local minimum in free energy. The formula for a misfit layered compound would thus need to be rewritten as $[(MX)_{1+\delta}]_m[TX_2]_n$. For each integer m and n , the energy of such a misfit layered compound should lie inside a local minimum as shown in Figure 17. Using kinetic control, the synthesis of MLCs with arbitrary m and n should be possible. Since MLCs are synthesized using vapor transport methods, only the thermodynamically stable product is accessible, which in most cases is $m = n = 1$ – only a few cases are known where $m = 2$, and $n = 2, 3$.

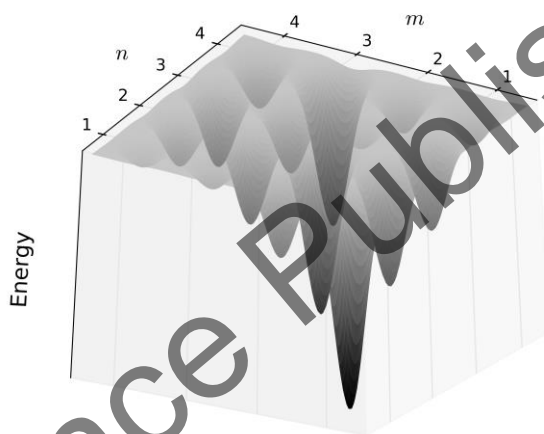


Figure 17. Hypothetical energy hypersurface as a function of the number of subunits in a MLC repeating unit m and n .

In the previous section, it was demonstrated that by depositing a layered precursor with atomically thin elemental layers, the Modulated Elemental Reactants (MER) method can access local minima if the precursor composition is close to the composition of the desired phase. Figure 18 shows the rationale for MER precursors to form $[(MX)_{1+\delta}]_m[TX_2]_n$: M-X and T-X layers are deposited m and n times to form the repeating unit. To ensure that only the desired number of layers form in the final compound, the thicknesses of these layers need to be carefully controlled to contain approximately the number of atoms required

to form the desired subunit, which typically corresponds to a thickness of around 6 Å.

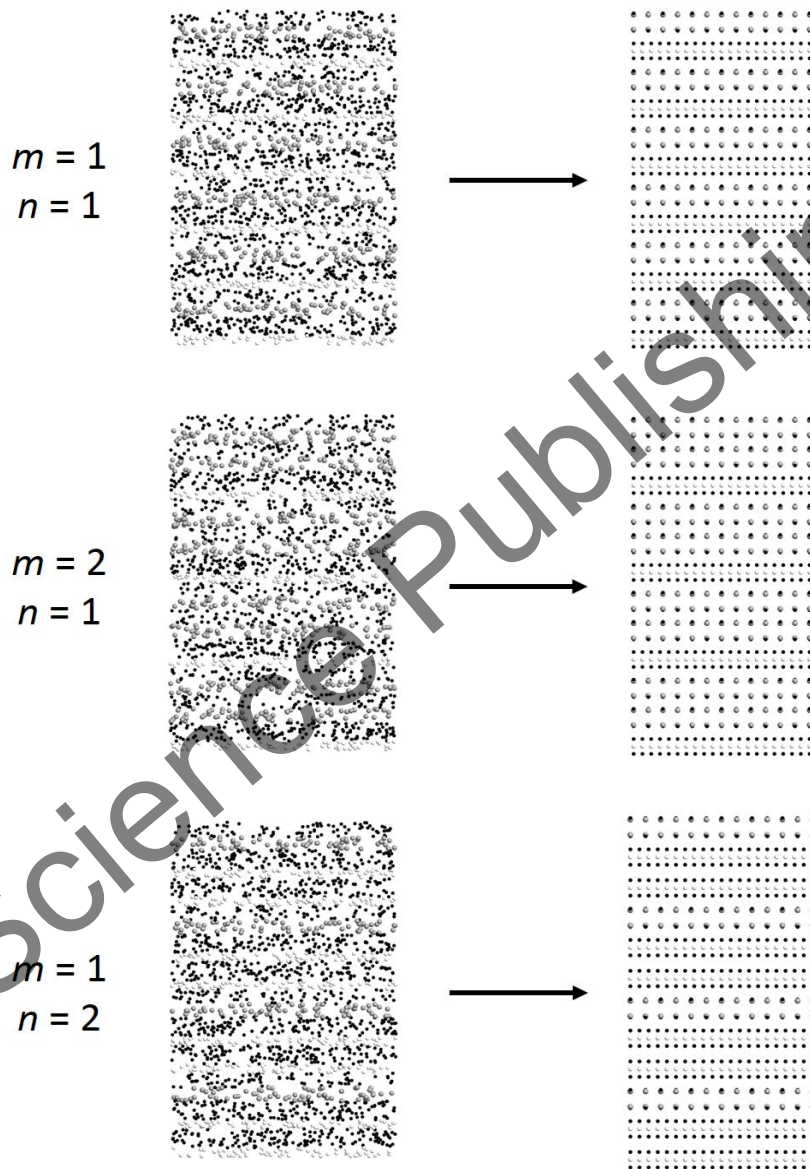


Figure 18. Schematic of MER precursors that react to $[(MX)_{1+\delta}]_m[TX_2]_n$ with $m = 1, 2$ and $n = 1, 2$.

The calibration procedure outlined for binary compounds is complicated by two factors. First, the repeat unit thickness is comprised of the thickness of both subunits, so x-ray diffraction on the precursor cannot resolve the individual thicknesses of the M-X and T-X layers. Second, determining the composition of the precursor cannot resolve the composition of the individual M-X and T-X layers. In order to determine the thickness and composition of individual layers, a more elaborate procedure needs to be developed.

The repeat unit thickness d is comprised of m layers of M-X and n layers T-X with the corresponding thicknesses d_{M-X} and d_{T-X} :

$$d = m \cdot d_{M-X} + n \cdot d_{T-X} \quad (7)$$

This can be rearranged to:

$$\frac{d}{m} = d_{M-X} + \frac{n}{m} d_{T-X} \quad (8)$$

$$\frac{d}{n} = \frac{m}{n} d_{M-X} + d_{T-X} \quad (9)$$

To determine the thickness of the individual layers, a series of precursors with varying m and n needs to be deposited. Plotting d/m against n/m yields a straight line, and a linear fit provides d_{T-X} from the slope and d_{M-X} from the intercept, and vice versa for a plot of d/n against m/n . Ideally, the results extracted from the slopes should be within error of the results from the intercepts. Deviations from linearity or significant differences point to inconsistencies between depositions. Figure 19 shows an example for a V-Se-Sn-Se precursor. While the V-Se thickness is close to the desired thickness, the Sn-Se thickness is too large and needs to be scaled down.

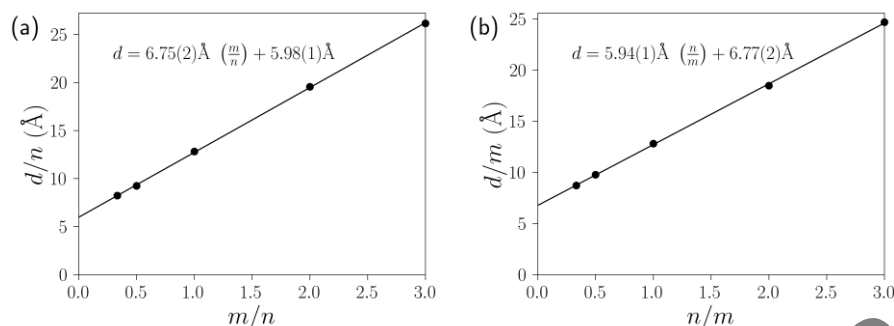


Figure 19. Thickness calibration for the M-X and T-X layers in an MLC MER precursor. A linear fit through (a) yields $d_{M-X} = 6.77 \pm 0.02 \text{ \AA}$ and $d_{T-X} = 5.91 \pm 0.01 \text{ \AA}$ and a linear fit through (b) yields $d_{M-X} = 6.75 \pm 0.02 \text{ \AA}$ and $d_{T-X} = 5.98 \pm 0.01 \text{ \AA}$.

Determining the composition also requires a series of samples because the chalcogen is present in both the T-X and M-X layer. The general formula of the precursor can be written as $[(MX_x)_y]_m[TX_z]_n$ or $M_{my}T_nX_{mxy+nz}$. The atomic ratios of each element are thus:

$$\frac{\text{at.}\% \text{ X}}{\text{at.}\% \text{ M}} = \frac{mxy + nz}{my} = x + \frac{nz}{my} \quad (10)$$

$$\frac{\text{at.}\% \text{ M}}{\text{at.}\% \text{ T}} = \frac{m}{n} \quad (11)$$

$$\frac{\text{at.}\% \text{ X}}{\text{at.}\% \text{ T}} = \frac{mxy + nz}{n} = z + \frac{mxy}{n} \quad (12)$$

Equations 10 and 12 can be rearranged to:

$$\frac{m}{n} \frac{\text{at.}\% \text{ X}}{\text{at.}\% \text{ M}} = \frac{m}{n} x + \frac{z}{y} \quad (13)$$

$$\frac{n}{m} \frac{\text{at.}\% \text{ X}}{\text{at.}\% \text{ T}} = \frac{n}{m} z + xy \quad (14)$$

These equations allow the direct determination of x , y , and z from the slopes of linear plots resulting from Equations 11, 13, and 14 as is shown in Figure 20. Using $y = 1.19(1)$ from Figure 20b, x and z can be additionally determined using the intercepts of the plots from Equations 13 and 14. In the case shown in Figure 20, x can be determined as 1.16(1) from the slope and 1.17(2) from the intercept, and z is found to 2.05(1) and 2.06(2), respectively. x and z should be 1 and 2, respectively, although some excess of the chalcogens is often added to account for evaporation loss during annealing. The determined values are thus close to the desired values. The ideal value for y is unknown, but can be estimated by calculating the misfit parameter using the in-plane lattice parameters of the bulk forms of TX_2 and rock salt MX . For VSe_2 and SnSe , $a_{\text{VSe}_2} = 3.35 \text{ \AA}$ and $a_{\text{SnSe}} = 5.99 \text{ \AA}$, which results in an ideal y value of 1.12, suggesting that the determined y value is too high. This is consistent with the determined Sn-Se layer thickness. For future depositions, the deposition parameters for the Sn and the Se layer deposited after the Sn layer both need to be decreased.

Once the precursor with the desired composition and layer thicknesses is prepared, an annealing study is performed to monitor the evolution of the superlattice using specular x-ray diffraction (Figure 21a). The as deposited sample shows sharp Bragg reflections at about 6° and $12^\circ 2\theta$ from the repeat unit thickness of the MER precursor, and broad reflections at about 14° and $28^\circ 2\theta$. The broad reflections sharpen and grow in intensity upon annealing. Annealing the precursor at 100°C for 20 minutes in a nitrogen atmosphere ($p_{\text{O}_2} < 0.6 \text{ ppm}$) results in a shift of the reflection at 6° to higher 2θ and a decrease in intensity while the reflection at 12° completely vanishes. The reflections sharpen and grow in intensity when annealing to 200°C , and new reflections appear. At higher temperatures, the reflections gain more in intensity, sharpen further and shift to higher 2θ values, which shows that the c -lattice parameter of the superlattice shrinks as the crystallites grow. At 400°C , the reflections are sharpest and most intense. Annealing above this temperature results in the decomposition of

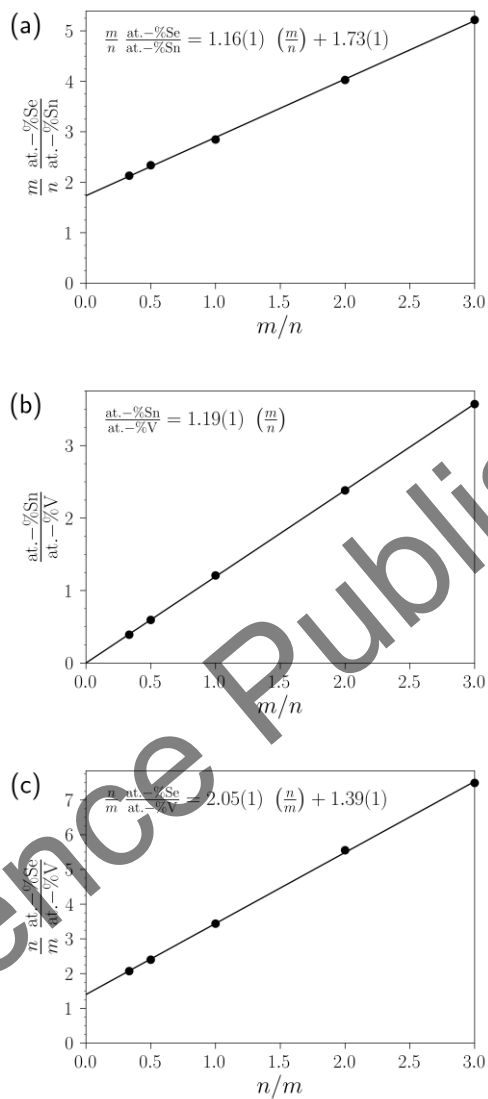


Figure 20. Composition calibration plots with linear fits. x can be determined from the slope of (a) and the intercept of (c), y can be determined from the slope of (b), and z can be determined from the slope of (a) and the intercept of (c). The insets show the results of the linear fits through the data.

the compound. The reflections can be indexed to $(00l)$ indices with the (006) reflection being absent, suggesting that the compound is highly

textured with crystallographic alignment along the c -axis. From these reflections, a lattice parameter of $c = 12.03 \text{ \AA}$ can be determined, which is close to what is expected for $[(\text{SnSe})_{1+\delta}]_1[\text{VSe}_2]_1$.

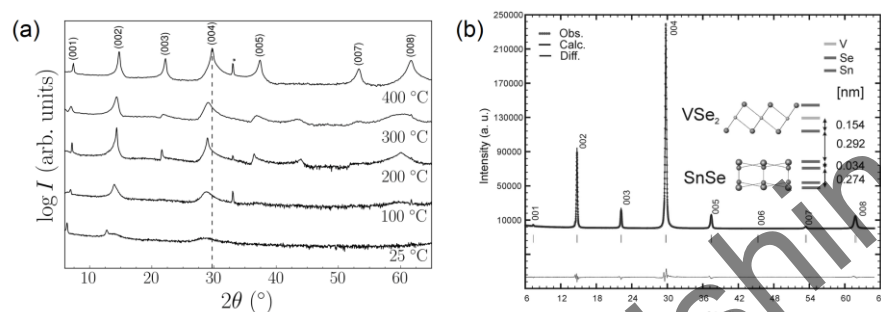


Figure 21. (a) XRD diffraction pattern of an annealing study of a precursor for $[(\text{SnSe})_{1+\delta}]_1[\text{VSe}_2]_1$. Reflections denoted with an asterisk belong to the Si substrate. The dashed line is a guide for the eye of the 2θ position of the (004) reflection of $[(\text{SnSe})_{1+\delta}]_1[\text{VSe}_2]_1$. (b) Rietveld refinement of the diffraction pattern annealed at 400°C [57].

The structure along the c -axis can be further determined using Rietveld refinement, which is challenging due to the strong preferred orientation of the film. The in-plane lattice parameters a and b are required for the refinement, but cannot affect the diffraction pattern since only (00 l) reflections are visible. The solution to this problem is to keep these lattice parameters artificially very small ($< 0.1 \text{ \AA}$) and use the coordinates (0, 0, z) for each atom, so that each atom represents a plane of atoms. This is only possible if elements of different types have different z -coordinates, which is the case for $[(\text{SnSe})_{1+\delta}]_1[\text{VSe}_2]_1$ due to the distortion in the SnSe lattice and the layered structure of VSe_2 (see Figure 16b and Figure 16c). The results of the Rietveld refinement on $[(\text{SnSe})_{1+\delta}]_1[\text{VSe}_2]_1$ are shown in Figure 21b, and confirm that the compound is layered like a misfit layer compound. They also show the distortion in the SnSe subsystem that is found in misfit layer compounds [57].

The layering of the compound can be directly observed using transmission electron microscopy (TEM) or high-angle annular dark-field detector scanning tunneling electron microscopy (HAADF-STEM). A

cross section HAADF-STEM image of $[(\text{SnSe})_{1+\delta}]_1[\text{VSe}_2]_1$ is shown in Figure 22a. The image shows layers of alternating darker and brighter contrasts, which shows that the compound is highly oriented along the c -axis. Since the brightness depends on the atomic number, the bright layers belong to SnSe and the darker layers to VSe_2 . The image shows that the compound has the layering sequence that was expected from the precursor. However, different crystal faces can be observed along the viewing direction, which suggests that the SnSe and VSe_2 layers are not aligned along the a -axis as they would be in a traditional misfit layer compound, but display random orientation in the ab -plane instead. The electron diffraction pattern in Figure 22b confirms this random orientation: while the $(00l)$ direction shows bright and discrete maxima, the (hkl) direction shows extensive streaking of low intensity, which suggests long coherence lengths parallel to the c -axis, but very short coherence lengths along any other directions outside the ab -plane [58]. This *turbostratic disorder* and the resulting short coherence lengths distinguish the MLCs synthesized by the MER method from MLCs synthesized by vapor transport methods, giving rise to a new class of materials called *ferrecrystals* (“almost crystals”).

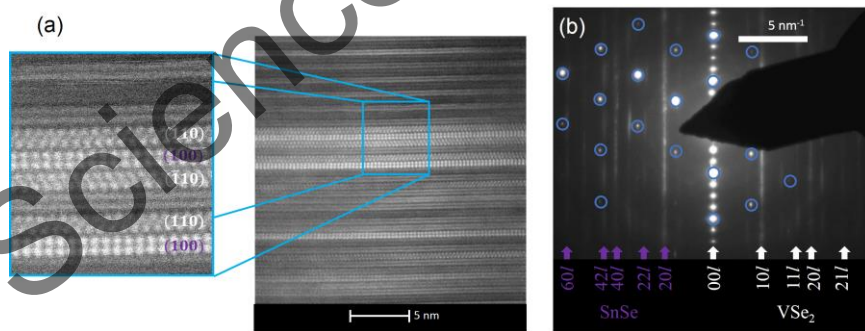


Figure 22. (a) HAADF-STEM images of $[(\text{SnSe})_{1+\delta}]_1[\text{VSe}_2]_1$ with different crystallographic orientations highlighted in the inset [75]. (b) Electron diffraction pattern image of a cross-section of $[(\text{SnSe})_{1+\delta}]_1[\text{VSe}_2]_1$. The diffraction maxima of the silicon substrate are circled blue [58].

The turbostratic disorder also leads to the structure being incommensurate along the b -axis, i.e., there is no common b -lattice parameter compared to misfit layer compounds. For ferecrystals, a more general definition of the misfit parameter needs to be used:

$$1 + \delta = \frac{\frac{Z_{MX}}{V_{MX}}}{\frac{Z_{TX_2}}{V_{TX_2}}} = \frac{2\sqrt{3}a_{TX_2}^2}{a_{MX}b_{MX}} \quad (15)$$

The determination of the in-plane lattice parameters, a_{TX_2} , a_{MX} and b_{MX} will be discussed later in this chapter. For SnSe-VSe₂ ferecrystals, δ is 0.15, so the chemical formula needs to be written as [(SnSe)_{1.15}]₁[VSe₂]₁.

Ferecrystals have been synthesized with numerous elements. Ti, V, Nb, Mo, Ta, and W have been successfully incorporated as the transition metals, and La, Ce, Sn, Pb, and Bi as the metal in the rock salt component (see periodic table in Figure 23) [59–71]. To date, many more rare earth metals have been used for MLCs compared to ferecrystals because these metals oxidize rapidly and are thus difficult to deposit consistently. While MLCs are mostly sulfides with only few selenides, ferecrystals have been almost exclusively synthesized as selenides [56, 72, 73]. There are no ferecrystalline sulfides yet because the controlled physical vapor deposition of atomically thin sulfur layers is very challenging. With [(PbTe)_{1.17}]_m[TlTe₂]_n, ferecrystalline tellurides have been synthesized as well, which do not exist as MLCs yet [74].

This approach can be generalized to other values of m and n . It was hypothesized earlier that any ferecrystal with integer m and n can be synthesized if the thicknesses and compositions of the individual layers are close to such a ferecrystal (see Figure 17 and Figure 18). Figure 24 shows the results of the Rietveld refinement of [(SnSe)_{1.15}]_m[VSe₂]_n for a variety of m and n , and HAADF-STEM images for [(SnSe)_{1.15}]₁[VSe₂]₃ and [(SnSe)_{1.15}]₃[VSe₂]₁, which demonstrate that a variety of layering sequences is possible [75, 76]. This is true for many other ferecrystals as well where values for m and n of up to 32 have been reached [77].

H																							He
Li	Be														B	C	N	O	F	Ne			
Na	Mg														Al	Si	P	S	Cl	Ar			
K	Ca	Sr	Ti	V	Cr	Mn	Fe	Co	Ni	Cu	Zn	Ga	Ge	As	Se	Br	Kr						
Rb	Sr	Y	Zr	Nb	Mo	Tc	Ru	Rh	Pd	Ag	Cd	In	Sn	Sb	Te	I	Xe						
Cs	Ba		Hf	Ta	W	Re	Os	Ir	Pt	Au	Hg	Tl	Pb	Bi	Po	At	Rn						
		La	Ce	Pr	Nd	Po	Sm	Eu	Gd	Tb	Dy	Ho	Er	Tm	Yb	Lu							

Legend:
 in MLCs
 in ferecrystals

Figure 23. Elements in the periodic table that are found in misfit layer compounds and ferecrystals.

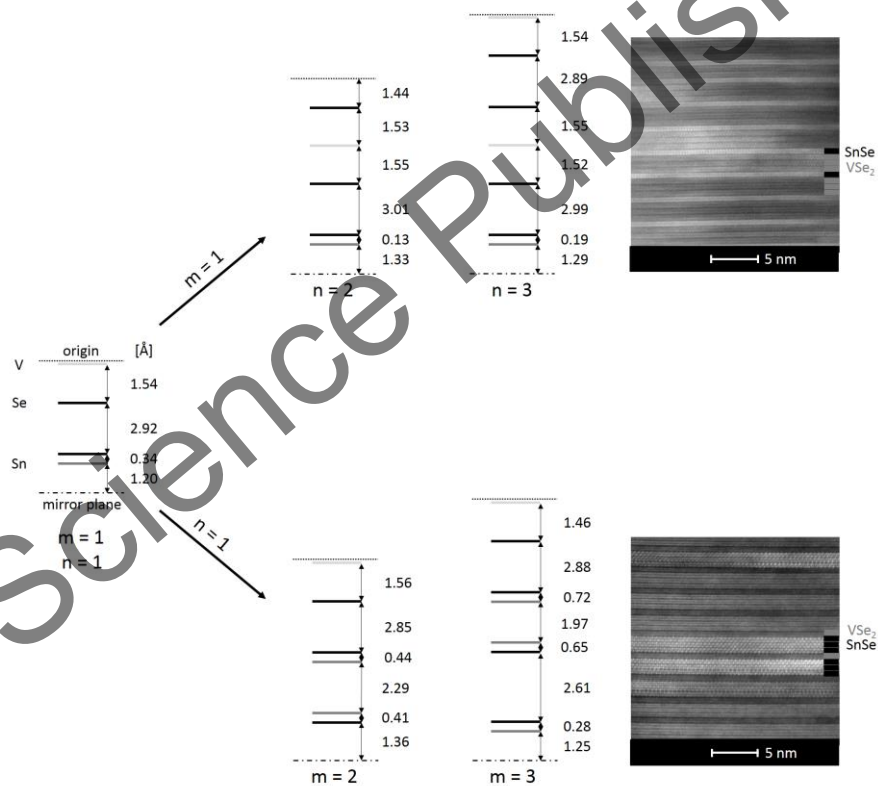


Figure 24. Results of the Rietveld refinements for $[(\text{SnSe})_{1.15}]_m[\text{VSe}_2]_n$ ($m = 1, n = 1 - 3$; and $m = 1 - 3, n = 1$), and HAADF-STEM images for $[(\text{SnSe})_{1.15}]_1[\text{VSe}_2]_3$ and $[(\text{SnSe})_{1.15}]_3[\text{VSe}_2]_1$ [75, 76, 57].

The figure also shows that the inter-planar distances are sensitive to m and n . The least sensitive are the distances between V and Se planes in the VSe_2 trilayers. With increasing n , the distances vary only by a few hundredths of an Ångström. For $n > 1$, the trilayers adjacent to a SnSe bilayer show small distortions where the distance between the V-planes and the Se-planes at the interface to the SnSe bilayer is $0.02 - 0.03$ Å larger than the distance between the V-planes and the Se-planes at the interface to another VSe_2 trilayer. This can be attributed to different interactions between the SnSe layers and a VSe_2 layer than between two VSe_2 layers: the SnSe- VSe_2 interaction is dominated by charge transfer, and the VSe_2 - VSe_2 interaction is mostly due to van-der-Waals forces. The layers for odd n (including $n = 1$) that are in the center do not show this distortion because of their symmetric environment. The distances between VSe_2 trilayers are independent of n and equal to $2.88(1)$ Å. For increasing m , the inter-planar distances in the VSe_2 trilayer do not change when m increases from 1 to 2, but significantly decreases by 0.1 Å when m is increased to 3. This can be attributed to increased charge transfer, which is known to “flatten” the VSe_2 lattice, i.e., to decrease the c -axis lattice parameter while increasing the in-plane lattice parameters [78].

The distances in the SnSe subunit are very sensitive especially to m . The distances between the Se and the Sn planes show the same asymmetry as the planes in the VSe_2 trilayers: the planes adjacent to a VSe_2 trilayer show a larger distortion than the planes adjacent to another SnSe bilayer whereas the bilayers in the center show a symmetric distortion. However, in contrast to VSe_2 , the distances change with m and n . When increasing n from 1 to 2, the distances between the Se and Sn planes decrease by 0.2 Å, but increase again from 0.13 Å to 0.19 Å when n is increased to 3. For increasing m , the distances increase significantly, which can also be attributed to increased charge transfer between SnSe and VSe_2 layers for increasing SnSe thickness. The distances between Sn-planes in the SnSe bilayer adjacent to VSe_2 trilayers show the opposite trend for increasing n , and increase by the same amount the distances between the Se and Sn planes decrease, which points to a strong correlation between these planes. For increasing m , the distances between Sn layers decrease systematically,

but not, in contrast to increasing n , by the same amount as the distances between Se and Sn layers decrease. For $m = 3$, the distances between planes in the central SnSe bilayer are close to the distances in bulk SnSe with the TII structure, suggesting that the interactions with VSe₂ are the cause for the structural distortions in SnSe [79]. This also explains why the distances between planes change drastically when $m, n \neq 1$. The distances between SnSe bilayers decrease with increasing m .

The distances between the VSe₂ and SnSe subunits vary depending on m and n . Increasing n above 1 leads to an increase in the distance between the outer Se layers of the subunits by 0.1 Å, and decreases by only a few hundredth of an Ångström for $n = 3$. For m , the distance decreases by 0.7 Å and then increases by only 0.03 Å when going from $m = 1$ to $m = 2$ and 3. This suggests that the interactions between the layers are significantly different for [(SnSe)_{1.15}]_m[VSe₂]_n when $m = n \neq 1$ than for other values of m and n . The effect of this confinement can also be observed in the temperature dependent resistivity, which shows a large increase in electrical resistivity below 110 K that can be attributed to a charge density wave transition. The magnitude of this increase is suppressed with increasing n , but increased with increasing m , showing that the layering sequence also has systematic effects on the electronic properties of the ferecrystal [75, 76].

Ferecrystals with PbSe show different distortions for the MX layer. Figure 25 shows the distances between the Pb layers in the PbSe subunit for a series of [(PbSe)_{1+δ}]_m[MoSe₂]_n ferecrystals with $m = n$ as determined by HAADF-STEM [63]. With 0.5 Å, the $m = n = 2$ compound shows a large difference between the distances of the Pb planes within a bilayer (d_{intra}) and the distances of the Pb planes between bilayers (d_{inter}). The distances are also shorter than for a ferecrystal with $m = n = 1$. This difference shrinks with increasing m and n as the bilayers move closer together (d_{inter} decreases) while the individual bilayers expand (d_{intra} increases), both in a linear fashion until $m = n = 4$. At $m = n = 5$, both distances are the same at 3.2 Å, i.e., the PbSe unit consists of ten equally spaced PbSe layers, which is a very different behavior compared to SnSe.

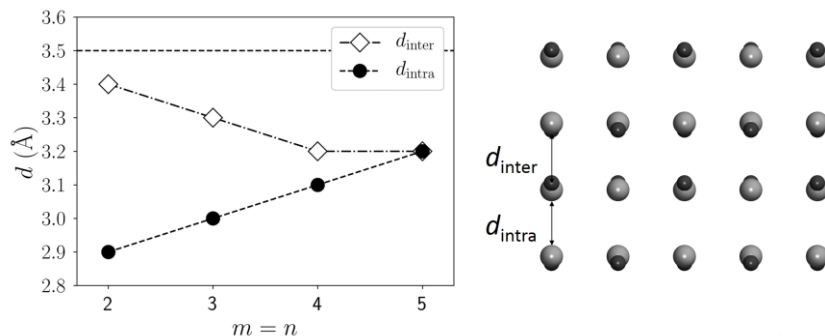


Figure 25. Distances between Pb layers in the PbSe subunit of $[(\text{PbSe})_{1-s}]_m[\text{MoSe}_2]_n$ ($m = n$). d_{intra} is the distance within a PbSe bilayer, d_{inter} is the distance between the bilayers. The horizontal line in the plot is the distance between the Pb layers for $m = n = 1$.

The In-Plane Structure of Ferecrystals

Even though ferecrystals show no crystallographic alignment in the ab -plane, the STEM images show that each individual layer is fully crystalline. To get a complete picture of the structure of ferecrystals, the in-plane structure is of as much interest as the structure along the c -axis. Since the ferecrystals have a strong preferred orientation along the c -axis, only $(hk0)$ reflections should appear in an in-plane XRD pattern. As an example, Figure 26 shows the in-plane XRD pattern of $[(\text{PbSe})_{1-s}]_1[\text{TiSe}_2]_1$. Due to the turbostratic disorder, both constituents diffract independently. This is a great advantage because the individual structures can then be extracted independently, but on the other hand, there is a significant degree of overlap between the reflections of the TX_2 and the MX components.

Historically, the in-plane structures of the subunits in misfit layer compounds were treated as quasi two-dimensional (001) slabs of the transition metal dichalcogenide and NaCl bulk structures [56, 80]. Bulk TiSe_2 crystallizes in the CdI_2 structure (space group: $P\bar{3}m1$, no. 164) and

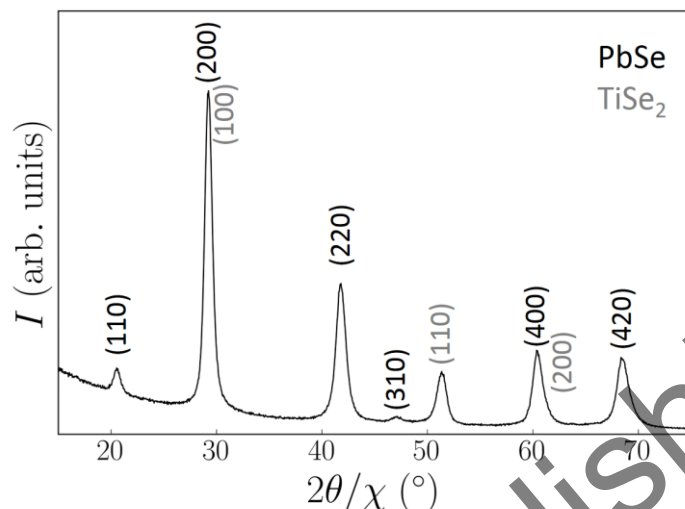


Figure 26. In-plane diffraction pattern of $[(\text{PbSe})_{1.16}][\text{TiSe}_2]_1$. The black indices belong to the PbSe, the gray indices to the TiSe_2 subunit.

the $(hk0)$ indices of $P\bar{3}m1$ fit very well to the diffraction pattern. The in-plane lattice parameters can now be calculated using the relationships between the d -spacing and the lattice parameters for hexagonal lattices with $l = 0$:

$$\frac{1}{d^2} = \frac{4h^2 + k^2}{3a_{Tx_2}^2} \quad (16)$$

The remaining reflections can be indexed for a cubic structure and can be calculated using the relationship between the d -spacing and the lattice parameter for cubic lattices with $l = 0$:

$$\frac{1}{d^2} = \frac{h^2 + k^2}{a_{MX}^2} \quad (17)$$

This results in an a -axis lattice parameter of $3.552(7) \text{ \AA}$ for TiSe_2 , and of $6.133(3) \text{ \AA}$ for PbSe. The error for TiSe_2 is much higher because there are fewer reflections for this constituent, and many of them also overlap

with the reflections of PbSe. Using Equation 15, the misfit parameter $1 + \delta$ calculates to 1.16. A summary of misfit parameters for different ferecrystals along with the values for the corresponding MLC (where available) is given in Table 3.

This interpretation, however, is problematic because in the NaCl structure (space group: $Fm\bar{3}m$, no. 225), the (110) and the (310) reflection are extinct. To explain these reflections, it was proposed to collapse the structure into the plane group $p4gm$, which changes the diffraction conditions to $h + k = 2n$ (n : integer), which is fulfilled by the (110) and (310) reflections as well [81]. However, the PbSe bilayer consists two of these layers where the atoms have the in-plane coordinates of (0, 0) and $(\frac{1}{2}, \frac{1}{2})$ for one layer, and $(0, \frac{1}{2})$ and $(\frac{1}{2}, 0)$ for the other, which results in a structure factor for the (110) reflection of:

$$S_{110} = f \cdot \left[1 + e^{2\pi i(\frac{1}{2} + \frac{1}{2})} + e^{\frac{2\pi i}{2}} + e^{\frac{2\pi i}{2}} \right] = 0 \quad (18)$$

where f is the atomic form factor of either Pb or Se. The structure factor of the (310) reflection becomes zero as well, so using the $p4gm$ plane group cannot explain the reflections either. One way to get a non-zero structure factor is to shift one PbSe layer with respect to the other layer by $(\Delta x, \Delta y)$, which results in:

$$S_{110} = f \cdot \left[1 + e^{2\pi i(\frac{1}{2} + \frac{1}{2})} + e^{2\pi i(\Delta x + \frac{1}{2} + \Delta y)} + e^{2\pi i(\frac{1}{2} + \Delta x + \Delta y)} \right] \quad (19a)$$

$$= 4f \sin^2[\pi(\Delta x + \Delta y)] \quad (19b)$$

This structure factor is only zero when $\Delta x + \Delta y$ is an integer, i.e., for any deviation from the high symmetry rock salt positions, the structure factor has a non-zero value. The question is why such a shift would occur and why it would not occur in misfit layer compounds where the (110) and (310) reflections are absent. In ferecrystals, the in-plane structures are completely incommensurate in different layers, which results in turbostratic disorder. This disorder causes each atom to be in a slightly

different environment, and thus to experience different interactions with the adjacent dichalcogenide layer. These inhomogeneous forces could lead to a small in-plane distortion with a distribution of Δx and Δy values. This would be consistent with the (110) and (310) reflections being much smaller in intensity and broader than the others. Misfit-layer compounds with its commensurate b -axis exhibit much longer range order compared to ferecrystals and thus do not exhibit these in-plane distortions. However, there is no experimental probe yet that could confirm the existence and the magnitude of this shift. The shifts would be too small to be resolved by microscopy techniques, and a model for Rietveld refinement for the in-plane structure has not yet been found.

Table 3. Values for $1+\delta$ for $[(MSe)_{1+\delta}]_1[TSe_2]_1$ ($M = Sn, Pb, Bi$) for different transition metals T. The value for the equivalent MLC is given in parentheses if available. Values with an asterisk are taken from a $[(MSe)_{1+\delta}]_1[TSe_2]_2$ MLC [81]

T	Sn	Pb	Bi
Ti	1.2	1.14 (1.16*)	1.15 (1.13*)
V	1.15	1.12	1.12
Nb	1.16 (1.16)	1.14 (1.10)	1.11 (1.10)
Mo	1.06	0.99	—
Ta	1.14	—	— (1.09)
W	—	0.99	—

While the in-plane lattice for PbSe in ferecrystals is square, it is not necessarily the case for SnSe and BiSe. Figure 27a compares the in-plane XRD patterns for different $[(MSe)_{1+\delta}]_1[TiSe_2]_1$ compounds near the (200) and (220) reflections for PbSe. For SnSe, the (200) reflection splits, which suggest that the basal plane is rectangular instead of square, so the reflections can be indexed as (200) and (002). For BiSe, there is no splitting near the (200) reflection, but there is splitting near the (220) reflection instead. This suggests that BiSe crystallizes in a different structure with a smaller unit cell and strong rectangular distortion. The reflections can be indexed with the $(hk0)$ reflections of the orthorhombic

3D space group $Pcmn$, even though other orthorhombic space groups are possible as well. A summary of the proposed in-plane structures is shown in Figure 27b. The images show that the in-plane unit cell for BiSe has the same structure as the distorted primitive cell of PbSe [81].

The in-plane lattice parameter of the transition metal dichalcogenide is relatively insensitive to m and n : Investigations on $[(\text{SnSe})_{1+\delta}]_m[\text{TaSe}_2]_n$ show that a stays constant at 3.45 – 3.46 Å regardless of m and n [82, 83]. PbSe and SnSe show a similar insensitivity to n , but show changes when m is increased. PbSe shows an increased lattice parameter in the $[(\text{PbSe})_{1+\delta}]_m[\text{NbSe}_2]_1$ series ($m = 1 - 5$), presumably due to reduced out-of-plane distortions. Since the in-plane lattice parameter of the transition metal dichalcogenide stays constant, the misfit parameter is reduced from 1.14 for $m = 1$ to 1.10 for $m = 5$, which correlates well with the change in out-of-plane distortion that was shown in Figure 25.

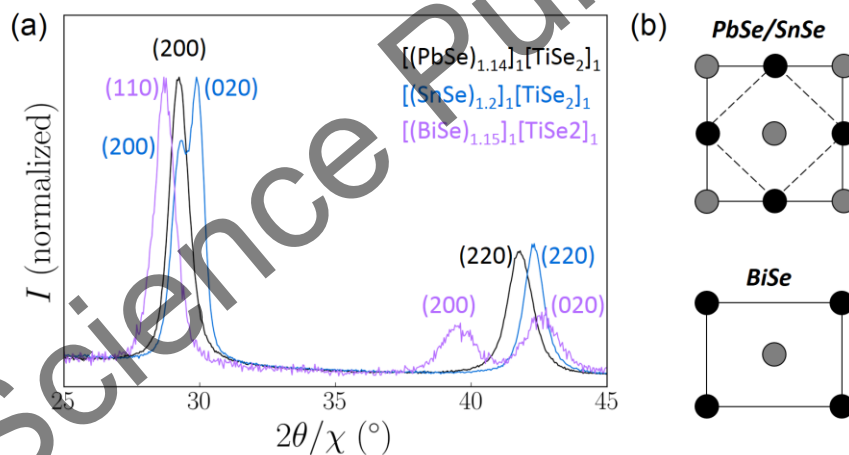


Figure 27. (a) Comparison of the in-plane XRD patterns for $[(\text{MSe})_{1+\delta}]_m[\text{TiSe}_2]_1$ ($M = \text{Pb}, \text{Sn}, \text{Bi}$) between 25° and 45° $2\theta/\chi$. Intensities were normalized to the reflection with the highest intensity for each pattern. (b) Proposed in-plane structures for PbSe and SnSe (top) and BiSe (bottom) layers as viewed along the c -axis. The dashed line in the PbSe and SnSe indicate the primitive cell [81].

SnSe shows a much stronger sensitivity not just to m , but also to the transition metal dichalcogenide. Figure 28a shows the in-plane lattice

parameters of the SnSe layer as a function of m for $[(\text{SnSe})_{1+\delta}]_m[(\text{TSe}_2)]_1$ ($T = \text{Nb, Mo, Ta}$) [81, 82]. For $[(\text{SnSe})_{1+\delta}]_1[(\text{NbSe}_2)]_1$, the in-plane lattice is rectangular, which is consistent with $[(\text{SnSe})_{1.2}]_1[(\text{TSe}_2)]_1$. When more SnSe layers are added, the a -axis lattice parameter increases almost continuously with increasing m whereas the b -axis lattice parameter stays constant, increasing the area of the SnSe basal plane considerably. $[(\text{SnSe})_{1+\delta}]_m[(\text{MoSe}_2)]_1$ on the other hand is square for $m < 4$. The a -axis lattice parameter for $m = 1$ is 0.1 \AA smaller than for the Nb ferecrystal, and approximately the same for $m > 1$. At $m = 4$, the lattice undergoes a rectangular distortion and the b -axis lattice parameter decreases, but stays above the b -axis lattice parameter for $[(\text{SnSe})_{1+\delta}]_m[(\text{NbSe}_2)]_1$. $[(\text{SnSe})_{1+\delta}]_m[(\text{TaSe}_2)]_1$ also starts with a square in-plane lattice until $m = 3$ with an a -axis lattice parameter smaller than the other ferecrystals. For $m > 3$, the basal plane shows a rectangular distortion where the a -axis lattice parameter is similar to $[(\text{SnSe})_{1+\delta}]_m[(\text{NbSe}_2)]_1$. The b -axis lattice parameter converges to the value for $[(\text{SnSe})_{1+\delta}]_m[(\text{NbSe}_2)]_1$ at $m = 6$. The areas of the SnSe basal planes are largest for $[(\text{SnSe})_{1+\delta}]_m[(\text{MoSe}_2)]_1$ and smallest for $[(\text{SnSe})_{1+\delta}]_m[(\text{NbSe}_2)]_1$, which is the opposite trend of the areas of the dichalcogenides where NbSe_2 has the largest area (10.38 \AA^2), followed by TaSe_2 (10.34 \AA^2) and MoSe_2 (9.55 \AA^2) [81].

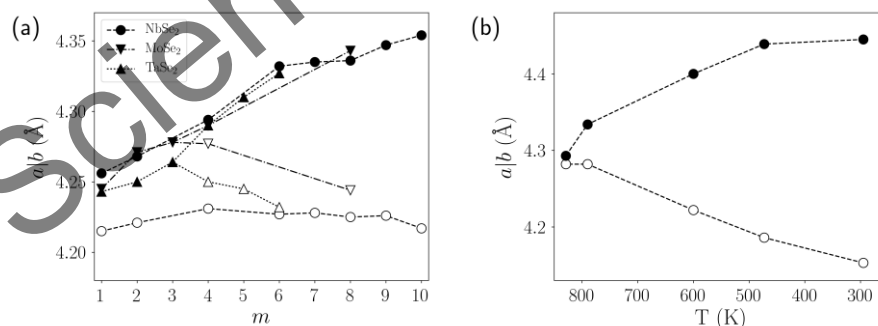


Figure 28. (a) In-plane lattice parameters for SnSe as a function of m for different ferecrystals with NbSe_2 , MoSe_2 , and TaSe_2 as the transition metal dichalcogenide layer [81]. (b) In-plane lattice parameters for bulk SnSe as a function of temperature. Filled markers are the a -axis and open markers are the b -axis lattice parameters [79]. For the in-plane lattices, the lattice vectors for α -SnSe (GeS structure) were used.

Another interesting trend is the evolution of the lattice parameters of SnSe with m . For all ferecrystals, the lattice parameters for large m values are closer to room temperature SnSe (α -SnSe, GeS structure). With decreasing m , the SnSe in-plane lattice becomes more and more square, similar to bulk SnSe at high temperatures (Figure 27b). At 807 K, SnSe undergoes a phase transition to β -SnSe (TII structure) and becomes nearly square in a second order phase transition [79]. Density functional theory calculations on isolated SnSe multilayers predicted that reducing the number of SnSe layers leads from a rectangular basal plane to a square basal plane at $m = 1$, which suggests that this transition occurs without interaction with the TSe₂ layer and is thus size-induced [84]. The fact that the “transition m ” is different for different ferecrystals (if there is one at all), however, shows that there are significant interactions with the transition metal dichalcogenide layer that influence the m value for which this transition occurs. In the case of [(SnSe)_{1+ δ}] _{m} [(NbSe₂)₁], this transition does not happen at all, so the transition metal dichalcogenide can either accelerate or hinder the transition from square to rectangular. Since Nb and Ta both have one less d -electron than Mo, charge transfer cannot be the (only) explanation for this phenomenon.

As shown in Figure 26, the structure of the proposed BiSe basal plane is different from PbSe: it is a rectangular, primitive cell that can be derived from the primitive in-plane unit cell PbSe by performing an orthorhombic distortion. If the proposed structure is correct, looking at the structure along the (100) axis should show alternating Bi and Se atoms along the plane perpendicular to this axis. However, as it is shown in a HAADF-STEM image [(BiSe)_{1.14}]₁[(TiSe₂)₂] (Figure 29) along the (100) zone axis of BiSe, there are Bi-Bi pairings every 28 Å. These pairings appear in roughly one third of the atomically resolved layers [71].

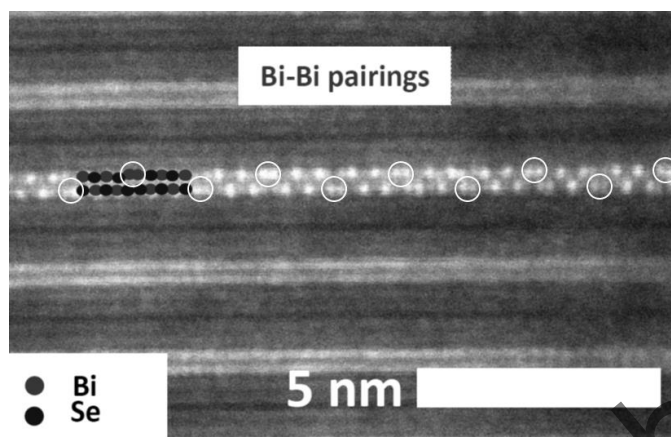


Figure 29. HAADF-STEM image of $[(\text{BiSe})_{1.14}]_1[\text{TiSe}_2]_2$ along the BiSe (100) zone axis. Bi atoms appear as bright dots. The Bi-Bi pairings are circled white [71].

These pairings are also found in the ferecrystals $[(\text{BiSe})_{1.12}]_1[\text{VSe}_2]_1$ (period: 34 Å) and $[(\text{BiSe})_{1+\delta}]_1[(\text{NbSe}_2)]_n$ (period: 15 Å), and the misfit layer compound $[(\text{BiSe})_{1.09}]_1[\text{TaSe}_2]_1$ (period: 37.6 Å) [69, 70, 85]. The period is obviously sensitive to the transition metal dichalcogenide. A systematic analysis of the occurrence of these pairings was conducted for the ferecrystals $[(\text{BiSe})_{1+\delta}]_1[(\text{NbSe}_2)]_n$. Increasing n above 1 leads to square lattice with a lattice parameter of 4.24 Å for $n = 2 - 4$, which corresponds to the b -axis lattice parameter for $n = 1$ (a for $n = 1$ is 4.45 Å). This is different from $[(\text{BiSe})_{1.14}]_1[\text{TiSe}_2]_n$ ($n = 2 - 4$) where the BiSe in-plane lattice stays rectangular. HAADF-STEM and x-ray photoelectron spectroscopy (XPS) show that the number of layers that show Bi-Bi pairings reduces systematically from 75% to 20%, 15%, and 5% when n is increased from 1 to 4 [86]. A systematic analysis of the BiSe lattice with increasing m could not be performed yet because BiSe ferecrystals with $m > 1$ have not been successfully synthesized.

The reason for this behavior is still not fully understood. Compared to PbSe and SnSe, BiSe has an additional valence electron, and its bulk modification crystallizes in a trigonal structure with elemental Bi layers sandwiched between Bi_2Se_3 layers [87]. Crystal orbital overlap population (COOP) analysis using the extended Hückel approach showed that Bi-Bi

bonds are bonding and stabilize the lattice. In the NaCl structure on the other hand, the COOP at the Fermi level point to anti-bonding interactions in the crystal [88]. If the Bi-Bi bonds form to stabilize the BiSe lattice, it raises the question why the period (and thus the frequency) of these Bi-Bi pairings change with the transition metal dichalcogenide, and why the number of layers with Bi-Bi pairings decreases with increasing number of NbSe₂ layers. The most obvious hypothesis would be that differences in charge transfer from the BiSe to the transition metal dichalcogenide layers is responsible for this behavior. However, Hall measurements suggest that the charge transfer is independent of n for NbSe₂, but that significant interlayer charge transfer occurs in the TiSe₂ ferecrystal [71, 86].

The in-plane structure of ferecrystals is still not fully understood. While the in-plane structures of the transition metal dichalcogenide subunit is insensitive to the layering sequence and the other components of the film, SnSe shows a strong dependence not only on its thickness but also on the dichalcogenide layer around it. PbSe shows reflections that should vanish in an undistorted rock salt structure, which is an indicator that the structure is distorted inside the ab -plane. BiSe, which has one valence electron more than SnSe and PbSe, adopts a different crystal structure and contains Bi-Bi pairings which have different periods and abundances with different dichalcogenide layers in the ferecrystal. The in-plane structures of SnSe and BiSe show that there are significant interactions between the layers, but a complete description of these interactions still needs to be developed.

A New Type of Structural Isomers

In the previous sections, ferecrystals with simple structures of the form $[(MX)_{1+\delta}]_m[TX_2]_n$ were discussed, i.e., m layers of MX were followed by n layers of TX₂. However, there is no reason to require such a structure – given the kinetic control of the reaction, it is conceivable that any permutation of MX and TX₂ is possible in ferecrystalline compounds. For $m = n = 1$, there is only one combination, $[(MX)_{1+\delta}]_1[TX_2]_1$. for $m = n = 2$,

there are six unique permutations shown below where A and B denote $(MX)_{1+\delta}$ and TX_2 for brevity:

AABB, *ABAB*, **ABBA**, **BAAB**, *BABA*, **BBAA**

This amounts to only two unique compounds because of the translational symmetry of the crystal. For example, **AABB** and **ABBA** correspond to $[(MX)_{1+\delta}]_2[TX_2]_2$ and $[(MX)_{1+\delta}]_1[TX_2]_2[(MX)_{1+\delta}]_1$, respectively. Shifting the origin past the TX_2 layers would result in the **AABB** compound, so **AABB** and **ABBA** describe the same ferecrystal. The italicized permutations are identical for the same reason, and result in the compound $[(MX)_{1+\delta}]_1[TX_2]_1[(MX)_{1+\delta}]_1[TX_2]_1$. This is the compound $[(MX)_{1+\delta}]_1[TX_2]_1$ doubled along the c -axis and thus does not constitute a new compound.

For $m = n = 3$, there are 20 unique permutations:

ABABAB, BABABA

AAABBB, AABBBB, ABBBAA, BBBAAA, BBAAAB, BAAABB

AABBAB, AABABB, ABAABB, ABABBA, ABBAAB, ABBABA

BBAABA, BBABAA, BABAAB, BABBAA, BAABBA, BAABAB

The first row is again $[(MX)_{1+\delta}]_1[TX_2]_1$, the second row $[(MX)_{1+\delta}]_3[TX_2]_3$ and its translationally symmetric varieties. The third and fourth row are identical to each other and represent the compound $[(MX)_{1+\delta}]_2[TX_2]_2[(MX)_{1+\delta}]_1[TX_2]_1$, which cannot be transformed into the compound $[(MX)_{1+\delta}]_3[TX_2]_3$ using symmetry operations. Since the full formula or the AB-notation is cumbersome, especially for larger m and n , $[(MX)_{1+\delta}]_3[TX_2]_3$ or **AAABBB** will be referred to as **3:3** in a shorthand notation where the number in bold face represents the number of TX_2 layers. $[(MX)_{1+\delta}]_2[TX_2]_2[(MX)_{1+\delta}]_1[TX_2]_1$ or **AABBAB** is thus **2:2:1:1**.

For $m = n = 4$, there are 70 unique permutations with only six distinct compounds (excluding 1:1 and 2:2), which are shown in Figure 30: **4:4**, **3:3:1:1**, **2:3:2:1**, **3:2:1:2**, **2:2:1:1:1:1**, and **2:1:1:2:1:1**. For these compounds

(and analogously for 3:3 and 2:2:1:1), the stoichiometry and the c -axis lattice parameter are the same, but the arrangement of the individual layers is different, i.e., they are isomers analogous to the isomers in organic compounds. C_4H_8 for example has three linear modifications ((*E*)-2-butene, (*Z*)-2-butene, 1-butene), one branched modification (2-methylpropene), and two cyclic modifications (cyclobutane, methylcyclopropane). The isomers in ferecrystals can be grouped by the number of interfaces per unit cell. For $m = n = 4$, there are isomers with one (4:4), two (3:3:1:1, 3:2:1:2, 2:3:2:1), and three (2:1:1:2:1:1, 2:2:1:1:1:1) interfaces. This type of structural isomerism is unique to ferecrystals.

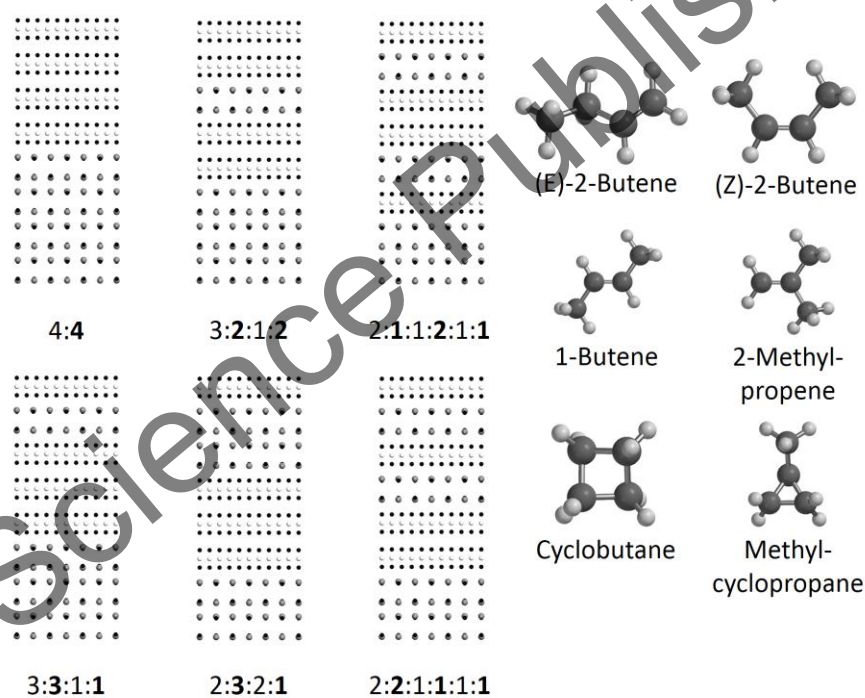


Figure 30. Unique permutations of MX and TX₂ layers for $m = n = 4$ (excluding 1:1 and 2:2), and isomers of C_4H_8 .

Figure 31 shows HAADF-STEM images and XRD patterns of annealed precursors designed to form the different isomers of $[(\text{PbSe})_{1.14}]_4[\text{NbSe}_2]_4$. The STEM images clearly show the different layering structures, demonstrating that the individual isomers can be formed. The XRD patterns show that all compounds have the same c -axis lattice parameter, as indicated by the dashed line through the $(00l)$ reflections ($l = 8, 16, 24, 32$). While the positions of the reflections are identical for all six isomers, the reflections that are extinct are different in each pattern, which reflects the different layering sequences in the individual isomers [89].

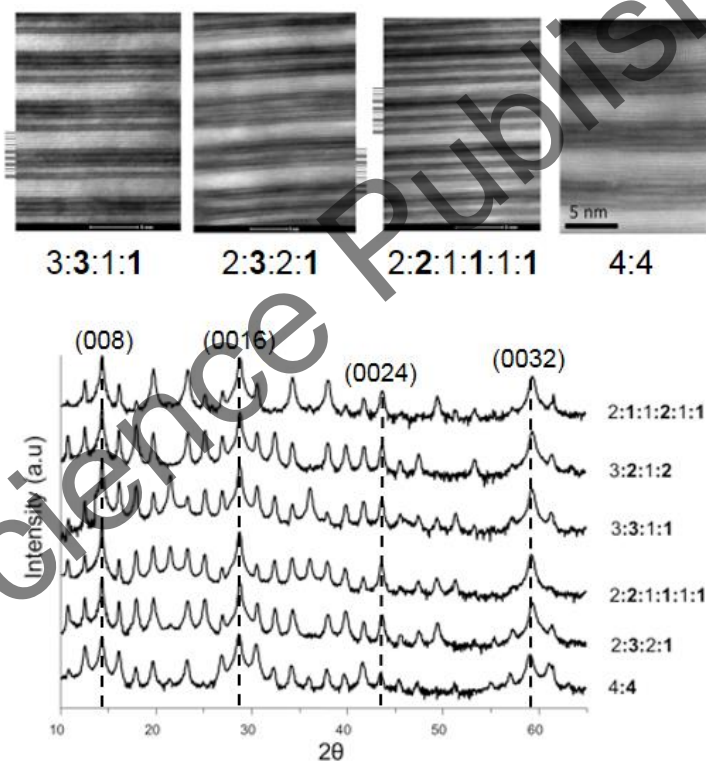


Figure 31. HAADF-STEM images (top) and XRD patterns (bottom) of ferecrystal isomers for $[(\text{PbSe})_{1.14}]_m[\text{NbSe}_2]_4$. Bright areas in the STEM image correspond to PbSe layers, and dark areas correspond to NbSe₂ layers. The dashed lines in the XRD patterns are a guide for the eye for select $(00l)$ reflections ($l = 8, 16, 24, 32$) in all isomers.

The same isomers were successfully prepared for the ferecrystals $[(\text{SnSe})_{1.15}]_4[\text{NbSe}_2]_4$ and $[(\text{SnSe})_{1.1}]_4[\text{MoSe}_2]_4$ [90, 91]. For these compounds, in-plane lattice parameters were determined as well. The a -axis lattice parameters of the dichalcogenides were all within error for each isomer, and are $3.463(3)$ Å for NbSe_2 and $3.31(1)$ Å for MoSe_2 . In the MoSe_2 compound, SnSe has a square basal plane with $a = 6.03(1)$ Å. For the ferecrystal containing NbSe_2 , the a -axis lattice parameter is $6.00(1)$ Å for all isomers, except for the 4:4 isomer where the width of the reflections suggests that SnSe crystallizes in a rectangular basal plane with an a -axis lattice parameter of $6.04(1)$ Å.

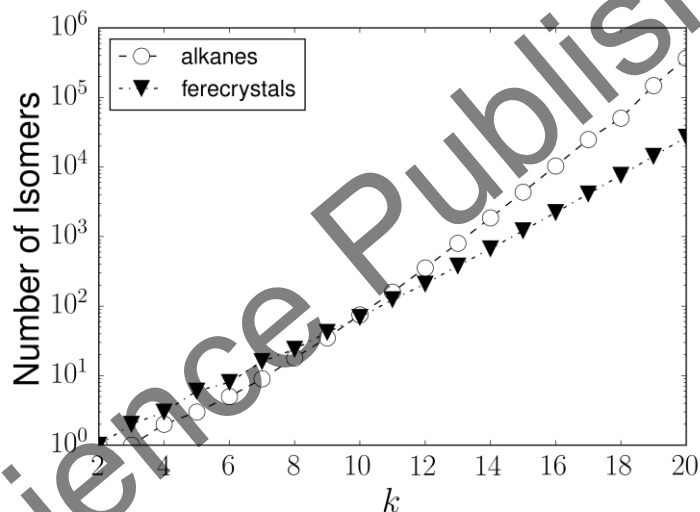


Figure 32. Number of isomers for ferecrystals with $k = m + n$ structural units compared to the number of isomers in alkenes $\text{C}_k\text{H}_{2k+2}$.

The ability to synthesize these isomers greatly enhances the number of ferecrystalline compounds that can be synthesized. Figure 32 compares the number of isomers for a given number of layers, $k = m + n$, and one combination of M, T, and X, with the number of isomers for the alkenes $\text{C}_k\text{H}_{2k+2}$. It demonstrates how with increasing m and n , the number of theoretically accessible compounds rises rapidly, and quickly reaches more than ten thousand different compounds, comparable to the number of

alkanes. These numbers increase by another order of magnitude when different combinations of M, T, and X are factored in. This parameter space is too large to explore experimentally, which demonstrates the need for a comprehensive understanding of the interactions between layers to predict structures and properties of compounds with arbitrary m and n . However, the vast number of compounds also provides great opportunities to systematically alter the interactions between layers to investigate these trends.

Quaternary Ferecrystals and Alloys

The ferecrystals discussed so far are ternary compounds with one MSe and one TSe₂ component. Using the same rationale, it should be possible to synthesize quaternary compounds with either two different M or two different T elements. There are two possible approaches: ferecrystalline alloys where the MSe or TSe₂ layer forms alloys with the additional M or T element, or heterojunctions where the different MSe or TSe₂ layers are separated by TSe₂ or MSe layers, respectively. The following section will discuss both concepts, starting with the transition metal dichalcogenide layers.

To synthesize a ferecrystalline alloy, two approaches are possible. The first approach uses alloys of the transition metals as the deposition source. For example, in order to synthesize an alloy of [(SnSe)_{1+δ}][Nb_xMo_{1-x}Se₂], one could weigh the appropriate amount of elemental niobium and molybdenum for a Nb_xMo_{1-x} alloy, melt these elements in an arc melter, and deposit the sequence Nb_xMo_{1-x}-Se-Sn-Se. This is essentially a three-component system like the other ferecrystals and can be easily calibrated. However, the vapor pressure of niobium is higher than of molybdenum so that the precursor is more niobium rich than the deposition source [92, 93]. The niobium in the deposition source on the other hand will deplete over time so that the partial pressure of niobium in the deposited vapor will decrease over time. The consequence is that the precursor will become increasingly molybdenum rich with subsequent depositions. The advantage

of this technique is that a series of alloys can be prepared this way, but there is no control over the composition. Furthermore, this approach only works if the elements are miscible. These drawbacks can be overcome by using separate deposition sources for niobium and molybdenum and by depositing the sequences Sn-Se-Nb-Se-Mo-Se or Sn-Se-Nb-Mo-Se with targeted Nb:Mo ratios, which can be determined using electron probe microanalysis (EPMA) [94].

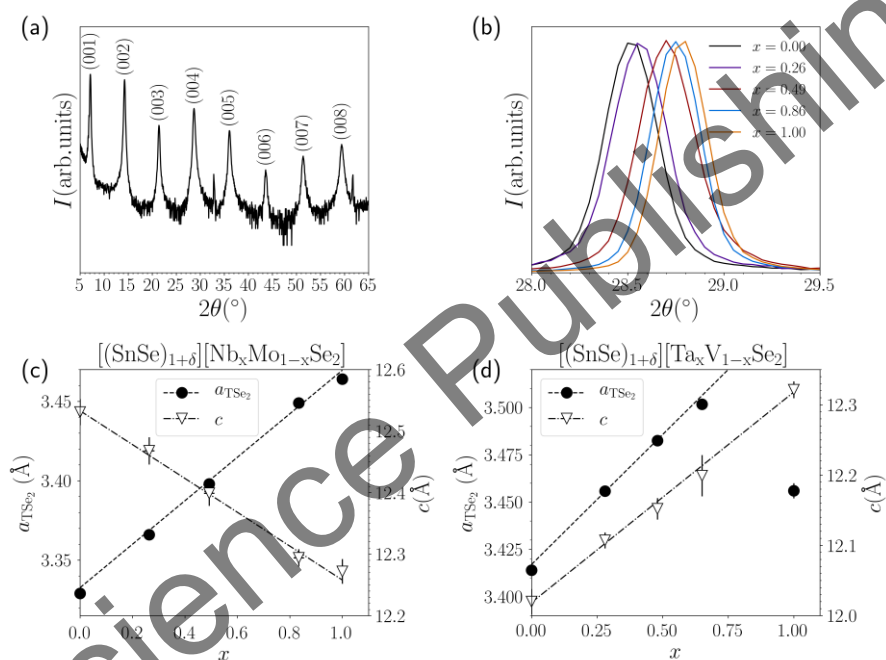


Figure 33. (a) Out-of-plane XRD pattern of $[(SnSe)_{1.13}][Nb_{0.49}Mo_{0.51}Se_2]$. (b) Evolution of the (004) reflection in $[(SnSe)_{1+\delta}][Nb_xMo_{1-x}Se_2]$ as a function of x . (c, d) In-plane lattice parameter a_{TSe_2} of the transition metal dichalcogenide and the out-of-plane lattice parameter c of the ferecrystals (c) $[(SnSe)_{1+\delta}][Nb_xMo_{1-x}Se_2]$ and (d) $[(SnSe)_{1+\delta}][Ta_xV_{1-x}Se_2]$ (d) as a function of x . The lines represent linear fits through the data [93, 94, 98].

The precursors form superlattice structures in the out-of-plane diffraction patterns typical of other ferecrystals (Figure 33a) [93]. The position of the reflections depends on the Nb:Mo ratio as illustrated in

Figure 33b. The (004) reflection shows a clear shift to higher 2θ values as the amount of niobium increases. Figure 33c shows the c -axis lattice parameters and the a -axis lattice parameter of the transition metal dichalcogenide as a function of x , where x was determined by EPMA. The c -lattice and a -axis lattice parameters both follow a linear progression as predicted by Vegard's law because bulk NbSe_2 and MoSe_2 both crystallize in a hexagonal structure with trigonal prismatic TSe_6 units ($\text{T} = \text{Nb, Mo}$), and are known to form solid solutions with each other [95, 96]. Since NbSe_2 has a larger a -axis but a smaller c -axis lattice parameter, the slopes are of opposite sign.

The ability to form alloys is not limited to transition metal dichalcogenides with the same coordination environment though, which is evidenced by ferecrystalline $[(\text{SnSe})_{1+\delta}][\text{Ta}_x\text{V}_{1-x}\text{Se}_2]$ alloys. In TaSe_2 , tantalum is coordinated in a trigonal prismatic geometry whereas in VSe_2 , vanadium is coordinated octahedrally. The bulk constituents are known to form a solid solution up to $x = 0.6$ [97]. Figure 36d shows the evolution of the in-plane lattice parameter of $\text{Ta}_x\text{V}_{1-x}\text{Se}_2$ and the c -axis lattice parameter of the ferecrystal. The in-plane lattice parameters have a larger slope than Vegard's law would suggest. The increase is linear until $x = 0.65$, but the TaSe_2 endmember has a smaller lattice parameter than the alloy with $x = 0.28$. Since VSe_2 and TaSe_2 have different crystal structures, Vegard's law does not apply here. The inclusion of tantalum into VSe_2 leads to a large distortion in the VSe_2 lattice, but the change in coordination environments does not occur until after $x = 0.65$. The c -axis lattice parameter, however, follows a linear progression along the entire composition range with a positive slope since tantalum is larger than vanadium. Along the c -axis, ferecrystals appear to have the same crystal structure regardless of the in-plane geometry of the transition metal dichalcogenide and thus the c -axis lattice parameter can be described with Vegard's law [94, 98].

It was already discussed that the in-plane lattice parameters of the SnSe subunit depend heavily on the transition metal dichalcogenide in the ferecrystal (see Figure 28). Figure 34 shows that this is also true for the alloys. In ferecrystals containing NbSe_2 , SnSe has a rectangular basal plane whereas in ferecrystals containing MoSe_2 , the basal plane is square. There

is a linear increase of the b -axis lattice parameter of SnSe with increasing x . The a -axis lattice parameter on the other hand decreases with increasing x , but not in a linear fashion. Both lattice parameters converge towards the in-plane lattice parameter found in $[(\text{SnSe})_{1.16}][\text{MoSe}_2]$ [93].

The in-plane lattice parameters of SnSe in the $[(\text{SnSe})_{1+\delta}][\text{Ta}_x\text{V}_{1-x}\text{Se}_2]$ alloys follow a trend similar to the trend found for transition metal dichalcogenides. SnSe crystallizes in a square basal plane for both $[(\text{SnSe})_{1.15}][\text{VSe}_2]$ and $[(\text{SnSe})_{1.15}][\text{TaSe}_2]$, but it does not stay square for all alloys. With a Ta content above 28% in the alloy, the SnSe lattice shows an orthorhombic distortion with a maximum at approximately 50% Ta. At 65% Ta, the lattice is almost square again as the a -axis lattice parameter decreases while the b -axis lattice parameter continues to increase. The lattice becomes square again at the TaSe_2 endmember with a smaller lattice parameter than in the alloys, which correlates well with the a -axis lattice parameters of the $\text{Ta}_x\text{V}_{1-x}\text{Se}_2$ subunit [94, 98].

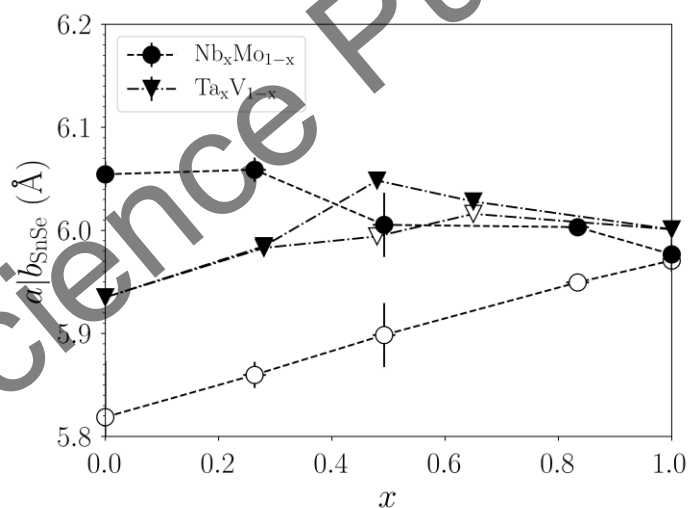


Figure 34. In-plane lattice parameters of SnSe in the ferecrystals $[(\text{SnSe})_{1+\delta}][\text{Nb}_x\text{Mo}_{1-x}\text{Se}_2]$ and $[(\text{SnSe})_{1+\delta}][\text{Ta}_x\text{V}_{1-x}\text{Se}_2]$. The a -axis lattice parameters are displayed with filled markers and the b -axis lattice parameters with open markers [93, 94, 98].

As with the ternary ferecrystals, different amounts of charge transfer may be responsible for this behavior, especially for the $[(\text{SnSe})_{1+\delta}][\text{Nb}_x\text{Mo}_{1-x}\text{Se}_2]$ alloys because Mo has one more valence electron than Nb. Ta and V have the same amount of valence electrons, but prefer different coordination geometries (Ta is trigonal prismatic and V octahedrally coordinated), which influences the band structure of the dichalcogenides. This influences the interactions that exist between the dichalcogenide and the SnSe layer. The evolution of the in-plane lattice parameters of both SnSe and the transition metal dichalcogenide alloy correlate very well with each other, which confirms this hypothesis. Since ferecrystals do not grow epitaxially, strain is unlikely to have a significant effect on the structure.

For heterojunctions, a different layering sequence in the MER precursor needs to be chosen. To avoid the formation of a ferecrystalline alloy, an additional Sn-Se bilayer needs to be deposited between the T-Se layers. To synthesize the heterojunction $[(\text{SnSe})_{1+\delta}][(\text{MoSe}_2)_{1+\gamma}][(\text{SnSe})_{1+\delta}][\text{NbSe}_2]$, for example, the precursor should have the layering sequence Sn-Se-Mo-Se-Sn-Se-Nb-Se. The XRD pattern of an annealed precursor with this sequence is shown in Figure 35a along with the alloy XRD pattern for comparison. The annealed precursor for the heterojunction shows twice as many reflections as the alloy, with the additional reflections being in-between the reflections that can be found in the alloy. This shows that the *c*-axis lattice parameter is twice as large than for the alloy, as expected for the heterojunction [99].

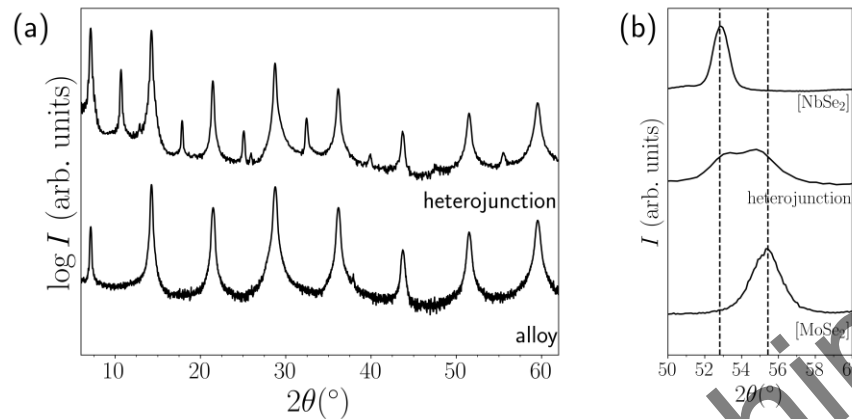


Figure 35. (a) Out-of-plane XRD pattern of the heterojunction $[(\text{SnSe})_{1+\delta}][(\text{MoSe}_2)_{1+\gamma}][(\text{SnSe})_{1+\delta}][\text{NbSe}_2]$ (top) and an $[(\text{SnSe})_{1+\delta}][\text{Nb}_{0.5}\text{Mo}_{0.5}\text{Se}_2]$ alloy. (b) The (110) reflection of $[(\text{SnSe})_{1+\delta}][\text{NbSe}_2]$, the heterojunction, and $[(\text{SnSe})_{1+\delta}][\text{MoSe}_2]$. The dashed lines are a guide for the eye and show the reflection maxima of the two ferecrystals [99].

However, the in-plane XRD pattern suggests that the heterojunction does not contain pure NbSe_2 and MoSe_2 layers. It is expected that the lattice parameters of the NbSe_2 and the MoSe_2 subunits are the same as in the ternary ferecrystals, i.e., the in-plane XRD pattern of the heterojunction should show two reflections with the same 2θ positions as in the in-plane XRD patterns of $[(\text{SnSe})_{1.16}][\text{NbSe}_2]$ and $[(\text{SnSe})_{1.09}][\text{MoSe}_2]$. The (110) reflection of the heterojunction (Figure 35b), however, shows two broad maxima in-between the reflections of the ternary ferecrystals. As demonstrated before, NbSe_2 and MoSe_2 can form ferecrystalline alloys that follow Vegard's law. The deviation of the 2θ positions of the diffraction maxima from the ferecrystalline compounds with pure NbSe_2 and MoSe_2 can be attributed to alloying of the NbSe_2 layer with Mo and the of the MoSe_2 layer with Nb, suggesting that diffusion of the transition metals through the Sn-Se layers occurs. The true formula of the heterojunction thus needs to be written as $[(\text{SnSe})_{1+\delta}][(\text{Nb}_x\text{Mo}_{1-x}\text{Se}_2)_{1+\gamma}][(\text{SnSe})_{1+\delta}][\text{Mo}_y\text{Nb}_{1-y}\text{Se}_2]$ [99].

Determining x is a challenging task because compositional analysis measures the entire film, Rietveld refinement for the in-plane XRD pattern

is not possible yet, and Rietveld refinement of the out-of-plane XRD pattern is not very robust because of the similar electron densities of niobium and molybdenum. Since the $\text{Nb}_x\text{Mo}_{1-x}\text{Se}_2$ alloys follow Vegard's law, however, x can be estimated by determining the in-plane lattice parameters of both layers, which results in $x = 0.10(2)$ and $y = 0.12(2)$. The error is fairly large because of a large degree of overlap between the reflections. The formula of this heterojunction can finally be written as $[(\text{SnSe})_{1+\delta}][(\text{Nb}_{0.1}\text{Mo}_{0.9}\text{Se}_2)_{1.06}][(\text{SnSe})_{1+\delta}][\text{Mo}_{0.1}\text{Nb}_{0.9}\text{Se}_2]$ [99].

These findings raise the question whether it is possible to prevent the diffusion of the transition metals by creating a large enough diffusion barrier in the precursor. To investigate this, precursors of the structure $(\text{Sn-Se})_m-(\text{Mo-Se})-(\text{Sn-Se})_m-(\text{Nb-Se})$ were deposited and annealed. The evolution of the (110) reflection as a function of m is shown in Figure 36a. For $m = 0$, i.e., with no Sn-Se diffusion barrier, a broad reflection can be found that splits when m is increased to 1. The distance between the diffraction maxima increases with m until $m = 3$, after which the distance stays constant. The 2θ positions of the reflections for $m \geq 3$ agree well with the 2θ positions of (110) reflection of the ternary ferecrystals, indicating that no alloys are present in the compound [100].

The values for x and y as a function of m can be estimated using Vegard's law (Figure 36b). The results suggest that Mo has a stronger tendency to diffuse into NbSe_2 than the other way around without a diffusion barrier present. Introducing a diffusion barrier significantly decreases the amount of Mo that gets incorporated into the NbSe_2 lattice. Increasing the diffusion barrier thickness results in less and less Mo diffusing whereas the diffusion of Nb is relatively constant until it sharply decreases to zero at $m = 3$, which coincides with the diffusion of Mo going to zero as well [100]. An interesting question is whether no Nb diffusion occurs because the SnSe diffusion barrier is too large for Nb to overcome, or if the formation of pure MoSe_2 in the other layer, which occurs because Mo diffusion is suppressed, prevents Nb from being incorporated into the MoSe_2 lattice. Additional research needs to be performed to answer this question.

At last, the in-plane lattice parameters of SnSe are expected to change with m as they do for the ternary ferecrystals. As Figure 36c shows, SnSe is square for $m = 1$ as in $[(\text{SnSe})_{1.06}][\text{MoSe}_2]$, but with a smaller lattice parameter. With larger separation and thus thicker SnSe layers, the SnSe basal plane undergoes an orthorhombic distortion with increasing a/b ratio as m increases, similar to what was found for ternary ferecrystals. The in-plane lattice parameters are slightly larger than in the ternary ferecrystals though, suggesting different interactions such as charge transfer in the heterojunction compared to the alloys and ternary ferecrystals.

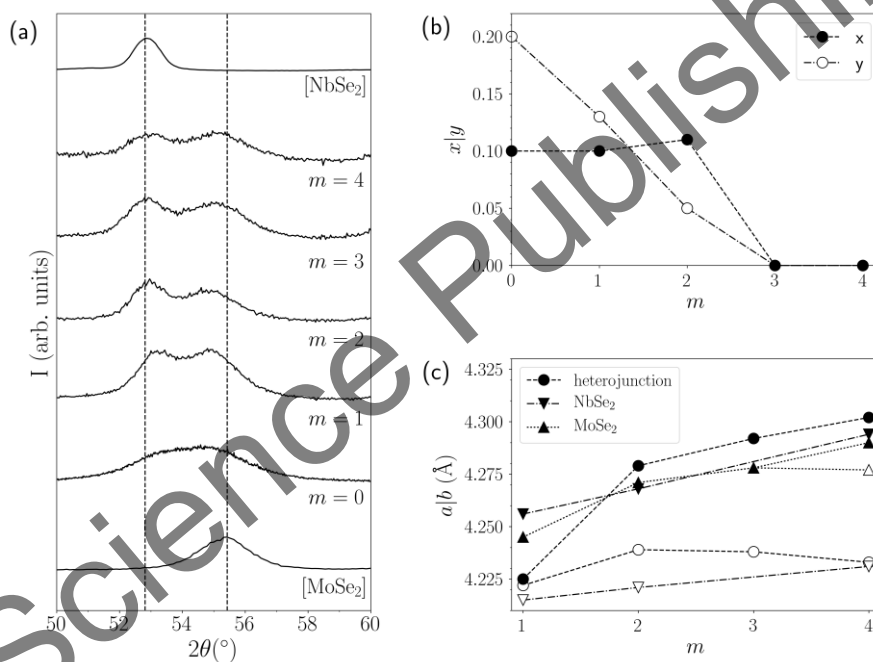


Figure 36. (a) Evolution of the (110) reflection as a function of m in the $[(\text{SnSe})_{1+\delta}]_m[(\text{NbSe}_2)_{1+\gamma}][(\text{SnSe})_{1+\delta}]_m[\text{MoSe}_2]$ heterojunction. The (110) reflection of the ferecrystals $[(\text{SnSe})_{1+\delta}][\text{NbSe}_2]$ and $[(\text{SnSe})_{1+\delta}][\text{MoSe}_2]$ are added for comparison. The dashed lines are a guide for the eye and show the reflection maxima of the two ferecrystals. (b) Evolution of the parameters x and y in the heterojunction $[(\text{SnSe})_{1+\delta}]_m[(\text{Nb}_{1-x}\text{Mo}_x\text{Se}_2)_{1+\gamma}][(\text{SnSe})_{1+\delta}]_m[\text{Nb}_y\text{Mo}_{1-y}\text{Se}_2]$ as a function of m . (c) In-plane lattice parameters of SnSe as a function of m in the heterojunction and the ternary endmembers. The a -axis lattice parameters are displayed with filled markers and the b -axis lattice parameters are displayed with open markers [100].

Using Vegard's law to estimate the degree of intermixing has the drawback that it cannot be used with alloys with endmembers that adopt different crystal structures such as the heterojunction $[(\text{SnSe})_{1+\delta}][(\text{Ta}_x\text{V}_{1-x}\text{Se}_2)_{1+\gamma}][(\text{SnSe})_{1+\delta}][(\text{V}_y\text{Ta}_{1-y}\text{Se}_2)]$. In this case, energy dispersive x-ray spectroscopy (EDX) line scans can be used to estimate these values if x and y are equal. Figure 37 shows EDX maps of the V K line and the Ta M line and show the layered structure of the heterojunction. These layers show alternating layers of brighter and lesser intensity for the V and Ta regions, suggesting that there are Ta-rich and V-rich dichalcogenide layers and that these layers alternate as expected in a heterojunction. The line scans, also shown in Figure 37, confirm this assertion. If x and y are equal, then the ratio of the areas under the V peaks in the V-rich and V-poor regions is the same as the ratio of the areas under the Ta peaks because all instrument and x-ray line dependent factors cancel out. Using this approach, x can be estimated to be 0.68(5). The large uncertainty comes from the low signal to noise ratio, which makes background subtraction difficult to perform. This value is supported by temperature dependent resistivity measurements which can be modeled using a $\text{Ta}_{0.3}\text{V}_{0.7}\text{Se}_2$ and a $\text{V}_{0.3}\text{Ta}_{0.7}\text{Se}_2$ layer in parallel.

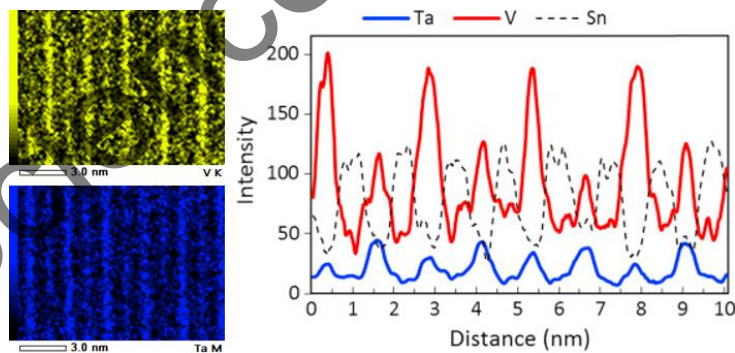


Figure 37. EDX maps and line scans of the ferecrystalline heterojunction $[(\text{SnSe})_{1+\delta}][(\text{Ta}_x\text{V}_{1-x}\text{Se}_2)_{1+\gamma}][(\text{SnSe})_{1+\delta}][(\text{V}_y\text{Ta}_{1-y}\text{Se}_2)]$ [94].

To summarize, transition metal dichalcogenides can form ferecrystalline alloys as well as heterojunctions. The c -axis lattice

parameters of the ferecystals follow Vegard's law whereas the in-plane lattice parameter of the transition metal dichalcogenide only follows it when the endmembers have the same structure. Heterojunctions exhibit a significant amount of interdiffusion between the dichalcogenide layers, which can be suppressed by a sufficiently thick SnSe layer.

The question that naturally arises at this point is whether the same observations can be made for alloys and heterojunctions with two different MSe constituents. To test this, precursors with the layering sequence Sn-Se-Ti-Se-Pb-Se-Ti-Se were deposited and annealed. The out-of-plane XRD pattern of the product is presented in Figure 38a and shows that the final precursor did not form a heterojunction, but an alloy (compare with Figure 35a) [101]. The EDX map and the EDX line scan shown in Figure 38b confirm that Sn and Pb completely interdiffused to form a $\text{Sn}_{0.5}\text{Pb}_{0.5}\text{Se}$ alloy sandwiched between TiSe_2 bilayers [102]. While there was also interdiffusion in the heterojunctions with two different transition metal dichalcogenide components, there was no example where the transition metals formed alloys instead of a heterojunction. To date, no heterojunction with two MSe components have been successfully synthesized.

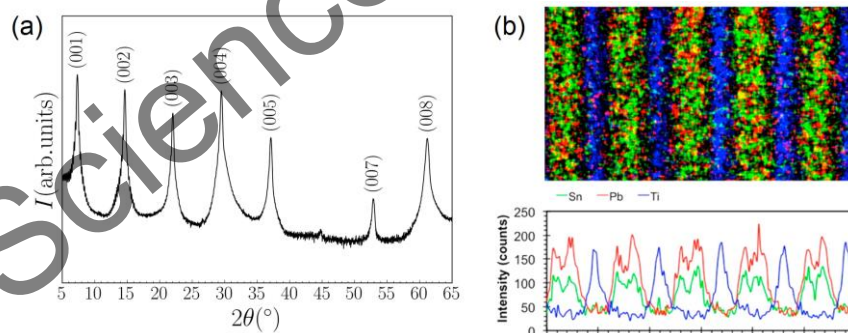


Figure 38. (a) Indexed out-of-plane XRD pattern of an MER precursor with the sequence Sn-Se-Ti-Se-Pb-Se-Ti-Se. (b) EDX map and line scan of $[(\text{Sn}_{0.5}\text{Pb}_{0.5})_{1+6}][\text{TiSe}_2]$ [101, 102].

However, these observations show that alloys of MSe compounds can easily be made. Figure 39a shows the out-of-plane XRD patterns of

$[(\text{Sn}_x\text{Pb}_{1-x})_{1+\delta}][\text{TiSe}_2]$ ferecrystal alloys. Following the evolution of the (004) reflection shows a systematic shift to higher 2θ with increasing Pb content, which is expected due to Pb being larger than Sn. The progression of the c -axis lattice parameter with increasing x follows Vegard's law as it did for the transition metal dichalcogenide ferecrystal alloys [103].

Figure 39b shows the (400) and (420) reflections of these alloys. For $x = 1$, the basal plane is square because PbSe exclusively forms square in-plane structures. Upon introducing Sn, the reflections become broader and show noticeable splitting at $x = 0.48$ into the (400) and (040) and into the (420) and (240) reflections, respectively. The splitting increases with increasing x until $x = 1$. This transition is to be expected because SnSe has a square basal plane in $[(\text{SnSe})_{1.2}][\text{TiSe}_2]$. The broadening of the (400) and (420) reflections for $x = 0.70$ suggests that the orthorhombic distortion already occurs with 30% Sn in the PbSe lattice [103]. Some of the alloys may be metastable since in bulk, PbSe and SnSe show a miscibility gap between $x = 0.2$ and $x = 0.6$, but two of the ferecrystals shown have values of x inside that miscibility gap [104]. The in-plane lattice parameter of TiSe_2 is $3.55(1) \text{ \AA}$, independent of x .

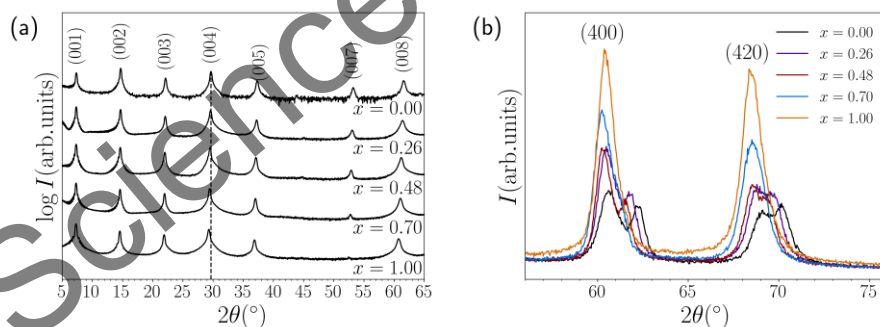


Figure 39. (a) Out-of-plane XRD pattern of $[(\text{Sn}_x\text{Pb}_{1-x})_{1+\delta}][\text{TiSe}_2]$ for $0 \leq x \leq 1$. The dashed line is a guide for the eye for maximum of the (004) reflection with $x = 0$. (b) Evolution of the (400) and (420) reflections as a function of x [103].

Alloys of SnSe with bismuth have even larger miscibility gaps. In the bulk at 400°C , the SnSe lattice can only hold 4% Bi. Higher Bi contents lead to the formation of SnBi_4Se_5 and $\text{Bi}_{0.04}\text{Sn}_{0.96}\text{Se}$. The BiSe lattice can

hold up to 10% Sn [105]. However, SnSe and BiSe crystallize in a different structure in the bulk than in ferecrystals, so ferecrystals may be able to form alloys along the entire composition range.

Ferecrystals with $\text{Bi}_x\text{Sn}_{1-x}\text{Se}$ alloys have been successfully synthesized with NbSe_2 , VSe_2 , and TiSe_2 (VSe_2 only until $x = 0.57$) where the $\text{Bi}_x\text{Sn}_{1-x}\text{Se}$ layers form a solid solution over the entire composition range [106–108]. Figure 40a shows the c -axis lattice parameters of each ferecrystalline alloy as a function of x . There are distinct differences between the ferecrystals of first-row and second-row transition metals. The c -axis lattice parameter of the first-row transition metals decreases in a linear progression until $x = 0.48$ for TiSe_2 , even though bismuth is larger than tin. Above this value at $x = 0.71$, the lattice parameter goes through a saddle-point like transition before ending up at 11.77(1) Å. For VSe_2 , the c -axis lattice parameter decreases linearly for the measured composition range. Since no Bi contents higher than 57% were measured, it cannot be excluded that the c -axis lattice parameter follows the same saddle-point like transition as for the TiSe_2 -ferecrystal. Comparing with the $[(\text{BiSe})_{1+\delta}][\text{VSe}_2]$ ferecrystal ($c = 11.78$ Å), however, suggests that it would. Whereas the c -axis lattice parameters of the first-row transition metal ferecrystals are of similar value, it is more than 0.2 Å larger in the alloys containing NbSe_2 , which is due to the size of niobium. Another key difference is that the alloy with NbSe_2 does not follow the same linear progression as the ferecrystals with first-row transition metals. The c -axis lattice parameters with NbSe_2 decrease in an almost exponential way and quickly level off at 12.1 Å near $x = 0.50$ [106–108].

The evolution of the in-plane lattice parameters (Figure 40b) on the other hand cannot be split between first-row and second-row transition metals. For NbSe_2 , the basal plane is square until $x = 0.50$ and there is no change in the lattice parameter. Once the Bi content is above 50%, the lattice parameter drastically decreases from 6.0 Å to $a = 4.30(2)$ Å and $b = 4.23(2)$ Å because the symmetry reduces to $Pcmm$, i.e., the BiSe structure becomes dominant over the SnSe structure. The orthorhombic distortion that is introduced this way increases with increasing x . Similar observations can be made with TiSe_2 , except for that SnSe is already

orthorhombic at $x = 0$. The a -axis lattice parameter increases with x while the b -axis lattice parameter stays constant, and it undergoes the same symmetry transformation above 50% Bi as the ferecrystal with NbSe₂. The in-plane lattice parameters of NbSe₂ (3.48(1) Å) and TiSe₂ (3.57(1) Å) are unaffected by x [106, 107].

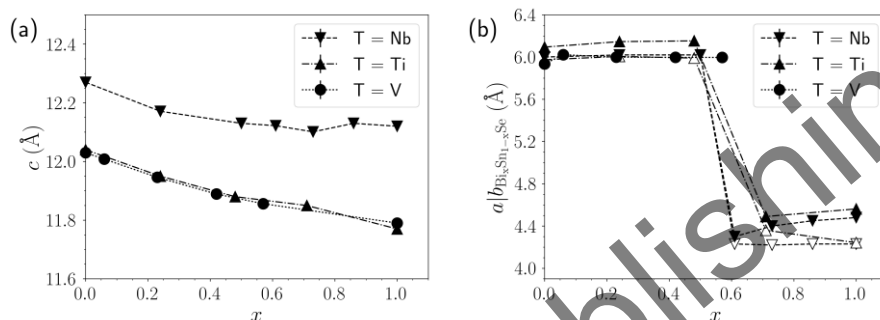


Figure 40. (a) c -axis lattice parameters of the ferecrystalline alloys $[(\text{Bi}_x\text{Sn}_{1-x})_{1+\delta}][\text{TSe}_2]$ ($T = \text{Ti}, \text{V}, \text{Nb}$). The c -axis lattice parameter of $[(\text{BiSe})_{1+\delta}][\text{VSe}_2]$ was taken from ref. [69]. (b) In-plane lattice parameters for the $\text{Bi}_x\text{Sn}_{1-x}\text{Se}$ component in the ferecrystalline alloys. Filled markers denote a -axis lattice parameters and open markers denote b -axis lattice parameters [106–108].

Bi-Bi pairings were found in both alloys. In the alloy with NbSe₂, these pairings appear already at a Bi content of 50% with an abundance of about 20% according to HAADF-STEM. The sample with 73% Bi content has a Bi-Bi pairing abundance of 40%, and the endmember has an abundance of 75%. EDX line scans indicate no phase segregation between SnSe and BiSe, which suggests that these pairings appear within the alloy lattice. Hall measurements show a positive Hall coefficient that increases until $x = 0.5$, after which it decreases again with increasing x . Since NbSe₂ is a hole conductor, the increase of the Hall coefficient suggests charge donation by the NbSe₂ layer, which could explain the decrease in the c -axis lattice parameter, but not that the a -axis lattice parameter stays constant since charge donation should influence the ab -plane of the lattice as well. For ferecrystals with $x > 0.5$, the abundance of Bi-Bi pairings correlates with an increase of the Hall coefficient, which indicates the creation of holes in the $\text{Bi}_x\text{Sn}_{1-x}\text{Se}$ layer, even though Bi has one more valence electron than

Sn. Having carriers in the $\text{Bi}_x\text{Sn}_{1-x}\text{Se}$ as well as in the NbSe_2 layer would complicate drawing conclusions about charge transfer and its effect on the structure. These pairings also distort the $\text{Bi}_x\text{Sn}_{1-x}\text{Se}$ lattice along the a -axis, which explains the increasing orthogonal distortion with increasing Bi content [106]. For TiSe_2 , Bi-Bi pairings have been reported for $x = 0.48$ and $x = 0.7$ with 13% and 50% abundance, respectively. Hall measurements show that the Hall coefficient is negative and increases in magnitude with increasing Bi content. This increase, however, is smaller than expected if one Bi atom donated one electron to the TiSe_2 layer. This deviation increases with increasing x , which correlates well with the increasing abundance of Bi-Bi pairings, suggesting that increasing Bi content reduces the doping efficiency of the alloy layer [107]. These results show that charge donation within ferecrystals is very complex – more research is necessary to elucidate the interactions between the layers in ferecrystalline compounds.

The ferecrystal $[(\text{Bi}_x\text{Sn}_{1-x}\text{Se})_{1+\delta}][\text{VSe}_2]$ shows different behavior than the other two alloys since it does not undergo the same symmetry reduction above 50% Bi content. The in-plane lattice parameter of the $\text{Bi}_x\text{Sn}_{1-x}\text{Se}$ layer only changes by less than 0.1 Å when 6% Bi is introduced and remains constant at 6.00(1) Å upon further introduction of Bi. Since no in-plane XRD for compounds with $x \geq 0.57$ were collected, it is unclear if this is true for even higher Bi contents.

Another aspect that makes these $[(\text{Bi}_x\text{Sn}_{1-x}\text{Se})_{1+\delta}][\text{VSe}_2]$ ferecrystals so different is that the a -axis lattice parameter of VSe_2 changes systematically with increasing x from 3.414(2) Å to 3.475(2) Å. Rietveld refinement of the out-of-plane XRD patterns show that this correlates with a decrease in the d/a ratio for the VSe_2 layer from 1.76 to 1.71. Temperature dependent resistivity and Hall measurements indicate that the charge density wave is enhanced when $x = 0.06$, but then depressed for $x \geq 0.2$ where the positive Hall coefficient is almost temperature independent. The charge density wave transition temperature is not affected by x , however, which is different to what is observed for $[(\text{SnSe})_{1.15}]_m[\text{VSe}_2]_n$ compounds where an increasing n decreases the charge density wave transition temperature. At $x = 0.66$, the Hall coefficient becomes negative, but no structural information

is available to correlate this with an effect on the structure of the ferecrystal. This change in the Hall coefficient was also observed in the $[(\text{SnSe})_{1.15}]_1[\text{VSe}_2]_n$ ferecrystals with increasing n , which suggests stronger coupling between the $\text{Sn}_x\text{Bi}_{1-x}\text{Se}$ and VSe_2 layers with increasing Bi content. The existence of Bi-Bi pairings in these alloys has not been investigated yet [108].

These findings suggest different interactions between the $\text{Bi}_x\text{Sn}_{1-x}\text{Se}$ alloy layer and the VSe_2 layer compared to the ferecrystalline alloys with NbSe_2 and TiSe_2 . Investigating these differences will be subject of future research. Synthesizing alloyed ferecrystals, especially MSe alloys containing bismuth, may enhance our knowledge about interactions in ferecrystals and other heterojunctions and can help designing compounds with desired structures and properties.

Summary – MER Synthesis of Ferecrystals

Ferecrystals are complex heterostructures of the misfit-layer-compound family. They consist of stacks of rock-salt like MX bilayers ($M = \text{Sn, Pb, Bi, La, Ce}$; $X = \text{Se, Te}$) and transition metal dichalcogenide trilayers, and have the general formula $[(\text{MX})_{1+\delta}]_m[\text{TX}_2]_n$ where $1 + \delta$ is the misfit parameter, which accounts for the lattice mismatch of the two constituents. While misfit layer compounds have one commensurate axis, the b -axis, and typically can only access $m = n = 1$, ferecrystals show turbostratic disorder and can access nearly any integer m and n .

The lack of commensurate in-plane axes leads to different in-plane distortions of the constituents. While the structure of the transition metal dichalcogenide is virtually unaffected by m or n (except for when n transitions from 1 to 2), the structure of the MSe subunit depends not only on m and n , but also on the transition metal dichalcogenide in the ferecrystal, likely due to charge transfer. This is especially true for SnSe , which shows a variety of lattice parameters and either adopts square or rectangular basal planes. The in-plane structure of the MX subunit is still not fully understood. Both PbSe and SnSe show reflections that are

forbidden in a pure NaCl structure, suggesting that there are in-plane distortions. BiSe shows lower symmetry and exhibits Bi-Bi pairings with periods and abundances that depend on the thickness of the transition metal dichalcogenide layer and the transition metal in the ferecrystal.

Ferecrystals show a unique type of structural isomers for $m, n \geq 2$ (except $m = n = 2$). These isomers have the same c -axis lattice parameter, but different layering structures. For $m = n = 3$, two isomers exist, and for $m = n = 4$, there are six. The number of isomers increases rapidly for a given combination of m and n , and thus increases the number of theoretically accessible ferecrystals into tens of thousands of compounds for each combination of M and T.

Quaternary ferecrystals exist mostly as alloys either of the transition metal dichalcogenide or the MX components. The degree of alloying can be controlled with the composition of the precursor, even if the bulk analog has a miscibility gap at these compositions. The c -axis lattice parameter follows Vegard's law, except for alloys containing Bi for which the changes are more complex. The a -axis lattice parameter of the transition metal dichalcogenide follows Vegard's law only if both endmembers have the same structure. Heterojunctions have only been successfully synthesized with two transition metal dichalcogenide components. There is a significant amount of diffusion through the MSe layer, which can be prevented with a sufficiently high m . Precursors for heterojunctions with different MSe components result in alloys because the M elements diffuse quickly through the transition metal dichalcogenide layers. The behavior of alloys containing Bi is significantly different and strongly depends on the transition metal in the dichalcogenide layer. Alloys with BiSe also exhibit Bi-Bi pairings starting at approximately 50% Bi in the MSe layer.

The nearly unlimited combinations of m and n , the ability to produce isomers, and the ability to synthesize heterojunctions and alloys open the gates to a vast number of new compounds, a parameter space that is impossible to explore empirically. Future research efforts need to investigate the interactions between the subunits to develop guidelines for the synthesis of ferecrystals with designed structures and physical properties.

ACKNOWLEDGMENTS

The authors acknowledge Danielle Hamann (University of Oregon) for providing the TiSe₂ calibration data, and Matthias Falmbigl (Drexel University) for providing x-ray diffraction patterns and TEM images, for helpful discussions, and for providing Figure 21b. The authors also acknowledge support from the National Science Foundation under grant DMR-1266217.

REFERENCES

- [1] M. Jansen, A concept for synthesis planning in solid-state chemistry, *Angew. Chemie - Int. Ed.* 41 (2002) 3746–3766. doi:10.1002/1521-3773(20021018)41:20<3746::AID-ANIE3746>3.0.CO;2-2.
- [2] W.W. Tipton, R.G. Hennig, A grand canonical genetic algorithm for the prediction of multi-component phase diagrams and testing of empirical potentials., *J. Phys. Condens. Matter.* 25 (2013) 495401. doi:10.1088/0953-8984/25/49/495401.
- [3] J.C. Schön, Nanomaterials - what energy landscapes can tell us, *Process. Appl. Ceram.* 9 (2015) 157–168. doi:10.2298/PAC1503157S.
- [4] E.J. Corey, The Logic of Chemical Synthesis: Multistep Synthesis of Complex Carbogenic Molecules (Nobel Lecture), *Angew. Chemie Int. Ed. English.* 30 (1991) 455–465. doi:10.1002/anie.199104553.
- [5] J. Law, Z. Zsoldos, A. Simon, D. Reid, Y. Liu, S.Y. Knew, et al., Route Designer: A Retrosynthetic Analysis Tool Utilizing Automated Retrosynthetic Rule Generation, *J. Chem. Inf. Model.* 49 (2009) 593–602. doi:10.1021/ci800228y.
- [6] M.E. Davis, R.F. Lobo, Zeolite and molecular sieve synthesis, *Chem. Mater.* 4 (1992) 756–768. doi:10.1021/cm00022a005.
- [7] T. Goebel, Y. Prots, A. Ormeci, O. Pecher, F. Haarmann, Synthesis, Crystal Structure and Chemical Bonding of the Zintl Phase Rb₇NaSi₈,

- Z. Anorg. Allg. Chem.* 637 (2011) 1982–1991. doi:10.1002/zaac.201100349.
- [8] O. Pecher, M. Esters, A. Görne, B. Mausolf, A. Ormeci, F. Haarmann, The Zintl Phase Cs_7NaSi_8 - From NMR signal line shape analysis and quantum mechanical calculations to chemical bonding, *Z. Anorg. Allg. Chem.* 640 (2014) 2169–2176. doi:10.1002/zaac.201400194.
- [9] J. Gopalakrishnan, Chimie Douce Approaches to the Synthesis of Metastable Oxide Materials, *Chem. Mater.* 7 (1995) 1265–1275. doi:10.1021/cm00055a001.
- [10] J. Gopalakrishnan, N.S.P. Bhuvanesh, K.K. Rangan, Towards rational synthesis of inorganic solids, *Curr. Opin. Solid State Mater. Sci.* 1 (1996) 285–294. doi:10.1016/S1359-0286(96)80096-9.
- [11] D.C. Johnson, Controlled synthesis of new compounds using modulated elemental reactants, *Curr. Opin. Solid State Mater. Sci.* 3 (1998) 159–167. doi:10.1016/S1359-0286(98)80082-X.
- [12] L. Fister, X.-M. Li, J. McConnell, T. Novet, D.C. Johnson, Deposition system for the synthesis of modulated, ultrathin-film composites, *J. Vac. Sci. Technol. A.* 11 (1993) 3014–3019. doi:10.1116/1.578290.
- [13] T.M. Phung, J.M. Jensen, D.C. Johnson, J.J. Donovan, B.G. Mccburnett, Determination of the composition of ultra-thin Ni-Si films on Si: constrained modeling of electron probe microanalysis and x-ray reflectivity data, *X-Ray Spectrom.* 37 (2008) 608–614. doi:10.1002/xrs.1102.
- [14] R. Sitko, B. Zawisza, Quantification in X-Ray Fluorescence Spectrometry, in: *X-Ray Spectrosc.*, 2012: pp. 137–162.
- [15] M. Fukuto, M.D. Hornbostel, D.C. Johnson, Use of Superlattice Structure To Control Reaction Mechanism: Kinetics and Energetics of Nb_5Se_4 Formation, *J. Am. Chem. Soc.* 116 (1994) 9136–9140.
- [16] L. Fister, C. David, Controlling Solid-State Reaction Mechanisms Using Diffusion Length in Ultrathin-Film Superlattice Composites, *J. Am. Chem. Soc.* 114 (1992) 4639–4644.

- [17] R.M. Walser, R.W. Bené, First phase nucleation in silicon-transition-metal planar interfaces, *Appl. Phys. Lett.* 28 (1976) 624–625. doi:10.1063/1.88590.
- [18] W. Köster, T. Gödecke, Fe-Si Phase Diagram, in: P. Villars, H. Okamoto, K. Cenzual (Eds.), ASM Alloy Phase Diagrams Database, ASM International, Materials Park, OH, 2016. <http://www.asminternational.org>.
- [19] T. Novet, D.C. Johnson, New synthetic approach to extended solids: selective synthesis of iron silicides via the amorphous state, *J. Am. Chem. Soc.* 113 (1991) 3398–3403. doi:10.1021/ja00009a027.
- [20] T. Novet, J.M. McConnell, D.C. Johnson, Low-Temperature Reaction of Buried Metal-Silicon Interfaces: The Evolution of Interfacial Structure, *Chem. Mater.* 4 (1992) 473–478. doi:10.1021/cm00020a043.
- [21] O.S. Gorelkin, V.S. Mikhailov, Calorimetric investigation of an iron-vanadium-silicon system, *Russ. J. Phys. Chem.* (English Transl. 45 (1971) 1523–1524.
- [22] B. Jounel, J.-C. Mathieu, P. Desré, Mesure de la chaleur de formation du composé FeSi par calorimétrie de dissolution dans l'aluminium, *Comptes Rendus Hebd. Des Séances l'Académie Des Sci. Série C, Sci. Chim.* 266 (1968) 773–776.
- [23] F. Sommer, Modern methods in high temperature calorimetry, *J. Therm. Anal.* 33 (1988) 15–28. doi:10.1007/BF01914580.
- [24] O. Oyelaran, T. Novet, C.D. Johnson, D.C. Johnson, Controlling Solid-State Reaction Pathways: Composition Dependence in the Nucleation Energy of InSe, *J. Am. Chem. Soc.* 118 (1996) 2422–2426. doi:10.1021/ja953560k.
- [25] J.W. Sharp, E.C. Jones, R.K. Williams, P.M. Martin, B.C. Sales, Thermoelectric properties of CoSb₃ and related alloys, *J. Appl. Phys.* 78 (1995) 1013–1018.
- [26] B.C. Sales, D. Mandrus, R.K. Williams, Filled Skutterudite Antimonides: A New Class of Thermoelectric Materials, *Science* 272 (1996) 1325–1328. doi:10.1126/science.272.5266.1325.

- [27] J.R. Salvador, J.Y. Cho, Z. Ye, J.E. Moczygemba, A.J. Thompson, J.W. Sharp, et al., Thermal to Electrical Energy Conversion of Skutterudite-Based Thermoelectric Modules, *J. Electron. Mater.* 42 (2013) 1389–1399. doi:10.1007/s11664-012-2261-9.
- [28] G.S. Nolas, G.A. Slack, D.T. Morelli, T.M. Tritt, A.C. Ehrlich, The effect of rare-earth filling on the lattice thermal conductivity of skutterudites, *J. Appl. Phys.* 79 (1996) 4002–4008. doi:10.1063/1.361828.
- [29] G.P. Meisner, D.T. Morelli, S. Hu, J. Yang, C. Uher, Structure and Lattice Thermal Conductivity of Fractionally Filled Skutterudites: Solid Solutions of Fully Filled and Unfilled End Members, *Phys. Rev. Lett.* 80 (1998) 3551–3554. doi:10.1103/PhysRevLett.80.3551.
- [30] D.J. Braun, W. Jeitschko, Preparation and structural investigations of antimonides with the $\text{LaFe}_4\text{P}_{12}$ structure, *J. Less Common Met.* 72 (1980) 147–156. doi:10.1016/0022-5088(80)90260-X.
- [31] N.T. Stetson, S.M. Kauzlarich, H. Hope, The synthesis and structure of two filled skutterudite compounds: $\text{BaFe}_4\text{Sb}_{12}$ and $\text{BaRu}_4\text{Sb}_{12}$, *J. Solid State Chem.* 91 (1991) 140–147. doi:10.1016/0022-4596(91)90067-R.
- [32] C.B.H. Evers, L. Boonk, W. Jeitschko, Alkaline Earth Transition Metal Antimonides $\text{AT}_4\text{Sb}_{12}$ (A = Ca, Sr, Ba; T = Fe, Ru, Os) with $\text{LaFe}_4\text{P}_{12}$ -Structure, *Z. Anorg. Allg. Chem.* 620 (1994) 1028–1032. doi:10.1002/zaac.19946200613.
- [33] C.B.H. Evers, W. Jeitschko, L. Boonk, D.J. Braun, T. Ebel, U.D. Scholz, Rare earth and uranium transition metal pnictides with $\text{LaFe}_4\text{P}_{12}$ structure, *J. Alloys Compd.* 224 (1995) 184–189. doi:10.1016/0925-8388(95)01540-X.
- [34] J.W. Kaiser, W. Jeitschko, The antimony-rich parts of the ternary systems calcium, strontium, barium and cerium with iron and antimony; structure refinements of the $\text{LaFe}_4\text{Sb}_{12}$ -type compounds $\text{SrFe}_4\text{Sb}_{12}$ and $\text{CeFe}_4\text{Sb}_{12}$, *J. Alloys Compd.* 291 (1999) 66–72.
- [35] E. Bauer, S. Berger, A. Galatanu, M. Galli, H. Michor, G. Hilscher, et al., Crystal structure and physical properties of $\text{Eu}_{0.83}\text{Fe}_4\text{Sb}_{12}$, *Phys. Rev. B.* 63 (2001) 224414. doi:10.1103/PhysRevB.63.224414.

- [36] D. Bérardan, C. Godart, E. Alleno, S. Berger, E. Bauer, Chemical properties and thermopower of the new series of skutterudite $Ce_{1-p}Yb_pFe_4Sb_{12}$, *J. Alloys Compd.* 351 (2003) 18–23.
- [37] A. Leithe-Jasper, W. Schnelle, H. Rosner, M. Baenitz, A. Rabis, A.A. Gippius, et al., Weak itinerant ferromagnetism and electronic and crystal structures of alkali-metal iron antimonides: $NaFe_4Sb_{12}$ and KFe_4Sb_{12} , *Phys. Rev. B.* 70 (2004) 214418. doi:10.1103/PhysRevB.70.214418.
- [38] H. Okamoto, Fe-Sb Phase Diagram, in: P. Villars, H. Okamoto, K. Cenzual (Eds.), ASM Alloy Phase Diagrams Database, ASM International, Materials Park, OH, 2016. <http://www.asminternational.org>.
- [39] E. Bjerkelund, A. Kjekshus, Compounds with the Marcasite Type Crystal Structure VII: On the Phases $Cr_{1-u}Fe_uSb_2$, $Fe_{1-u}Co_uSb_2$, $Co_{1-u}Ni_uSb_2$ and $Ni_{1-u}Fe_uSb_2$, *Acta Chem. Scand.* 24 (1970) 3317–3325.
- [40] J. Navrátil, F. Laufek, T. Plecháček, J. Plášil, Synthesis, crystal structure and thermoelectric properties of the ternary skutterudite $Fe_2Pd_2Sb_{12}$, *J. Alloys Compd.* 493 (2010) 50–54. doi:10.1016/j.jallcom.2009.12.085.
- [41] M.D. Hornbostel, E.J. Hyer, J. Thiel, D.C. Johnson, Rational Synthesis of Metastable Skutterudite Compounds Using Multilayer Precursors, *J. Am. Chem. Soc.* 119 (1997) 2665–2668. doi:10.1021/ja964084g.
- [42] J.R. Williams, M. Johnson, D.C. Johnson, Composition Dependence of the Nucleation Energy of Iron Antimonides from Modulated Elemental Reactants, *J. Am. Chem. Soc.* 123 (2001) 1645–1649. doi:10.1021/ja003791d.
- [43] J.R. Williams, D.C. Johnson, Synthesis of the New Metastable Skutterudite Compound $NiSb_3$ from Modulated Elemental Reactants, *Inorg. Chem.* 41 (2002) 4127–4130.
- [44] M. Sergent, R. Chevrel, Sur des phases $M_xMo_3Se_4$ (M = élément métallique) admettant Mo_3Se_4 comme structure d'accueil, *Comptes Rendus Hebd. Des Séances l'Académie Des Sci. Série C, Sci. Chim.* 274 (1972) 1965–1967.

- [45] R. Flükinger, R. Baillif, E. Walker, Single Crystals of Chevrel-Type Compounds: Growth, Stoichiometry and Electrical Resistivity, *Mater. Res. Bull.* 13 (1978) 743–750.
- [46] L. Fister, D.C. Johnson, R. Brown, Synthesis of $\text{Cu}_x\text{Mo}_6\text{Se}_8$ without Binary Compounds as Intermediates: A Study Using Superlattices to Kinetically Control a Solid-State Reaction, *J. Am. Chem. Soc.* 116 (1994) 629–633.
- [47] R. Schneidmiller, M.D. Hornbostel, D.C. Johnson, Kinetics of Formation of Molybdenum Selenides from Modulated Reactants and Structure of the New Compound Mo_3Se , *Inorg. Chem.* 36 (1997) 5894–5899. doi:10.1021/ic9708125.
- [48] R. Schneidmiller, A. Bentley, M.D. Hornbostel, D.C. Johnson, The Use of Ternary Cations to Control Nucleation: Avoiding Binary Compounds as Reaction Intermediates, *J. Am. Chem. Soc.* 121 (1999) 3142–3149. doi:10.1021/ja983405g.
- [49] H. Sellinschegg, S.L. Stuckmeyer, M.D. Hornbostel, D.C. Johnson, Synthesis of Metastable Post-Transition-Metal Iron Antimony Skutterudites Using the Multilayer Precursor Method, *Chem. Mater.* 10 (1998) 1096–1101.
- [50] G.S. Nolas, H. Yoon, H. Sellinschegg, A. Smalley, D.C. Johnson, Synthesis and transport properties of $\text{HfFe}_4\text{Sb}_{12}$, *Appl. Phys. Lett.* 86 (2005) 42141. doi:10.1063/1.1854747.
- [51] M.D. Anderson, J.O. Thompson, D.C. Johnson, Avoiding binary compounds as reaction intermediates in solid state reactions, *Chem. Mater.* 25 (2013) 3996–4002. doi:10.1021/cm4019259.
- [52] M. Esters, A. Liebig, J.J. Ditto, M. Falmbigl, M. Albrecht, D.C. Johnson, Synthesis, structure and magnetic properties of crystallographically aligned CuCr_2Se_4 thin films, *J. Alloys Compd.* 671 (2016) 220–225. doi:10.1016/j.jallcom.2016.02.025.
- [53] L. Zhang, J. Fan, X. Zhu, W. Ning, Z. Qu, M. Ge, et al., Critical behavior of single crystal $\text{CuCr}_2\text{Se}_{4-x}\text{Br}_x$ ($x = 0.25$), *Appl. Phys. A.* 113 (2013) 201–206. doi:10.1007/s00339-012-7515-0.
- [54] D.B. Moore, L. Sitts, M.J. Stolt, M. Beekman, D.C. Johnson, Characterization of nonstoichiometric $\text{Ti}_{1+x}\text{Se}_2$ prepared by the

- method of modulated elemental reactants, *J. Electron. Mater.* 42 (2013) 1647–1651. doi:10.1007/s11664-012-2361-6.
- [55] R. Atkins, D.B. Moore, D.C. Johnson, Insights into the Self-Assembly of Ferecrystalline Compounds from Designed Amorphous Precursors, *Chem. Mater.* 25 (2013) 1744–1750. doi:10.1021/cm400218z.
- [56] G.A. Wiegers, Misfit layer compounds: Structures and physical properties, *Prog. Solid State Chem.* 24 (1996) 1–139. doi:10.1016/0079-6786(95)00007-0.
- [57] I. Häusler, R. Atkins, M. Falmbigl, S.P. Rudin, W. Neumann, D.C. Johnson, Insights from STEM and NBED studies into the local structure and growth mechanism of misfit layered compounds prepared using modulated reactants, *Z. Kristallog. – Cryst. Mater.* 230 (2015) 45–54. doi:10.1515/zkri-2014-1761.
- [58] R. Atkins, S. Disch, Z. Jones, I. Häusler, C. Grosse, S.F. Fischer, et al., Synthesis, structure and electrical properties of a new tin vanadium selenide, *J. Solid State Chem.* 202 (2013) 128–133. doi:10.1016/j.jssc.2013.03.008.
- [59] C. Heideman, N. Nyugen, J. Hanni, Q. Lin, S. Duncombe, D.C. Johnson, et al., The synthesis and characterization of new $[(\text{BiSe})_{1.10}]_m[\text{NbSe}_2]_n$, $[(\text{PbSe})_{1.10}]_m[\text{NbSe}_2]_n$, $[(\text{CeSe})_{1.14}]_m[\text{NbSe}_2]_n$ and $[(\text{PbSe})_{1.12}]_m[\text{TaSe}_2]_n$ misfit layered compounds, *J. Solid State Chem.* 181 (2008) 1701–1706. doi:10.1016/j.jssc.2008.06.017.
- [60] Q. Lin, M. Smeller, C.L. Heideman, P. Zschack, M. Koyano, M.D. Anderson, et al., Rational Synthesis and Characterization of a New Family of Low Thermal Conductivity Misfit Layer Compounds $[(\text{PbSe})_{0.99}]_m(\text{WSe}_2)_n$, *Chem. Mater.* 22 (2010) 1002–1009. doi:10.1021/cm901952v.
- [61] R. Atkins, J. Wilson, P. Zschack, C. Grosse, W. Neumann, D.C. Johnson, et al., Synthesis of $[(\text{SnSe})_{1.15}]_m(\text{TaSe}_2)_n$ Ferecrystals: Structurally Tunable Metallic Compounds, *Chem. Mater.* 24 (2012) 4594 – 4599. doi:10.1021/cm302948x

- [62] D.B. Moore, M.J. Stolt, R. Atkins, L. Sitts, Z. Jones, S. Disch, et al., Structural and electrical properties of $(\text{PbSe})_{1.16}\text{TiSe}_2$, *Emerg. Mater. Res.* 1 (2012) 292–298. doi:10.1680/emr.12.00024.
- [63] M.D. Anderson, C.L. Heideman, Q. Lin, M. Smeller, R. Kokenyesi, A.A. Herzing, et al., Size-Dependent Structural Distortions in One-Dimensional Nanostructures, *Angew. Chemie Int. Ed.* 52 (2013) 1982–1985. doi:10.1002/anie.201207825.
- [64] D.B. Moore, M. Beekman, S. Disch, P. Zschack, I. Häusler, W. Neumann, et al., Synthesis, Structure, and Properties of Turbostratically Disordered $(\text{PbSe})_{1.18}(\text{TiSe}_2)_2$, *Chem. Mater.* 25 (2013) 2404–2409. doi:10.1021/cm400090f.
- [65] C.L. Heideman, D.C. Johnson, Structural influence on transport properties in $[(\text{PbSe})_{1.00}]_m(\text{MoSe}_2)_n$ misfit layered compounds, *Semicond. Sci. Technol.* 29 (2014) 64007. doi:10.1088/0268-1242/29/6/064007.
- [66] M.B. Alemayehu, G. Mitchson, B.E. Hanken, M. Asta, D.C. Johnson, Charge Transfer between PbSe and NbSe₂ in $[(\text{PbSe})_{1.14}]_m(\text{NbSe}_2)_1$, *Chem. Mater.* 26 (2014) 1859–1866. doi:10.1021/cm404018a.
- [67] D.R. Merrill, D.B. Moore, M.N. Coffey, A.W. Jansons, M. Falmbigl, D.C. Johnson, Synthesis and characterization of turbostratically disordered $(\text{BiSe})_{1.15}\text{TiSe}_2$, *Semicond. Sci. Technol.* 29 (2014) 64004. doi:10.1088/0268-1242/29/6/064004.
- [68] D.R. Merrill, D.B. Moore, J. Ditto, D.R. Sutherland, M. Falmbigl, M. Winkler, et al., The Synthesis, Structure, and Electrical Characterization of $(\text{SnSe})_{1.2}\text{TiSe}_2$, *Eur. J. Inorg. Chem.* 2015 (2015) 83–91. doi:10.1002/ejic.201402814.
- [69] O.K. Hite, M. Nellist, J. Ditto, M. Falmbigl, D.C. Johnson, Transport properties of VSe₂ monolayers separated by bilayers of BiSe, *J. Mater. Res.* 8 (2015) 886–892. doi:10.1557/jmr.2015.354.
- [70] G. Mitchson, M. Falmbigl, J. Ditto, D.C. Johnson, Antiphase Boundaries in the Turbostratically Disordered Misfit Compound $(\text{BiSe})_{1+\delta}\text{NbSe}_2$, *Inorg. Chem.* 54 (2015) 10309–10315. doi:10.1021/acs.inorgchem.5b01648.

- [71] S.R. Wood, D.R. Merrill, M. Falmbigl, D.B. Moore, J. Ditto, M. Esters, et al., Tuning Electrical Properties through Control of TiSe₂ Thickness in (BiSe)_{1+δ}(TiSe₂)_n Compounds, *Chem. Mater.* 27 (2015) 6067–6076. doi:10.1021/acs.chemmater.5b02572.
- [72] N. Giang, Q. Xu, Y. Hor, A. Williams, S. Dutton, H. Zandbergen, et al., Superconductivity at 2.3 K in the misfit compound (PbSe)_{1.16}(TiSe₂)₂, *Phys. Rev. B.* 82 (2010) 24503. doi:10.1103/PhysRevB.82.024503.
- [73] B.A. Trump, K.J.T. Livi, T.M. McQueen, The new misfit compound (BiSe)_{1.15}(TiSe₂)₂ and the role of dimensionality in the Cu_x(BiSe)_{1+δ}(TiSe₂)_n series, *J. Solid State Chem.* 209 (2014) 6–12. doi:10.1016/j.jssc.2013.10.014.
- [74] D.B. Moore, M. Beekman, S. Disch, D.C. Johnson, Telluride misfit layer compounds: [(PbTe)_{1.17}]_m(TiTe₂)_n, *Angew. Chemie - Int. Ed.* 53 (2014) 5672–5675. doi:10.1002/anie.201401022.
- [75] M. Falmbigl, A. Fiedler, R.E. Atkins, S.F. Fischer, D.C. Johnson, Suppressing a Charge Density Wave by Changing Dimensionality in the Ferrecrystalline Compounds ([SnSe]_{1.15})₁(VSe₂)_n with n = 1, 2, 3, 4, *Nano Lett.* 15 (2015) 943–948. doi:10.1021/nl503708j.
- [76] R. Atkins, M. Dolgos, A. Fiedler, C. Grosse, S.F. Fischer, S.P. Rudin, et al., Synthesis and Systematic Trends in Structure and Electrical Properties of [(SnSe)_{1.15}]_m(VSe₂)₁, m = 1, 2, 3, and 4, *Chem. Mater.* 26 (2014) 2862–2872. doi:10.1021/cm5004774.
- [77] M. Beekman, S. Disch, N. Gunning, D.C. Johnson, Preparation, Formation, and Structure of [(SnSe)_{1.04}]_m(MoSe₂)_n Intergrowth Compounds (0 < m and n < 32) from Designed Precursors, *Inorg. Chem.* 54 (2015) 1091–1099. doi:10.1021/ic502427c.
- [78] Y. Ren, J. Baas, A. Meetsma, J.L. de Boer, G. a. Wiegers, Vacancies and electron localization in the incommensurate intergrowth compound (La_{0.95}Se)_{1.21}VSe₂, *Acta Crystallogr. Sect. B.* 52 (1996) 398–405. doi:10.1107/S0108768195010536.
- [79] T. Chattopadhyay, J. Pannetier, H.G. von Schnering, Neutron Diffraction Study of The Structural Phase Transition in SnS and SnSe, *J. Phys. Chem. Solids.* 47 (1986) 879–885.

- [80] S. van Smaalen, Superspace Description of Incommensurate Intergrowth Compounds and the Application to Inorganic Misfit Layer Compounds, *Mater. Sci. Forum.* 100–101 (1992) 173–222. doi:10.4028/www.scientific.net/MSF.100-101.173.
- [81] M. Falmbigl, M.B. Alemayehu, D.R. Merrill, M. Beekman, D.C. Johnson, In-plane structure of ferecrystalline compounds, *Cryst. Res. Technol.* 472 (2015) 464–472. doi:10.1002/crat.201500019.
- [82] M.B. Alemayehu, M. Falmbigl, K. Ta, C. Grosse, R.D. Westover, S.R. Bauers, et al., Structural and Electrical Properties of $[(\text{SnSe})_{1+\delta}]_m(\text{NbSe}_2)_1$ Compounds: Single NbSe_2 Layers Separated by Increasing Thickness of SnSe , *Chem. Mater.* 27 (2015) 867–875. doi:10.1021/cm5039864.
- [83] M.B. Alemayehu, M. Falmbigl, K. Ta, D.C. Johnson, Effect of Local Structure of NbSe_2 on the Transport Properties of $[(\text{SnSe})_{1.16}]_1[(\text{NbSe}_2)]_n$ Ferecrystals, *Chem. Mater.* 27 (2015) 2158–2164. doi:10.1021/acs.chemmater.5b00131.
- [84] M. Beekman, S. Disch, S. Rouvimov, D. Kasinathan, K. Koepf, H. Rosner, et al., Controlling size-induced phase transformations using chemically designed nanolaminates, *Angew. Chemie - Int. Ed.* 52 (2013) 13211–13214. doi:10.1002/anie.201305377.
- [85] V. Petříček, I. Cisarova, J.L. de Boer, W. Zhou, A. Meetsma, G. a. Wieggers, et al., The modulated structure of the commensurate misfit-layer compound $(\text{BiSe})_{1.09}\text{TaSe}_2$, *Acta Crystallogr. Sect. B.* 49 (1993) 258–266. doi:10.1107/S0108768192009996.
- [86] G. Mitchson, E. Hadland, F. Göhler, M. Wanke, M. Esters, J. Ditto, et al., Structural Changes in 2D BiSe Bilayers as n Increases in $(\text{BiSe})_{1+\delta}(\text{NbSe}_2)_n$ ($n = 1-4$) Heterostructures, *ACS Nano.* 10 (2016) 9489–9499. doi:10.1021/acsnano.6b04606.
- [87] H. Gobrecht, K.-E. Boeters, G. Pantzer, Über Kristallstruktur und elektrische Eigenschaften der Wismutselenide Bi_2Se_2 und Bi_2Se_3 , *Z. Phys.* 177 (1964) 68–83. doi:10.1007/BF01375404.
- [88] E. Gaudin, S. Jobic, M. Evain, R. Brec, J. Rouxel, Charge balance in some Bi_xSe_y phases through atomic structure determination and band

- structure calculations, *Mater. Res. Bull.* 30 (1995) 549–561. doi:10.1016/0025-5408(95)00030-5.
- [89] M. Esters, M.B. Alemayehu, Z. Jones, N.T. Nguyen, M.D. Anderson, C. Grosse, et al., Synthesis of Inorganic Structural Isomers By Diffusion-Constrained Self-Assembly of Designed Precursors: A Novel Type of Isomerism, *Angew. Chemie Int. Ed.* 54 (2015) 1130–1134. doi:10.1002/anie.201409714.
- [90] M.B. Alemayehu, M. Falmbigl, K. Ta, D.C. Johnson, The Influence of Interfaces on Properties of Thin-Film Inorganic Structural Isomers Containing SnSe-NbSe₂ Subunits, *ACS Nano.* 9 (2015) 4427–4434. doi:10.1021/acsnano.5b01770.
- [91] N.S. Gunning, J. Feser, M. Beekman, D.G. Cahill, D.C. Johnson, Synthesis and Thermal Properties of Solid-State Structural Isomers: Ordered Intergrowths of SnSe and MoSe₂, *J. Am. Chem. Soc.* 137 (2015) 8803–8809. doi:10.1021/jacs.5b04351.
- [92] D.R. Lide, ed., CRC Handbook of Chemistry and Physics, 84th ed., CRC Press LLC, Boca Raton, 2003.
- [93] R.D. Westover, R.A. Atkins, J. Ditto, D.C. Johnson, Synthesis of [(SnSe)_{1.16-1.09}]₁[(Nb_xMo_{1-x})Se₂]₁ Ferecrystal Alloys, *Chem. Mater.* 26 (2014) 3443–3449. doi:10.1021/cm500720x.
- [94] R. Westover, R.A. Atkins, M. Falmbigl, J.J. Ditto, D.C. Johnson, Self-assembly of designed precursors: A route to crystallographically aligned new materials with controlled nanoarchitecture, *J. Solid State Chem.* 236 (2015) 173–185. doi:10.1016/j.jssc.2015.08.018.
- [95] L. Vegard, Die Konstitution der Mischkristalle und die Raumfüllung der Atome, *Z. Phys.* 5 (1921) 17–26. doi:10.1007/BF 01349680.
- [96] V.L. Kalikhman, T.A. Lobova, L.L. Pravoverova, X-ray diffraction study of tungsten selenide-tantalum selenide, molybdenum selenide-tantalum selenide, and molybdenum selenide-niobium selenide solid solutions, *Neorg. Mater.* 9 (1973) 923–936.
- [97] F.J. Di Salvo, J.A. Wilson, B.G. Bagley, J. V. Waszczak, Effects of doping on charge-density waves in layer compounds, *Phys. Rev. B.* 12 (1975) 2220–2235. doi:10.1103/PhysRevB.12.2220.

- [98] R.D. Westover, G. Mitchson, O.K. Hite, K. Hill, D.C. Johnson, Suppression of a Charge Density Wave in $([\text{SnSe}]_{1.15})_1(\text{VSe}_2)_1$ Ferecrystals Via Isoelectronic Doping with Ta, *J. Electron. Mater.* 45 (2016) 4898–4902. doi:10.1007/s11664-016-4662-7.
- [99] R.D. Westover, J. Ditto, M. Falmbigl, Z.L. Hay, D.C. Johnson, Synthesis and Characterization of Quaternary Monolayer Thick $\text{MoSe}_2/\text{SnSe}/\text{NbSe}_2/\text{SnSe}$ Heterojunction Superlattices, *Chem. Mater.* 27 (2015) 6411–6417. doi:10.1021/acs.chemmater.5b02588.
- [100] R.D. Westover, G. Mitchson, J. Ditto, D.C. Johnson, Synthesis of a Family of $([\text{SnSe}]_{1+\delta})_m([\{\text{Mo}_x\text{Nb}_{1-x}\}\text{Se}_2]_{1+\gamma})_{1-x}([\text{SnSe}]_{1+\delta})_m([\{\text{Nb}_x\text{Mo}_{1-x}\}\text{Se}_2)_1$ Superlattice Heterostructures, *Eur. J. Inorg. Chem.* 2016 (2016) 1225–1231. doi:10.1002/ejic.201501324.
- [101] D.R. Merrill, D.R. Sutherland, J.J. Ditto, D.B. Moore, M. Falmbigl, D.L. Medlin, et al., The synthesis of $([\text{PbSe}]_{1+\delta})_m(\text{TiSe}_2)_n$ $([\text{SnSe}_2]_{1+\gamma})_m(\text{TiSe}_2)_n$ heterostructures with designed nanoarchitectures by self assembly of amorphous precursors, *Nanoscale*. 8 (2016) 13646–13651. doi:10.1039/c6nr03406c.
- [102] J. Ditto, D. Merrill, D.L. Medlin, D.C. Johnson, Quantitative High Resolution Chemical Analysis of the $(\text{Pb}_x\text{Sn}_{1-x}\text{Se})_{1+\delta}\text{TiSe}_2$ Intergrowth System, *Microsc. Microanal.* 21 (2015) 1327–1328. doi:10.1017/S1431927615007424.
- [103] D.R. Merrill, D.R. Sutherland, J. Ditto, S.R. Bauers, M. Falmbigl, D.L. Medlin, et al., Kinetically Controlled Site-Specific Substitutions in Higher-Order Heterostructures, *Chem. Mater.* 27 (2015) 4066–4072. doi:10.1021/acs.chemmater.5b01071.
- [104] T.C. Harman, I. Melngailis, Narrow Gap Semiconductors, *Appl. Solid State Sci.* 4 (1974) 1–94. doi:10.1016/B978-0-12-002904-4.50008-5.
- [105] A.A. Sher, I.N. Odin, A. V. Novoselova, Interaction in the system Sn-Bi-Se, *Inorg. Mater.* 14 (1978) 993–998.
- [106] G. Mitchson, S.R. Bauers, P. Schädlich, J.J. Ditto, D.C. Johnson, Correlation of reduced interlayer charge transfer with antiphase boundary formation in $\text{Bi}_x\text{Sn}_{1-x}\text{Se}-\text{NbSe}_2$ heterostructures, *Eur. J. Inorg. Chem.* (2016). doi:10.1002/ejic.201601401.

- [107] S.R. Wood, D.R. Merrill, G. Mitchson, A.C. Lygo, S.R. Bauers, D.M. Hamann, et al., Modulation Doping in Metastable Heterostructures via Kinetically Controlled Substitution, *Chem. Mater.* 29 (2017) 773–779. doi:10.1021/acs.chemmater.6b04688.
- [108] M. Falmbigl, Z.L. Hay, J.J. Ditto, D.C. Johnson, Modifying a charge density wave transition by modulation doping: ferecrystalline compounds $([\text{Sn}_{1-x}\text{Bi}_x\text{Se}]_{1.15})_1(\text{VSe}_2)_1$ with $0 \leq x \leq 0.66$, *J. Mater. Chem. C.* 3 (2015) 12308–12315. doi:10.1039/C5TC03130C.

In: Crystal Growth
Editors: J. Li, J. Li and Y. Chu

ISBN: 978-1-53612-203-9
© 2017 Nova Science Publishers, Inc.

Chapter 3

**ANALYSIS FOR THE MORPHOLOGY
PREDICTION OF MATERIALS FROM FIRST
PRINCIPLES CALCULATIONS**

*Marisa Carvalho de Oliveira^{1,2},
Thiago Marinho Duarte^{1,3}, Lourdes Gracia^{4,*},
Elson Longo² and Juan Andres¹*

¹Department of Analytical and Physical Chemistry,
University Jaume I (UJI), Castelló, Spain

²CDME-UFSCar, Federal University of São Carlos,
São Carlos, SP, Brazil

³Department of Chemistry, Federal University of Paraíba,
João Pessoa, PB, Brazil

⁴Department of Physical Chemistry, University of Valencia,
Burjassot, Spain

* Corresponding author: Email: Lourdes.Gracia@uv.es, lgracia@uji.es.

ABSTRACT

As various physical and chemical processes occur at surfaces, an understanding of surface structures and the factors that affect morphology is mandatory. The control of (nano)crystal morphology is a complex and difficult process that depends on both the internal structures of the crystals and external growth conditions, such as the synthesis process, the solvents used, and the process additives. The morphologies of (nano)crystals grown under or near equilibrium conditions are governed mainly by surface energies, resulting in the formation of simple shapes with well-defined facets to minimize the surface energy. However, surface energy values are not readily acquired experimentally, and computer modeling and simulation are necessary to obtain these values. Such techniques are powerful tools for exploring the morphological mechanisms at the atomistic/molecular level. The observed (nano)crystal morphologies are often interpreted in terms of Wulff constructions, which offers a simple method to determine the equilibrium (nano)crystal shape. As recently developed by our research group, first-principles calculations can be used to explicitly predict the evolution of morphologies in different environments.

The complete set of morphologies obtained theoretically may serve as a guide for researchers analyzing electron microscopy images to gain a further understanding of how to control crystal shapes synthetically by tuning the surface chemistry and by controlling the relative surface energy values. Then, this feature chapter introduces recent work, based on combined experimental findings and first-principles calculations, to provide a deeper knowledge of the electronic, structural, and energetic properties controlling the morphology and the transformation mechanisms of different (nano)materials, such as BaWO_4 , BaMoO_4 , CaZrO_3 , and BaSnO_3 . These considerations reveal a close resemblance between experimental and calculated morphologies, but also elaborate on some of the current and future trends to illustrate why (nano)morphology is at the core of current scientific development in chemistry and physics, and the appropriate handling of complexity is discussed along these lines.

Keywords: morphology, surface energy, Wulff construction, complex metallic oxides

INTRODUCTION

Morphologies and exposed surfaces are important factors that influence the application of (nano)materials (Tian et al. 2007), directly affecting their efficiency in various devices (Lieber 1998). Steady-state morphologies of micro/nanocrystal particles with several exposed facets present different physical and chemical characteristics owing to crystal anisotropy, i.e., different crystal planes exhibit different anisotropic responses towards various mechanical, physical, and chemical activities like hardness, piezoelectricity, and reactivity (Schmidt et al. 2012); (Dandekar et al. 2013). These characteristics are controlled by the synthesis parameters of the materials, such as reagent concentration, precursor pH, reaction temperature and time, and synthesis method.

Morphological control of (nano)crystals and understanding the mechanism for morphology evolution have been meaningful topics of research in materials science and nanoscience, as obtaining a fundamental understanding of the stability of (nano)crystal surface structures and morphology–structure–function relationships is of considerable importance for further development of highly stable and functional materials for practical applications. In particular, the activity of nanocrystals as catalysts depends strongly on the surface structures of the facets enclosing the crystals (Ahmadi et al. 1996); (Lee et al. 2006b); (Lee et al. 2006a); (Gao, Ju, et al. 2013); (Li and Shen 2014), (Araújo et al. 2014); (Wang et al. 2015).

Morphologies, preferred orientations, and crystal facets are characterized experimentally using scanning electron microscopy, selected-area electron diffraction, and high-resolution transmission electron microscopy. The relative growth rates of (nano)crystal faces cause crystal morphology transformations because of the appearance and/or disappearance of faces. These transformations are due to geometric constraints imposed by the (nano)crystal structure and are associated with the relative surface energy values of each face. Among the influential factors, surface chemistry, including surface energy, tension, and

configuration, has a significant impact on the final (nano)crystal morphology.

A significant challenge in the development of functional (nano)materials is understanding the shape-selective growth of (nano)crystals to synthesize (nano)crystals with controlled shapes. A solid fundamental understanding will allow for better design and control of these syntheses and will enable larger-scale production of (nano)crystals with targeted shapes. Further, establishment of a pathway between (nano)crystal morphology and the arrangement of atoms in a (nano)crystal lattice will allow development of shape control for the rational design of external morphologies. Very recently, Zhuang, Tkalych and Carter (2016) (Zhuang et al. 2016), explored the correlation between experimental catalytic activity and three surface properties (surface energy, work function, and potential of zero charge) of 15 traditional and novel catalysts. These authors discovered a strong volcano-shaped correlation between the catalytic activity and the surface energy, indicating that the surface energy can be used as a novel, efficient descriptor of catalytic activity because it reflects the degree of coordinative unsaturation of the surface atoms and, thus, the reactivity of the surface.

Morphology-controlled synthesis of inorganic materials on the nano/micrometer scale has progressed considerably in the past decade (Huang, Rej, et al. 2014). Many facet-dependent properties have been discovered owing to the successful synthesis of nanocrystals with a series of well-defined morphologies. Control of nanocrystal morphology is important in various applications, such as heterogeneous catalysis (Ahmadi et al. 1996); (Zaera 2013), solar cells (Huynh et al. 1999), light-emitting diodes (Schlamp et al. 1997); (Mattoussi et al. 1998), and biological labeling (Bruchez et al. 1998); (Chan et al. 1998). In particular, recent advances in colloidal synthesis have realized controlled preparation of catalytic nanocrystals with various types of uniform morphologies. For example, morphology-dependent catalytic behavior of oxide nanocrystals has been often observed, and oxide nanocrystals are being explored as novel model catalysts for fundamental studies of metal oxide catalysts, such as CeO_2 and TiO_2 (Dinh et al. 2009); (Pan et al. 2011); (Zheng et al.

2011); (Gordon et al. 2012); (Zhou et al. 2012); (Qiao et al. 2013); (Huang 2013); (Huang and Gao 2014), (Huang 2016).

Nanocrystals with well-defined crystallographic facets (Zhou et al. 2012); (Wu et al. 2013); (Kuang et al. 2014) have been designed for improved catalytic (Hu et al. 2008); (Han, Jin, et al. 2009), optical (Wang, Li, et al. 2014), magnetic (Luo et al. 2014), and electrochemical properties (Yu et al. 2013); (Tan et al. 2015). In particular, high-energy facets that contain abundant unsaturated coordination atoms exhibit high reactivity (Jiang et al. 2005); (Tian et al. 2007); (Fan et al. 2008); (Liao et al. 2008a); (Liao et al. 2008b); (Ma et al. 2008b); (Ma et al. 2008a); (Tian et al. 2008); (Yang et al. 2008); (Tian et al. 2009); (Xie et al. 2009); (Xu et al. 2009), (Yang et al. 2009); (Leng et al. 2010), because active facets usually have higher densities of unsaturated, dangling, or distorted atoms than inert facets (Pal et al. 2015), resulting in higher surface reactivity (Yang et al. 2008); (Miao et al. 2013); (Roy et al. 2013); (Xu et al. 2013), (Roy et al. 2013). In this context, shape-controlled synthesis of inorganic nanocrystals with exposed high-energy or reactive facets has attracted intensive interest over the past decade, owing to their fascinating shape dependent properties (Jun et al. 2006); (Tao et al. 2008); (Wang et al. 2008), as well as their great importance in fundamental studies and technological applications (Tian et al. 2007); (Jiang et al. 2010); (Liu, Khare, et al. 2011).

Thermodynamics usually ensures that crystal facets evolve to have the lowest surface energy during a crystal growth process. Owing to the fact that high-index faces possess high surface energies, high-energy facets decrease quickly during the crystal growth process, and the crystal spontaneously evolves into a specific shape with exposed facets that minimize the surface energy of the crystal. Consequently, only (nano)crystals enclosed by low-index facets and with low surface energy are obtained. High-energy facets of micro/nanocrystals, which possess high densities of unsaturated coordination sites, usually exhibit higher surface reactivity than low-index facets owing to differences in exposed (dangling) bonds, surface defects, and electronic structure (Van Santen 2009); (Pal et al. 2015). Further, such high-energy facets are expected to exhibit extraordinary performances in energy and environmental applications,

(Yang et al. 2008); (Dai et al. 2009); (Han, Jin, et al. 2009); (Han, Kuang, et al. 2009); (Xiao et al. 2012); (Hu et al. 2016); (Wang et al. 2016). However, as high-energy facets disappear easily during conventional crystal growth, few high-energy facets are exposed on the crystal surface (Liu, Yu, et al. 2011); (Zhang et al. 2013). Therefore, the synthesis and control of (nano)crystals enclosed by high-index facets are still challenging research topics (Zhou et al. 2011); (Wang, Han, et al. 2012); (Wang, Zang, et al. 2012).

A prerequisite for application of nanocrystals as model catalysts is to obtain well-defined surface structures for metal oxide nanocrystals with different morphologies. Presently, morphologies are determined experimentally using microscopy-based techniques in combination with Wulff construction models, which can be obtained from first-principles calculations, to identify the facets exposed on nanocrystals (Han, Kuang, et al. 2009); (Tan et al. 2011); (Liu et al. 2013); (Lin et al. 2014). For example, uniform cubic and octahedral nanocrystals of CeO₂ with a cubic fluorite structure are enclosed with six {100} facets and eight {111} facets, respectively. However, this approach encounters some difficulties in determining the exposed facets for nanocrystals with low symmetries (Vantomme et al. 2005); (Sayle et al. 2011); (Agarwal et al. 2013); (Wang et al. 2013).

Up to now, based on a geometrical approach, the Wulff construction model has had a fundamental role in the theoretical characterization of nano(crystal) morphologies. Instead, as was recently recognized by Marks and Peng (2016) (Marks et al. 2016), the seminal paper of Wulff (1901) (Wulff 1901) titled “On the question of speed of growth and dissolution of crystal surfaces” envisaged the possibility of kinetic control of morphologies based on a mathematical relationship between the surface energy and the growth rate (which is not necessarily correct). Consequently, substantial efforts have been devoted to understanding and predicting the structure and stability of complex oxide surfaces by utilizing state-of-the-art experimental techniques and advanced theoretical approaches, (Freund et al. 1996); (Noguera 2000a); (Goniakowski et al. 2008); (Noguera et al. 2013).

However, there remains a lack of fundamental understanding of the surface structure, composition, and stability of certain complex oxides, particularly ternary oxides. This can be attributed to the inherent complexity of these materials, which renders experimental preparation and characterization of oxide surfaces extremely arduous, especially the preparation of different crystallographic orientations of ionic polar surfaces, for which cleavage is not a favorable option. It is also very challenging to address these materials from a theoretical perspective, as in addition to surface nonstoichiometry, certain facets are dipolar, necessitating special treatment that involves the creation of surface defects (Davies et al. 1994); (Wander et al. 2001); (Barbier et al. 2008); (Eglitis et al. 2008). Nevertheless, theoretical frameworks providing fresh insight into the structure and stability of ternary complex oxide surfaces are a vital step towards realizing the true potential of complex oxide nanostructures and thin films.

The development of a particular morphology for a growing crystal depends on the relative rate of growth along different crystallographic directions. Different growth rates of the crystal planes determine the appearance of the crystal. A crystal consists of a finite number of low-energy faces that are represented by their Miller indices and interplanar spacing. Although studies have provided some insight into the factors that control crystal growth and ultimately determine the morphologies of crystals, shape evolution mechanisms are mostly speculative and based on experimental results. Thus, there is an urgent call for a theoretical understanding of the relationship between the growth environment and the resulting crystal morphology.

Density functional theory (DFT) calculations, as an effective tool for exploring surface chemistry, have been widely used to investigate the underlying mechanism by which growth environments affect crystal morphologies (Piskorz et al. 2012). For instance, Yang et al. used DFT calculations to predict that anatase TiO_2 with high (001) exposure can be successfully synthesized by using fluorine ions as an agent to control surface energies (Yang et al. 2008). Barnard et al. carried out a series of

investigations on the shape transitions of TiO₂ nanocrystals using DFT calculations (Barnard et al. 2005).

Further strengthening of theory and simulation in this research area, with a focus on understanding morphology, can guide the efficient synthesis of outstanding materials. First-principles investigations are well established in the study of the morphology and surface properties of various materials, from simple to complex metal oxides (Beltrán et al. 2003); (Leite et al. 2003); (Barnard et al. 2008); (Seyed-Razavi et al. 2010); (Gurlo 2011); (Longo et al. 2011); (Stroppa et al. 2011); (Barnard 2012); (Kim, Lee, et al. 2012); (Li et al. 2012); (Piskorz et al. 2012); (Bomio et al. 2013); (Karim et al. 2013); (Lee et al. 2013); (Tompsett et al. 2013); (Hörmann et al. 2014); (Li, Zhang, et al. 2014); (Stroppa et al. 2014); (Whiteside et al. 2014); (Barmparis et al. 2015); (Kanaki et al. 2015); (Suleiman et al. 2015). There are several insightful reviews that report experimental results and theoretical calculations on the most important aspects that govern crystal shape modulation in semiconductors and in metal nanoparticles (Lovette et al. 2008); (Chen et al. 2009); (Jiang et al. 2010); (Lee et al. 2010); (Seyed-Razavi et al. 2010). In addition, there are good reviews on theoretical methods for surface chemistry (Groß 2009) and the modeling of nanoparticles (Barnard 2010).

Here, we apply a recent experimental and theoretical strategy by combining experimental findings and first-principles calculations, based on Wulff constructions, to determine the electronic, structural, and energetic properties that control the morphology and the transformation mechanism of complex crystals (Ferrer et al. 2016) (Andrés et al. 2015). In this work, we provide a comprehensive set of first-principles computations that quantify the stability of all relevant BaWO₄, BaMoO₄, CaZrO₃, and BaSnO₃ crystal surfaces, which allows us to obtain a complete map of available morphologies. In addition, based on these results, we are able to rationalize how the energies of different surfaces change throughout the synthesis process, and we are able to propose a path for which the experimental and theoretical morphologies match. Using corrected surface energies, a straightforward understanding was provided by Wulff constructions. We have introduced computational methodology for

modeling different complex metal oxides, as discussed in detail below. Our research seeks to capture the structure and thermodynamics of these systems using an atomistic level description, allowing us to derive general stability rules for the (nano)morphologies of BaWO₄, BaMoO₄, CaZrO₃, and BaSnO₃ to rationalize the outcome of previous as-synthesized morphologies, and to provide predictive guidelines for future experimental work. Furthermore, we consider the advantages, disadvantages, and possible difficulties of this approach.

COMPUTATIONAL METHODOLOGY AND MODELING

First-principles calculations were conducted within the framework of DFT using the CRYSTAL14 software package (R. Dovesi 2014). The gradient-corrected correlation functional by Lee, Yang, and Parr (Lee et al. 1988) combined with Becke's exchange functional (B3LYP) (Becke 1993) was used for BaMoO₄, BaWO₄ and CaZrO₃ calculations. This method has been successfully employed in various studies on the bulk and surface electronic and structural properties of perovskite (Moreira et al. 2013), tungstate (L. Gracia et al. 2011); (Longo et al. 2014); (Batista et al. 2015), Ag₂CrO₄ (Silva et al. 2016), LaVO₄ (Gouveia et al. 2016), and molybdate-based materials (Beltrán et al. 2014); (Fabbro et al. 2015). The Brillouin zone was sampled using the Monkhorst–Pack method at different k-point grids according to the system size. The thresholds controlling the accuracy of the Coulomb and exchange integral calculations were set to 10⁻⁸ (ITOL1 to ITOL4) and 10⁻¹⁴ (ITOL5), which assures a convergence in the total energy of better than 10⁻⁷ a.u., whereas the percentage of Fock/Kohn–Sham matrix mixing was set to 40 (IPMIX = 40) (Monkhorst et al. 1976).

The atomic centers were described using pseudopotential basis sets for the Mo (http://Www.Crystal.Unito.It/Basis_Sets/Molibdenum.Html) atom in BaMoO₄ and large-core effective core potentials derived by Hay and Wadt and modified by Cora et al. (Cora et al. 1996) for the W atom in BaWO₄. Meanwhile, the O (http://Www.Crystal.Unito.It/Basis_Sets/Oxygen.Html) and Ba (<http://Www.Tcm.Phy.Cam.Ac.Uk/~Mdt26/>

Basis_Sets/Ba_Basis.Txt) atoms in each system were described by standard all-electron basis sets (6-31G* basis set). In CaZrO₃, all-electron basis set were used to describe the atomic orbitals of the Ca (Valenzano et al. 2006), Zr (L et al. 2011), and O (Cora 2005) atoms. In BaSnO₃, the PBESOL0 functional (Adamo et al. 1999) was used and the Ba, Sn, and O atoms were described by SC_HAYWSC-31(1d)G_baranek (Sophia et al. 2013), ECP28MDF-411(51d)G_baranek (Dovesi et al.), and 8-411(1d)G_baranek (Dovesi et al.), respectively, by optimizing the outer valence shell functions (Duarte et al. 2016).

The surface energy, E_{surf} (Andrés et al. 2015); (Ferrer et al. 2016), was calculated using the following equation:

$$E_{surf} = \frac{E_{slab} - n \cdot E_{bulk}}{2A}$$

where $n \cdot E_{bulk}$ is the number of surface molecular units multiplied by the energy of the bulk, E_{slab} is the total energy of the surface slab per molecular unit, and A is the surface area. The equilibrium shape of a crystal can be calculated by using Wulff constructions that minimize the total surface free energy for a fixed volume, providing a simple relationship between the surface energy, E_{surf} , of an (hkl) plane and its distance from the center of the crystallite in the normal direction (Wulff 1901).

For nonstoichiometric slabs in the BaSnO₃ system, the surface energy was determined by accounting for the simultaneous existence of two types of surface terminations in the surface modeling:

$$E_{surf} = \frac{E_{term_A} + E_{term_B} - n \cdot E_{bulk}}{4A}$$

where E_{term_A} and E_{term_B} are the total energies of the two terminations. The number 4 denotes the creation of four surfaces upon crystal cleavage (Bandura et al. 2010).

The Visualization for Electronic and Structural Analysis (VESTA) program (Momma et al. 2011) was utilized to obtain morphologies for BaMoO₄, BaWO₄, CaZrO₃, and BaSnO₃ crystals. Band structures were calculated for 80 K points along the appropriate high-symmetry paths of an adequate Brillouin zone. Density of state (DOS) plots were obtained to analyze the corresponding electronic structures.

APPLICATIONS: MORPHOLOGY MAPPING OF METAL OXIDES

The following studies have used a combination of experimental and theoretical investigations to gain insights into the electronic, structural, and energetic properties controlling the morphology and transformation mechanisms. The corresponding computational methodology, based on Wulff constructions (Wulff 1901), can be found in each study.

BaWO₄

Barium tungstate (BaWO₄) is a semiconductor in the family of scheelites with crystallized tetragonal structures that belong to the I4₁/space group with C_{4h} symmetry. In this structure, Ba atoms are coordinated to eight O atoms, whereas W atoms exhibit tetragonal coordination by O atoms; thus, the building blocks of the BaWO₄ crystal are octahedral [BaO₈] and tetrahedral [WO₄] clusters (Phuruangrat et al. 2012), (Luo et al. 2007), (Anicete-Santos et al. 2011).

The (001), (101), (110), (100), (111), and (112) surfaces of BaWO₄ were simulated by considering symmetrical slabs (with respect to the mirror plane). All surfaces were terminated with O planes. After the optimization process and thickness convergence tests, the resulting slab models consisted of four molecular units containing 24 atoms. We note

that the (101), (111), and (112) surfaces are terminated with W and O atoms, whereas the other listed surfaces have Ba–O termination. The W surface atoms are coordinated to three or four O atoms, forming [WO₃] or [WO₄] clusters, respectively, whereas the Ba surface atoms are coordinated to three, five, or six O atoms, forming [BaO₃], [BaO₅], or [BaO₆] clusters, respectively.

Presently, equilibrium morphology models are derived from calculated surface energies (Gibbs et al. 1875); (Wulff 1901); (Herring 1981), using the assumption that the crystal faces with the lowest surface energies control the crystal morphology (Xie et al. 2002); (Liu et al. 2005); (Wang et al. 2005). As surface stability depends on the atomic configurations of the exposed facets (Marks 1983), the local coordination of both the W and Ba atoms controls the crystal morphology of BaWO₄ and the corresponding behavior of each surface.

The E_{gap} values of the surfaces follow the same order of stability as the BaWO₄ surfaces obtained using theoretical calculations (Table 1), namely, (112) > (001) > (110) > (100) > (101) > (111). This result is in agreement with our present results and those obtained in previous studies on BaMoO₄. A comparison between BaWO₄ and BaMoO₄ shows that the ideal morphology of both scheelites is similar. However, experimental field emission scanning electron microscopy (FE-SEM) images of these materials are different, i.e., contributions of 99.5% of (112), 0.4% of (100), and 0.1% of (001) were found for BaWO₄ (Oliveira et al. 2016a), whereas contributions of 46.5% of (101), 46.9% of (100), 5.8% of (112), and 0.8% of (001) were found for BaMoO₄ (Oliveira et al. 2016b).

Crystal morphologies can be modified by tuning the surface energy values for various facets using the Wulff theorem and the related construction method (Wulff 1901). Taking into account the (001), (101), (110), (100), (111), and (112) facets, various possible crystal morphologies for BaWO₄ are displayed in Figure 1(a-b).

Table 1. Calculated surface energy, surface tension, gap energy, and change in total energy (ΔE_{tot}) for a given dilation area (ΔA) for each surface

Surface	$E_{surf}(J/m^2)$	$\Delta E_{tot}(\text{Hartree})$	$\Delta A(\text{\AA}^2)$	$\Delta (J/m^2)$	$E_{gap}(eV)$
(112)	0.92	0.034	2.350	0.73	6.60
(001)	1.02	0.034	1.263	0.57	6.52
(110)	1.10	0.034	1.982	0.85	6.45
(100)	1.22	0.039	2.803	1.09	6.47
(101)	1.31	0.039	1.537	0.91	6.17
(111)	2.06	0.020	4.161	2.58	conductor

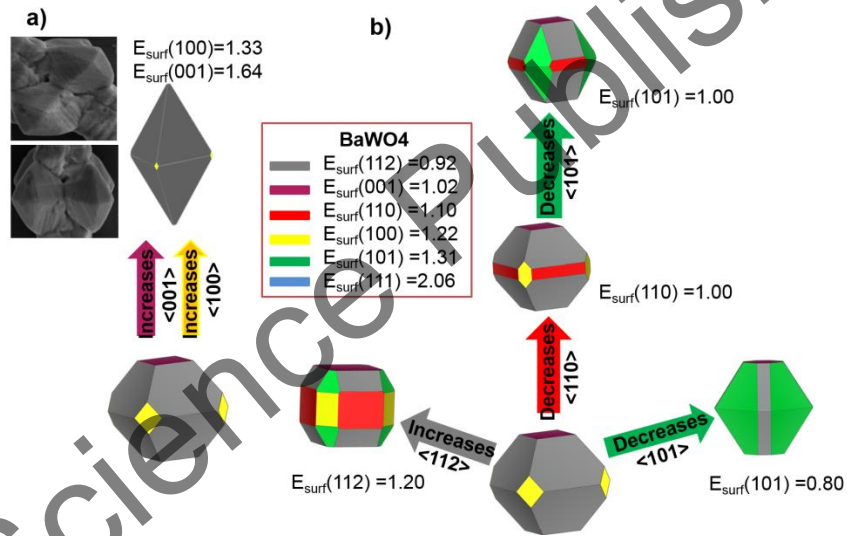


Figure 1. Morphology map for BaWO₄ with (001), (112), (100), (101), (111), and (110) crystal planes. Surface energies are expressed in Joules per square meter. a) Experimental FE-SEM images of the studied BaWO₄ microcrystal samples are included for comparison. b) Equilibrium crystal shapes predicted by Wulff constructions by tuning the surfaces energy values.

Analysis of the theoretical results indicates that the most stable surfaces are the (112), (001), and (100) facets (Gao, Sun, et al. 2013), which can form a truncated octahedron corresponding to the ideal morphology (shown in the central part of Figure 1). When the relative stability of the facets changes (increases or decreases), more than one facet type appears in the resulting morphology, producing morphological variations. A truncated cube can be obtained if the surface energy of (112) is increased to 1.20 J/m^2 , whereas an edge-truncated octahedron can be produced if the surface energy of (101) is decreased to 0.80 J/m^2 . The FE-SEM images in Figure 1(a) show well-faceted crystals obtained experimentally that can be compared with the predicted morphologies. Good agreement between the experimental and theoretical morphologies is obtained when the surface energy values for the (001) and (100) facets increase simultaneously (Figure 1). Thus, variations in the ratios between surface energy values affect morphology, and thus, these values can be used to obtain correlations with experimental results.

BaMoO₄

Barium molybdate (BaMoO₄) is a prototypical member of the molybdate family with a scheelite-type tetragonal structure (Ryu et al. 2006); (Wu et al. 2007), (Sczancoski et al. 2010), similar to BaWO₄ (Nogueira et al. 2013). The morphology of a simulated BaMoO₄ system was calculated using Wulff constructions for the surface energy values, E_{surf} , of the (001), (101), (110), (100), (111), and (112) surfaces (Table 2). Considering the surface atom distributions, we note that the most stable surface, (001), has exposed [BaO₆] clusters, corresponding to the presence of two oxygen vacancies compared with the bulk structure. However, on the (100), (110), (101), and (111) surfaces, there are undercoordinated [BaO₅] clusters associated with the presence of three oxygen vacancies. On the (112) surface, there are four oxygen vacancies, i.e., undercoordination

at [BaO₄]. Only the (111) surface has [MoO₃] clusters, implying breakage of a Mo–O bond in comparison with the bulk structure. As the bonding interaction of a Mo–O bond is stronger than that of a Ba–O bond, the stability of this surface is reduced compared with those of the other surfaces.

According to theoretical calculations, the order of stability found for BaMoO₄ surfaces is (001) > (112) > (100) > (110) > (101) > (101) > (111). The ideal morphology of BaMoO₄ is controlled by the (001), (112), and (100) surfaces, which have contributions of 15.1%, 70.9%, and 14.0%, respectively, based on experimental micrographs.

The available morphologies, as depicted in Figure 2(a-b), reflect changes in the surface energy values, i.e., modifying the stability of the surface generates the corresponding morphology. Recently, Gao et al. (2013) (Gao, Sun, et al. 2013) reported that the surfaces of scheelite crystals predominantly consist of exposed (001), (112), and (100) surfaces, with the (112) crystal surface as the most commonly exposed surface.

Table 2. Calculated surface energy (E_{surf}), surface tension (σ), and change in total energy (ΔE_{tot}) for the dilation area (ΔA) and gap energy of each surface

Surface	E_{surf} (J/m ²)	ΔE_{tot} (Hartree)	ΔA (Å ²)	σ (J/m ²)	E_{gap} (eV)
(001)	0.99	0.035	1.273	0.54	5.69
(112)	1.02	0.032	2.385	0.85	5.81
(100)	1.17	0.039	2.853	1.04	5.38
(110)	1.23	0.033	2.017	1.01	5.63
(101)	1.34	0.039	1.562	0.94	5.09
(111)	2.23	0.016	4.231	2.51	Conductor

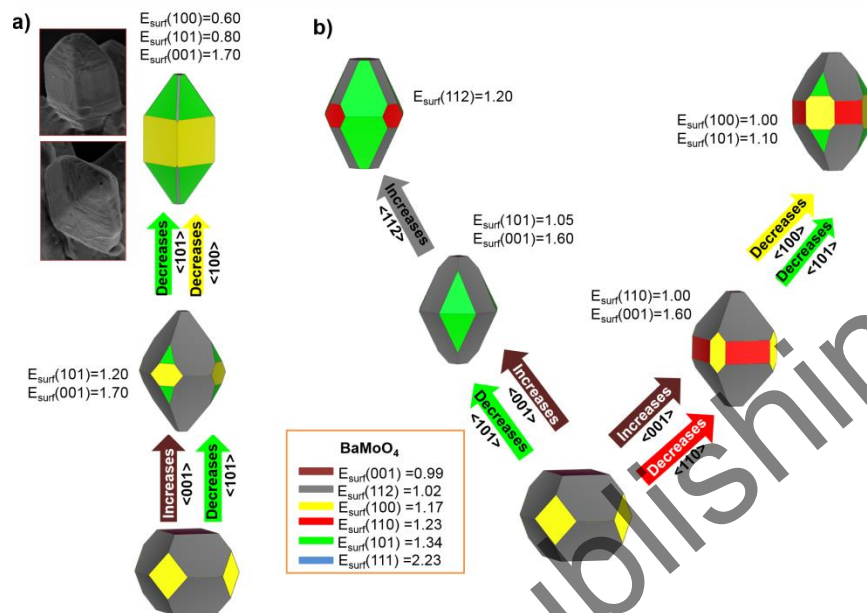


Figure 2. Crystallographic structures and morphology map for BaMoO₄ crystals. Surface energies are expressed in Joules per square meter). a) Experimental FE-SEM images and b) equilibrium crystal shapes predicted by Wulff constructions by tuning the surfaces energy values.

The essential features of the different surfaces are constant, but significant differences in the distribution of the electronic states are observed for the (001), (100), (110), and (101) surfaces, where the reduced coordination environment of the surface-terminated oxygen atoms gives rise to split-off features in the O 2p and Mo 4d partial DOS at the bottom of the conduction band. Further, surface states reduce the bulk band gap (5.8 eV) by 0.1–0.7 eV, depending on the specific surface.

CaZrO₃

Calcium zirconate (CaZrO₃) is a multifunctional material that has many applications and has been investigated frequently, both theoretically and experimentally (Dravid et al. 1987); (Stoch et al. 2012); (Hou 2013);

(M.G.Brik et al. 2013); (Boobalan et al. 2015). CaZrO_3 is a perovskite-type material with an orthorhombic structure of space group $Pcmn$ (Rosa et al. 2015).

The variation in the equilibrium shapes for these systems obtained using Wulff constructions (Wulff 1901) can be a powerful tool for evaluating the morphology. When the relative stability of the facets changes (increases or decreases), more than one facet type can appear in the resulting morphology, producing morphological variations (Figure 3). The computed surface energy and band gap values for the (121), (100), (010), (101), (001), (111), and (011) surfaces are summarized in Table 3. Analysis of the theoretical results indicates a band gap value of 6.23 eV for bulk CaZrO_3 .

All surfaces are Ca–O-terminated, with $[\text{CaO}_4]$ or $[\text{CaO}_5]$ as exposed clusters, and the stability order is $(121) > (100) > (010) > (101) > (001) > (111) > (011)$, and the ideal morphology of CaZrO_3 is controlled by the (121), (100), (101), (001), and (010) facets, as can be seen in Figure 3.

Based on the theoretical results, the ideal morphology of CaZrO_3 is controlled by the (001), (121), (101), (010) and (100) facets, which have contributions of 11.3%, 56.2%, 11.5%, 7.5%, and 13.5%, respectively. An analysis of the results shows that the present equilibrium morphology models are consistent with the atomic configurations and the local coordination atoms for each surface.

Table 3. Surface energy and band gap values for the (121), (100), (010), (101), (001), (111), and (011) surfaces of CaZrO_3 crystals

Surface	E_{surf} (J/m^2)	Area (\AA)	E_{gap} (eV)
(121)	1.25	91.13	6.61
(100)	1.26	44.21	6.41
(010)	1.28	32.23	5.62
(101)	1.39	64.41	6.39
(001)	1.37	44.87	6.28
(111)	1.52	72.03	5.64
(011)	1.99	55.25	5.69

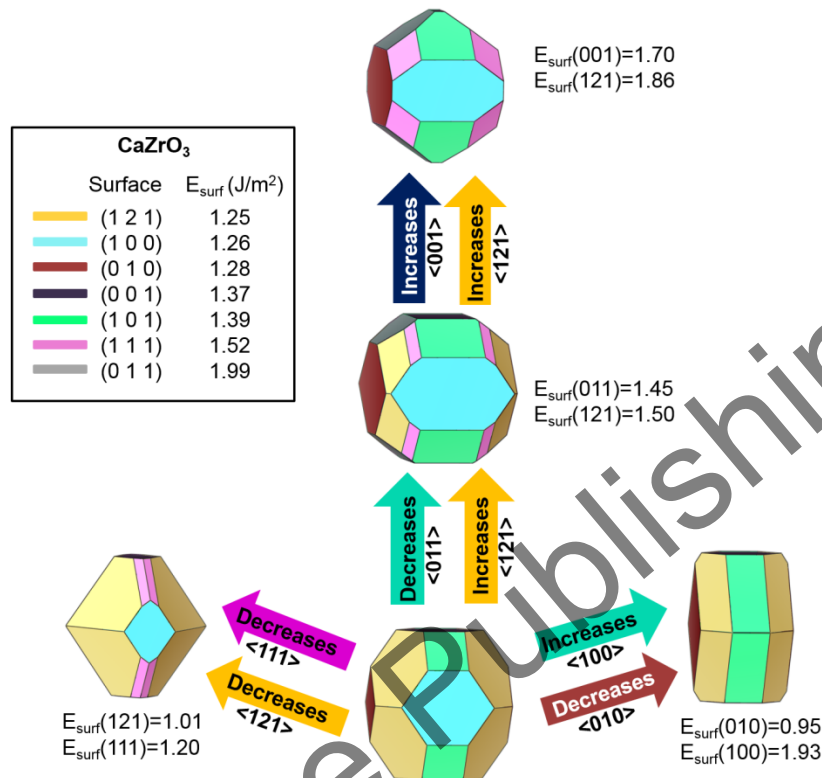


Figure 3. Morphology map for CaZrO₃ based on Wulff constructions. Surface energies are expressed in Joules per square meter.

BaSnO₃

BaSnO₃ exhibits a wide of interesting properties with potential technological applications as capacitor dielectrics, gas sensors for a large variety of molecules (Murugaraj et al. 1997); (Ostrick et al. 1997); (Kreuer 1999); (Aydi et al. 2008); (Kim, Kim, et al. 2012); (Wang, Chesnaud, et al. 2012); (Bevillon et al. 2014); (Hadjarab et al. 2015); (Li et al. 2015); (Marikutsa et al. 2015); (Zhu et al. 2016), humidity detectors, and photocatalysts for dye degradation (Lu et al. 2007); (Liu et al. 2012); (Sales et al. 2014). The properties of this material are correlated with its morphology (Zhang et al. 2017). Moreover, various other synthesis

parameters, such as pH, surfactant additives, ion concentration, and synthesis method, can significantly alter the morphology (Kumar et al. 2006); (Sales et al. 2014); (Wang, Liang, et al. 2014); (Huang et al. 2015).

BaSnO₃ is a cubic perovskite with space group *Pm3m*, in which the Sn⁴⁺ cations are located at the centers of regular oxygen octahedra, forming SnO₆ clusters, whereas the local coordination of the Ba²⁺ cations forms a BaO₁₂ dodecahedral cluster (Huang et al. 2015); (Duarte et al. 2016). The aim of this study was to understand how BSO morphologies are formed and behave in stoichiometric and nonstoichiometric slabs.

Nonstoichiometric and symmetric slabs for (001), (011), and (111) slabs of BaSnO₃ are presented in Figure 4(a). The (001) surface is neutral, with only two terminations and alternating BaO and SnO₂ layers, depicted as A and B. However, the (011) and (111) surfaces have polar characteristics, and studies of similar perovskites have demonstrated that some treatments, such as charge neutrality achieved by imposing a zero net charge on the unit cell, are not very effective at eliminating the generated dipole momentum (Poiani et al. 1999); (Noguera 2000b); (Bottin et al. 2003). In the case of the (011) surface, as an alternative option, a neutral slab can be obtained. For nonsymmetrical surfaces with O–O termination, it is possible to remove oxygen atoms from the top and bottom of the slab, whereas for symmetric and nonstoichiometric surfaces with BaSnO termination, it is possible to remove Ba or Sn atoms, or both, and O atoms at the top and bottom of the slab (Bottin et al. 2003), as shown by pictures C and D in Figure 4(a). The (111) surface is formed by successive layers of BaO₃ and Sn atoms (pictures E and F, Figure 4(a)), following the polarity compensation criterion that the formal charge of the various (111) surfaces of BaSnO₃ must be equal to half of the bulk value, i.e., ± 2 (Liu et al. 2009).

The simulation data are summarized in Table 4.

A variety of surface reconstructions are reported for BaSnO₃-like systems, for both stoichiometric (Charlton et al. 2000); (Liborio et al. 2005) and nonstoichiometric surfaces (Poiani et al. 1999); (Eglitis 2013); (Eglitis 2015), with the (001) surface being the most studied surface.

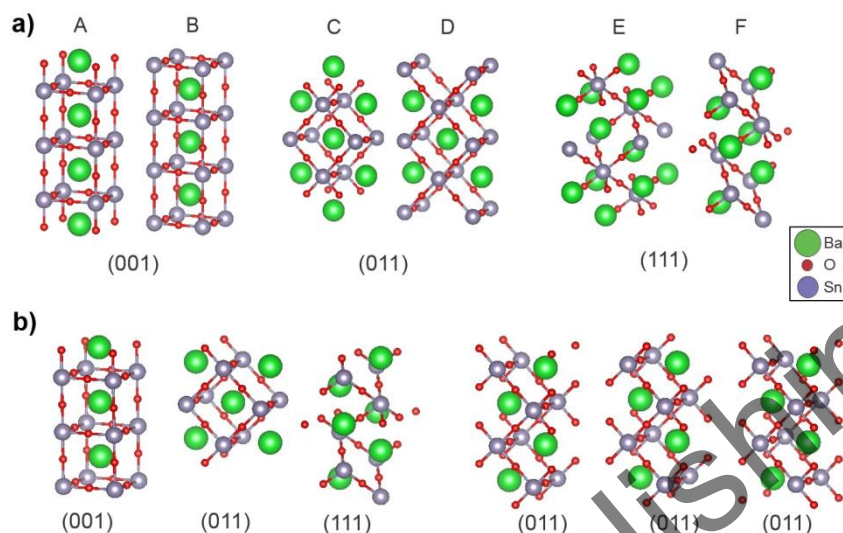


Figure 4. a) Nonstoichiometric and symmetric slabs for (001), (011), and (111) surfaces, and b) stoichiometric slabs for (001), (011), and (111) surfaces.

Table 4. Surface energy values for nonstoichiometric and symmetric slabs of BaSnO₃

Termination	Surface	n	E_{surf} ($\text{J}\cdot\text{m}^{-2}$)	Area (\AA^2)	Thickness (\AA)
Ba-O/Sn-O	(0 0 1)	7	1.37	16.918	12.20
Ba-O/Sn	(0 1 1)	8	2.33	23.926	11.18
Sn/BaO ₃	(1 1 1)	11	3.74	23.303	11.94

Table 5 presents surface energy data for stoichiometric slabs. In this case, the (001) surface is BaO-terminated, whereas the (011) surfaces is SnO- and O₂-terminated. It is possible to observe that there is not a great variation of slab stability (011). Thus, the contribution of different slab thicknesses or even different positions of the outermost oxygen atom is assumed to be small.

Table 5. Surface energy values for stoichiometric and symmetric slabs of BaSnO₃

Termination	Surface	<i>n</i>	<i>E</i> _{surf} (J·m ⁻²)	Area (Å ²)	Thickness (Å)
Ba-O/Sn-O	(0 0 1)	3	1.37	16.92	10.12
BaSnO	(0 1 1)	4	1.69	23.93	11.05
Sn-BaO ₃	(1 1 1)	5	3.05	23.30	10.84

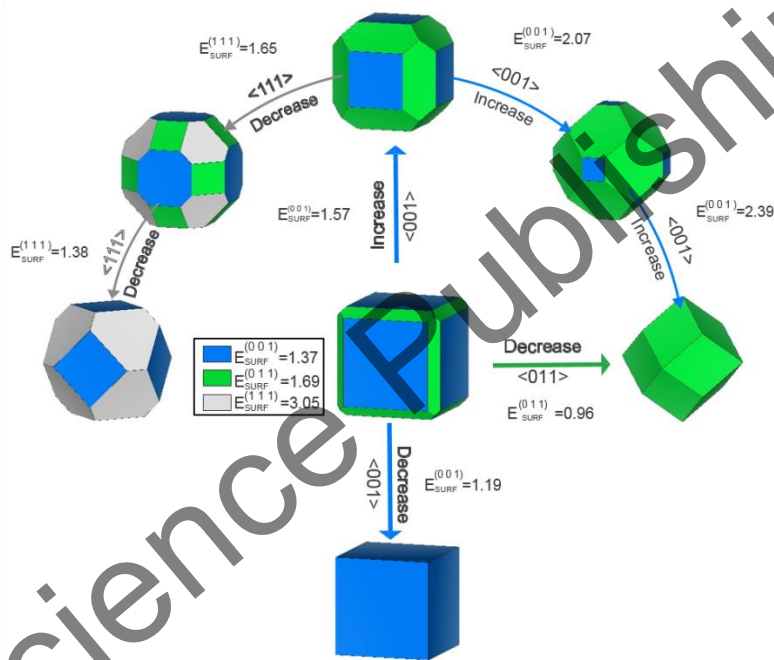


Figure 5. Morphology map for BaSnO₃ based on Wulff constructions. Surface energies are expressed in Joules per square meter.

The stability order for stoichiometric and nonstoichiometric slabs is the same: (001) > (011) > (111), although the stability of the stoichiometric (011) surface is higher than that of the corresponding nonstoichiometric slab. Therefore, based on the surface energy values in Table 5, a morphology map was constructed for BaSnO₃, as shown in Figure 5, where the ideal morphology is controlled by the (001) surface.

CONCLUSION

“It is a test of true theories not only to account for but to predict phenomena” W. Whewell, 1847 in *The Philosophy of the Inductive Sciences, Founded Upon Their History* (Whewell 1847).

Computer modeling is highly likely to play a part in understanding the shape of (nano)crystals and in predicting morphological transformations. We have introduced first-principles surface models for all relevant low-index surfaces of BaWO₄, BaMoO₄, CaZrO₃, and BaSnO₃. By simulating clean surfaces with different chemical natures and translating surface stabilities into equilibrium morphologies, we have realized almost the entire range of available morphologies, thereby lending microscopic understanding to experimental results.

Rather than individual values, the most important outcome of these simulations is the general, chemical trends they have revealed. The predicted morphologies were compared with experimentally observed morphologies. To achieve a given morphology, the relative values of the surface energies were changed. In this way, predictive atomistic simulations should likely play an increasingly important role. Therefore, synthesis processes should be controlled to reduce/increase the presence of various surfaces. It has been established that the proposed procedure is easy to apply, provides accurate predictions of crystal morphologies, and can be applied to complex systems.

It should be noted that our calculations have been carried out in a vacuum, and this can be considered a simple approximation. Recent studies show improvements in this area, such as the inclusion of solvent or consideration of specific interactions with surfactants present in the synthesis environment. For example, calculation of the surface Gibbs free energy per unit surface area for an *i*-terminated surface, including variations in entropy and temperature, was recently reported by Kim and Kim to analyze changes in morphology as a function of partial pressure of O₂. Moreover, the authors analyzed the equilibrium crystal shape of BaZrO₃ and space charge formation in the (011) surface of BaZrO₃ (Kim et al. 2017). Further, Jiang et al. (Jiang et al. 2016) have performed first-

principles calculations to clarify the effect of hydrogen adsorption on the surface facets of Pd–Cu nanocrystals. The results indicate that adsorbates could largely modify the equilibrium surface energy, and Wulff constructions based on corrected surface energies are consistent with the experiments, providing microscopic insight into the behavior of nanocrystals at realistic gas pressures. Such an approach is promising for shaping nanocatalysts by gas-assisted treatments. Qi et al. (Qi et al. 2014) have performed DFT calculations to study the surface chemistry of ionic liquids adsorbed on TiO₂ facets. The results of this study revealed how ionic liquids achieve the synthesis of shape-controlled nanocrystals by tuning the surface chemistry, which is a valuable step toward the ultimate goal of controlling the synthesis of inorganic nanomaterials.

We strongly believe in the philosophy of natural sciences, where experiments should inspire predictive models that in turn are verified or disproved by more experiments. Rather than just showing qualitative agreement between theory and experiment, it is more important to be able to predict phenomena, and we urge authors to consider going beyond just reporting results (and referees to allow predictive hypotheses to be included).

ACKNOWLEDGMENTS

This work was supported by the following Spanish research funding projects: *PrometeoII*/2014/022, ACOMP/2014/270, and ACOMP72015/1202 (Generalitat-Valenciana); Ministerio de Economía y Competitividad (CTQ2015-652017-P); and Programa de Cooperación Científica con Iberoamérica (Brasil) of Ministerio de Educación (PHBP14-00020); and CAPES/DGPU (project 312/15 and process 99999.000374/2015-04), as well as the following Brazilian research funding institutions: Federal University of Paraíba and Federal University of São Carlos. M.C. acknowledges Generalitat Valenciana for the Santiago Grisolia Program 2015/033. We also acknowledge Servei Informàtica, Universitat Jaume I for a generous allotment of computer time.

REFERENCES

- Adamo, Carlo. & Vincenzo, Barone. (1999). "Toward reliable density functional methods without adjustable parameters: The PBE0 model." *The Journal of Chemical Physics*, 110, 6158-6170. doi: 10.1063/1.478522.
- Agarwal, Shilpa., Leon, Lefferts., Barbara, L. Mojet., Michel Ligthart, D. A. J., Emiel, J. M. Hensen., David, R. G. Mitchell., Willem, J. Erasmus., Bruce, G. Anderson., Ezra, J. Olivier., Johannes, H. Neethling. & Abhaya, K. Datye. (2013). "Exposed Surfaces on Shape-Controlled Ceria Nanoparticles Revealed through AC-TEM and Water-Gas Shift Reactivity." *ChemSusChem*, 6 (10), 1898-1906. doi: 10.1002/cssc.201300651.
- Ahmadi, T. S., Wang, Z. L., Green, T. C., Henglein, A. & El-Sayed, M. A. (1996). "Shape controlled synthesis of colloidal platinum nanoparticles." *Science*, 272 (5270), 1924-1926.
- Andrés, J., Gracia, L., Gouveia, A. F., Ferrer, M. M. & Longo, E. (2015). "Effects of surface stability on the morphological transformation of metals and metal oxides as investigated by first-principles calculations." *Nanotechnology*, 26, 405703.
- Anicete-Santos, M., Picon, F. C., Nahum Alves, C., Pizani, P. S., Varela, J. A. & Longo, E. (2011). "The Role of Short-Range Disorder in BaWO₄ Crystals in the Intense Green Photoluminescence." *J. Phys. Chem. C*, 115, 12180-12186.
- Araújo, V. D., Tranquilin, R. L., Motta, F. V., Paskocimas, C. A., Bernardi, M. I. B., Cavalcante, L. S., Andres, J., Longo, E. & Bomio, M. R. D. (2014). "Effect of polyvinyl alcohol on the shape, photoluminescence and photocatalytic properties of PbMoO₄ microcrystals." *Materials Science in Semiconductor Processing*, 26, 425-430. doi: <http://dx.doi.org/10.1016/j.mssp.2014.05.027>.
- Aydi, Abdelhedi., Souad, Chkoundali., Hamadi, Khemakhem., Annie, Simon. & Régnauld, Von Der Mühl. (2008). "X-ray diffraction, dielectric measurements and Raman spectroscopy: Studies of the (1-x)CaSnO₃ - xNaNbO₃ solid solution." *Journal of Alloys and*

- Compounds*, 465 (1–2), 222–226. doi: <http://dx.doi.org/10.1016/j.jallcom.2007.10.108>.
- Bandura, A. V., Evarestov, R. A. & Kuruch, D. D. (2010). “Hybrid HF–DFT modeling of monolayer water adsorption on (001) surface of cubic BaHfO₃ and BaZrO₃ crystals.” *Surface Science*, 604 (19–20), 1591–1597. doi: <http://dx.doi.org/10.1016/j.susc.2010.05.030>.
- Barbier, A., Stierle, A., Finocchi, F. & Jupille, J. (2008). “Stability and stoichiometry of (polar) oxide surfaces for varying oxygen chemical potential.” *J. Phys.: Condens. Matter*, 20, 184014.
- Barmparis, Georgios D., Zbigniew, Lodziana., Nuria, Lopez, & Ioannis, N. Remediakis. (2015). “Nanoparticle shapes by using Wulff constructions and first-principles calculations.” *Beilstein Journal of Nanotechnology*, 6, 361–368. doi: 10.3762/bjnano.6.35.
- Barnard, A. S. (2010). “Modelling of nanoparticles: approaches to morphology and evolution.” *Reports on Progress in Physics*, 73 (8), 086502. doi: 10.1088/0034-4885/73/8/086502.
- Barnard, A. S. & Kirkland, A. I. (2008). “Combining Theory and Experiment in Determining the Surface Chemistry of Nanocrystals.” *Chemistry of Materials*, 20 (17), 5460–5463. doi: 10.1021/cm8001892.
- Barnard, A. S., Zapol, P. & Curtiss, L. A. (2005). “Modeling the Morphology and Phase Stability of TiO₂ Nanocrystals in Water.” *Journal of Chemical Theory and Computation*, 1 (1), 107–116. doi: 10.1021/ct0499635.
- Barnard, Amanda S. (2012). “Direct Comparison of Kinetic and Thermodynamic Influences on Gold Nanomorphology.” *Accounts of Chemical Research*, 45 (10), 1688–1697. doi: 10.1021/ar3000184.
- Batista, F. M. C., La Porta, F. A., Gracia, L., Cerdeiras, E., Mestres, L., Siu Li, M., Batista, N. C., Andrés, J., Longo, E. & Cavalcante, L. S. (2015). “A joint experimental and theoretical study on the electronic structure and photoluminescence properties of Al₂(WO₄)₃ powders.” *Journal of Molecular Structure*, 1081, 381–388.
- Becke, A. D. (1993). “Density-functional thermochemistry. III. The role of exact exchange.” *J. Chem. Phys.*, 98, 5648–5652. doi: 10.1063/1.464913.

- Beltrán, A., Andrés, J., Longo, E. & Leite, E. R. (2003). “Thermodynamic argument about SnO₂ nanoribbon growth.” *Applied Physics Letters*, 83 (4), 635-637. doi: 10.1063/1.1594837.
- Beltrán, A., Gracia, L., Longo, E. & Andrés, J. (2014). “First-Principles Study of Pressure-Induced Phase Transitions and Electronic Properties of Ag₂MoO₄.” *J. Phys. Chem. C*, 118, 3724-3732.
- Bevillon, Emile., Jessica, Hermet., Guilhem, Dezanneau. & Gregory, Geneste. (2014). “How dopant size influences the protonic energy landscape in BaSn_{1-x}MxO_{3-x/2} (M = Ga, Sc, In, Y, Gd, La).” *Journal of Materials Chemistry A*, 2 (2), 460-471. doi: 10.1039/C3TA12870A.
- Bomio, M. R. D., Tranquilin, R. L., Motta, F. V., Paskocimas, C. A., Nascimento, R. M., Gracia, L., Andres, J. & Longo, E. (2013). “Toward Understanding the Photocatalytic Activity of PbMoO₄ Powders with Predominant (111), (100), (011), and (110) Facets. A Combined Experimental and Theoretical Study.” *The Journal of Physical Chemistry C*, 117 (41), 21382-21395. doi: 10.1021/jp407416h.
- Boobalan, K., Varun, A., Vijayaraghavan, R., Chidambaram, K. & Kamachi Mudali, U. (2015). “Facile, scalable synthesis of nanocrystalline calcium zirconate by the solution combustion method.” *Ceramics International*, 41, 3069–3074.
- Bottin, François., Fabio, Finocchi. & Claudine, Noguera. (2003). “Stability and electronic structure of the (1×1) SrTiO₃ (110) polar surfaces by first-principles calculations.” *Physical Review B*, 68 (3), 035418.
- Bruchez, M., Moronne, M., Gin, P., Weiss, S. & Alivisatos, A. P. (1998). “Semiconductor Nanocrystals as Fluorescent Biological Labels.” *Science*, 281, 2013–2016.
- Chan, W. C. W. & Shuming, N. (1998). “Quantum Dot Bioconjugates for Ultrasensitive Nonisotopic Detection.” *Science*, 281 (5385), 2016-2018. doi: 10.1126/science.281.5385.2016.
- Charlton, G., Brennan, S., Muryn, C. A., McGrath, R., Norman, D., Turner, T. S. & Thornton, G. (2000). “Surface relaxation of SrTiO₃ (001).” *Surface Science*, 457 (1–2), L376-L380. doi: [http://dx.doi.org/10.1016/S0039-6028\(00\)00403-9](http://dx.doi.org/10.1016/S0039-6028(00)00403-9).

- Chen, Jingyi., Byungkwon, Lim., Eric, P. Lee. & Younan, Xia. (2009). "Shape-controlled synthesis of platinum nanocrystals for catalytic and electrocatalytic applications." *Nano Today*, 4 (1), 81-95. doi: <http://dx.doi.org/10.1016/j.nantod.2008.09.002>.
- Cora, F. (2005). "The performance of hybrid density functionals in solid state chemistry: the case of BaTiO₃." *Mol. Phys.*, 103, 2483-2496.
- Cora, F., Patel, A., Harrison, N. M., Dovesi, R. & Catlow, C. R. A. (1996). "An Ab Initio Hartree-Fock Study of the Cubic and Tetragonal Phases of Bulk Tungsten Trioxide." *J. Am. Chem. Soc.*, 118, 12174-12182.
- Dai, Yunqian., Claire, M. Cobley., Jie, Zeng., Yueming, Sun. & Younan, Xia. (2009). "Synthesis of Anatase TiO₂ Nanocrystals with Exposed {001} Facets." *Nano Letters*, 9 (6), 2455-2459. doi: 10.1021/nl901181n.
- Dandekar, Preshit., Zubin, B. Kuvadiah. & Michael, F. Doherty. (2013). "Engineering Crystal Morphology." *Annual Review of Materials Research*, 43 (1), 359-386. doi: 10.1146/annurev-matsci-071312-121623.
- Davies, Mark J., Stephen, C. Parker. & Graeme, W. Watson. (1994). "Atomistic simulation of the surface structure of spinel." *Journal of Materials Chemistry*, 4 (6), 813-816. doi: 10.1039/JM9940400813.
- Dinh, Cao-Thang., Thanh-Dinh, Nguyen., Freddy, Kleitz. & Trong-On, Do. (2009). "Shape-Controlled Synthesis of Highly Crystalline Titania Nanocrystals." *ACS Nano*, 3 (11), 3737-3743.
- Dovesi, R., Saunders, V. R., Orlando C. Roetti, R., Zicovich-Wilson, C. M., Civalieri F. Pascale, B., Doll, K., Harrison, N. M., Bush, I. J., D'Arco, Ph., Llunel, M. & Causa, Y. N. [http:// www.crystal.unito.it/basis-sets.php](http://www.crystal.unito.it/basis-sets.php).
- Dovesi, R., Saunders, V. R., Roetti, C., Orlando, R., Zicovich-Wilson, C. M., Pascale, F., Civalieri, B., Doll, K., Harrison, N. M., Bush, I. J., D'Arco, Ph., Llunel, M., Caus`a, M., No`e, Y. (2014). CRYSTAL14. edited by University Of Torino. Torino- Italy.
- Dravid, V. P., Notis, M. R. & Lyman, C. E. (1987). "Electron microscopy of boundary structure in calcium zirconate." *journal of materials science*, 22, 4546-4549.

- Duarte, Thiago M., Prescila, G. C. Buzolin., Ieda, M. G. Santos., Elson, Longo. & Julio, R. Sambrano. (2016). "Choice of hybrid functional and basis set optimization to calculate the structural, electronic, mechanical, and vibrational properties of BaSnO₃." *Theoretical Chemistry Accounts*, 135 (6), 151. doi: 10.1007/s00214-016-1901-1.
- Eglitis, R. I. (2013). "Ab initio calculations of the atomic and electronic structure of BaZrO₃ (111) surfaces." *Solid State Ionics*, 230, 43-47. doi: <http://dx.doi.org/10.1016/j.ssi.2012.10.023>.
- Eglitis, R. I. & David, Vanderbilt. (2008). "First-principles calculations of atomic and electronic structure of SrTiO₃ (001) and (011) surfaces." *Physical Review B*, 77 (19), 195408.
- Eglitis, Roberts I. (2015). "Theoretical Modelling of the Energy Surface (001) and Topology of CaZrO₃ Perovskite." *Ferroelectrics*, 483 (1), 75-85. doi: 10.1080/00150193.2015.1058690.
- Fabbro, M. T., Saliby, C., Rios, L. R., La Porta, F. A., Gracia, L. E., Li, M. S., Andrés, J., Santos, L. P. S. & Longo, E. (2015). "Identifying and rationalizing the morphological, structural, and optical properties of B-Ag₂MoO₄ microcrystals, and the formation process of Ag nanoparticles on their surfaces: combining experimental data and first-principles calculations." *Sci. Technol. Adv. Mater*, 16, 065002.
- Fan, Dongbo., John Thomas, P. & Paul, O'Brien. (2008). "Pyramidal Lead Sulfide Crystallites With High Energy {113} Facets." *Journal of the American Chemical Society*, 130 (33), 10892-10894. doi: 10.1021/ja804516q.
- Ferrer, M. M., Gouveia, A. F., Gracia, L., Longo, E. & Andrés, J. (2016). "A 3D platform for the morphology modulation of materials: first principles calculations on the thermodynamic stability and surface structure of metal oxides: Co₃O₄, α -Fe₂O₃, and In₂O₃." *Modelling Simul. Mater. Sci. Eng.*, 24, 025007.
- Freund, H. J., Kuhlenbeck, H. & Staemmler, V. (1996). "Oxide surfaces." *Rep. Prog. Phys.*, 59, 283-347.
- Gao, Qiang., Yi-Ming, Ju., Duo, An., Min-Rui, Gao., Chun-Hua, Cui., Jian-Wei, Liu., Huai-Ping, Cong. & Shu-Hong, Yu. (2013). "Shape-

- Controlled Synthesis of Monodisperse PdCu Nanocubes and Their Electrocatalytic Properties.” *ChemSusChem*, 6 (10), 1878-1882.
- Gao, Z. Y., Sun, W., Hu, Y. H. & Liu, X. W. (2013). “Surface energies and appearances of commonly exposed surfaces of scheelite crystal.” *T. Nonferr. Metal. Soc.*, 23, 2147-2152.
- Gibbs, J. W. & Smith, A.W. (1875). “On the Equilibrium of Heterogeneous Substances.” *Trans. Conn. Acad. of Arts Sci.*, 3, 108-248.
- Goniakowski, Jacek., Fabio, Finocchi. & Claudine, Noguera. (2008). “Polarity of oxide surfaces and nanostructures.” *Reports on Progress in Physics*, 71 (1), 016501. doi: 10.1088/0034-4885/71/1/016501.
- Gordon, Thomas R., Matteo, Cargnello., Taejong, Paik., Filippo, Mangolini., Ralph, T. Weber., Paolo, Fornasiero. & Christopher, B. Murray. (2012). “Nonaqueous Synthesis of TiO₂ Nanocrystals Using TiF₄ to Engineer Morphology, Oxygen Vacancy Concentration, and Photocatalytic Activity.” *Journal of the American Chemical Society*, 134 (15), 6751-6761. doi: 10.1021/ja300823a.
- Gouveia, Amanda F., Mateus, M Ferrer., Júlio, R Sambrano., Juan, Andrés. & Elson, Longo. (2016). “Modeling the atomic-scale structure, stability, and morphological transformations in the tetragonal phase of LaVO₄.” *Chemical Physics Letters*, 660, 87-92.
- Groß, Axel. (2009). *Theoretical Surface Science: A Microscopic Perspective*. 2nd ed ed. Germany: Berlin: Springer.
- Gurlo, Aleksander. (2011). “Nanosensors: towards morphological control of gas sensing activity. SnO₂, In₂O₃, ZnO and WO₃ case studies.” *Nanoscale*, 3 (1), 154-165. doi: 10.1039/c0nr00560f.
- Hadjarab, B., Trari, M. & Kebir, M. (2015). “Physical characterization of the semiconducting deficient perovskite BaSnO_{3-δ}.” *Materials Science in Semiconductor Processing*, 29, 283-287. doi: <http://dx.doi.org/10.1016/j.mssp.2014.04.041>.
- Han, Xiguang., Mingshang, Jin., Shuifen, Xie., Qin, Kuang., Zhiyuan, Jiang., Yaqi, Jiang., Zhaoxiong, Xie. & Lansun, Zheng. (2009). “Synthesis of Tin Dioxide Octahedral Nanoparticles with Exposed High-Energy {221} Facets and Enhanced Gas-Sensing Properties.”

Angewandte Chemie International Edition, 48 (48), 9180-9183. doi: 10.1002/anie.200903926.

Han, Xiguang., Qin, Kuang., Mingshang, Jin., Zhaoxiong, Xie. & Lansun, Zheng. (2009). "Synthesis of Titania Nanosheets with a High Percentage of Exposed (001) Facets and Related Photocatalytic Properties." *Journal of the American Chemical Society*, 131 (9), 3152-3153. doi: 10.1021/ja8092373.

Herring, C. (1981). "Some Theorems on the Free Energies of Crystal Surface." *Phys. Rev*, 82, 87-93.

Hörmann, N. G. & Groß, A. (2014). "Stability, composition and properties of $\text{Li}_2\text{FeSiO}_4$ surfaces studied by DFT." *Journal of Solid State Electrochemistry*, 18 (5), 1401-1413. doi: 10.1007/s10008-013-2189-x.

Hou, Z. F. (2013). "Ab initio calculations of elastic modulus and electronic structures of cubic CaZrO_3 ." *Physica B-Condensed Matter.*, 403, 2624-2628.

http://Www.Crystal.Unito.It/Basis_Sets/Molibdenum.Html.

http://Www.Crystal.Unito.It/Basis_Sets/Oxygen.Html.

http://Www.Tcm.Phy.Cam.Ac.Uk/~Mdt26/Basis_Sets/Ba_Basis.Txt.

Hu, Linhua., Qing, Peng. & Yadong, Li. (2008). "Selective Synthesis of Co_3O_4 Nanocrystal with Different Shape and Crystal Plane Effect on Catalytic Property for Methane Combustion." *J. Am. Chem. Soc.*, 130, 16136-16137.

Hu, Yidong., Gang, Chen., Chunmei, Li., Yansong, Zhou., Jingxue, Sun., Sue, Hao. & Zhonghui, Han. (2016). "Fabrication of {010} facet dominant BiTaO_4 single-crystal nanoplates for efficient photocatalytic performance." *Journal of Materials Chemistry A*, 4 (14), 5274-5281. doi: 10.1039/C6TA00468G.

Huang, Chuande., Xiaodong, Wang., Quan, Shi., Xin, Liu., Yan, Zhang., Fei, Huang. & Tao, Zhang. (2015). "A Facile Peroxo-Precursor Synthesis Method and Structure Evolution of Large Specific Surface Area Mesoporous BaSnO_3 ." *Inorganic Chemistry*, 54 (8), 4002-4010. doi: 10.1021/acs.inorgchem.5b00269.

- Huang, Michael H., Sourav, Rej. & Shih-Chen, Hsu. (2014). "Facet-dependent properties of polyhedral nanocrystals." *Chemical Communications*, 50 (14), 1634. doi: 10.1039/c3cc48527g.
- Huang, Weixin. (2013). "Crystal Plane-Dependent Surface Reactivity and Catalytic Property of Oxide Catalysts Studied with Oxide Nanocrystal Model Catalysts." *Topics in Catalysis*, 56 (15), 1363-1376. doi: 10.1007/s11244-013-0139-6.
- Huang, Weixin. (2016). "Oxide Nanocrystal Model Catalysts." *Accounts of Chemical Research*, 49 (3), 520-527. doi: 10.1021/acs.accounts.5b00537.
- Huang, Weixin. & Yuxian, Gao. (2014). "Morphology-dependent surface chemistry and catalysis of CeO₂ nanocrystals." *Catal. Sci. Technol.*, 4 (11), 3772-3784. doi: 10.1039/c4cy00679h.
- Huynh, Wendy U., Xiaogang, Peng. & Paul Alivisatos, A. (1999). "CdSe Nanocrystal Rods/Poly(3-hexylthiophene) Composite Photovoltaic Devices." *Adv. Mater.*, 11 (11), 923-927.
- Jiang, Ying., Hengbo, Li., Zhemin, Wu., Wenying, Ye., Hui, Zhang., Yong, Wang., Chenghua, Sun. & Ze, Zhang. (2016). "In Situ Observation of Hydrogen-Induced Surface Faceting for Palladium-Copper Nanocrystals at Atmospheric Pressure." *Angewandte Chemie International Edition*, 55 (40), 12427-12430. doi: 10.1002/anie.201605956.
- Jiang, Zhi-Yuan., Qin, Kuang., Zhao-Xiong, Xie. & Lan-Sun, Zheng. (2010). "Syntheses and Properties of Micro/Nanostructured Crystallites with High-Energy Surfaces." *Advanced Functional Materials*, 20 (21), 3634-3645. doi: 10.1002/adfm.201001243.
- Jiang, Zhi-Yuan., Tao, Xu., Zhao-Xiong, Xie., Zhi-Wei, Lin., Xi, Zhou., Xin, Xu., Rong-Bin, Huang. & Lan-Sun, Zheng. (2005). "Molten Salt Route toward the Growth of ZnO Nanowires in Unusual Growth Directions." *The Journal of Physical Chemistry B*, 109 (49), 23269-23273. doi: 10.1021/jp054566r.
- Jun, Young-wook., Jin-sil, Choi. & Jinwoo, Cheon. (2006). "Shape Control of Semiconductor and Metal Oxide Nanocrystals through

- Nonhydrolytic Colloidal Routes.” *Angewandte Chemie International Edition*, 45 (21), 3414-3439. doi: 10.1002/anie.200503821.
- Kanaki, Elisavet., Sebastian, Gohr., Carsten, Müller. & Beate, Paulus. (2015). “Theoretical study on the morphology of MgF_2 nanocrystals at finite temperature and pressure.” *Surface Science*, 632, 158-163. doi: <http://dx.doi.org/10.1016/j.susc.2014.10.007>.
- Karim, Altaf., Sonia, Fosse. & Kristin, A. Persson. (2013). “Surface structure and equilibrium particle shape of the $LiMn_2O_4$ spinel from first-principles calculations.” *Physical Review B*, 87 (7), 075322.
- Kim, Hyung Joon., Useong, Kim., Tai, Hoon Kim., Jiyeon, Kim., Hoon, Min Kim., Byung-Gu, Jeon., Woong-Jhae, Lee., Hyo, Sik Mun., Kwang, Taek Hong., Jaejun, Yu., Kookrin, Chan. & Kee, Hoon Kim. (2012). “Physical properties of transparent perovskite oxides $(Ba,La)SnO_3$ with high electrical mobility at room temperature.” *Physical Review B*, 86 (16), 165205.
- Kim, Ji-Su. & Yeong-Cheol, Kim. (2017). “Equilibrium crystal shape of $BaZrO_3$ and space charge formation in the (011) surface by using ab-initio thermodynamics.” *Journal of the Korean Physical Society*, 70 (1), 75-80. doi: 10.3938/jkps.70.75.
- Kim, Yongseon., Hyundeok, Lee. & Shinhoo, Kang. (2012). “First-principles and experimental investigation of the morphology of layer-structured $LiNiO_2$ and $LiCoO_2$.” *Journal of Materials Chemistry*, 22 (25), 12874-12881. doi: 10.1039/C2JM31145C.
- Kreuer, K. D. (1999). “Aspects of the formation and mobility of protonic charge carriers and the stability of perovskite-type oxides.” *Solid State Ionics*, 125 (1-4), 285-302. doi: [http://dx.doi.org/10.1016/S0167-2738\(99\)00188-5](http://dx.doi.org/10.1016/S0167-2738(99)00188-5).
- Kuang, Qin., Xue, Wang., Zhiyuan, Jiang., Zhaoxiong, Xie. & Lansun, Zheng. (2014). “High-Energy-Surface Engineered Metal Oxide Micro- and Nanocrystallites and Their Applications.” *Accounts Of Chemical Research*, 308-318 (2), 308-318.
- Kumar, Ashok., Choudhary, R. N. P., Singh, B. P. & Awalendra, K. Thakur. (2006). “Effect of strontium concentration on electrical conduction properties of Sr-modified $BaSnO_3$.” *Ceramics*

- International*, 32 (1), 73-83. doi: <http://dx.doi.org/10.1016/j.ceramint.2004.12.010>.
- Valenzano, L., Civalleri, B., Chavan, S., Bordiga, S., Nilsen, M. H., Jakobsen, S., Lillerud, K. P. & Lamberti, C. (2011). "Disclosing the Complex Structure of UiO-66 Metal Organic Framework: A Synergic Combination of Experiment and Theory." *Chem. Mater.*, 23, 1700–1718.
- Gracia, L., Longo, V. M., Cavalcante, L. S., Beltrán, A., Avansi, W., Li, M. S., Mastelaro, V. R., Varela, J. A., Longo, E. & Andrés, J. (2011). "Presence of excited electronic state in CaWO_4 crystals provoked by a tetrahedral distortion: An experimental and theoretical investigation." *J. Appl. Phys.*, 110, 043501.
- Lee, C. T., Yang, W. T. & Parr, R. G. (1988). "Development of the Colle-Salvetti correlation-energy formula into a functional of the electron density." *Phys. Rev. B: Condens. Matter*, 37, 785-789. doi: 10.1103/PhysRevB.37.785.
- Lee, Eunseok. & Kristin, A Persson. (2013). "First-principles study of the nano-scaling effect on the electrochemical behavior in $\text{LiNi}_{0.5}\text{Mn}_{1.5}\text{O}_4$." *Nanotechnology*, 24, 424007.
- Lee, Hyunjoo., Susan, E. Habas., Sasha, Kweskin., Derek, Butcher., Gabor, A. Somorjai. & Peidong, Yang. (2006a). "Morphological Control of Catalytically Active Platinum Nanocrystals." *Angewandte Chemie International Edition*, 45, 7824 –7828. doi: 10.1002/anie.200603068.
- Lee, Hyunjoo., Susan, E. Habas., Sasha, Kweskin., Derek, Butcher., Gabor, A. Somorjai. & Peidong, Yang. (2006b). "Morphological Control of Catalytically Active Platinum Nanocrystals." *Angewandte Chemie International Edition*, 118, 7988-7992.
- Lee, Kwangyeol., Minsik, Kim. & Heonjo, Kim. (2010). "Catalytic nanoparticles being facet-controlled." *Journal of Materials Chemistry*, 20 (19), 3791-3798. doi: 10.1039/B921857B.
- Leite, E. R., Giraldo, T. R., Pontes, F. M., Longo, E., Beltrán, A. & Andrés, J. (2003). "Crystal growth in colloidal tin oxide nanocrystals induced

- by coalescence at room temperature.” *Applied Physics Letters*, 83 (8), 1566-1568. doi: 10.1063/1.1605241.
- Leng, Mei., Mingzhu, Liu., Yibo, Zhang., Zhenqing, Wang., Chao, Yu., Xiangguang, Yang., Hongjie, Zhang. & Cheng, Wang. (2010). “Polyhedral 50-Facet Cu₂O Microcrystals Partially Enclosed by {311} High-Index Planes: Synthesis and Enhanced Catalytic CO Oxidation Activity.” *Journal of the American Chemical Society*, 132 (48), 17084-17087. doi: 10.1021/ja106788x.
- Li, Pan., Xian, Zhao., Chun-Jiang, Jia., Honggang, Sun., Yanlu, Li., Liming, Sun., Xiufeng, Cheng., Li, Liu. & Weiliu, Fan. (2012). “Mechanism of Morphology Transformation of Tetragonal Phase LaVO₄ Nanocrystals Controlled by Surface Chemistry: Experimental and Theoretical Insights.” *Crystal Growth & Design*, 12 (10), 5042-5050. doi: 10.1021/cg3009927.
- Li, Yong. & Wenjie, Shen. (2014). “Morphology-dependent nanocatalysts: Rod-shaped oxides.” *Chem. Soc. Rev.*, 43 (5), 1543-1574. doi: 10.1039/c3cs60296f.
- Li, Yuhan., Jingping, Zhang., Fengmei, Yang., Jing, Liang., Hao, Sun., Shuwei, Tang. & Rongshun, Wang. (2014). “Morphology and surface properties of LiVOPO₄: a first principles study.” *Physical Chemistry Chemical Physics*, 16 (44), 24604-24609. doi: 10.1039/C4CP03628J.
- Li, Yuwei., Lijun, Zhang., Yanming, Ma. & David, J. Singh. (2015). “Tuning optical properties of transparent conducting barium stannate by dimensional reduction.” *APL Materials*, 3 (1), 011102. doi: 10.1063/1.4906785.
- Liao, Hong-Gang., Yan-Xia, Jiang., Zhi-You, Zhou., Sheng-Pei, Chen. & Shi-Gang, Sun. (2008a). “Shape-Controlled Synthesis of Gold Nanoparticles in Deep Eutectic Solvents for Studies of Structure-Functionality Relationships in Electrocatalysis.” *Angewandte Chemie International Edition*, 120, 9240-9243. doi: 10.1002/anie.200803202.
- Liao, Hong-Gang., Yan-Xia, Jiang., Zhi-You, Zhou., Sheng-Pei, Chen. & Shi-Gang, Sun. (2008b). “Shape-Controlled Synthesis of Gold Nanoparticles in Deep Eutectic Solvents for Studies of Structure-

- Functionality Relationships in Electrocatalysis.” *Angew. Chem*, 47, 9100–9103.
- Liborio, M. L., Sánchez, G. C., Paxton, T. A. & Finnis, W. M. (2005). “Stability of Sr adatom model structures for SrTiO₃ (001) surface reconstructions.” *Journal of Physics: Condensed Matter*, 17 (23), L223.
- Lieber, Charles M. (1998). “One-Dimensional Nanostructures: Chemistry, Physics & Applications.” *Solid State Communications*, 107 (11), 607-616.
- Lin, Yuyuan., Zili, Wu., Jianguo, Wen., Kenneth, R. Poepplmeier. & Laurence, D. Marks. (2014). “Imaging the Atomic Surface Structures of CeO₂ Nanoparticles.” *Nano Letters*, 14 (1), 191-196. doi: 10.1021/nl403713b.
- Liu, Bin., Ankur, Khare. & Eray, S. Aydil. (2011). “TiO₂-B/Anatase Core-Shell Heterojunction Nanowires for Photocatalysis.” *ACS Applied Materials & Interfaces*, 3 (11), 4444-4450. doi: 10.1021/am201123u.
- Liu, Gang., Jimmy, C. Yu., Gao, Qing Lu. & Hui-Ming, Cheng. (2011). “Crystal facet engineering of semiconductor photocatalysts: motivations, advances and unique properties.” *Chemical Communications*, 47 (24), 6763-6783. doi: 10.1039/C1CC10665A.
- Liu, Lichen., Xianrui, Gu., Zeyang, Ji., Weixin, Zou., Changjin, Tang., Fei, Gao. & Lin, Dong. (2013). “Anion-Assisted Synthesis of TiO₂ Nanocrystals with Tunable Crystal Forms and Crystal Facets and Their Photocatalytic Redox Activities in Organic Reactions.” *The Journal of Physical Chemistry C*, 117 (36), 18578-18587. doi: 10.1021/jp4064774.
- Liu, Qinzhuang., Bing, Li., Jianjun, Liu., Hong, Li., Zhongliang, Liu., Kai, Dai., Guangping, Zhu., Peng, Zhang., Feng, Chen. & Jianming, Dai. (2012). “Structure and band gap tuning of transparent (Ba_{1-x}Sr_x)SnO₃ thin films epitaxially grown on MgO substrates.” *EPL*, 98 (4), 47010.
- Liu, Wei., Chuncheng, Wang., Jie, Cui. & Zhen-Yong, Man. (2009). “Ab initio calculations of the (111) polar surfaces.” *Solid State*

- Communications*, 149 (43–44), 1871-1876. doi: <http://dx.doi.org/10.1016/j.ssc.2009.08.006>.
- Liu, Y. & Chu, Y. (2005). "Surfactant-assisted synthesis of single crystal BaWO₄ octahedral microparticles." *Mater. Chem. Phys.*, 92, 59-63.
- Longo, E., Volanti, D. P., Longo, V. M., Gracia, L., Nogueira, I. C., Almeida, M. A. P., Pinheiro, A. N., Ferrer, M. M., Cavalcante, L. S. & Andrés, J. (2014). "Toward an Understanding of the Growth of Ag Filaments on α -Ag₂WO₄ and Their Photoluminescent Properties: A Combined Experimental and Theoretical Study." *J. Phys. Chem. C*, 118, 1229-1239.
- Longo, Valéria M., Lourdes, Gracia., Daniel, G. Stroppa., Laécio, S. Cavalcante., Marcelo, Orlandi., Antônio, J. Ramirez., Edson, R. Leite., Juan, Andrés., Armando, Beltrán., José, A. Varela. & Elson, Longo. (2011). "A Joint Experimental and Theoretical Study on the Nanomorphology of CaWO₄ Crystals." *The Journal of Physical Chemistry C*, 115 (41), 20113-20119. doi: 10.1021/jp205764s.
- Lovette, Michael A., Andrea, Robben Browning., Derek, W. Griffin., Jacob, P. Sizemore., Ryan, C. Snyder. & Michael, F. Doherty. (2008). "Crystal Shape Engineering." *Industrial & Engineering Chemistry Research*, 47 (24), 9812-9833. doi: 10.1021/ie800900f.
- Lu, Wensheng. & Helmut, Schmidt. (2007). "Preparation and characterization of BaSnO₃ powders by hydrothermal synthesis from tin oxide hydrate gel." *Journal of Materials Science*, 42 (24), 10007-10013. doi: 10.1007/s10853-007-2069-9.
- Luo, Tao., Qiang-Qiang, Meng., Chao, Gao., Xin-Yao, Yu., Yong, Jia., Bai, Sun., Zhen, Jin., Qun-Xiang, Li., Jin-Huai, Liu. & Xing-Jiu, Huang. (2014). "Sub-20 nm-Fe₃O₄ square and circular nanoplates: synthesis and facet-dependent magnetic and electrochemical properties." *Chemical Communications*, 50 (100), 15952-15955. doi: 10.1039/C4CC06064D.
- Luo, Z., Li, H., Xia, J., Zhu, W., Guo, J. & Zhang, B. (2007). "Controlled synthesis of different morphologies of BaWO₄ crystals via a surfactant-assisted method." *J. Cryst. Growth.*, 300, 523-529.

- M.G.Brik, C. G. Ma. & Krasnenko, V. (2013). "First-principles calculations of the structural and electronic properties of the cubic CaZrO_3 (001) surfaces." *Surface Science*, 608, 146-153.
- Ma, Yanyun., Qin, Kuang., Zhiyuan, Jiang., Zhaoxiong, Xie., Rongbin, Huang. & Lansun, Zheng. (2008a). "Synthesis of Trisoctahedral Gold Nanocrystals with Exposed High-Index Facets by a Facile Chemical Method." *Angew. Chem*, 120, 9033–9036.
- Ma, Yanyun., Qin, Kuang., Zhiyuan, Jiang., Zhaoxiong, Xie., Rongbin, Huang. & Lansun, Zheng. (2008b). "Synthesis of Trisoctahedral Gold Nanocrystals with Exposed High-Index Facets by a Facile Chemical Method." *Angewandte Chemie International Edition*, 47 (46), 8901-8904. doi: 10.1002/anie.200802750.
- Marikutsa, Artem., Marina, Romyantseva., Alexander, Baranchikov. & Alexander, Gaskov. (2015). "Nanocrystalline BaSnO_3 as an Alternative Gas Sensor Material: Surface Reactivity and High Sensitivity to SO_2 ." *Materials*, 8 (9), 5311.
- Marks, L. D. & Peng, L. (2016). "Nanoparticle shape, thermodynamics and kinetics." *Journal of Physics: Condensed Matter*, 28 (5), 053001. doi: 10.1088/0953-8984/28/5/053001.
- Marks, L. D. (1983). "Modified Wulff constructions for twinned particles." *J. Crys. Growth*, 61, 556-566.
- Mattoussi, Hedi., Leonard, H. Radzilowski., Bashir, O. Dabbousi., Edwin, L. Thomas., Mounji, G. Bawendi. & Michael, F. Rubner. (1998). "Electroluminescence from heterostructures of poly(phenylene vinylene) and inorganic CdSe nanocrystals." *Journal of Applied Physics*, 83 (12), 7965-7974. doi: 10.1063/1.367978.
- Miao, Jianwei. & Bin, Liu. (2013). "Anatase TiO_2 microspheres with reactive {001} facets for improved photocatalytic activity." *RSC Advances*, 3 (4), 1222-1226. doi: 10.1039/C2RA22312K.
- Momma, K. & Izumi, F. (2011). "VESTA 3 for three-dimensional visualization of crystal, volumetric and morphology data." *J. Appl. Cryst.*, 44, 1272-1276.
- Monkhorst, H. J. & Pack, J. D. (1976). "Special points for Brillouin-zone integrations." *Phys. Rev. B: Condens. Matter.*, 13, 5188-5192.

- Moreira, Mário L., Juan, Andrés., Lourdes, Gracia., Armando, Beltrán., Luciano, A. Montoro., José, A. Varela. & Elson, Longo. (2013). "Quantum mechanical modeling of excited electronic states and their relationship to cathodoluminescence of BaZrO₃." *J. Appl. Phys.*, *114*, 043714 doi: 10.1063/1.4816247.
- Murugaraj, P., Kreuer, K. D., He, T., Schober, T. & Maier, J. (1997). "High proton conductivity in barium yttrium stannate Ba₂YSnO_{5.5}." *Solid State Ionics*, *98* (1–2), 1–6. doi: [http://dx.doi.org/10.1016/S0167-2738\(97\)00102-1](http://dx.doi.org/10.1016/S0167-2738(97)00102-1).
- Nogueira, I. C., Cavalcante, L. S., Pereira, P. F. S., de Jesus, M. M., Rivas Mercury, J. M., Batista, N. C., Li, M. S. & Longo, E. (2013). "Rietveld refinement, morphology and optical properties of (Ba_{1-x}Sr_x)MoO₄ crystals." *J. Appl. Cryst.*, *46*, 1434.
- Noguera, Claudine. (2000a). "Polar oxide surfaces." *J. Phys.: Condens. Matter*, *12*, R367–R41.
- Noguera, Claudine. (2000b). "Polar oxide surfaces." *J. Phys.: Condens. Matter*, *12*, R367–R341. doi: 10.1088/0953-8984/12/31/201.
- Noguera, Claudine. & Jacek, Goniakowski. (2013). "Polarity in Oxide Nano-objects." *Chemical Reviews*, *113* (6), 4073–4105. doi: 10.1021/cr3003032.
- Oliveira, M. C., Gracia, L., Nogueira, I. C., Gurgel, M. F. C., Mercury, J. M. R., Longo, E. & Andrés, J. (2016a). "Synthesis and morphological transformation of BaWO₄ crystals: Experimental and theoretical insights." *Ceram. Inter.*, *42*, 10913–10921.
- Oliveira, Marisa Carvalho., Lourdes, Gracia., Ic,amira C. Nogueira., Maria, Fernanda C. Gurgel., Jose, Manuel R. Mercury., Elson, Longo. & Juan, Andrés. (2016b). "On the morphology of BaMoO₄ crystals: A theoretical and experimental approach." *Cryst. Res. Technol*, *51*, 634–644.
- Ostrick, Bernhard., Maximilian, Fleischer. & Hans, Meixner. (1997). "High-Temperature Hall Measurements on BaSnO₃Ceramics." *Journal of the American Ceramic Society*, *80* (8), 2153–2156. doi: 10.1111/j.1151-2916.1997.tb03102.x.

- Pal, Jaya. & Tarasankar, Pal. (2015). "Faceted metal and metal oxide nanoparticles: design, fabrication and catalysis." *Nanoscale*, 7 (34), 14159-14190. doi: 10.1039/C5NR03395K.
- Pan, Jian., Gang, Liu., Gao, Qing Max Lu. & Hui-Ming, Cheng. (2011). "On the True Photoreactivity Order of {001}, {010}, and {101} Facets of Anatase TiO₂ Crystals." *Angewandte Chemie International Edition*, 50 (9), 2133-2137. doi: 10.1002/anie.201006057.
- Phuruangrat, A., Thongtem, T. & Thongtem, S. (2012). "Precipitate synthesis of BaMoO₄ and BaWO₄ nanoparticles at room temperature and their photoluminescence properties." *Superlattice. Microst.*, 52, 78-83.
- Piskorz, Witold., Joanna, Gryboś., Filip, Zasada., Piotr, Zapala., Sylvain, Cristol., Jean-François, Paul. & Zbigniew, Sojka. (2012). "Periodic DFT Study of the Tetragonal ZrO₂ Nanocrystals: Equilibrium Morphology Modeling and Atomistic Surface Hydration Thermodynamics." *The Journal of Physical Chemistry C*, 116 (36), 19307-19320. doi: 10.1021/jp3050059.
- Pojani, Ariana., Fabio, Finocchi. & Claudine, Noguera. (1999). "Polarity on the SrTiO₃ (111) and (110) surfaces." *Surface Science*, 442 (2), 179-198. doi: [http://dx.doi.org/10.1016/S0039-6028\(99\)00911-5](http://dx.doi.org/10.1016/S0039-6028(99)00911-5).
- Qi, Kezhen., Di, Li., Jiaqi, Fu., Lianjie, Zhu., Xiaochuan, Duan., Qing, Qin., Guichang, Wang. & Wenjun, Zheng. (2014). "Elucidating Ionic Liquid Environments That Affect the Morphology of TiO₂ Nanocrystals: A DFT+D Study." *The Journal of Physical Chemistry C*, 118 (40), 23320-23327. doi: 10.1021/jp503891s.
- Qiao, Zhen-An., Zili, Wu. & Sheng, Dai. (2013). "Shape-Controlled Ceria-based Nanostructures for Catalysis Applications." *ChemSusChem*, 6, 1821 – 1833 1. doi: 10.1002/cssc.v6.10/issuetoc.
- Rosa, I. L. V., Oliveira, M. C., Assis, M., Ferrer, M., André, R. S., Longo, E. & Gurgel, M. F. C. (2015). "A theoretical investigation of the structural and electronic properties of orthorhombic CaZrO₃." *Ceramics International*, 41 (2), 3069–3074.
- Roy, Nitish., Youngku, Sohn. & Debabrata, Pradhan. (2013). "Synergy of Low-Energy {101} and High-Energy {001} TiO₂ Crystal Facets for

- Enhanced Photocatalysis.” *ACS Nano*, 7 (3), 2532-2540. doi: 10.1021/nm305877v.
- Ryu, J. H., Yoon, J. W. & Shim, K. B. (2006). “Microwave-assisted synthesis of BaMoO₄ nanocrystallites by a citrate complex method and their anisotropic aggregation.” *J. Alloy Compd*, 413, 144-149.
- Sales, Herbert Bezerra., Valérie, Bouquet., Stéphanie, Députier., Sophie, Ollivier., Francis, Gouttefangeas., Maryline, Guilloux-Viry., Vincent, Dorcet., Ingrid, Távora Weber., Antônio, Gouveia de Souza. & Iêda, Maria Garcia dos Santos. (2014). “Sr_{1-x}Ba_xSnO₃ system applied in the photocatalytic discoloration of an azo-dye.” *Solid State Sciences*, 28, 67-73. doi: <http://dx.doi.org/10.1016/j.solidstatesciences.2013.12.007>.
- Sayle, Thi X. T., Beverley, J. Inkson., Ajay, Karakoti., Amit, Kumar., Marco, Molinari., Gunter, Mobus., Stephen, C. Parker., Sudipta, Seal. & Dean, C. Sayle. (2011). “Mechanical properties of ceria nanorods and nanochains; the effect of dislocations, grain-boundaries and oriented attachment.” *Nanoscale*, 3 (4), 1823-1837. doi: 10.1039/CONR00980F.
- Schlamp, M. C., Xiaogang, Peng. & Alivisatos, A. P. (1997). “Improved efficiencies in light emitting diodes made with CdSe(CdS) core/shell type nanocrystals and a semiconducting polymer.” *Journal of Applied Physics*, 82 (11), 5837-5842. doi: 10.1063/1.366452.
- Schmidt, C. & Ulrich, J. (2012). “Morphology prediction of crystals grown in the presence of impurities and solvents — An evaluation of the state of the art.” *Journal of Crystal Growth*, 353 (1), 168-173. doi: <http://dx.doi.org/10.1016/j.jcrysgro.2012.05.001>.
- Sczancoski, J. C., Cavalcante, L. S., Marana, N. L., Silva, R. O. D., Tranquilin, R. L., Joya, M. R., Pizani, P. S., Varela, J. A., Sambrano, J. R., Li, M. S., Longo, E. & Andrés, J. (2010). “Electronic structure and optical properties of BaMoO₄ powders.” *Curr. Appl. Phys*, 10, 614-624.
- Seyed-Razavi, Alireza., Ian, K. Snook. & Amanda, S. Barnard. (2010). “Origin of nanomorphology: does a complete theory of nanoparticle evolution exist?” *Journal of Materials Chemistry*, 20 (3), 416-421. doi: 10.1039/B915383G.

- Silva, Gabriela S., Lourdes, Gracia., Maria, T. Fabbro., Luis, P. Serejo., dos, Santos., Hector, Beltrán-Mir., Eloisa, Cordoncillo., Elson, Longo., & Juan, Andrés. (2016). "Theoretical and Experimental Insight on Ag_2CrO_4 Microcrystals: Synthesis, Characterization, and Photoluminescence Properties." *Inorganic Chemistry*, 55 (17), 8961-8970. doi: 10.1021/acs.inorgchem.6b01452.
- Sophia, Gustavo., Philippe, Baranek., Christian, Sarrazin., Michel, Réat. & Roberto, Dovesi. (2013). "First-principles study of the mechanisms of the pressure-induced dielectric anomalies in ferroelectric perovskites." *Phase Transitions*, 86 (11), 1069-1084. doi: 10.1080/01411594.2012.754442.
- Stoch, P., Szczerba, J., Lis, J., Madej, D. & Pędzich, Z. (2012). "Crystal structure and ab initio calculations of CaZrO_3 ." *Journal of the European Ceramic Society*, 32 (3), 665-670.
- Stroppa, Daniel G., Luciano, A. Montoro., Armando, Beltrán., Tiago, G. Conti., Rafael, O. da Silva., Juan, Andrés., Edson, R. Leite. & Antonio, J. Ramirez. (2011). "Dopant Segregation Analysis on $\text{Sb}:\text{SnO}_2$ Nanocrystals." *Chemistry – A European Journal*, 17 (41), 11515-11519. doi: 10.1002/chem.201100972.
- Stroppa, Daniel G., Luciano, A. Montoro., Antonio, Campello., Lourdes, Gracia., Armando, Beltran., Juan, Andres., Edson, R. Leite. & Antonio, J. Ramirez. (2014). "Prediction of dopant atom distribution on nanocrystals using thermodynamic arguments." *Physical Chemistry Chemical Physics*, 16 (3), 1089-1094. doi: 10.1039/C3CP53427H.
- Suleiman, Ibrahim A., Marian, W. Radny., Michael, J. Gladys., Phillip, V. Smith., John, C. Mackie., Eric, M. Kennedy. & Bogdan, Z. Dlugogorski. (2015). "Thermodynamic stability and structure of cuprous chloride surfaces: a DFT investigation." *Physical Chemistry Chemical Physics*, 17 (10), 7038-7045. doi: 10.1039/C4CP05340K.
- Tan, Chih-Shan., Shih-Chen, Hsu., Wei-Hong, Ke., Lih-Juann, Chen. & Michael, H. Huang. (2015). "Facet-Dependent Electrical Conductivity Properties of Cu_2O Crystals." *Nano Letters*, 15 (3), 2155-2160. doi: 10.1021/acs.nanolett.5b00150.

- Tan, Joyce Pei Ying., Hui, Ru Tan., Chris, Boothroyd., Yong, Lim Foo., Chao Bin, He. & Ming, Lin. (2011). "Three-Dimensional Structure of CeO₂ Nanocrystals." *The Journal of Physical Chemistry C*, 115 (9), 3544-3551. doi: 10.1021/jp1122097.
- Tao, Andrea R., Susan, Habas. & Peidong, Yang. (2008). "Shape Control of Colloidal Metal Nanocrystals." *Small*, 4 (3), 310-325. doi: 10.1002/sml.200701295.
- Tian, N., Zhou, Z. Y., Sun, S. G., Ding, Y. & Wang, Z. L. (2007). "Synthesis of Tetrahedral Platinum Nanocrystals with High-Index Facets and High Electro-Oxidation Activity." *Science*, 316 (5825), 732-735. doi: 10.1126/science.1140484.
- Tian, Na., Zhi-You, Zhou. & Shi-Gang, Sun. (2008). "Platinum Metal Catalysts of High-Index Surfaces: From Single-Crystal Planes to Electrochemically Shape-Controlled Nanoparticles." *The Journal of Physical Chemistry C*, 112 (50), 19801-19817. doi: 10.1021/jp804051e.
- Tian, Na., Zhi-You, Zhou. & Shi-Gang, Sun. (2009). "Electrochemical preparation of Pd nanorods with high-index facets." *Chemical Communications*, (12), 1502-1504. doi: 10.1039/B819751B.
- Tompsett, David A., Steve, C. Parker., Peter, G. Bruce. & Saiful Islam, M. (2013). "Nanostructuring of β -MnO₂: The Important Role of Surface to Bulk Ion Migration." *Chemistry of Materials*, 25 (4), 536-541. doi: 10.1021/cm303295f.
- Valenzano, L., Torres, F. J., Doll, K., Pascale, F., Zicovich-Wilson, C. M. & Dovesi, R. (2006). "Ab Initio study of the vibrational spectrum and related properties of crystalline compounds; the case of CaCO₃ calcite." *Z. Phys. Chem.*, 220, 893-912.
- Van Santen, Rutger A. (2009). "Complementary Structure Sensitive and Insensitive Catalytic Relationships." *Accounts of Chemical Research*, 42 (1), 57-66. doi: 10.1021/ar800022m.
- Vantomme, Aurélien., Zhong-Yong, Yuan., Gaohui, Du. & Bao-Lian, Su. (2005). "Surfactant-Assisted Large-Scale Preparation of Crystalline CeO₂ Nanorods." *Langmuir*, 21 (3), 1132-1135. doi: 10.1021/la047751p.

- Wander, A., Schedin, F., Steadman, P., Norris, A., McGrath, R., Turner, T. S., Thornton, G. & Harrison, N. M. (2001). "Stability of Polar Oxide Surfaces." *Physical Review Letters*, 86 (17), 3811-3814.
- Wang, Chao., Hideo, Daimon., Taigo, Onodera., Tetsunori, Koda. & Shouheng, Sun. (2008). "A General Approach to the Size- and Shape-Controlled Synthesis of Platinum Nanoparticles and Their Catalytic Reduction of Oxygen." *Angewandte Chemie International Edition*, 47 (19), 3588-3591. doi: 10.1002/anie.200800073.
- Wang, Lan., Ling, Zang., Jincan, Zhao. & Chuanyi, Wang. (2012). "Green synthesis of shape-defined anatase TiO₂ nanocrystals wholly exposed with {001} and {100} facets." *Chemical Communications*, 48 (96), 11736-11738. doi: 10.1039/C2CC36005E.
- Wang, Lei., Haibo, Li., Shuling, Xu., Qiaoli, Yue. & Jifeng, Liu. (2014). "Facet-dependent optical properties of nanostructured ZnO." *Materials Chemistry and Physics*, 147 (3), 1134-1139. doi: 10.1016/j.matchemphys.2014.06.069.
- Wang, Liangbing., Songtao, Zhao., Chenxuan, Liu., Chen, Li., Xu, Li., Hongliang, Li., Youcheng, Wang., Chao, Ma., Zhenyu, Li. & Jie, Zeng. (2015). "Aerobic Oxidation of Cyclohexane on Catalysts Based on Twinned and Single-Crystal Au₇₅Pd₂₅Bimetallic Nanocrystals." *Nano Letters*, 15 (5), 2875-2880. doi: 10.1021/nl5045132.
- Wang, Shengping., Lifang, Zhao., Wei, Wang., Yujun, Zhao., Guanglin, Zhang., Xinbin, Ma. & Jinlong, Gong. (2013). "Morphology control of ceria nanocrystals for catalytic conversion of CO₂ with methanol." *Nanoscale*, 5 (12), 5582-5588. doi: 10.1039/C3NR00831B.
- Wang, Wanjun., Shijing, Liang., Kaining, Ding., Jinhong, Bi., Jimmy, C. Yu., Po, Keung Wong. & Ling, Wu. (2014). "Microwave hydrothermal synthesis of MSnO₃ (M²⁺=Ca²⁺, Sr²⁺, Ba²⁺): effect of M²⁺ on crystal structure and photocatalytic properties." *Journal of Materials Science*, 49 (4), 1893-1902. doi: 10.1007/s10853-013-7880-x.
- Wang, X., Xu, H., Wang, H. & Yan, H. (2005). "Morphology-controlled BaWO₄ powders via a template-free precipitation technique." *J. Cryst. Growth*, 284, 254-261.

- Wang, Xue., Xiguang, Han., Shuifen, Xie., Qin, Kuang., Yaqi, Jiang., Subing, Zhang., Xiaoliang, Mu., Guangxu, Chen., Zhaoxiong, Xie. & Lansun, Zheng. (2012). "Controlled Synthesis and Enhanced Catalytic and Gas-Sensing Properties of Tin Dioxide Nanoparticles with Exposed High-Energy Facets." *Chemistry – A European Journal*, 18 (8), 2283-2289. doi: 10.1002/chem.201103280.
- Wang, Yanzhong., Anthony, Chesnaud., Emile, Bevillon. & Guilhem, Dezanneau. (2012). "Properties of Y-doped BaSnO₃ proton conductors." *Solid State Ionics*, 214, 45-55. doi: <http://dx.doi.org/10.1016/j.ssi.2012.02.045>.
- Wang, Zhenni., Guang, Yang., Zhaorui, Zhang., Mingshang, Jin. & Yadong, Yin. (2016). "Selectivity on Etching: Creation of High-Energy Facets on Copper Nanocrystals for CO₂ Electrochemical Reduction." *ACS Nano*, 10 (4), 4559-4564. doi: 10.1021/acsnano.6b00602.
- Whewell, William. (1847). *The Philosophy of the Inductive Sciences Founded Upon their History*. New York, London: Johnson Reprint Corporation.
- Whiteside, Alexander., Craig, A. J. Fisher., Stephen, C. Parker. & Saiful Islam, M. (2014). "Particle shapes and surface structures of olivine NaFePO₄ in comparison to LiFePO₄." *Physical Chemistry Chemical Physics*, 16 (39), 21788-21794. doi: 10.1039/C4CP02356K.
- Wu, Binghui. & Nanfeng, Zheng. (2013). "Surface and interface control of noble metal nanocrystals for catalytic and electrocatalytic applications." *Nano Today*, 8 (2), 168-197. doi: 10.1016/j.nantod.2013.02.006.
- Wu, X., Du, J., Li, H., Zhang, M., Xi, B., Fan, H., Zhu, Y. & Qian, Y. (2007). "Aqueous mineralization process to synthesize uniform shuttle-like BaMoO₄ microcrystals at room temperature." *J. Solid State Chem.*, 180, 3288-3295.
- Wulff, G. (1901). "On the question of speed of growth and dissolution of crystal surfaces." *Kristallogr. Miner*, 34, 449-530.
- Xiao, Xiaoling., Xiangfeng, Liu., Hu, Zhao., Dongfeng, Chen., Fengzhen, Liu., Junhui, Xiang., Zhongbo, Hu. & Yadong, Li. (2012). "Facile

- Shape Control of Co_3O_4 and the Effect of the Crystal Plane on Electrochemical Performance." *Advanced Materials*, 24 (42), 5762-5766. doi: 10.1002/adma.201202271.
- Xie, B., Wu, Y., Jiang, Y., Li, F., Wu, J., Yuan, S., Yu, W. & Qian, Y. (2002). "Shape-controlled synthesis of BaWO_4 crystals under different surfactants." *J. Crys. Growth*, 235, 283-286.
- Xie, Xiaowei., Yong, Li., Zhi-Quan, Liu., Masatake, Haruta. & Wenjie, Shen. (2009). "Low-temperature oxidation of CO catalysed by Co_3O_4 nanorods." *Nature*, 458 (7239), 746-749. doi: 10.1038/nature07877.
- Xu, Hua., Pakpoom, Reunchan., Shuxin, Ouyang., Hua, Tong., Naoto, Umezawa., Tetsuya, Kako. & Jinhua, Ye. (2013). "Anatase TiO_2 Single Crystals Exposed with High-Reactive {111} Facets Toward Efficient H_2 Evolution." *Chemistry of Materials*, 25 (3), 405-411. doi: 10.1021/cm303502b.
- Xu, Tao., Xi, Zhou., Zhiyuan, Jiang., Qin, Kuang., Zhaoxiong, Xie. & Lansun, Zheng. (2009). "Syntheses of Nano/Submicrostructured Metal Oxides with All Polar Surfaces Exposed via a Molten Salt Route." *Crystal Growth & Design*, 9 (1), 192-196. doi: 10.1021/cg8002096.
- Yang, Hua Gui., Gang, Liu., Shi, Zhang Qiao., Cheng Hua, Sun., Yong, Gang Jin., Sean, Campbell Smith., Jin, Zou., Hui, Ming Cheng. & Gao, Qing Lu. (2009). "Solvothermal Synthesis and Photoreactivity of Anatase TiO_2 Nanosheets with Dominant {001} Facets." *Journal of the American Chemical Society*, 131 (11), 4078-4083. doi: 10.1021/ja808790p.
- Yang, Hua Gui., Cheng, Hua Sun., Shi, Zhang Qiao., Jin, Zou., Gang, Liu., Sean Campbell, Smith., Hui, Ming Cheng. & Gao, Qing Lu. (2008). "Anatase TiO_2 single crystals with a large percentage of reactive facets." *Nature*, 453 (7195), 638-641. doi: 10.1038/nature06964.
- Yu, Xin-Yao., Qiang-Qiang, Meng., Tao, Luo., Yong, Jia., Bai, Sun., Qun-Xiang, Li., Jin-Huai, Liu. & Xing-Jiu, Huang. (2013). "Facet-dependent electrochemical properties of Co_3O_4 nanocrystals toward heavy metal ions." *Scientific Reports*, 3, 2886. doi: 10.1038/srep02886.<http://www.nature.com/articles/srep02886#supplementary-information>.

- Zaera, Francisco. (2013). "Shape-Controlled Nanostructures in Heterogeneous Catalysis." *ChemSusChem*, 6, 1797 – 1820. doi: 10.1002/cssc.20130039810.1002/cssc.v6.10/issuetoc.
- Zhang, Da., Jing, Li., Qigang, Wang. & Qingsheng, Wu. (2013). "High {001} facets dominated BiOBr lamellas: facile hydrolysis preparation and selective visible-light photocatalytic activity." *Journal of Materials Chemistry A*, 1 (30), 8622-8629. doi: 10.1039/C3TA11390F.
- Zhang, Luo., Xiaoyan, Wang., Zhongju, Zhang. & Xin, Wang. (2017). "Effect of surface chemistry on morphology evolution of LaPO₄: Experiment and density functional theory calculations." *Computational Materials Science*, 127, 22-28. doi: <http://dx.doi.org/10.1016/j.commatsci.2016.10.024>.
- Zheng, Zhaoke., Baibiao, Huang., Jibao, Lu., Xiaoyan, Qin., Xiaoyang, Zhang. & Ying, Dai. (2011). "Hierarchical TiO₂ Microspheres: Synergetic Effect of {001} and {101} Facets for Enhanced Photocatalytic Activity." *Chemistry - A European Journal*, 17 (52), 15032-15038. doi: 10.1002/chem.201101466.
- Zhou, Kebin. & Yadong, Li. (2012). "Catalysis Based on Nanocrystals with Well-Defined Facets." *Angewandte Chemie International Edition*, 51 (3), 602-613. doi: 10.1002/anie.201102619.
- Zhou, Zhi-You., Na, Tian., Jun-Tao, Li., Ian, Broadwell. & Shi-Gang, Sun. (2011). "Nanomaterials of high surface energy with exceptional properties in catalysis and energy storage." *Chemical Society Reviews*, 40 (7), 4167-4185. doi: 10.1039/C0CS00176G.
- Zhu, Liangzheng., Zhipeng, Shao., Jiajiu, Ye., Xuhui, Zhang., Xu, Pan. & Songyuan, Dai. (2016). "Mesoporous BaSnO₃ layer based perovskite solar cells." *Chemical Communications*, 52 (5), 970-973. doi: 10.1039/C5CC08156D.
- Zhuang, Houlong., Alexander, J. Tkalych. & Emily, A. Carter. (2016). "Surface Energy as a Descriptor of Catalytic Activity." *The Journal of Physical Chemistry C*, 120 (41), 23698-23706. doi: 10.1021/acs.jpcc.6b09687.

In: Crystal Growth
Editors: J. Li, J. Li and Y. Chu

ISBN: 978-1-53612-203-9
© 2017 Nova Science Publishers, Inc.

Chapter 4

**GROWTH BEHAVIORS OF CaCO_3
POLYMORPHS UNDER VARIOUS
ENVIRONMENTAL CONDITIONS**

*Clifford Y. Tai**, *Meng-Chieh Lin*, *Su-Chun How*,
Yu-Hong Cheng and *Steven S.-S. Wang**

Department of Chemical Engineering
National Taiwan University, Taipei, Taiwan

ABSTRACT

Using the constant-composition technique, in which two autotitrators were applied for maintaining the composition and pH constant in a growth process, the growth rates of calcium carbonate polymorphs, i.e., calcite and aragonite, were measured at different operating conditions. The conditions were chosen as closely as possible to that in the magnetic

* Corresponding Author : Steven S.-S. Wang, Ph.D. Department of Chemical Engineering National Taiwan University No.1, Sec.4, Roosevelt Rd, Taipei 10617, Taiwan Voice: +886-2-3366-5870 Fax: +886-2-2362-3040 Email: sswang@ntu.edu.tw.

Corresponding Author: Clifford Y. Tai, Ph.D. Department of Chemical Engineering National Taiwan University No.1, Sec.4, Roosevelt Rd, Taipei 10617, Taiwan Voice: +886-2-2362-0832 Fax: +886-2-2362-3040 Email: cytai@ntu.edu.tw.

water- treatment for preventing scale formation. The transient effects of magnetic field on the growth of CaCO_3 polymorphs were presented first. Then, the steady growth rates of calcite and aragonite were measured in the absence/presence of magnetic field at various conditions as follows: temperature between 25°C and 40°C , pH between 8.0 and 10.0, activity ratio of $\text{Ca}^{2+}/\text{CO}_3^{2-}$ (R) between 0.2 and 6.0, impurity concentration of Fe^{2+} and Sr^{2+} between 0 and 2.0 ppm. The growth rates of polymorphs responded differently to a change in operating variables. The results were most surprising with regard to the effects of impurities. In addition, a hypothesis of cluster- transformation mechanism was proposed to explain the experimental results obtained in our laboratory and some cases reported in the literature.

NOTATION

$a_{\text{Ca}^{2+}}$	activity of Ca^{2+} , mol/L
$a_{\text{CO}_3^{2-}}$	activity of CO_3^{2-} , mol/L
C_i	concentration of i component, mol/L
$[\text{Ca}^{2+}]_a$	Ca^{2+} concentration of the original solution in the storage tank, mol/L
$[\text{Ca}^{2+}]_o$	Ca^{2+} concentration of the titrated solution in the dosimat, mol/L
I	ionic strength, kmol/m^3
K_{sp}	solubility product, mol^2/L^2
L	characteristic length of seed crystals, m
M	molecular weight of CaCO_3
R	activity ratio, $a_{\text{Ca}^{2+}}/a_{\text{CO}_3^{2-}}$
G	crystal growth rate, m/s
T	temperature, $^\circ\text{C}$
T Ca	total calcium content, ppm
t	growth time, s
V_a	volume of titration solution, mL
W	total weight of seed crystals, g
γ_2	activity coefficient
σ_i	relative supersaturation of i component

INTRODUCTION

Magnetic water treatment for scale prevention of heat exchanger has been around for about a century. However, this technique has become a controversial issue because effective and ineffective cases have been reported and the working mechanism of magnetic effect has not been confirmed [1]. The major constituent of the scale is calcite, which is one of the CaCO₃ polymorphs. The other two polymorphs commonly encountered are aragonite and vaterite. Calcite is the most stable form at room temperature, and vaterite converts to calcite easily under certain environments. Anti-scale effects can be judged from the two steps of solid formation, i.e., nucleation and crystal growth. The first deposition of scale on a fresh surface is caused by nucleation, then further deposition of scale is due to crystal growth. From this point of view, any measure that suppresses nucleation and crystal growth of calcite is considered to be effective for anti-scaling. To explore the effect of magnetic field, a study on the crystallization of CaCO₃ under the common operating conditions existing in a heat exchanger of water cooling system should be carried out first in the absence and then in the presence of magnetic field. Usually, the cooling water with a pH value of 9.0 or lower contains impurities and its temperature is between 40°C and 50°C when contacting with the exchanger wall. Thus, the effects of pH, temperature, magnetic field, and impurity on the crystallization of CaCO₃ should be investigated systematically in order to reach a solid conclusion.

Most earlier studies of CaCO₃ crystallization are on crystal formation, and only a few on crystal growth. The temperature effect on the formation of CaCO₃ polymorphs was first investigated by Wray and Daniels in 1957 [2]. They prepared the crystals of CaCO₃ polymorphs by adding a Ca(NO₃)₂ solution to a Na₂CO₃ solution at various temperatures. Aragonite crystals dominated at the very onset of nucleation, when the operating temperature was higher than 45°C. The formation of aragonite favored at high temperature was also confirmed by Tai and Chen, using the constant-composition method [3]. As far as the magnetic effect is concerned, a magnetic field would favor the formation of aragonite [4, 5]. For example,

Kobe et al. [5] applied a magnetic field with intensity that varied from 4,000 Gauss to 12,200 Gauss to treat a circulating $\text{CaCO}_3\text{-Ca}(\text{HCO}_3)_2\text{-H}_2\text{O}$ equilibrium system for 8 h. They found that the portion of aragonite increased with the intensity of magnetic field. The presence of impurity in a crystallization solution has long been considered as a nasty problem, even at a concentration of ppm level, due to its possible influence on solubility, nucleation rate, crystal growth rate, crystal habit, and crystal morphology [6]. In an early study, Söhnel and Mullin [7] investigated the effect of cation on the morphology and habit of CaCO_3 crystal and established a general trend according to the ion radius. An ion with a radius smaller than Ca^{2+} , such as Mg^{2+} , Fe^{2+} , and Cu^{2+} , would favor the formation of aragonite. On the other hand, Mn^{2+} , Sr^{2+} , and Ba^{2+} with larger radius favored calcite. In the succeeding studies on cation impurities, Katz and his co-workers [8, 9] reported that Fe^{2+} , Fe^{3+} , and Cu^{2+} all inhibited calcite growth.

In view of the experimental facts mentioned above, we decided to study the crystal growth of calcite and aragonite under various environments. The experimental technique used was the constant-composition method, which was originally designed by Tomson and Nancollas [10] to study the crystallization of sparingly soluble salts and was adopted in our laboratory for investigating the polymorphism of CaCO_3 precipitated in a constant-composition environment [3], and the growth kinetics of calcite [11-13]. Several operating variables, which include temperature, impurity type, and impurity concentration, did significantly affect the crystal formation and crystal growth of CaCO_3 . In addition, solution supersaturation (σ), pH value, and activity ratio of $\text{Ca}^{2+}/\text{CO}_3^{2-}$ (R) also have a profound influence. Later, a magnetic device was incorporated into the growth system to explore the magnetic effect and its interaction with other operating variables in the crystal growth of calcite and aragonite [14-20]. Because different polymorphs precipitated in different environments and the growth rate of polymorphs responded differently to a change in operating variable, a cluster-transformation mechanism was proposed to explain the temperature and magnetic effects [16, 17] based on the following information of cluster formation.

The formation of clusters in a supersaturated solution has long been recognized. For nucleation to occur, it is presumed that a sequence of bimolecular addition gives rise to clusters until the clusters exceed a critical size to be called nuclei, which is a function of supersaturation. Then the nuclei become crystals by growth [21]. This mechanism of primary nucleation was proposed when there was no instrument available for detecting the existence of clusters. However, the concept of cluster formation has been accepted since then. To identify the existence of clusters using Raman spectroscopy, the pioneer work of Frost and James [22] for detecting the degree of association of ions and molecules in aqueous solution was followed by Larson and his co-workers [23, 24]. They would be able to differentiate between low-order species (monomers, dimers) and high-order species (clusters) in a supersaturated solution. The clusters were also believed to be the precursor of nuclei in the contact nucleation, which is one type of secondary nucleation. McCabe and his co-workers [25, 26] performed the experiment of contact nucleation, in which a solid rod was used to contact the surface of a growing seed crystal placed in a flowing supersaturated solution, so as to generate secondary nuclei. They proposed a hypothesis that the clusters gathering in the adsorption layer near the crystal surface and tending to incorporate into the crystal lattice were detached from the seed crystal. Then, the portion of dropped clusters, that were larger than the nuclei corresponding to the surrounding supersaturation, grew and became crystals. Using the technique fashioned after that of Clontz and McCabe [25], Denk and Botsaris [27] studied contact nucleation of sodium chlorate crystal, which crystallizes in two enantiomorphic forms. They found that all nuclei produced by contact had the same form as the parent seed crystal, yet each form of nearly 50% was generated without seeding, i.e., nuclei induced by primary nucleation. In the literature, most studies of contact (secondary) nucleation were on the readily-soluble salt. Tai et al. [28] found that secondary nuclei of calcite, which is one of the sparingly-soluble salts, were generated by contact mechanism, when calcite seeds larger than 165 μm were suspended in a supersaturated solution. Important features of contact nucleation for readily-soluble and sparingly-soluble crystals were quite similar, such as

more crystals produced at higher supersaturation and magma density. In addition, Gebuer et al. [29] demonstrated that calcium carbonate solution contained stable prenucleation ion clusters, even in an undersaturated solution. Although they did not differentiate the clusters of CaCO_3 polymorphs, they concluded that prenucleation-stage clusters exhibited “solute character”.

This communication summarized the growth-rate data of CaCO_3 polymorphs collected in our laboratory, either published or unrevealed, using the constant-composition method with an aim to give a more complete picture of magnetic effects and the interaction of magnetic field with other operating variables, such as temperature (T), acidity (pH), activity ratio of $\text{Ca}^{2+}/\text{CO}_3^{2-}$ (R), and impurity. In order to explain the growth-rate variation caused by the environmental conditions, a hypothesis of cluster-transformation mechanism, i.e., calcite-like and aragonite-like clusters are interchangeable depending on the environmental conditions, will be presented first in the section of Result and Discussion. The hypothesis is able to give a satisfactory explanation on most experimental results. However, a few cases that include the impurity effect remain unclear. In addition, it should be noticed that there is lacking of instrument to identify a cluster form existing in a supersaturated solution at the present time.

EXPERIMENT SECTION

Metastable Region of CaCO_3

Metastable region of a readily-soluble salt is defined as the area between supersolubility curve and solubility curve on the concentration-temperature diagram. In this region spontaneous nucleation is improbable; however, growth of seed crystals would occur. The metastable region of a sparingly-soluble salt, on the other hand, should be plotted on a precipitation diagram, i.e., pC_A vs. pC_B , where $pC_i = -\log C_i$ and C_i is the

concentration of reacting ion [30]. The supersolubility curve is not well-defined as that of solubility curve. Its position in the diagram is affected by many ways, such as the intensity of agitation, the method of detecting the presence of solid phase, the time that elapses between the establishment of supersaturation and the onset of nucleation, and the rate at which supersaturation is generated. Following this definition, Tai et al. [31] mixed CaCl₂ and Na₂CO₃ solutions of various concentrations directly and then stirred the solutions for 2 h under constant temperature (25°C) and constant pH (8.5, 9.5, and 10.5, respectively) to find the supersolubility curve, which was the boundaries that the mixed solutions remained clear and became turbid. By plotting $pa_{Ca^{2+}}$ vs. $pa_{CO_3^{2-}}$, where a_i was the activity of reacting ions of the turbid solutions, the solubility and supersolubility curves were straight and parallel, irrespective of pH values. The subsequent growth experiments were performed at supersaturations within the metastable region not too far from the solubility curve. Although a few experimental runs were lasted longer than 2 h or were operated at different temperatures that might change the width of metastable region, no nuclei were ever detected during the course of the growth processes.

Apparatus and Procedures

The key to success for measuring the growth rates of CaCO₃ polymorphs was the constant-composition technique, an original concept proposed by Tomson and Nancollas [10]. In the course of this research project, the crystallizer adopted was either a fluidized bed or a stirred tank. The latter was used to study the temperature effect due to its ease of temperature control. There was; however, a disadvantage associated with the operation of stirred tank in which vigorous agitation caused a contact between seed crystals and agitator to give a narrower metastable region. It meant that nucleation would occur at a lower supersaturation and pH. Two

kinds of magnetic device, i.e., a commercial magnetic water-treatment device (Descal A-Matic DC-1) and a pair of permanent magnet (MagnGen Medel 100) were used in this study. The detailed structure of the two devices are illustrated elsewhere [16]. The effective field intensity was 1800 Gauss for the former, and a field intensity of 1265 Gauss for the latter, which was only used in the fluidized-bed experiment. Both of the magnetic fields induced by the two magnetic devices had a profound influence on crystal growth of the CaCO_3 polymorphs.

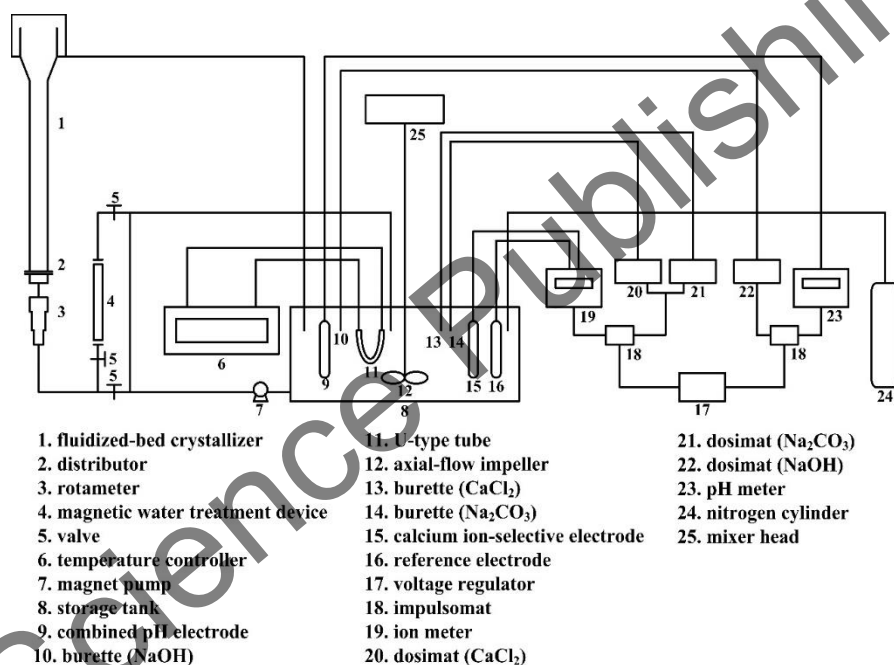


Figure 1. Schematic diagram of equipment set-up for measuring the crystal growth of CaCO_3 polymorphs, according to the constant-composition concept.

The apparatus used in the experiment is shown in Figure 1, in which every component of the set-up is numbered, using fluidized bed as the crystallizer. A detailed description of the set-up can be referred to a previous paper [16]. The set-up was designed for its versatility. When the temperature effect was studied, the fluidized bed (1) was removed and the storage tank (8) was utilized as the stirred-tank crystallizer. The constant

temperature was maintained by a U-type tube (11) connected to a temperature controller (6). To investigate the effect of operating variables other than magnetic field, the magnetic device (4) can be isolated from the set-up simply by closing the inlet and outlet valves (5) in the front and at the rear of the magnetic device. The advantage of using the constant-composition method were in two aspects, i.e., the solution pH and composition could be kept constant during a growth run by means of autotitrators and the growth time for an experimental run could be shortened to a few hours by evaluating the growth rate from the titration curve, which was recorded automatically. The autotitrator for pH control is a combination of a pH-meter (23) a dosimat (22), and an impulsomat (18), and for composition control is a combination of a calcium ion meter (19), two dosimats (20 and 21), and an impulsomat (18). The CaCl₂ and Na₂CO₃ solutions were added simultaneously. The constant composition was checked at the end of every single run and occasionally during the growth process, using an inductively coupled plasma (ICP) spectrometer or an atomic absorption (AA) spectrometer. A typical calcium concentration profile is shown in Figure 2, in which σ is the supersaturation of solution,

R is the activity ratio ($a_{Ca^{2+}}/a_{CO_3^{2-}}$), and I is the ionic strength. If the calcium concentration was 0.3 ppm away from the setting point, the titration curve was discarded. The titration curve should be a straight line to ensure a steady growth, and then the slope of the titration curve was used to evaluate the crystal growth rate according to the following equation, which was derived by Tai et al. [17]:

$$G = \frac{LM}{3W} ([Ca^{2+}]_a - [Ca^{2+}]_0) \frac{dV_a}{dt} \quad (1)$$

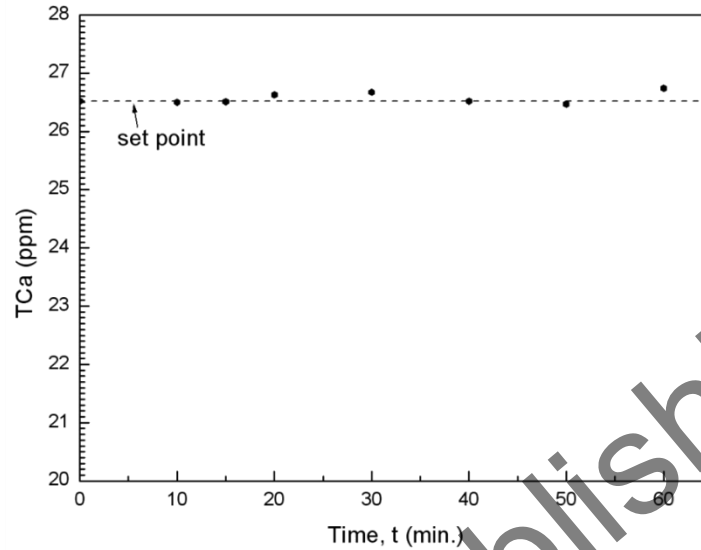


Figure 2. Calcium concentration profile showing constant composition of the supersaturated solution during a growth process for pH = 9.0, R = 5.54, $\sigma = 1.0$, I = 0.018M, and T = 25°C.

Where G is the growth rate, W is the total mass of seed crystals, L is the characteristic length of seed crystals, M is the molecular weight of CaCO₃, V_a is the volume of titrated solution, t is the growth time, and [Ca²⁺]_o and [Ca²⁺]_a are the concentrations of the Ca²⁺ of the original solution in the storage tank and the titrated solution in the dosimat, respectively.

Expressions of Supersaturation

The relative supersaturation σ was used as the driving force for crystal growth.

$$\sigma = \sqrt{(\gamma_2^2 [Ca^{2+}] [CO_3^{2-}]) / K_{sp}} - 1 \quad (2)$$

A computer program, containing mass-action equations, mass balance equations, charge-balance equation, and the modified Debye-Hückle equation, was used to calculate the relative supersaturation [28]. The equilibrium constants in the mass-action equations, the solubility product K_{sp} , and the activity coefficient γ_2 were corrected for temperature as presented in a previous study [17]. The solubility product of aragonite is different from that of calcite, so σ_{cal} is not equal to σ_{ara} for the same solution concentration. For example, when σ_{cal} is 1.0 at 25°C, the corresponding σ_{ara} is 0.73.

Preparation of Seed Crystals

Three types of calcite seed have been chosen at the beginning of this study, i.e., sand covered with calcite (seed I) taken from a pellet reactor for testing water softening, natural calcite mineral (seed II), and egg shell (seed III). The three seeds were confirmed to be calcite by XRD diffraction. At the early stage of growth experiment, the growth-rate data were not reproducible, not only between seeds of different sources, but also between seeds of the same kind. After examining the surface of seed crystals before and after growth and the shape of titration curves, we realized that the seed crystals needed curing for at least 5 h in order to obtain reproducible data for the same kind of seed. The surface structure of calcite seeds before and after curing are presented in Figure 3. The surfaces of the three calcite seeds are quite different before curing; however, they are covered with rhombohedral calcite particles after curing. The size of rhombohedron is similar for seed I and seed II, but quite larger for seed III. This is due to the difference in composition on the seed surface. The seed surface is nearly pure calcite for seed I and seed II, and the egg shell (seed III) contains several percent of protein matrix besides calcite. The growth rates of the seeds from different sources at various levels of supersaturation are shown in Figure 4 under the following conditions: pH = 9.0, R = 5.54, I = 0.018 M, and T = 25°C. The growth rates of seed I and seed II are quite similar, yet the growth rates of seed III are almost off by 50%. This is due

to the difference in the size of rhombohedral particles adhered to the seed surfaces. The particle sizes on seed I and seed II are almost the same (Figures 3(b) and 3(d)), but quite larger for seed III shown in Figure 3(f). Recall that the linear growth rate defined in this study is the increment of solute volume deposited on the rhombohedral calcites divided by the surface area of the uncured seed crystals. Because the surface area available for growth is related to the particle size of the adhered calcites, it is understood that the growth rates of seed I and seed II are almost equal and the growth rate of seed III is much lower.

As far as the aragonite seed is concerned, one seed of natural aragonite from Morocco was used. The photographs of aragonite seed surface at different curing stages are shown in Figure 5. It should be noted that the magnetic device was applied before and during the growth process. The premagnetization time required for reproducing growth data was about 20 h. The premagnetization of solution for aragonite growth was essential, otherwise the aragonite seeds would not grow at temperatures lower than 25°C. An explanation of this phenomenon will be presented in the section of Results and Discussion. Figures 5(a), 5(b), 5(c), and 5(d) show the seed surfaces of uncured aragonite, after 5 h curing, after 10 h curing, and after several experimental runs, respectively. It should be noted that the scale bar is 10 μ m for Figure 5(b) instead of 1 μ m for the others. The surface of uncured aragonite is rather flat, with some crystal dusts adhered to it. When the curing process started, acicular aragonite particles grew on the seed surface gradually, then the acicular particles became larger and larger as growth process proceeded. Since the growth rate measured in this study was the increment of solution volume deposited on the acicular crystals divided by the surface area of the uncured crystals, the larger particles had less surface per unit area of the uncured crystal and thus less growth rate. To overcome this problem, the grown aragonite seeds were replaced by a fresh batch of cured seed after five runs. The reproducibility of growth-rate data was checked using this procedure [19]. The same procedure of seed replacement was applied to the calcite-growth experiment either.

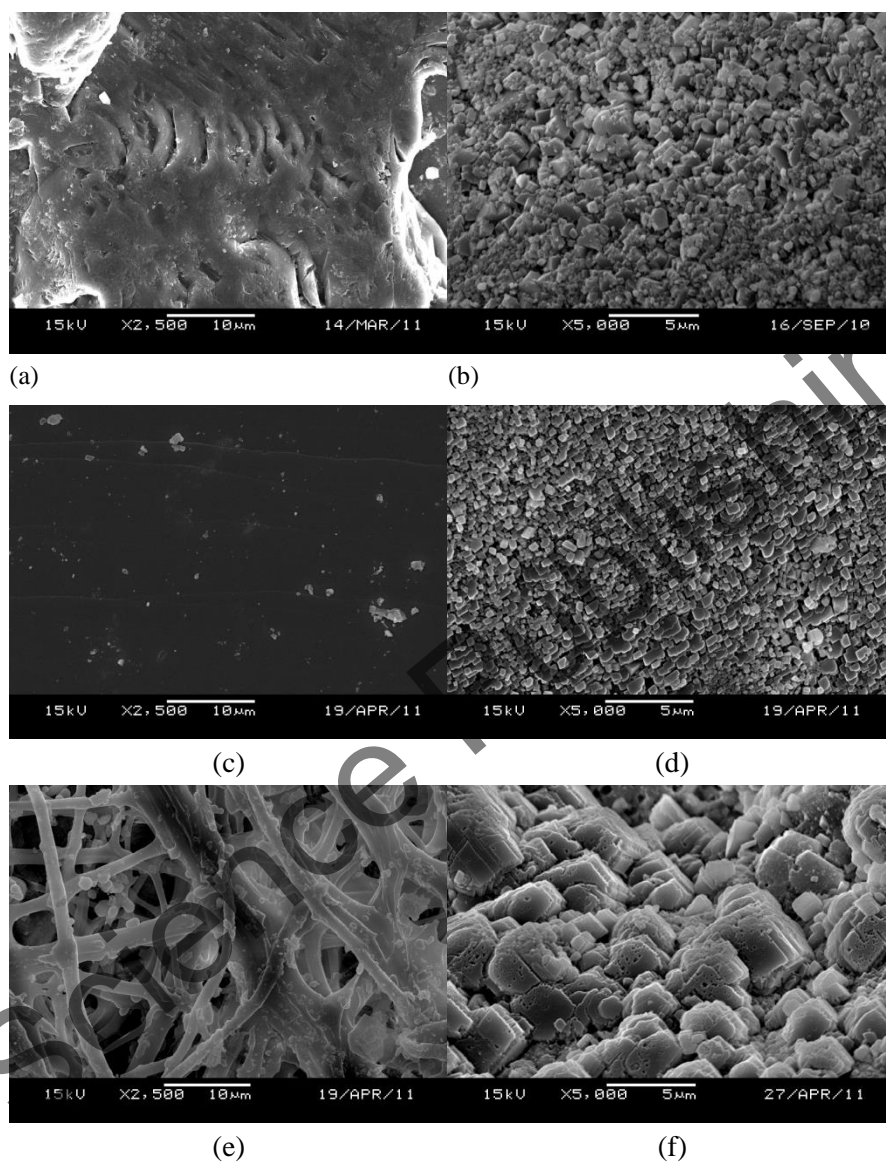


Figure 3. The calcite crystal surfaces of different sources.

- (a) Sand covered with calcite (seed I) before curing.
- (b) Sand covered with calcite (seed I) after curing.
- (c) Natural calcite (seed II) before curing.
- (d) Natural calcite (seed II) after curing.
- (e) Egg shell (seed III) before curing.
- (f) Egg shell (seed III) after curing.

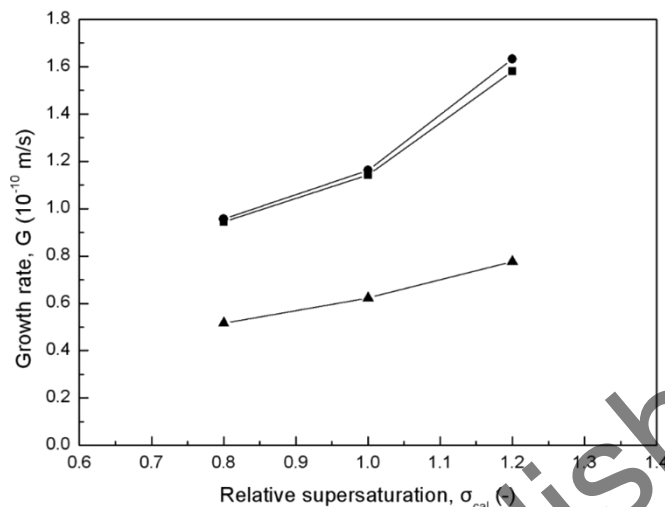


Figure 4. Comparison of the growth rates of calcite from three different sources under the same solution conditions: pH = 9.0, R = 5.54, I = 0.018M, and T = 25°C. (■) sand covered with calcite (seed I); (●) natural calcite (seed II); (□▲) egg shell (seed III).

RESULTS AND DISCUSSION

Hypothesis of the Cluster- Transformation Mechanism

In order to explain the growth-rate data of calcite and aragonite crystals collected in our laboratory through the past fifteen years, the cluster-transformation mechanism is first proposed here. The mechanism is based on several experimental works cited earlier, including the identification of clusters performed by Larson and his co-workers using the Raman spectrometer [23, 24], the secondary nuclei that originated from clusters gathering on the surface of growing seeds as demonstrated by McCabe and his co-workers using the single-crystal contacting device [25, 26], the similarity in crystallization phenomena between readily-soluble and sparingly-soluble salts brought up by Tai and his co-workers using the constant-composition or constant-pH technique [12, 28], the work of Gebuer et al. to infer that the prenucleation-stage clusters processed “solute

character” in a CaCO₃ solution [29], and the one, which is most relevant to the proposed mechanism, conducted by Denk and Botsaris using sodium chlorate as a model compound [27]. They produced two enantiomorphic forms of sodium chlorate without seeding, and generated the same form of crystals as the seed crystal. The result of the former experiment implied that two forms of cluster coexisted in a supersaturated solution, and of the latter experiment implied that only one type of clusters had the affinity for the seed crystal.

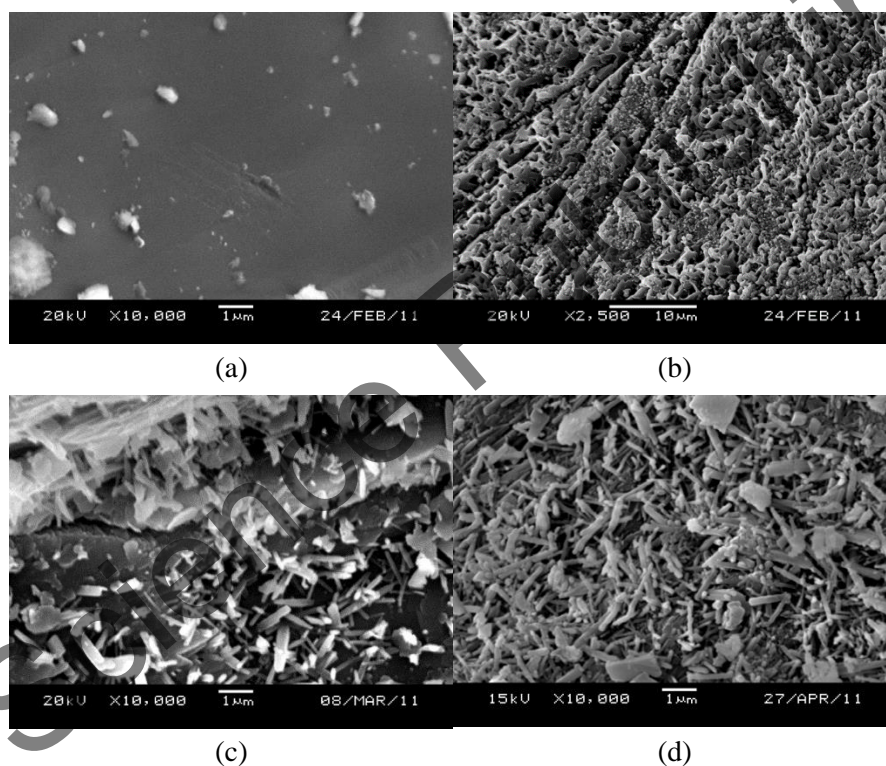


Figure 5. The surface structure of natural aragonite at different stages of growth process.

- (a) Uncured seeds.
- (b) After curing 5 h.
- (c) After curing 10 h.
- (d) After several growth runs.

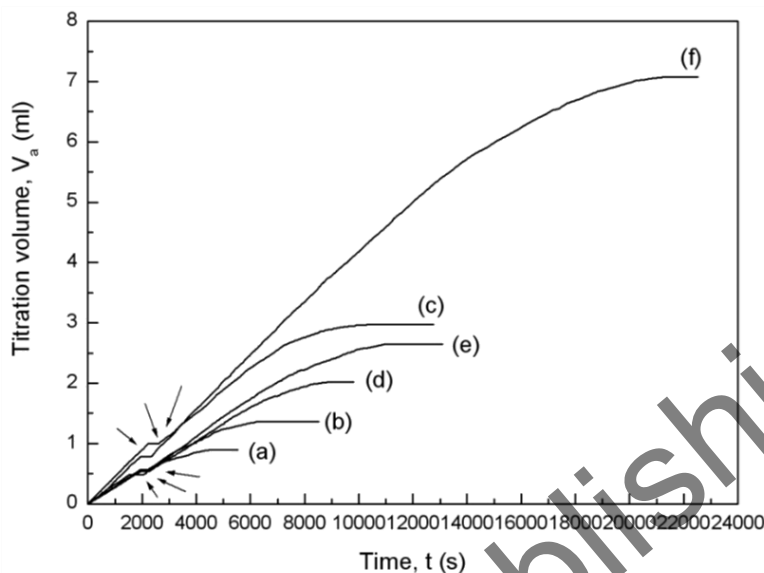


Figure 6. Titration curves showing the transient effect of two types of magnetic device on calcite growth at three levels of supersaturation. The symbol “→” indicates the starting point of magnetization.

$\sigma = 0.6$, Descal device; (b) $\sigma = 0.8$, Descal device; (c) $\sigma = 1.0$, Descal device; (d) $\sigma = 0.6$, permanent magnet; (e) $\sigma = 0.8$, permanent magnet; (f) $\sigma = 1.0$, permanent magnet.

A general description of the cluster-transformation mechanism for the CaCO_3 supersaturated solution is as follows. Two types of clusters, one of which has an affinity to calcite and the other one to aragonite, coexist in a solution and they are interchangeable depending on the solution conditions. The former and the latter will be referred to as calcite-like cluster and aragonite-like cluster respectively in this report. In other words, the calcite-like clusters and the aragonite-like clusters are in equilibrium with each other at a certain ratio under a specific environment. Furthermore, the polymorph-like clusters can only adsorb on and integrate into the surface of the same polymorphic crystal, similar to the enantiomeric forms of sodium chlorate [27]. Since the aragonite-like clusters are inert to the calcite seeds, the actual driving force of calcite growth should be the concentration of calcite-like clusters instead of the relative supersaturation (σ) defined in Equation (2). As far as the transformation rate is concerned,

it is a function of solution properties, such as pH, temperature, and others. One more striking phenomenon is that the transformation can be induced by foreign disturbance, such as magnetic field, impurity, and others. It is reasonable to assume that the Lorenz force induced by magnetic field activates the conversion of clusters [1]. However, it remains unknown how the impurity works in this respect.

Transient Effects of Magnetic Field on the Crystal Growth of CaCO₃ Polymorphs

The titration curves were used to examine the transient effects of a magnetic field on the growth of CaCO₃ polymorphs. In this series of experiment, the supersaturated solution was not subject to premagnetization. Recall that the growth rate was evaluated from the slope of the titration curve. Thus, a decreasing slope meant a decrease of growth rate, and vice versa. Figure 6 shows the titration curves of calcite growth experiment at three supersaturations for $\sigma = 0.6, 0.8$ and 1.0 , with other operating variables fixed at $\text{pH} = 9.0$, $R = 5.54$, $I = 0.018\text{M}$, and $T = 25^\circ\text{C}$, using two types of magnetic device, i.e., a magnetic water treatment device (Descal-A-Matic DC-1) and a set of permanent magnet. The former had a higher field intensity. The titration curves were straight before the magnetic field started and then the curves tended to level off after the starting point of magnetization, meaning that the growth rates of calcite seeds began to decrease slowly and the seeds stopped growing eventually. The time period for leveling-off increased with an increase in supersaturation (for example, compare curve (b) with curve (c)) and the time period was shorter as the magnetic intensity was higher (for example, compare curve (c) with curve (f)). Tai et al. [20] performed similar experiments at three temperature levels ($T = 25^\circ\text{C}, 30^\circ\text{C}$, and 40°C) and three pH values ($\text{pH} = 8.5, 9.0$ and 9.5). They found that the titration curves had similar trend as those shown in Figure 6. The time period of

leveling-off increased with a decrease of temperature and increased with an increase in pH. On the other hand, aragonite seeds behaved differently. Figure 7 shows the titration curves of aragonite growth experiment operated at 25°C, when the permanent magnet was placed at different position in the circulation loop passing the fluidized bed. Before the magnet was incorporated, the autotitrator did not function at all. The autotitrator was activated after the magnet was installed. The titration curve started to rise and then became straight, meaning that the growth rate became steady after a period of time. The time period was shorter when the magnet was clipped on the seed zone, and there is no difference whether the magnet was placed in the front or at the rear of fluidized bed. It is worth mentioning that the three curves became parallel after 6000s, meaning that the steady growth rates became identical eventually.

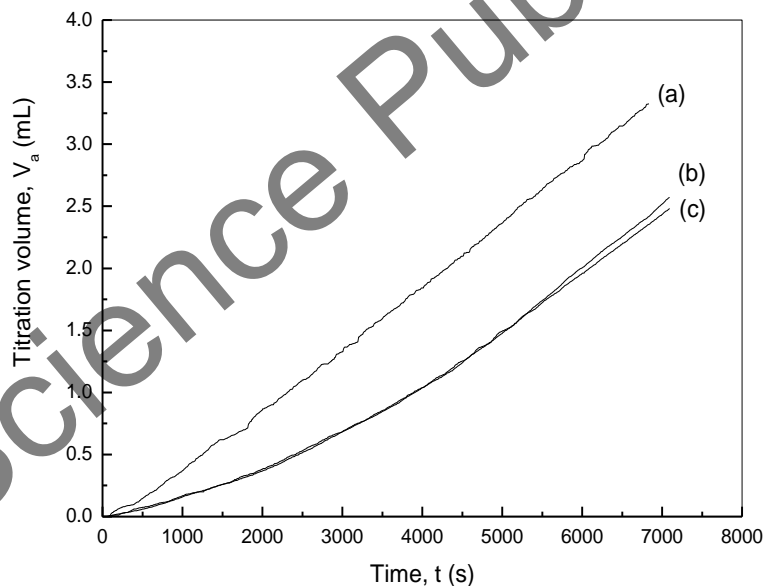


Figure 7. Titration curves showing the transient effect of the position that a permanent magnet was placed for aragonite growth. Magnetization started at the beginning of growth time. (a) on the crystal seed zone; (b) in front of the fluidized bed; (c) at the rear of the fluidized bed.

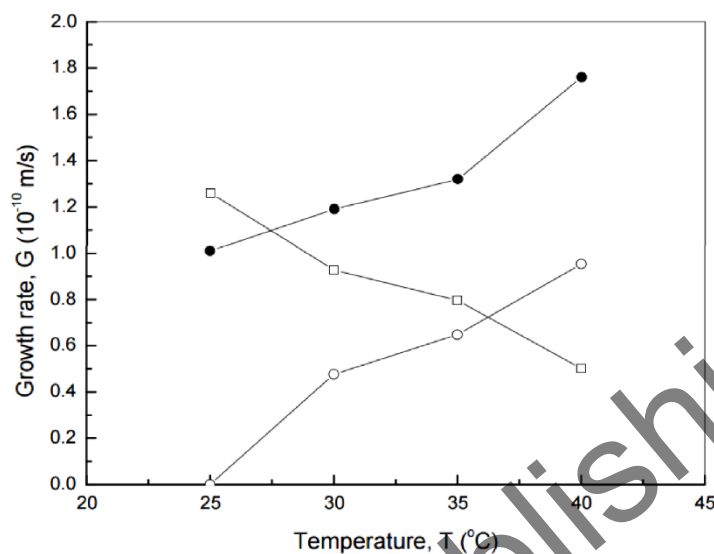


Figure 8. Growth rates of CaCO₃ polymorphs at various temperatures under similar solution conditions: pH = 9.0, I = 0.018M, $\sigma_{\text{cal}} = 1.2$ ($\sigma_{\text{ara}} = 0.91$), and R = 5.54.

- (□) Calcite in the absence of magnetic field.
- (○) Aragonite in the absence of magnetic field.
- (●) Aragonite in the presence of magnetic field.

The transient effects of magnetic field shown in Figure 6 and Figure 7 can be explained using the cluster-transformation mechanism. At room temperature (25°C), the aragonite-like clusters were negligible and the growth rate of aragonite seeds was nil. On the other hand, the calcite-like clusters prevailed and the number of clusters was higher at higher supersaturation. Since a portion of the clusters underwent transformation through a single-pass of solution, it took more time to convert all the calcite-like clusters to aragonite-like form and to stop the growth of calcite seeds at a higher supersaturation. Realizing the partial conversion of a single-pass, it is easy to understand that the magnetic device with a higher intensity had a shorter time for leveling-off as shown in Figure 6. In the case of aragonite growth shown in Figure 7, the rise of titration curves was due to the cluster transformation from calcite-like to aragonite-like form induced by the magnetic field. The titration curve became straight eventually, because most clusters had been converted to aragonite-like

form. The almost identical curves for case(b) and (c) was expected, because the magnetic field just magnetized the solution, irrespective of the position of magnetic device. For case (a), the magnetic field acted on the solution and the seeds surface, it seemed that the aragonite seed worked as catalyst to speed up the transformation of clusters. In the long run, most of the clusters turned out to be aragonite-like form after 6000s to give identical growth rate for the three cases. On the other hand, when the aragonite seeds were replaced by calcite seeds, the titration curves for clipping the magnet on the seed zone leveled off faster (not shown here). This is because the magnetic field acted on the calcite-like clusters in the solution as well as the calcite-like clusters adsorbed on the seed surface. As a result, the magnetic field speeded up the transformation of the clusters.

Effects of Temperature on the Growth Rates of CaCO₃ Polymorphs

The crystal growth rates of calcite and aragonite measured at various temperatures between 25°C and 40°C are shown in Figure 8, in which aragonite growth rates, but not the calcite growth rates, in the presence of magnetic field are included. This is because the calcite seeds did not show significant growth after a premagnetization of 20 h for all temperatures. The growth rate of calcite in the absence of magnetic field decreased with an increase in temperature and varied by a factor of 2.4 between 25°C and 40°C, which is a drastic change for a 15°C difference. On the other hand, the growth rate of aragonite increased from nil at 25°C to 9.2×10^{-11} m/s at 40°C. When the solution was premagnetized for 20 h, a synergetic effect of magnetic field and temperature was significant, almost increased by a factor of 2. The experimental results can be explained using the cluster-transformation mechanism. Below 25°C, the calcite-like clusters prevailed, and the growth rate of aragonite was negligible, if any. At the temperatures higher than 25°C, a portion of calcite-like clusters would transform to aragonite-like clusters and the two types of clusters were in equilibrium

with more aragonite-like clusters existing at higher temperatures. When the solution was subject to magnetization, more calcite-like clusters would be converted to aragonite-like form. After a 20 h of magnetization time, the conversion of cluster-like form proceeded to a great extent and to give a zero growth rate of calcite. The increase in growth rate of aragonite at higher temperatures was not just due to an increase in the concentration of aragonite-like clusters (driving force), the higher activation energy of the surface-integration step also played an important role as reported by Tai et al. [17].

Effects of pH on the Growth Rates of CaCO₃ Polymorphs

Figure 9 shows the growth rates of calcite and aragonite seeds measured at various pHs with and without magnetization, keeping other variables constant for $I = 0.018\text{M}$, $\sigma_{\text{cal}} = 1.0$ ($\sigma_{\text{ara}} = 0.73$), $R = 5.54$, and $T = 25^\circ\text{C}$. The growth rates of aragonite seeds in the absence of magnetic field were missing in the figure, because the concentration of aragonite-like clusters was not high enough to enable the aragonite seeds to grow at 25°C . After the solution was magnetized for 20 h, the aragonite seeds grew and their growth rates decreased with an increase in pH, but keeping constant in the pH range between 9.0 and 10.0. The growth behavior of calcite seeds was opposite to that of aragonite seeds. The calcite seeds grew in the absence of magnetic field and their growth rates increased with the increasing pH. After a premagnetization time of 20h, the growth rates of calcite seeds were almost nil at lower pHs and were barely detectable at higher pHs. Maybe a longer magnetization time was needed to eliminate calcite growth at higher pHs. Judging from the experimental results shown in Figure 9, it is obvious that the magnetic effects overpowered the pH effects on the crystal growth of CaCO₃ polymorphs. As to the decrease or increase in the growth rate of the polymorphs influenced by pH, Tai et al. [13] ascribed the variation to a change in the growth kinetics, instead of a change in driving force related to cluster transformation.

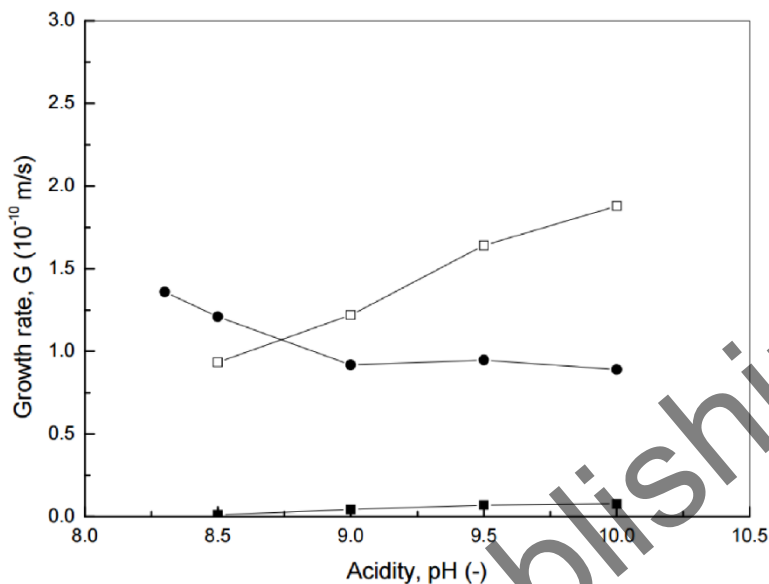


Figure 9. Growth rates of CaCO_3 polymorphs at different pH values under similar solution conditions: $I = 0.018\text{M}$, $\sigma_{\text{cal}} = 1.0$ ($\sigma_{\text{ara}} = 0.73$), $R = 5.54$, and $T = 25^\circ\text{C}$.

- (□) Calcite in the absence of magnetic field.
- (■) Calcite in the presence of magnetic field.
- (●) Aragonite in the presence of magnetic field.

Effects of Activity Ratio (R) on the Growth Rates of CaCO_3 Polymorphs

This series of experiment investigated the effects of R in a range between 0.2 and 6.0 as shown in Figure 10. The crystal growth rates of calcite and aragonite were measured in the absence/ presence of magnetic field. Several unexpected results were obtained here. The growth of aragonite seeds was barely detectable in the neighbourhood of $R = 1$ in the absence of magnetic field, and the growth rate exhibited a minimum at $R = 1$ in the presence of magnetic field. On the other hand, the calcite growth rate reached a maximum at $R = 1$ in the absence of magnetic field and remained almost the same at $R = 1$ in the presence of magnetic field. When the R values were far from 1.0, the calcite growth rates were reduced

greatly or even undetectable under the influence of magnetic field. Again, the growth rate of calcite showed an opposite trend to that of aragonite. This growth phenomenon was consistent with the cluster-transformation mechanism, i.e., an increase in aragonite-like clusters accompanied with a decrease of calcite-like clusters under the influence of a magnetic device. Following the cluster-transformation mechanism that the driving force of calcite growth is the concentration of calcite-like cluster, the highest concentration of calcite-like cluster contributed to the highest growth rate of calcite at $R = 1$. Thus, equal amount of Ca^{2+} and CO_3^{2-} in a supersaturated solution was most favorable for the formation of calcite cluster under the constraint of constant relative supersaturation (σ). The reason for the resistance of cluster transformation in the presence of magnetic field around $R = 1$; however, remained unknown.

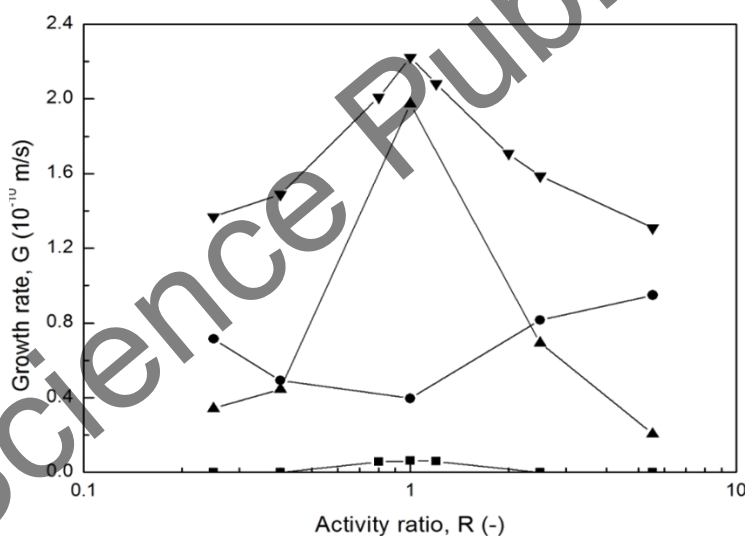


Figure 10. Growth rates of CaCO₃ polymorphs at different activity ratios of Ca²⁺/CO₃²⁻ (R) under similar solution conditions: I = 0.018M, $\sigma_{\text{cal}} = 1.0$, pH = 9.0, and T = 25°C.

- (▼) Calcite in the absence of magnetic field.
- (▲) Calcite in the presence of Descal device.
- (■) Aragonite in the absence of magnetic field.
- (●) Aragonite in the presence of Descal device.

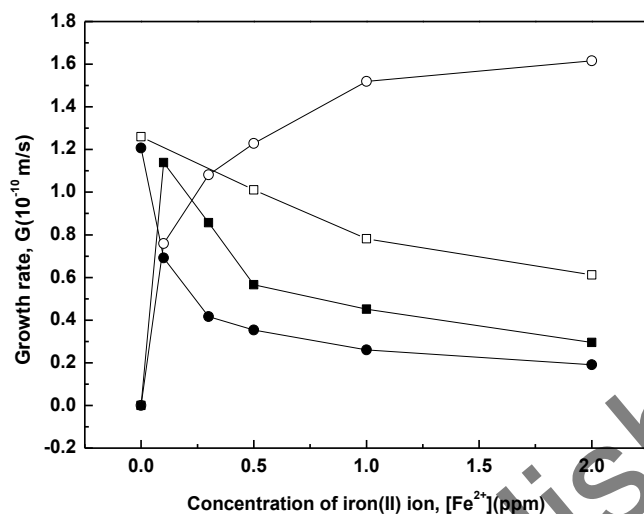


Figure 11. Growth rates of CaCO₃ polymorphs plotted against [Fe²⁺] under similar solution conditions: pH = 9.0, I = 0.018M, $\sigma_{\text{cal}} = 1.0$, R = 5.54, and T = 25°C.

- (□) Calcite in the absence of magnetic field.
- (■) Calcite in the presence of magnetic field.
- (○) Aragonite in the absence of magnetic field.
- (●) Aragonite in the presence of magnetic field.

Effects of Impurities on the Growth Rates of CaCO₃ Polymorphs

A general trend was established by Söhnel and Mullin [7] as follows: An ion with a radius smaller than Ca²⁺, such as Mg²⁺, Fe²⁺, and Cu²⁺, would favor the formation of aragonite and that larger than Ca²⁺, such as Mn²⁺, Sr²⁺, and Ba²⁺, would favor calcite. In this series of experiment, we chose an ionic impurity from each group for studying the impurity effects on the growth rates of CaCO₃ polymorphs. Before presenting the experimental results and giving explanation to them, we were aware that impurities could influence crystal growth rates in a variety of ways, such as the change in equilibrium saturation concentration (driving force), the blocking effect due to adsorption of impurities, the alteration of surface energy, the integration to lattice due to structure similarity, and others. It is usually difficult to identify the real cause of the impurity effect.

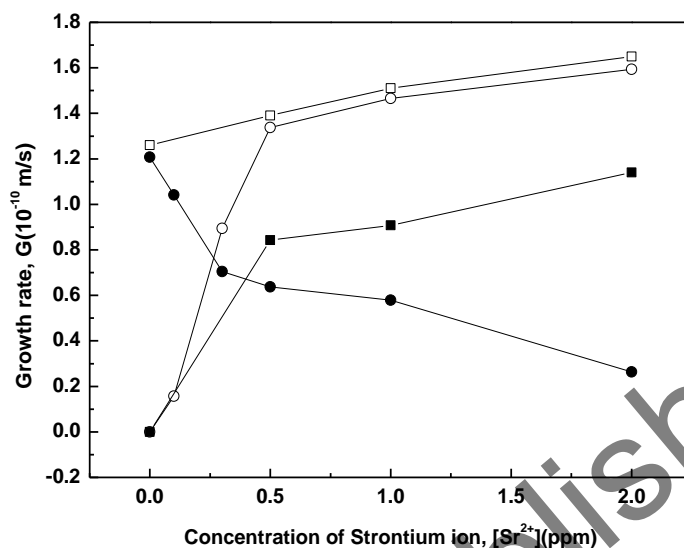


Figure 12. Growth rates of CaCO₃ polymorphs plotted against [Sr²⁺] under similar solution conditions as that in Figure 11.

- (□) Calcite in the absence of magnetic field.
- (■) Calcite in the presence of magnetic field.
- (○) Aragonite in the absence of magnetic field.
- (●) Aragonite in the presence of magnetic field.

The growth rates of calcite and aragonite were plotted against impurity concentration of Fe²⁺ between 0 and 2.0 ppm in the absence/presence of the Descal magnetic device as shown in Figure 11. The other operating variables were fixed at pH = 9.0, $\sigma_{\text{cal}} = 1.0$ ($\sigma_{\text{ara}} = 0.73$), $I = 0.018$ M, $R = 5.54$, and $T = 25^\circ\text{C}$. The growth rates of calcite decreased gradually with increasing Fe²⁺ concentration without magnetizing the solution. In the presence of magnetic field, the growth rate of calcite was insignificant without adding Fe²⁺. Then, it jumped to a high value of 1.14×10^{-10} m/s at 0.1 ppm Fe²⁺ and gradually decreased for a further increase in the Fe²⁺ concentration. The growth rate of aragonite in the presence of magnetic field decreased with increasing Fe²⁺ concentration, similar to the trend of calcite growth in the absence of magnetic field but with a greater extent. In the absence of magnetic field, the aragonite growth rates increased with an increase in Fe²⁺ concentration,

from zero growth rate to 1.6×10^{-10} m/s at 2.0 ppm Fe^{2+} . The effects of Fe^{2+} on the aragonite nucleation reported by Söhnel and Mullin [7] and on the aragonite growth rates measured in this study were in the favorable direction. Together with the results of calcite growth rates that decreased with increasing Fe^{2+} concentration, we may conclude that the Fe^{2+} promoted the formation of aragonite-like clusters at 25°C in the absence of magnetic field. In the presence of magnetic field; however, Fe^{2+} favored the formation of calcite-like clusters at the very low concentration of Fe^{2+} according to the following experimental evidences. An increase in calcite growth rate (jumped from zero to 1.14×10^{-10} m/s) accompanied with a decrease of aragonite growth rate (from 1.21×10^{-10} to 0.61×10^{-10} m/s) as the Fe^{2+} concentration changed from zero to 0.1 ppm, and the SEM photographs showed that the surface of calcite seeds under the influence of magnetic field were still covered with rhombohedral calcite particles (not shown here). So far, up to the Fe^{2+} concentration of 0.1 ppm, the Fe^{2+} had opposite effects to the crystal growth of the polymorphs with and without magnetizing the solution, and this could be caused by the cluster-transformation mechanism. For a further increase from 0.1 to 2.0 ppm of Fe^{2+} concentration, the Fe^{2+} had an unfavorable effect on both calcite and aragonite growth. In the circumstances, the cluster-transformation mechanism can not explain the experimental results. Other factors must have played a significant role in the growth process. It is worth mentioning that the Fe^{2+} had an opposite effect on the cases with and without magnetizing the solution for the aragonite growth, a decrease in the former case and an increase in the latter case.

Figure 12 shows the growth rates of calcite and aragonite in the absence/presence of the Descal magnetic device for the Sr^{2+} concentration between 0 and 2.0 ppm. The other operating variables were fixed as that of Figure 11. The calcite growth rates increased gradually without magnetizing the solution, and the aragonite growth rates decreased with an increase in Sr^{2+} concentration. The calcite growth rate in the presence of magnetic field and the aragonite growth rate in the absence of magnetic field were both increased rapidly from 0 ppm, at which both seeds did not grow, up to 0.5 ppm, then tended to lessen the increasing rate. It was

surprising to see that the presence of Sr²⁺ increase the growth rates of calcite and aragonite in the absence of magnetic field, and the two growth rates were so close to each other for the Sr²⁺ concentration higher than 0.5ppm. When examining the surface of the aragonite seeds after growth in the absence of magnetic field, we found that the surfaces of seeds were partially or fully covered with rhombohedral calcites, as shown in Figures 13(a) and 13(b) for [Sr²⁺] of 0.3 ppm and 2.0 ppm, respectively. Apparently, the Sr²⁺ impurity was adsorbed on the seed surface and then turned the acicular aragonite particles into the rhombohedral calcite particles, so that the measured growth rates of the polymorphs were almost identical as the Sr²⁺ concentration higher than 0.5ppm. In the cases with magnetization, there was no rhombohedral calcite particles appeared on the seed surface of aragonite, instead, the acicular aragonite on the seed surface seemed to be fused as shown in Figure 13(c) and 13(d) for the Sr²⁺ concentration of 0.3 ppm and 2.0 ppm, respectively. Considering the effects of Sr²⁺ on crystal nucleation and growth, the trends are similar, i.e., Sr²⁺ favored the formation [6] and growth of calcite crystals in the absence of magnetic field.

Growth Rates of CaCO₃ Polymorphs in a Simulated Cooling-Water Environment

The crystal growth rates of calcite and aragonite seeds were measured in a growing environment similar to the cool-water conditions: the pH was fixed at 9.0; the Descal water-treatment device was applied; the solution contained impurity; and the temperature was set at 35°C. The operation temperature was lower than the cooling-water temperature (40°C–50°C) due to the instrument limitation, i.e., the Ca²⁺ electrode became unstable at 40°C with the addition of impurity. Although there was a difference of 5°C between the two temperatures, the trend of growth rates should be similar. This can be seen when we compared the growth rate data of calcite at 25°C and 35°C as shown in Figure 12 and Figure 14 respectively for the case of adding Sr²⁺ and magnetizing the solution.

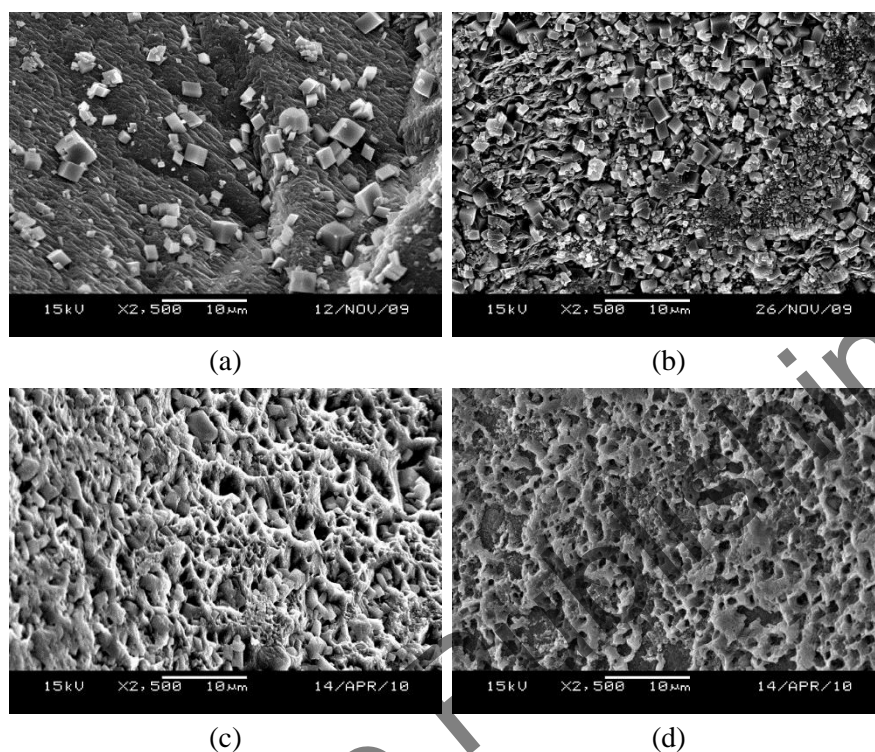


Figure 13. The SEM photographs of the crystal surface of aragonite seeds in the solutions of different Sr^{2+} concentrations.

(a) $[\text{Sr}^{2+}] = 0.3$ ppm and (b) $[\text{Sr}^{2+}] = 2.0$ ppm in the absence of magnetic field.

(c) $[\text{Sr}^{2+}] = 0.3$ ppm and (d) $[\text{Sr}^{2+}] = 2.0$ ppm in the presence of magnetic field.

Figure 14 shows the growth rates of calcite and aragonite seeds in the solutions with an addition of Fe^{2+} or Sr^{2+} at 35°C . In the presence of Fe^{2+} or Sr^{2+} in the solution, the growth rates of aragonite seeds decreased monotonically, even reduced to a very low value of 0.12×10^{-10} m/s in the latter case. On the other hand, the calcite growth rates increased from zero to a significant value as the Sr^{2+} concentration increased from 0 to 2.0 ppm. In the case of Fe^{2+} , the growth rates of calcite first increased and then reduced to a low value of 0.2×10^{-10} m/s. It should be noted that the four growth-rate curves tended to level off beyond 1.0 ppm of the impurity concentration and the growth rate at 2.0 ppm would be probably close to the steady growth-rate at higher concentrations. Judging from Figure 14,

the only effective situation for anti-scaling is the presence of Fe²⁺ at concentrations higher than 2.0 ppm, where the growth of calcite is almost suppressed.

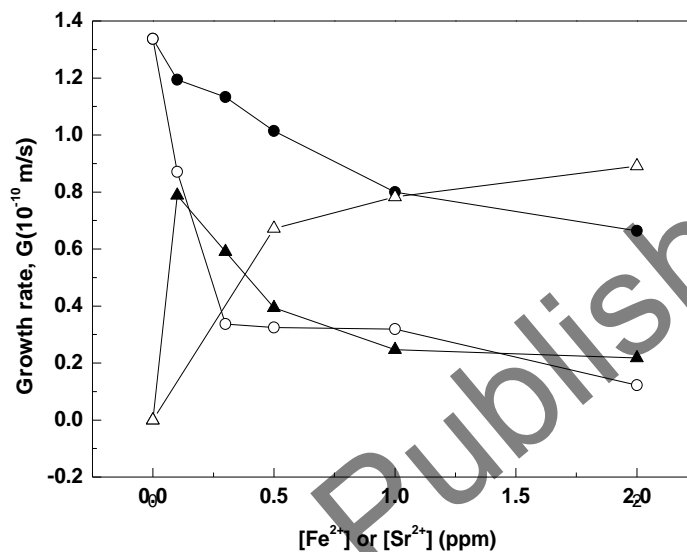


Figure 14. Growth rates of CaCO₃ polymorphs measured at various concentration of Fe²⁺ or Sr²⁺, using the Descal water-treatment device. Other operating variables fixed at T = 35°C, pH = 9.0, I = 0.018M, $\sigma_{\text{cal}} = 1.0$ ($\sigma_{\text{ara}} = 0.73$), and R = 5.54.

- (▲) Calcite with the addition of Fe²⁺.
- (△) Calcite with the addition of Sr²⁺.
- (●) Aragonite with the addition of Fe²⁺.
- (○) Aragonite with the addition of Sr²⁺.

CONCLUSION

The crystal growth rates of CaCO₃ polymorphs, i.e., calcite and aragonite, were measured successfully under various environments by conducting the growth experiment in the metastable region, using the constant-composition technique. In the experiment to explore the transient effects of magnetic field without adding impurities to the crystallizing solution, the growth rates of calcite and aragonite seeds decreased and

increased with the growth time, respectively. Finally, the calcite stopped growing and the aragonite reached a steady growth. Several operation variables, such as supersaturation, temperature, pH, magnetic intensity, and even the position of the magnetic device installed, had profound influence on the time period needed for the calcite seeds to stop growing or the aragonite seeds to reach steady growth. The time periods were shorter in the following situations: lower supersaturation, higher temperature, lower pH, higher magnetic intensity, and the magnetic device placed on the seed zone. All the experimental results of the polymorphs growth related to the study of transient effect can be explained using the cluster transformation mechanism, i.e., the calcite-like clusters originally existing in the solutions at 25°C were converted to the aragonite-like clusters gradually via a single pass through the magnetic device. This explains the failure of the single-pass operation of crystal-growth experiment reported in the literature. To obtain steady growth rates, the solutions should be premagnetized for a certain period of time, such as 20 h for the aragonite seeds.

The interaction of magnetic field with other operating variables, such as temperature, pH, activity ratio ($\text{Ca}^{2+}/\text{CO}_3^{2-}$), and impurity concentration, were manifest. The higher temperatures enhanced the aragonite growth rate and lowered the calcite growth rate in the absence of magnetic field. After the supersaturated solution was magnetized, a synergetic effect of magnetic field and temperature was tremendous for the aragonite growth and the suppression of calcite growth occurred between 20°C and 40°C. In a pH range between 8.0 and 10.0, the growth rates of aragonite seeds were significant and the calcite seeds almost stopped growing in the presence of magnetic field. The magnetic effects overpowered the pH effects on the growth of the polymorphs. As to the effect of activity ratio was concerned, surprising results were observed. A maximum and a minimum growth rate occurred at $R = 1$ for the calcite and aragonite seeds, respectively. If the cluster-transformation mechanism applied, equal amount of Ca^{2+} and CO_3^{2-} ($R = 1$) in a supersaturated solution was most favorable for the formation of calcite cluster. In addition, the calcite-like clusters resisted to proceed the conversion at $R = 1$ in the presence of magnetic field. With regard to the effects of impurities, the results were more complicated. In the absence

of magnetic field, the calcite growth-rate decreased and the aragonite growth-rate increased as the Fe²⁺ concentration increased. In the presence of magnetic field, the aragonite growth-rate decreased with increasing Fe²⁺ concentration, yet the calcite growth rate jumped from zero to a significant value at the Fe²⁺ concentration of 0.1 ppm and then decreased with increasing Fe²⁺ concentration. Without magnetizing the solution the calcite seeds grew faster at higher Sr²⁺ concentrations, yet the Sr²⁺ would convert the acicular aragonites adhered to the seed surface into rhombohedral calcite and the seeds continued to grow in the rate of calcite. With magnetizing the solution, the growth rates of aragonite decreased and the growth rates of calcite increased with an increase in Sr²⁺ concentration. The cluster-transformation mechanism could not explain some of the experimental results, such as the case of using Fe²⁺ as the impurity and applying the magnetic field at the same time. It is worth mentioning that the effects of the two impurities on the crystal growth of the two polymorphs are consistent with the trend of nucleation brought up by Söhnel and Mullin [6], i.e., Fe²⁺ favors the aragonite and Sr²⁺ favors the calcite in the absence of magnetic field.

From experimental facts that a magnetic field and a high operating temperature (above 40°C) would suppress the formation and crystal growth of calcite and promote the formation and crystal growth of the acicular aragonite. The acicular aragonite has a loose and less tenacious property and is rather difficult to deposit on the tube wall of a heat-exchanger. Therefore, a magnetic device incorporated into a cooling-water system should work well on anti-scaling, assuming that there are no impurities or impurities inactive to nucleation and crystal growth of CaCO₃ polymorphs. However, impurities usually influence nucleation and crystal growth even at a concentration lower than 1 ppm, such as Fe²⁺ and Sr²⁺ chosen in this study. From the growth rate data of calcite seeds measured in a simulated cooling-water environment shown in Figure 14 of this study, the scale prevention would be effective when Fe²⁺ is present in the cooling water at a concentration higher than 2.0 ppm in the presence of a magnetic device. At the present time, there is lacking a general rule that can be followed for the prediction of crystal growth rate influenced by ionic impurity due to

limited experimental data available. In addition, there are other types of impurity, such as anionic, organic, and polymeric impurities to be investigated. We hope this piece of work can be used as a reference for those who work on the water treatment using a magnetic device.

ACKNOWLEDGMENT

The authors gratefully acknowledge the support of the Ministry of Science and Technology of Taiwan through all the years.

REFERENCES

- [1] J.S. Baker, S.J. Judd, Magnetic Amelioration of Scale Formation, *Water Research*, 30 (1996) 247-260.
- [2] J.L. Wray, F. Daniels, Precipitation of Calcite and Aragonite, *Journal of the American Chemical Society*, 79 (1957) 2031-2034.
- [3] C.Y. Tai, F.B. Chen, Polymorphism of CaCO_3 , Precipitated in a Constant-Composition Environment, *AIChE Journal*, 44 (1998) 1790-1798.
- [4] K. Higashitani, A. Kage, S. Katamura, K. Imai, S. Hatade, Effects of a Magnetic Field on the Formation of CaCO_3 Particles, *Journal of Colloid and Interface Science*, 156 (1993) 90-95.
- [5] S. Kobe, G. Drazic, P.J. McGuinness, J. Strazisar, The Influence of the Magnetic Field on the Crystallisation form of Calcium Carbonate and the Testing of a Magnetic Water-Treatment Device, *Journal of Magnetism and Magnetic Materials*, 236 (2001) 71-76.
- [6] J.W. Mullin, *Crystallisation*, chapter 6, London, Butterworth & Co., 1972.
- [7] O. Söhnel, J.W. Mullin, Precipitation of Calcium Carbonate, *Journal of Crystal Growth*, 60 (1982) 239-250.

- [8] R.E. Herzog, Q. Shi, J.N. Patil, J.L. Katz, *Magnetic Water-Treatment - the Effect of Iron on Calcium Carbonate Nucleation and Growth*, *Langmuir*, 5 (1989) 861-867.
- [9] K.I. Parsiegl, J.L. Katz, Calcite Growth Inhibition by Copper(II) II. Effect of Solution Composition, *Journal of Crystal Growth*, 213 (2000) 368-380.
- [10] M.B. Tomson, G.H. Nancollas, Mineralization Kinetics - Constant Composition Approach, *Science*, 200 (1978) 1059-1060.
- [11] C.Y. Tai, H.P. Hsu, Crystal Growth Kinetics of Calcite and its Comparison with Readily Soluble Salts, *Powder Technology*, 121 (2001) 60-67.
- [12] C.Y. Tai, J.H. Lu, J.K. Wu, Crystal Growth Rate of Calcite in a Constant-Composition Environment, *Journal of the Chinese Institute of Chemical Engineers*, 36 (2005) 443-450.
- [13] C.Y. Tai, M.C. Chang, C.K. Wu, Y.C. Lin, Interpretation of Calcite Growth Data Using the Two-Step Crystal Growth Model, *Chemical Engineering Science*, 61 (2006) 5346-5354.
- [14] C.Y. Tai, M.C. Chang, R.J. Shieh, T.G. Chen, Magnetic Effects on Crystal Growth Rate of Calcite in a Constant-Composition Environment, *Journal of Crystal Growth*, 310 (2008) 3690-3697.
- [15] C.Y. Tai, C.K. Wu, M.C. Chang, Effects of Magnetic Field on the Crystallization of CaCO₃ Using Permanent Magnets, *Chemical Engineering Science*, 63 (2008) 5606-5612.
- [16] M.C. Chang, C.Y. Tai, Effect of the Magnetic Field on the Growth Rate of Aragonite and the Precipitation of CaCO₃, *Chemical Engineering Journal*, 164 (2010) 1-9.
- [17] C.Y. Tai, M.C. Chang, S.W. Yeh, Synergetic Effects of Temperature and Magnetic Field on the Aragonite and Calcite Growth, *Chemical Engineering Science*, 66 (2011) 1246-1253.
- [18] C.Y. Tai, M.C. Chang, C.C. Liu, S.S.S. Wang, *Calcite: Formation, Properties and Application*, Nova Science Publishers, New York, 2011.
- [19] S.S.S. Wang, M.C. Chang, H.C. Chang, M.H. Chang, C.Y. Tai, *Growth Behavior of Aragonite under the Influence of Magnetic*

- Field, Temperature, and Impurity, Industrial & Engineering Chemistry Research*, 51 (2012) 1041-1049.
- [20] C.Y. Tai, M.C. Chang, C.C. Liu, S.S.S. Wang, Growth of Calcite Seeds in a Magnetized Environment, *Journal of Crystal Growth*, 389 (2014) 5-11.
- [21] J.W. Mullin, *Crystallization*, chapter 5, London, Butterworth & Co., 1993.
- [22] R.L. Frost, D.W. James, Ion-Ion-Solvent Interactions in Solution. 3. Aqueous-Solutions of Sodium-Nitrate, *Journal of the Chemical Society-Faraday Transactions I*, 78 (1982) 3223-3234.
- [23] I.T. Rusli, G.L. Schrader, M.A. Larson, Raman-Spectroscopic Study of NaNO₃ Solution System-Solute Clustering in Supersaturated Solutions, *Journal of Crystal Growth*, 97 (1989) 345-351.
- [24] M.A. Larson, Solute Clustering and Secondary Nucleation, Oxford: Butterworth-Heinemann, *Advances in Industrial Crystallization*, 1991.
- [25] N.A. Clontz, W.L. McCabe, Contact Nucleation of Magnesium Sulfate Heptahydrate, *American Institute of Chemical Engineers Symposium Series*, 110 (1971) 32.
- [26] C.Y. Tai, W.L. McCabe, R.W. Rousseau, Contact Nucleation of Various Crystal Types, *AIChE Journal*, 21 (1975) 351-358.
- [27] E.G. Denk, G.D. Botsaris, Mechanism of Contact Nucleation, *Journal of Crystal Growth*, 15 (1972) 57-60.
- [28] C.Y. Tai, P.C. Chen, S.M. Shih, Size-Dependent Growth and Contact Nucleation of Calcite Crystals, *AIChE Journal*, 39 (1993) 1472-1482.
- [29] D. Gebauer, A. Völkel, H. Cölfen, Stable Prenucleation Calcium Carbonate Clusters, *Science*, 322 (2008) 1819-1822.
- [30] O. Söhnel, J. Garside, *Precipitation: Basic Principles and Industrial Applications*, (1992).
- [31] C.Y. Tai, W.C. Chien, C.Y. Chen, Crystal Growth Kinetics of Calcite in a Dense Fluidized-Bed Crystallizer, *AIChE Journal*, 45 (1999) 1605-1614.

In: Crystal Growth
Editors: J. Li, J. Li and Y. Chu

ISBN: 978-1-53612-203-9
© 2017 Nova Science Publishers, Inc.

Chapter 5

WEAK NONLINEAR THREE-DIMENSIONAL CONVECTIVE FLOW DURING THE SOLIDIFICATION OF BINARY ALLOYS

Dambaru Bhatta and Daniel N. Riahi *

School of Mathematical & Statistical Sciences
The University of Texas Rio Grande Valley,
Edinburg/Brownsville, Texas, US

Abstract

This chapter presents the weakly nonlinear analysis of three-dimensional convective flow during solidification of binary alloys and the corresponding research development that has been accomplished in recent years to determine the qualitative features of such flows. The corresponding flow obeys either the linear or nonlinear system of the relevant governing equations and the boundary conditions for the associated fluid mechanics and heat and mass transfer. An evolution equation satisfied by the amplitude for hexagonal cell is derived. Numerical solutions to the resulting weakly nonlinear equations are obtained using a fourth order Runge-Kutta via a shooting technique. Detailed flow features of the three dimensional solutions at the centers and near the boundaries of the cells are presented.

*E-mail address: dambaru.bhatta@utrgv.edu; daniel.riahi@utrgv.edu

AMS Subject Classification: 53D, 37C, 65P.

Keywords: three-dimensional, convective, solidification, alloys, weakly-nonlinear

1. Introduction

In solidification of binary alloys, experimentalists observed vertical chimneys or channels void of solid that are typically oriented in the direction of gravity. When a binary alloy is solidified from cooled boundary, due to the temperature difference at the solidification front, the binary alloy becomes unstable. Hence a heterogeneous region of both solid and liquid, famously referred as mushy layer, is formed. The fluid flow within the mushy layer, a partially solidified region which is formed during solidification binary alloys can cause impurity in the final form of solidified alloys. These are imperfections on the final product. The phenomenon of natural convection arises in a fluid when the temperature change causes density variations resulting in buoyancy forces. Convective flows in a horizontal mushy layer are known to produce chimneys during solidification of binary alloys. It is well known that convection in the chimneys causes a thin hair like structure called freckles. Because of its importance, there has been a growing interest in studying the chimney formation during the solidification of binary alloys both theoretically and experimentally. Nonlinear studies provide more insight into many systems in many branches of applied sciences and engineering. In 1944, Lev Landau [1944], proposed a nonlinear equation to analyze hydrodynamic stability. Landau equation for Benard convection, Couette flow and parallel shear flows have been discussed in details by Drazin and Reid [1981]. Thermal, hydrodynamic and hydromagnetic stabilities have been analyzed by Chandrasekhar [1981].

Numerous attempts, both theoretically and experimentally, have been made to understand the general transport mechanisms in binary alloy solidification leading to freckle formation. Fowler [1985] developed a mathematical model for the convective flow in chimneys and predicted a criterion for the onset of convection and freckling. A pioneering effort in studying the fluid mechanics of the mushy layer was carried out by Worster [1991]. He developed the governing

equations for the mushy layer in the asymptotic regime of large mush Rayleigh number. Chen and Chen [1991] conducted experimental study on directional solidification of aqueous chloride solution. Worster [1992] solved linear instability problem due to the stationary infinitesimal disturbances for infinite Prandtl number. He detected, using linear stability analysis, two modes of instability. The mushy-layer mode drives the convective flow downward everywhere except in and near the localized chimneys. He concluded that the mushy layer mode was responsible for the freckle formation. An experimental study for the planform of compositional convection and chimney formation in a mushy layer was done by Tait and Jaupart [1992]. They observed that the boundary layer at the top of the mush become unstable, leading to the convection in the overlying fluid. They also observed that up flow occurred at the cell boundaries and the down flow at the cell centers.

Amberg and Homsy [1993] introduced, a simplified, single layer model based on a near eutectic approximation and in the limit of large far-field temperature. They performed weakly nonlinear analysis and calculated a critical value of the combined parameter for the transition from supercritical to subcritical rolls. Emms and Fowler [1994] proposed a coupled mush-liquid model to study the onset of convection during the directional solidification of binary alloys. Anderson and Worster [1995] employed a weakly nonlinear analysis of simplified mushy layer model that was proposed by Amberg and Homsy. A near eutectic approximation was applied and the limit of large far-field temperature was considered. Such asymptotic limits allowed them to examine the dynamics of mushy layer. They also considered the limit of large Stefan number, which enabled them to reach a domain for the existence of the oscillatory mode of convection. Chen [1995] carried out some experimental studies on convection in a mushy layer during directional solidification.

Okhuysen and Riahi [2008a, 2008b] carried out a weakly nonlinear analysis of buoyant convection in binary alloy solidification for a permeable mush-liquid interface. They relaxed a number of assumptions assumed in some previous theoretical studies. They determined two-dimensional and some three dimensional solutions for the parameter values which were not similar to those for available experimental results of Tait et al. [1992]. Roper, Davis and Voorhees [2008] presented an analysis of convection in a mushy layer with deformable permeable interface. Study on oscillatory modes of nonlinear compositional

convection in mushy layers was carried out by Riahi [2009]. Guba and Worster [2010] studied interactions between steady and oscillatory convection. Their analysis were essentially based on the model due to Amberg and Homsy, which was under several restrictions that the concentration ratio is large, the thickness of the mushy layer is small, the far-field temperature is large. Bhatta, Riahi and Muddamallappa [2010, 2012] studied weakly nonlinear convective flow in mushy layer with permeable mush-liquid interface. They derived Landau type equations for the amplitude and computed the Landau constant for constant permeability and variable permeability cases. In both cases, they found that Landau constant is positive which indicates that there is slow transition to turbulence. Lee et al. [2012] carried out numerical modeling of one-dimensional binary alloy solidification with a mushy layer evolution. Fluxes through steady chimneys in a mushy layer during binary solidification was studied by Rees et al. [2013]. Wells et al. [2013] analyzed the stability and optimal solute fluxes for nonlinear mushy-layer convection.

In the present chapter we formulate the three-dimensional convective flow for a mushy layer. From the linear system we determine the critical Rayleigh number and use this to obtain the adjoint system which helps us to derive the Landau equation. Solutions to the first-order systems are obtained for constant amplitude case and both subcritical and supercritical flow cases. We present numerical results for the solid fraction and vertical velocity component with various parameters. The significance of this work is the results for the three dimensional flow near the onset of motion that generally observed for sufficiently small amplitude of motion. The present work is different compared to other published work since the present investigation considered for the first time the examination of the physically realistic three dimensional flow features which are for the parameter values of the experimental observation of Tait et al. [1992] for flow close to its onset of motion.

2. Nondimensional Governing System

Nondimensional system can be expressed as

$$\begin{aligned}
\vec{u} + \nabla P + \mathcal{R} \Theta \vec{k} &= 0 \\
\left(\frac{\partial}{\partial t} - \frac{\partial}{\partial z} \right) [(1 - \Phi) \Theta + C \Phi] + (\vec{u} \cdot \nabla) \Theta &= 0 \\
\left(\frac{\partial}{\partial t} - \frac{\partial}{\partial z} \right) [\Theta - S \Phi] + (\vec{u} \cdot \nabla) \Theta &= \nabla^2 \Theta \\
\nabla \cdot \vec{u} &= 0
\end{aligned} \tag{1}$$

Here \vec{u} , P , \mathcal{R} , Θ , \vec{k} , t , z , Φ , C and S respectively represents the velocity, pressure, Rayleigh number, temperature, unit vector along vertical upward direction, time variable, space variable in vertical direction, solid volume fraction, concentration ratio and the Stefan number. Geometry of the physical system is shown in 1.

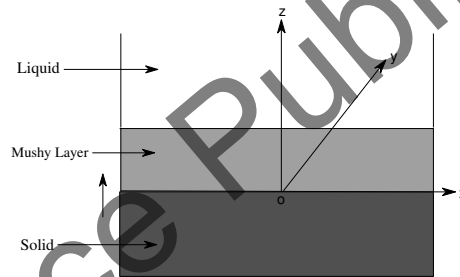


Figure 1. Physical System

The boundary conditions are

$$\begin{aligned}
\Theta = -1, \mathcal{W} = 0 & \quad \text{at } z = 0 \\
\Theta = \Phi = \mathcal{W} = 0 & \quad \text{at } z = \delta
\end{aligned}$$

where \mathcal{W} is the vertical component of \vec{u} and δ denotes the nondimensional thickness of the mushy layer.

2.1. Basic State and Perturbed Systems

Using perturbation, we assume the solutions of the form

$$\begin{aligned}
 \Theta(x, y, z, t) &= \theta_b(z) + \varepsilon\theta(x, y, z, t) \\
 \Phi(x, y, z, t) &= \phi_b(z) + \varepsilon\phi(x, y, z, t) \\
 \vec{U}(x, y, z, t) &= \varepsilon\vec{u}(x, y, z, t) \\
 \mathcal{P}(x, y, z, t) &= p_b(z) + \varepsilon p(x, y, z, t) \\
 \mathcal{R} &= \mathcal{R}_c + \varepsilon\mathcal{R}_1
 \end{aligned} \tag{2}$$

where θ_b, ϕ_b, p_b are solutions to the steady basic state system (system with no flow) and θ, ϕ, \vec{u}, p , are perturbed solutions, $\tau = \varepsilon t$ and ε is the perturbation parameter. Here \mathcal{R}_1 is the nonlinear contribution to \mathcal{R} beyond the value for the most critical neutrally stable linear solution. Solutions to the basic state system had been presented previously by various authors. The basic state solution θ_b can be expressed implicitly by the equation

$$z = \frac{\alpha - C}{\alpha - \beta} \ln \left[\frac{1 + \alpha}{\alpha - \theta_b} \right] + \frac{C - \beta}{\alpha - \beta} \ln \left[\frac{1 + \beta}{\beta - \theta_b} \right] \tag{3}$$

where α, β are given by

$$\alpha = \frac{C + S + \theta_\infty + \sqrt{(C + S + \theta_\infty)^2 - 4C\theta_\infty}}{2}$$

and

$$\beta = \frac{C + S + \theta_\infty - \sqrt{(C + S + \theta_\infty)^2 - 4C\theta_\infty}}{2}$$

Here θ_∞ represents temperature far away from the mush-liquid interface. The solution ϕ_b can be obtained from θ_b from the following relation

$$\phi_b = \frac{\theta_b}{\theta_b - C} \tag{4}$$

3. Perturbed System

Using (2) in the system (1), the perturbed system can be obtained as

$$\vec{u} + \nabla p + \mathcal{R}_c \theta \hat{k} = -\varepsilon \mathcal{R}_1 \theta \hat{k} \quad (5)$$

$$\left(\nabla^2 + \frac{\partial}{\partial z} \right) \theta - \mathcal{S} \frac{\partial \phi}{\partial z} - \theta'_b w = \varepsilon \left[\frac{\partial}{\partial \tau} (\theta - \mathcal{S} \phi) + \vec{u} \cdot \nabla \theta \right] \quad (6)$$

$$\begin{aligned} \frac{\partial}{\partial z} \{ (\theta_b - C) \phi - (1 - \phi_b) \theta \} + \theta'_b w = \varepsilon \left\{ -\vec{u} \cdot \nabla \theta - \frac{\partial}{\partial z} (\theta \phi) \right. \\ \left. + \frac{\partial}{\partial \tau} \{ (\theta_b - C) \phi - (1 - \phi_b) \theta \} + \varepsilon \frac{\partial}{\partial \tau} (\theta \phi) \right\} \quad (7) \end{aligned}$$

$$\nabla \cdot \vec{u} = 0 \quad (8)$$

with $\theta = w = 0$ at $z = 0$ and $\theta = \phi = w = 0$ at $z = \delta$. Here $\vec{u} = (u, v, w)$ and θ'_b denote the derivative of θ_b with respect to z . Now, we eliminate the pressure from the equation (5) by taking the double curl of that equation. Also using the continuity equation, the third component of $\nabla \times \nabla \times \vec{u}$ becomes $-\nabla^2 w$. Similarly, for the third component of $\nabla \times \nabla \times (\mathcal{R}_c \theta \hat{k})$, we have

$$-\mathcal{R}_c \left[\frac{\partial^2 \theta}{\partial x^2} + \frac{\partial^2 \theta}{\partial y^2} \right] = -\mathcal{R}_c (\Delta_2 \theta).$$

Here Δ_2 represents two dimensional Laplacian operator. These allow us to write equation (5) as

$$\nabla^2 w + \mathcal{R}_c (\Delta_2 \theta) = -\varepsilon \mathcal{R}_1 (\Delta_2 \theta) \quad (9)$$

3.1. Weakly Nonlinear Perturbed System

Considering

$$\theta = \theta_0 + \varepsilon \theta_1 + \varepsilon^2 \theta_2 + \dots$$

$$\phi = \phi_0 + \varepsilon \phi_1 + \varepsilon^2 \phi_2 + \dots$$

$$w = w_0 + \varepsilon w_1 + \varepsilon^2 w_2 + \dots$$

and denoting the solution of linear perturbed system by $q_0 = [w_0, \theta_0, \phi_0]^T$, where T_r is used to denote the transpose, the linear system can be obtained from equations (9), (6), (7) by comparing the

coefficients of ε^0 as follows

$$\nabla^2 w_0 + \mathcal{R}_c (\Delta_2 \theta_0) = 0 \quad (10)$$

$$\left(\nabla^2 + \frac{\partial}{\partial z} \right) \theta_0 - \mathcal{S} \frac{\partial \phi_0}{\partial z} - \theta'_b w_0 = 0 \quad (11)$$

$$\frac{\partial}{\partial z} [(\theta_b - C) \phi_0 - (1 - \phi_b) \theta_0] + \theta'_b w_0 = 0 \quad (12)$$

The boundary conditions at the solidifying front are $\theta_0 = w_0 = 0$ and at the mush-liquid interface are $\theta_0 = \phi_0 = w_0 = 0$. Thus, the perturbed linear system as

$$L_0 q_0 = 0 \quad (13)$$

with the operator L_0 given by

$$L_0 = \begin{bmatrix} \nabla^2 & \mathcal{R}_c \Delta_2 & 0 \\ -\theta'_b & \nabla^2 + \frac{\partial}{\partial z} & -\mathcal{S} \frac{\partial}{\partial z} \\ \theta'_b & \phi'_b - (1 - \phi_b) \frac{\partial}{\partial z} & \theta'_b + (\theta_b - C) \frac{\partial}{\partial z} \end{bmatrix} \quad (14)$$

4. Adjoint System

Here we use the sub-index a to denote the quantities belonging to the adjoint system, i.e., $q_a = [w_a \ \theta_a \ \phi_a]^T$. To obtain the adjoint system, we multiply the equations (10), (11) and (12) by w_a , θ_a and ϕ_a respectively, add them and integrate and then take the limit as follows

$$\begin{aligned} & \lim_{L \rightarrow \infty} \frac{1}{4L^2} \int_{-L}^L \int_{-L}^L [w_a (\nabla^2 w_0) + \mathcal{R}_c w_a (\Delta_2 \theta_0) \\ & + \theta_a \left(\nabla^2 + \frac{\partial}{\partial z} \right) \theta_0 - \mathcal{S} \theta_a \frac{\partial \phi_0}{\partial z} - \theta_a \theta'_b w_0 \\ & + \phi_a \left\{ \frac{\partial}{\partial z} [(\theta_b - C) \phi_0 - (1 - \phi_b) \theta_0] + \theta'_b w_0 \right\}] dV = 0 \quad (15) \end{aligned}$$

Here L denotes the length in xy -plane. The boundary conditions satisfied by adjoint solutions at the solidifying front are $\theta_a = w_a = \phi_a = 0$ and at the mush-liquid interface are $\theta_a = w_a = 0$.

The adjoint system can be obtained as (see appendix)

$$L_a q_a = 0 \quad (16)$$

with the operator L_a given by

$$L_a = \begin{bmatrix} \nabla^2 & -\theta'_b & \theta'_b \\ \mathcal{R}_c \Delta_2 & \nabla^2 - \frac{\partial}{\partial z} & (1 - \phi_b) \frac{\partial}{\partial z} \\ 0 & S \frac{\partial}{\partial z} & (C - \theta_b) \frac{\partial}{\partial z} \end{bmatrix} \quad (17)$$

5. Landau Type Equation for Amplitude

First order system is obtained from equations (9), (6), (7) by comparing the coefficients of ϵ^1 as

$$\nabla^2 w_1 + \mathcal{R}_c (\Delta_2 \theta_1) = -\mathcal{R}_1 (\Delta_2 \theta_0) \quad (18)$$

$$\left(\nabla^2 + \frac{\partial}{\partial z} \right) \theta_1 - S \frac{\partial \phi_1}{\partial z} - \theta'_b w_1 = \left[\frac{\partial}{\partial \tau} (\theta_0 - S \phi_0) + \vec{u}_0 \cdot \nabla \theta_0 \right] \quad (19)$$

$$\begin{aligned} \frac{\partial}{\partial z} \{ (\theta_b - C) \phi_1 - (1 - \phi_b) \theta_1 \} + \theta'_b w_1 &= -\vec{u}_0 \cdot \nabla \theta_0 - \frac{\partial}{\partial z} (\theta_0 \phi_0) \\ &+ \frac{\partial}{\partial \tau} \{ (\theta_b - C) \phi_0 - (1 - \phi_b) \theta_0 \} \end{aligned} \quad (20)$$

Using poloidal and toroidal decomposition of a divergence free vector (Chandrasekhar, [1981]), we can express

$$\vec{u}_0 \cdot \nabla \theta_0 = \frac{\partial^2 u_{P_0}}{\partial x \partial z} \frac{\partial \theta_0}{\partial x} + \frac{\partial^2 u_{P_0}}{\partial y \partial z} \frac{\partial \theta_0}{\partial y} - (\Delta_2 u_{P_0}) \frac{\partial \theta_0}{\partial z}$$

where u_{P_0} is the poloidal component of \vec{u}_0 . To derive the Landau type equation satisfied by the amplitude, we multiply (18), (19), (20) by w_a , θ_a , ϕ_a respectively and integrate the result with respect to x , y , z and take the limit. Left hand side

of this operation becomes

$$\begin{aligned} LHS = & \lim_{L \rightarrow \infty} \frac{1}{4L^2} \int_0^\delta \int_{-L}^L \int_{-L}^L [w_a \{ \nabla^2 w_1 + \mathcal{R}_c(\Delta_2 \theta_1) \} \\ & + \theta_a \left\{ \left(\nabla^2 + \frac{\partial}{\partial z} \right) \theta_1 - \mathcal{S} \frac{\partial \phi_1}{\partial z} - \theta'_b w_1 \right\} \\ & + \phi_a \left\{ \frac{\partial}{\partial z} \{ (\theta_b - C) \phi_1 - (1 - \phi_b) \theta_1 \} + \theta'_b w_1 \right\}] dV \quad (21) \end{aligned}$$

where $dV = dx dy dz$. Right hand side is given by

$$\begin{aligned} RHS = & \lim_{L \rightarrow \infty} \frac{1}{4L^2} \int_0^\delta \int_{-L}^L \int_{-L}^L [-w_a \mathcal{R}_1(\Delta_2 \theta_0) \\ & + \theta_a \left\{ \frac{\partial}{\partial \tau} (\theta_0 - \mathcal{S} \phi_0) + \frac{\partial^2 u_{P_0}}{\partial x \partial z} \frac{\partial \theta_0}{\partial x} + \frac{\partial^2 u_{P_0}}{\partial y \partial z} \frac{\partial \theta_0}{\partial y} - (\Delta_2 u_{P_0}) \frac{\partial \theta_0}{\partial z} \right\} \\ & + \phi_a \left\{ \frac{\partial}{\partial \tau} \{ (\theta_b - C) \phi_0 - (1 - \phi_b) \theta_0 \} - \frac{\partial}{\partial z} (\theta_0 \phi_0) \right. \\ & \left. - \frac{\partial^2 u_{P_0}}{\partial x \partial z} \frac{\partial \theta_0}{\partial x} - \frac{\partial^2 u_{P_0}}{\partial y \partial z} \frac{\partial \theta_0}{\partial y} + (\Delta_2 u_{P_0}) \frac{\partial \theta_0}{\partial z} \right\}] dV \quad (22) \end{aligned}$$

Integration by parts and use of boundary conditions simplify LHS as

$$\begin{aligned} LHS = & \lim_{L \rightarrow \infty} \frac{1}{4L^2} \int_0^\delta \int_{-L}^L \int_{-L}^L [w_1 \{ \nabla^2 w_a - \theta'_b (\theta_a - \phi_a) \} \\ & + \theta_1 \left\{ \mathcal{R}_c(\Delta_2 w_a) + \left(\nabla^2 - \frac{\partial}{\partial z} \right) \theta_a - (1 - \phi_b) \frac{\partial \phi_a}{\partial z} \right\} \\ & + \phi_1 \left\{ \mathcal{S} \frac{\partial \theta_a}{\partial z} + (C - \theta_b) \frac{\partial \phi_a}{\partial z} \right\}] dV \end{aligned}$$

which is zero because of the adjoint system. Now we simplify the RHS by writing as

$$RHS = I_1 + I_2 + I_3 + I_4 \quad (23)$$

where

$$\begin{aligned}
 I_1 &= \lim_{L \rightarrow \infty} \frac{1}{4L^2} \int_0^\delta \int_{-L}^L \int_{-L}^L \{-w_a \mathcal{R}_1(\Delta_2 \theta_0)\} dV \\
 I_2 &= \lim_{L \rightarrow \infty} \frac{1}{4L^2} \int_0^\delta \int_{-L}^L \int_{-L}^L \left\{ \theta_a \frac{\partial}{\partial \tau} (\theta_0 - \mathcal{S} \phi_0) + \phi_a \frac{\partial}{\partial \tau} \{(\theta_b - C) \phi_0 - (1 - \phi_b) \theta_0\} \right\} dV \\
 I_3 &= \lim_{L \rightarrow \infty} \frac{1}{4L^2} \int_0^\delta \int_{-L}^L \int_{-L}^L (\theta_a - \phi_a) \left\{ \frac{\partial^2 u_{P_0}}{\partial x \partial z} \frac{\partial \theta_0}{\partial x} + \frac{\partial^2 u_{P_0}}{\partial y \partial z} \frac{\partial \theta_0}{\partial y} \right\} dV \quad (24) \\
 I_4 &= \lim_{L \rightarrow \infty} \frac{1}{4L^2} \int_0^\delta \int_{-L}^L \int_{-L}^L \left\{ -(\theta_a - \phi_a) (\Delta_2 u_{P_0}) \frac{\partial \theta_0}{\partial z} - \phi_a \frac{\partial}{\partial z} (\theta_0 \phi_0) \right\} dV
 \end{aligned}$$

We assume that the linear and adjoint solutions take the following form

$$f(x, y, z, \tau) = A(\tau) \tilde{f}(z) \eta_1(x, y) \quad (25)$$

Here A represents the amplitude and $\eta_1(x, y) = \text{Re} \left[\sum_{j=1}^3 e^{i \bar{a}_j \cdot \bar{r}} \right]$, $\bar{a}_1 = \left(\frac{\alpha \sqrt{3}}{2}, \frac{\alpha}{2} \right)$, $\bar{a}_2 = \left(-\frac{\alpha \sqrt{3}}{2}, \frac{\alpha}{2} \right)$, $\bar{a}_3 = (0, -\alpha)$, $\bar{r} = (x, y)$ and α is the wavenumber. These yield

$$\eta_1(x, y) = \cos \frac{\alpha}{2} (x \sqrt{3} + y) + \cos \frac{\alpha}{2} (-x \sqrt{3} + y) + \cos(-\alpha y) \quad (26)$$

Now we can simplify the integrals appearing in (24) as follows

$$\begin{aligned}
 I_1 &= \left[\alpha^2 \mathcal{R}_1 A^2 \int_0^\delta \tilde{w}_a \tilde{\theta}_0 dz \right] (I_{\eta^{(2)}}) \\
 I_2 &= \left[A \frac{dA}{d\tau} \int_0^\delta \left\{ \tilde{\theta}_a (\tilde{\theta}_0 - \mathcal{S} \tilde{\phi}_0) + \tilde{\phi}_a [(\theta_b - C) \tilde{\phi}_0 - (1 - \phi_b) \tilde{\theta}_0] \right\} dz \right] (I_{\eta^{(2)}}) \\
 I_3 &= A^3 \left\{ \int_0^\delta (\tilde{\theta}_a - \tilde{\phi}_a) \tilde{\theta}_0 (D \tilde{u}_{P_0}) dz \right\} (I_{\eta^{(xy)}}) \quad (27) \\
 I_4 &= A^3 \left[\int_0^\delta \left\{ \alpha^2 (\tilde{\theta}_a - \tilde{\phi}_a) \tilde{u}_{P_0} (D \tilde{\theta}_0) - \tilde{\phi}_a D (\tilde{\theta}_0 \tilde{\phi}_0) \right\} dz \right] (I_{\eta^{(3)}})
 \end{aligned}$$

where $D = \frac{d}{dz}$ and $I_{\eta^{(2)}}$, $I_{\eta^{(xy)}}$, $I_{\eta^{(3)}}$ are given by

$$\begin{aligned} I_{\eta^{(2)}} &= \lim_{L \rightarrow \infty} \frac{1}{4L^2} \int_{-L}^L \int_{-L}^L \eta_1^2 dx dy \\ I_{\eta^{(xy)}} &= \lim_{L \rightarrow \infty} \frac{1}{4L^2} \int_{-L}^L \int_{-L}^L \left\{ \left(\frac{\partial \eta_1}{\partial x} \right)^2 + \left(\frac{\partial \eta_1}{\partial y} \right)^2 \right\} \eta_1 dx dy \\ I_{\eta^{(3)}} &= \lim_{L \rightarrow \infty} \frac{1}{4L^2} \int_{-L}^L \int_{-L}^L \eta_1^3 dx dy \end{aligned} \quad (28)$$

Carrying out the integrations and taking the limits, we obtain an equation satisfied by the amplitude as

$$c_1 \frac{dA}{d\tau} = c_2 A + c_3 A^2$$

where c_1, c_2, c_3 can be expressed as

$$\begin{aligned} c_1 &= \int_0^\delta \left\{ \tilde{\theta}_a (\mathcal{S}\tilde{\phi}_0 - \tilde{\theta}_0) + \tilde{\phi}_a [(C - \theta_b)\tilde{\phi}_0 + (1 - \phi_b)\tilde{\theta}_0] \right\} dz \\ c_2 &= \alpha^2 \mathcal{R}_I \int_0^\delta \tilde{w}_a \tilde{\theta}_0 dz \\ c_3 &= \int_0^\delta \left[\alpha^2 (\tilde{\theta}_a - \tilde{\phi}_a) \left\{ \tilde{u}_{p_0} (D\tilde{\theta}_0) + \frac{1}{2} \tilde{\theta}_0 (D\tilde{u}_{p_0}) \right\} - \tilde{\phi}_a D (\tilde{\theta}_0 \tilde{\phi}_0) \right] dz \end{aligned} \quad (29)$$

Thus a Landau type equation is

$$\frac{dA}{d\tau} = bA + cA^2 \quad (30)$$

where $b = \frac{c_2}{c_1}$, $c = \frac{c_3}{c_1}$, and c_1, c_2, c_3 are given in (29). Here b is known as the Landau constant. Solution of this Landau type equation (30) is obtained as

$$A(\tau) = \frac{A_0}{\left(1 + \frac{c}{b} A_0\right) e^{-b\tau} - \frac{c}{b} A_0} \quad (31)$$

Here $A_0 = A(0)$ the initial value of A . The steady state solution for the amplitude can be obtained as $A(\infty) = -\frac{b}{c}$.

6. First Order Solutions

Here we consider first-order solutions for time independent and constant amplitude case.

$$\nabla^2 w_1 + \mathcal{R}_c (\Delta_2 \theta_1) = -\mathcal{R}_1 (\Delta_2 \theta_0) \quad (32)$$

$$\begin{aligned} \left(\nabla^2 + \frac{\partial}{\partial z} \right) \theta_1 - \mathcal{S} \frac{\partial \phi_1}{\partial z} - \theta'_b w_1 &= \frac{\partial^2 u_{P_0}}{\partial x \partial z} \frac{\partial \theta_0}{\partial x} + \\ &+ \frac{\partial^2 u_{P_0}}{\partial y \partial z} \frac{\partial \theta_0}{\partial y} - (\Delta_2 u_{P_0}) \frac{\partial \theta_0}{\partial z} \end{aligned} \quad (33)$$

$$\begin{aligned} \frac{\partial}{\partial z} \{ (\theta_b - C) \phi_1 - (1 - \phi_b) \theta_1 \} + \theta'_b w_1 &= -\frac{\partial}{\partial z} (\theta_0 \phi_0) \\ - \frac{\partial^2 u_{P_0}}{\partial x \partial z} \frac{\partial \theta_0}{\partial x} - \frac{\partial^2 u_{P_0}}{\partial y \partial z} \frac{\partial \theta_0}{\partial y} + (\Delta_2 u_{P_0}) \frac{\partial \theta_0}{\partial z} \end{aligned} \quad (34)$$

Writing $[w_1, \theta_1, \phi_1] = \xi_1(x, y) [w_{10}(z), \theta_{10}(z), \phi_{10}(z)] + \xi_2(x, y) [w_{11}(z), \theta_{11}(z), \phi_{11}(z)]$ where $\xi_1(x, y) = \sum_{j=1}^3 e^{i\bar{a}_j \cdot \bar{r}}$, $\xi_2(x, y) = \sum_{j=1}^3 e^{2i\bar{a}_j \cdot \bar{r}}$, and \bar{a}_j 's are already defined in the previous section, it can be shown that (see appendix) the unknowns w_{10} , θ_{10} and ϕ_{10} are solutions of

$$(D^2 - \alpha^2) w_{10} - \alpha^2 \mathcal{R}_c \theta_{10} = \alpha^2 \mathcal{R}_1 \tilde{\theta}_0 \quad (35)$$

$$\begin{aligned} (D^2 + D - \alpha^2) \theta_{10} - \mathcal{S} (D\phi_{10}) - \theta'_b w_{10} \\ = \alpha^2 \left\{ \tilde{\theta}_0 (D\tilde{u}_{P_0}) + 2\tilde{u}_{P_0} (D\tilde{\theta}_0) \right\} \end{aligned} \quad (36)$$

$$\begin{aligned} D[(C - \theta_b) \phi_{10} + (1 - \phi_b) \theta_{10}] - \theta'_b w_{10} \\ = 2D(\tilde{\theta}_0 \tilde{\phi}_0) + \alpha^2 \left\{ \tilde{\theta}_0 (D\tilde{u}_{P_0}) + 2\tilde{u}_{P_0} (D\tilde{\theta}_0) \right\} \end{aligned} \quad (37)$$

and the unknowns w_{11} , θ_{11} and ϕ_{11} satisfy

$$(D^2 - 4\alpha^2) w_{11} - 4\alpha^2 \mathcal{R}_c \theta_{11} = 0 \quad (38)$$

$$\begin{aligned} (D^2 + D - 4\alpha^2) \theta_{11} - \mathcal{S} (D\phi_{11}) - \theta'_b w_{11} \\ = \alpha^2 \left\{ \tilde{u}_{P_0} (D\tilde{\theta}_0) - \tilde{\theta}_0 (D\tilde{u}_{P_0}) \right\} \end{aligned} \quad (39)$$

$$\begin{aligned} D[(C - \theta_b) \phi_{11} + (1 - \phi_b) \theta_{11}] - \theta'_b w_{11} \\ = D(\tilde{\theta}_0 \tilde{\phi}_0) + \alpha^2 \left\{ \tilde{u}_{P_0} (D\tilde{\theta}_0) - \tilde{\theta}_0 (D\tilde{u}_{P_0}) \right\} \end{aligned} \quad (40)$$

7. Numerical Results and Discussion

To obtain our computational results for the solutions of the basic state and the linear system, we choose the parameters $C = 9.0$, $S = 3.2$ and $\theta_\infty = 0.1$ from available experimental data (Tait et al. 1992, Chen 1995). The mushy layer depth is calculated from the solutions of the basic state. Computed value of the mushy layer depth is 1.989359.

After computing the basic state solutions using (3) and (4), we obtain the critical Rayleigh number and critical wavenumber by solving the system given by (14) numerically using the fourth-order Runge-Kutta in combination of shooting method. In order to solve this system, we first convert it into a system of five linear first-order ordinary differential equations. Critical Rayleigh number and critical wavenumber are found to be 18.5118 and 1.71 respectively.

Comparisons of linear solid fraction (ϕ_0) and nonlinear solid fraction ($\phi_0 + \epsilon\phi_1$) are presented in Figure 2 and Figure 3 for two set of values of (x, y) . We notice that solid fraction is positive at $(0, 0)$ and negative at $(1.6, 1.4)$ such locations can be indentified at center and near the boundary of one hexagonal cell, which is based on "zeroth order" linear perturbation system. Difference in nonlinear and linear solutions is highest at the solidifying front and diminishes towards the top of the layer.

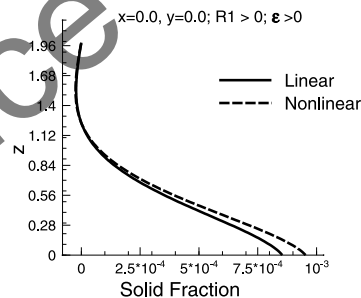


Figure 2. Linear and nonlinear solid fractions at $x = 0, y = 0$.

Figure 4 and Figure 5 depict the supercritical and subcritical results for nonlinear solid fraction. In both cases, from numerical results it is found that supercritical solutions dominate the subcritical solutions.

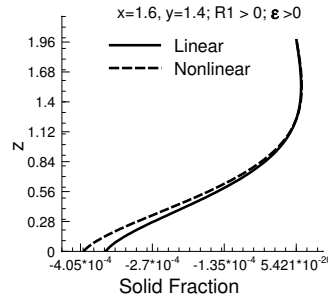


Figure 3. Linear and nonlinear solid fractions at $x = 1.6$, $y = 1.4$.

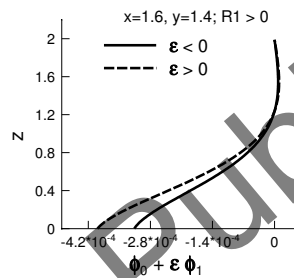


Figure 4. Supercritical and subcritical nonlinear solid fractions at $x = 1.6$, $y = 1.4$.

Comparison of linear vertical velocity component (w_0) and nonlinear counterpart ($w_0 + \varepsilon w_1$) is shown in Figure 6. We see that difference in nonlinear and linear solutions is maximum near the center, namely at $z = 0.796$, and it decreases towards the interfaces. Supercritical and subcritical results for nonlinear vertical velocity is given in Figure 7. From numerical data, it is clear that the supercritical solution dominates the subcritical solution.

Figure 8 and Figure 9 present nonlinear solid fraction and vertical velocity results respectively for $R_1 > 0$ and $R_1 < 0$ at $(1.6, 1.4)$. It is observed that changes in the sign of R_1 not only changes the sign of dependent variable, but also affect its magnitude.

Nonlinear vertical velocity and solid fraction are displayed in Figure 10 and

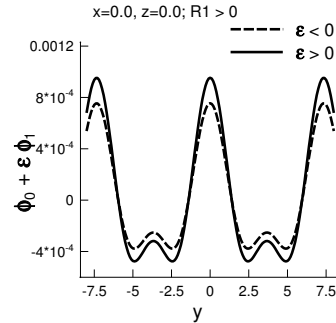


Figure 5. Supercritical and subcritical nonlinear solid fractions at the solidifying front.

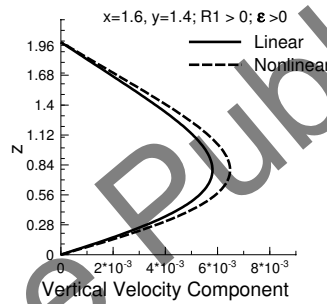


Figure 6. Linear and nonlinear vertical velocity components at $x = 1.6$, $y = 1.4$.

Figure 11 as a function of y for fixed values of x and z . It is observed that periodicity of y is approximately $(-3.9, 3.9)$.

Nonlinear vertical velocity and solid fraction are displayed in Figure 12 and Figure 13 as a function of x for fixed values of y and z . It is observed that periodicity of y is approximately $(-2.1, 2.1)$.

Figure 14 presents nonlinear solid fraction at the solidifying front as a function of y . Numerical results suggest that at $(2.1, 3.9)$ and $(2.1, -3.9)$, which are at boundary with respect to y , solid fractions are positive and but, at $(2.1, 0.0)$, it is negative. On the other hand, at $(0.0, 0.0)$, i.e., at the center solid fraction is

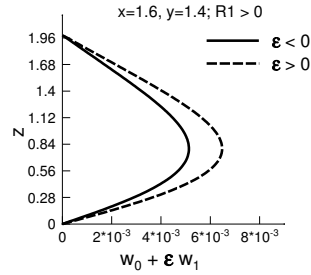


Figure 7. Supercritical and subcritical nonlinear vertical velocity components.

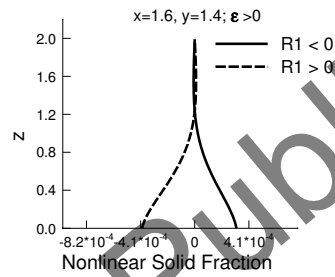


Figure 8. Nonlinear solid fraction for $R_1 > 0$ and $R_1 < 0$.

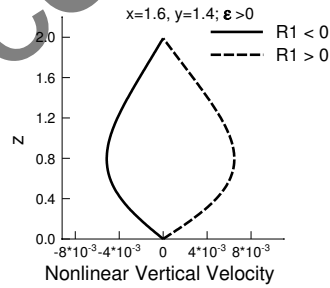


Figure 9. Nonlinear vertical velocity for $R_1 > 0$ and $R_1 < 0$.

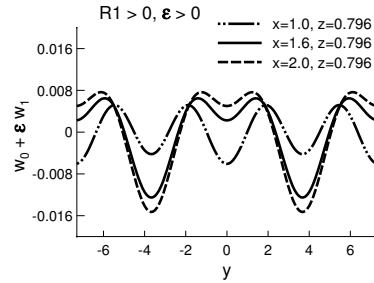


Figure 10. Nonlinear vertical velocity as function of y for fixed x and z .

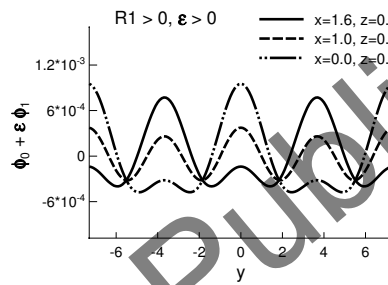


Figure 11. Nonlinear solid fraction as function of y for fixed x and z .

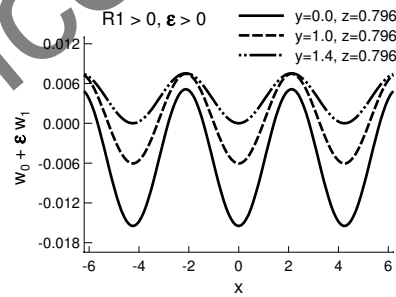


Figure 12. Nonlinear vertical velocity as function of x for fixed y and z .

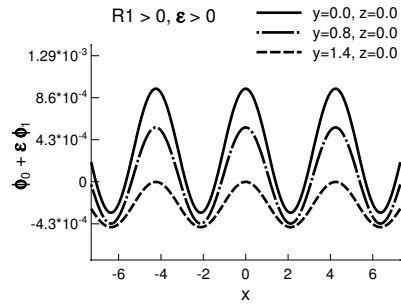


Figure 13. Nonlinear solid fraction as function of x for fixed y and z .

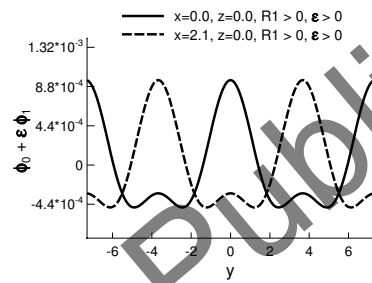


Figure 14. Nonlinear solid fraction at the center and boundary of a cell along x

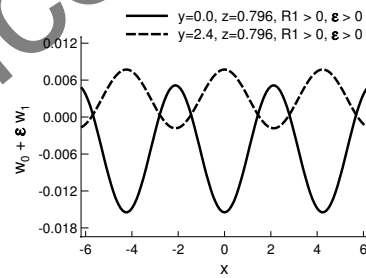


Figure 15. Nonlinear vertical velocity at the center and boundary of a cell along y

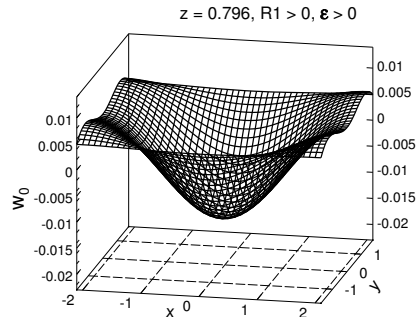


Figure 16. Linear vertical velocity for one period with respect to $x - y$ at $z = 0.796$.

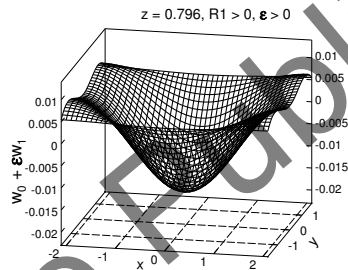


Figure 17. Nonlinear vertical velocity for one period with respect to $x - y$ at $z = 0.796$.

positive. Figure 15 presents nonlinear vertical velocity for $z = 0.796$. Minimum value of this variable occurs at the center. i.e. at $(0.0, 0.0)$. Vertical velocity is positive at the boundary.

Figure 16 and Figure 17 show comparison of linear and nonlinear vertical velocity for one period of x and y at $z = 0.796$. It is observed that vertical velocity is negative at the center of the cell suggesting a downward movement. Also magnitude of nonlinear solution is higher than that of linear solution.

Nonlinear vertical velocity is shown in Figure 18 for few cells for $z = 0.796$. Numerical investigation suggests that vertical velocity is highest and positive at the center cell boundaries. It is lowest and negative at the center of the cells.

Hence there is an upward flow at the boundaries and downward flow at the center of the cells.

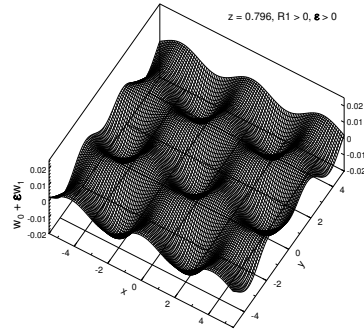


Figure 18. Nonlinear vertical velocity at $z = 0.796$.

Figure 19 displays nonlinear solid fraction, which attains its maximum or minimum at the solidifying front. It is noticed that at the center of the cells, solid fraction is positive and at the boundary of the cells, it is negative. At the solidifying front, vertical velocity is zero.

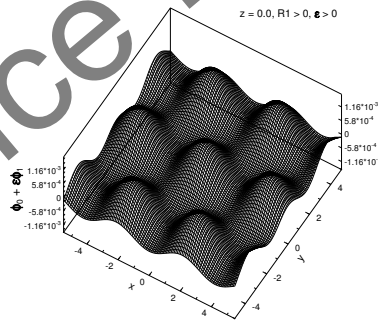


Figure 19. Nonlinear solid fraction at the solidifying front.

Conclusion

Here we have analyzed the nonlinear effect of a three dimensional convective flow in a mushy layer which is formed when a binary alloy is solidified from below. The solutions are obtained for hexagonal cell patterns since hexagonal cell patterns are experimentally observed for such a flow. After obtaining the critical Rayleigh number and wave number, we have derived the linear and adjoint systems analytically for the mushy layer with an impermeable mush-liquid interface. Numerical results are obtained by using fourth-order Runge-Kutta method in combination of shooting method. Finally we derive the first-order system by using the property of adjoint system. Nonlinear effects of dependent variables which depend on linear and adjoint solutions are computed numerically and presented in graphical forms. Numerical results suggest that that maximum variation of the vertical component occurs in the middle of the layer. For solid fraction maximum changes appear at the solid-liquid interface. Our observation is that nonlinear effects are not prominent for super-critical case whereas these have a important role for sub-critical case. We also found that tendency for chimney formation takes place mainly in the lower half of the mushy layer and with the highest of such tendency at the lower boundary of the layer which is consistent and in agreement with experimental observation.

References

- [1] L. D. Landau, *On the problem of turbulence*, C. R. Acad. Sci. U. R. S. S., 44 (1944), pp. 311–314.
- [2] P. G. Drazin and W. H. Reid, *Hydrodynamic Stability*, Cambridge University Press, Cambridge, 1981.
- [3] S. Chandrasekhar, *Hydrodynamic and hydromagnetic stability*, Oxford University Press, Oxford, 1981.
- [4] A. C. Fowler, *The formation of freckles in binary alloys*, IMA. J. Appl. Math., 35 (1985), pp. 159–174.
- [5] M. G. Worster, *Natural convection in a mushy layer*, J. Fluid Mech., 224 (1991), pp. 335–359.

- [6] C. F. Chen, and F. Chen, *Experimental study of directional solidification of aqueous ammonium chloride solution*, J. Fluid Mech., 227 (1991), pp. 567–586.
- [7] M. G. Worster, *Instabilities of the liquid and mushy regions during solidification of alloys*, J. Fluid Mech., 237 (1992), pp. 649–669.
- [8] S. Tait and C. Jaupart, *The planform of compositional convection and chimney formation in a mushy layer*, Nature, 359 (1992), pp. 406–408.
- [9] G. Amberg and G. M. Homsy, *Nonlinear analysis of buoyant convection in binary solidification with application to channel formation*, J. Fluid Mech., 252 (1993), pp. 79–98.
- [10] P. Emms and A. C. Fowler, *Compositional convection in the solidification of binary alloys*, J. Fluid Mech., 262 (1994) pp. 111–139.
- [11] D. M. Anderson and M. G. Worster, *Weakly nonlinear analysis of convection in mushy layers during the solidification of binary alloys*, J. Fluid Mech., 302 (1995), pp. 307–331.
- [12] C. F. Chen, *Experimental study of convection in a mushy layer during directional solidification*, J. Fluid Mech., 293 (1995), pp. 81–98.
- [13] B. S. Okhuysen and D. N. Riahi, *On weakly nonlinear convection in mushy layers during solidification of alloys*, J. Fluid Mech., 596 (2008a), pp. 143–167.
- [14] B. S. Okhuysen and D. N. Riahi, *Flow instabilities of liquid and mushy regions during alloy solidification and under high gravity environment induced by rotation*, Int. J. Eng. Sci., 46 (2008b), pp. 189–201.
- [15] S. M. Roper, S. H. Davis and P. W. Voorhees, *An analysis of convection in a mushy layer with deformable permeable interface*, J. Fluid Mech., 596 (2008), 333-352.
- [16] D. N. Riahi, *On oscillatory modes of nonlinear compositional convection in mushy layers*, Nonlinear Analysis: Real World Applications, 10 (2009), pp. 209–226.

- [17] P. Guba and M. G. Worster, (2010) *Interaction between steady and oscillatory convection in mushy layers*, J. Fluid Mech., 645 (2010), pp. 411–434.
- [18] D. Bhatta, M. S. Muddamallappa and D. N. Riahi, *On weakly nonlinear evolution of convective flow in a passive mushy layer*, Nonlinear Analysis: Real World Applications, 11 (2010), pp. 4010–4020.
- [19] D. Bhatta, D. N. Riahi and M. S. Muddamallappa, *On nonlinear evolution of convective flow in an active mushy layer*, Journal of Engineering Mathematics, 74 (2012), pp. 73–89.
- [20] D. Lee, D. Alexandrov and H. N. Huang, *Numerical modeling of one-dimensional binary solidification with a mushy layer evolution*, Numer. Math. Theory Methods Appl., 5, no. 2 (2012), pp. 157–185.
- [21] J. Rees, W. David and M. G. Worster, *Fluxes through steady chimneys in a mushy layer during binary alloy solidification*, J. Fluid Mech., 714 (2013), pp. 127–151.
- [22] A. J. Wells, J. S. Wettlaufer, and S. A. Orszag, *Nonlinear mushy-layer convection with chimneys: stability and optimal solute fluxes*, J. Fluid Mech., 716 (2013), pp. 203–227.

Nova Science Publishing, Inc.

APPENDIX

Derivation of the Adjoint System

The first term in (15) can be expressed as

$$\begin{aligned}
 & \lim_{L \rightarrow \infty} \frac{1}{4L^2} \int_0^\delta \int_{-L}^L \int_{-L}^L w_a (\nabla^2 w_0) dV \\
 &= \lim_{L \rightarrow \infty} \left[\int_{z=0}^\delta \left\{ \frac{1}{2L} \int_{y=-L}^L \left(\frac{1}{2L} \int_{x=-L}^L w_a \frac{\partial^2 w_0}{\partial x^2} dx \right) dy \right\} dz \right] \\
 &+ \lim_{L \rightarrow \infty} \left[\int_{z=0}^\delta \left\{ \frac{1}{2L} \int_{x=-L}^L \left(\frac{1}{2L} \int_{y=-L}^L w_a \frac{\partial^2 w_0}{\partial y^2} dy \right) dx \right\} dz \right] \\
 &+ \lim_{L \rightarrow \infty} \left[\frac{1}{4L^2} \int_{y=-L}^L \int_{x=-L}^L \left\{ \int_{z=0}^\delta w_a \frac{\partial^2 w_0}{\partial z^2} dz \right\} dx dy \right] \quad (41)
 \end{aligned}$$

For the first term on the right hand side of (41), we get

$$\int_{-L}^L w_a \frac{\partial^2 w_0}{\partial x^2} dx = \left[w_a \frac{\partial w_0}{\partial x} - w_0 \frac{\partial w_a}{\partial x} \right]_{-L}^L + \int_{-L}^L w_0 \frac{\partial^2 w_a}{\partial x^2} dx \quad (42)$$

As the first term and second term in right hand side of (42) yield a fixed value, say K , we obtain

$$\begin{aligned}
 \lim_{L \rightarrow \infty} \frac{1}{2L} \int_{x=-L}^L w_a \frac{\partial^2 w_0}{\partial x^2} dx &= \lim_{L \rightarrow \infty} \left[\frac{K}{2L} + \frac{1}{2L} \int_{x=-L}^L w_0 \frac{\partial^2 w_a}{\partial x^2} dx \right] \\
 &= \lim_{L \rightarrow \infty} \frac{1}{2L} \int_{-L}^L w_0 \frac{\partial^2 w_a}{\partial x^2} dx
 \end{aligned}$$

For the third term on the right hand side of (41), we obtain

$$\int_{z=0}^\delta w_a \frac{\partial^2 w_0}{\partial z^2} dz = \left[w_a \frac{\partial w_0}{\partial z} \right]_0^\delta - \left[w_0 \frac{\partial w_a}{\partial z} \right]_0^\delta + \int_{z=0}^\delta w_0 \frac{\partial^2 w_a}{\partial z^2} dz$$

Usage of the boundary conditions for linear and adjoint solutions w_0 and w_a at $z = 0$ and $z = \delta$, above result yields $\int_0^\delta w_a \frac{\partial^2 w_0}{\partial z^2} dz = \int_0^\delta w_0 \frac{\partial^2 w_a}{\partial z^2} dz$. Thus, the first term in (15) becomes

$$\lim_{L \rightarrow \infty} \frac{1}{4L^2} \int_0^\delta \int_{-L}^L \int_{-L}^L w_0 (\nabla^2 w_a) dV \quad (43)$$

Similarly, we can write the second term in (15) as

$$\lim_{L \rightarrow \infty} \frac{1}{4L^2} \int_0^\delta \int_{-L}^L \int_{-L}^L [\theta_0 \mathcal{R}(\Delta_2 w_a)] dV \quad (44)$$

The third term in (15)

$$\lim_{L \rightarrow \infty} \frac{1}{4L^2} \int_0^\delta \int_{-L}^L \int_{-L}^L \theta_a \left(\nabla^2 \theta_0 + \frac{\partial \theta_0}{\partial z} \right) dV \quad (45)$$

First two terms of (45) can be simplified by using integration by parts and the boundary conditions on θ_0 and θ_a as

$$\lim_{L \rightarrow \infty} \frac{1}{4L^2} \int_0^\delta \int_{-L}^L \int_{-L}^L \theta_0 \left(\nabla^2 \theta_a - \frac{\partial \theta_a}{\partial z} \right) dV$$

Now, considering all terms, (15) becomes

$$\begin{aligned} & \lim_{L \rightarrow \infty} \frac{1}{4L^2} \int_0^\delta \int_{-L}^L \int_{-L}^L [w_0 \{ \nabla^2 w_a - \theta'_b \theta_a + \theta'_b \phi_a \} \\ & + \theta_0 \left\{ \mathcal{R}(\Delta_2 w_a) + \left(\nabla^2 - \frac{\partial}{\partial z} \right) \theta_a + (1 - \phi_b) \frac{\partial \phi_a}{\partial z} \right\} \\ & + \phi_0 \left\{ \mathcal{S} \frac{\partial \theta_a}{\partial z} + (C - \theta_b) \frac{\partial \phi_a}{\partial z} \right\}] dV = 0 \end{aligned} \quad (46)$$

Thus the adjoint system is

$$\begin{aligned} \nabla^2 w_a - \theta'_b \theta_a + \theta'_b \phi_a &= 0 \\ \mathcal{R}(\Delta_2 w_a) + \left(\nabla^2 - \frac{\partial}{\partial z} \right) \theta_a + (1 - \phi_b) \frac{\partial \phi_a}{\partial z} &= 0 \\ \mathcal{S} \frac{\partial \theta_a}{\partial z} + (C - \theta_b) \frac{\partial \phi_a}{\partial z} &= 0 \end{aligned}$$

Derivation of the First-Order System

If $\xi_1(x, y) = \sum_{j=1}^3 e^{i\bar{a}_j \bar{r}}$ and $\xi_2(x, y) = \sum_{j=1}^3 e^{2i\bar{a}_j \bar{r}}$, it can be shown that $\xi_1^2 = \xi_2 + 2\bar{\xi}_1$ because of the properties of \bar{a}_j . Here $\bar{\xi}_1$ is the conjugate of ξ_1 . Now for the first order system, the equation corresponding to (32) can be written as

$$\nabla^2 (\xi_1 w_{10}) + \mathcal{R}_c \Delta_2 (\xi_1 \theta_{10}) + \nabla^2 (\xi_2 w_{11}) + \mathcal{R}_c \Delta_2 (\xi_2 \theta_{11}) = -\mathcal{R}_1 \Delta_2 (\xi_1 \tilde{\theta}_0)$$

Equivalent equation for (33) is given by

$$\begin{aligned} & \left(\nabla^2 + \frac{\partial}{\partial z} \right) (\xi_1 \theta_{10}) - S \frac{\partial}{\partial z} (\xi_1 \phi_{10}) - \theta'_b \xi_1 w_{10} \\ & + \left(\nabla^2 + \frac{\partial}{\partial z} \right) (\xi_2 \theta_{11}) - S \frac{\partial}{\partial z} (\xi_2 \phi_{11}) - \theta'_b \eta \xi_2 w_{11} \\ & = \frac{\partial^2 (\xi_1 \tilde{u}_{p_0})}{\partial x \partial z} \frac{\partial (\xi_1 \tilde{\theta}_0)}{\partial x} + \frac{\partial^2 (\xi_1 \tilde{u}_{p_0})}{\partial y \partial z} \frac{\partial (\xi_1 \tilde{\theta}_0)}{\partial y} \\ & \quad - \Delta_2 (\xi_1 \tilde{u}_{p_0}) \frac{\partial (\xi_1 \tilde{\theta}_0)}{\partial z} \end{aligned}$$

The equation corresponding to (34) yields

$$\begin{aligned} & \frac{\partial}{\partial z} \{ (\theta_b - C) \xi_1 \phi_{10} - (1 - \phi_b) \xi_1 \theta_{10} \} + \theta'_b \xi_1 w_{10} \\ & \frac{\partial}{\partial z} \{ (\theta_b - C) \xi_2 \phi_{11} - (1 - \phi_b) \xi_2 \theta_{11} \} + \theta'_b \xi_2 w_{11} \\ & = - \frac{\partial}{\partial z} (\xi_1^2 \tilde{\theta}_0 \tilde{\phi}_0) + \frac{\partial^2 (\xi_1 \tilde{u}_{p_0})}{\partial x \partial z} \frac{\partial (\xi_1 \tilde{\theta}_0)}{\partial x} \\ & \quad + \frac{\partial^2 (\xi_1 \tilde{u}_{p_0})}{\partial y \partial z} \frac{\partial (\xi_1 \tilde{\theta}_0)}{\partial y} - \Delta_2 (\xi_1 \tilde{u}_{p_0}) \frac{\partial (\xi_1 \tilde{\theta}_0)}{\partial z} \end{aligned}$$

Using $Re [\xi_1^2] = \eta_2 + 2\eta_1$, $Re \left[\left(\frac{\partial \xi_1}{\partial x} \right)^2 + \left(\frac{\partial \xi_1}{\partial y} \right)^2 \right] = -\alpha^2 \{ \eta_2 - \eta_1 \}$ where $\eta_1(x, y) = Re [\xi_1(x, y)]$ and $\eta_2(x, y) = Re [\xi_2(x, y)]$ and then comparing the coefficients of η_1 and η_2 , we obtain the first-order system (35)-(40).

Nova Science Publishing, Inc.

In: Crystal Growth
Editors: J. Li, J. Li and Y. Chu

ISBN: 978-1-53612-203-9
© 2017 Nova Science Publishers, Inc.

Chapter 6

**METAL–ORGANIC FRAMEWORKS:
DESIGN AND APPLICATIONS**

*Yue Liang, Xia Zhang and Da-Bin Qin**

Key Laboratory of Chemical Synthesis and Pollution Control of
Sichuan Province, School of Chemistry and Chemical Engineering,
China West Normal University, Nanchong, P.R. China

ABSTRACT

Metal–organic frameworks are a new class of organic-inorganic hybrid porous materials with high physical surface areas, robust porosity, diverse and designable structure. This areas has obtained a fast development over the past few decades. In this mini review, we describe the synthetic strategies, structures, properties and applications of metal–organic frameworks (MOFs) with a number of selected examples.

Keywords: Metal–Organic Frameworks (MOFs), synthetic strategies, porous functional materials

* Corresponding author. E-mail: qdbkyl@cwnu.edu.cn; Fax: (+86)-817-256-8081.

INTRODUCTION

Metal-organic frameworks (MOFs), also named porous coordination polymers (PCPs), are originated from the subject of supramolecular chemistry and inspired by crystal engineering. Generally, MOFs are self-assembled by metal ions (or metal clusters) and polydentate organic ligands via ionocovalent or coordinate bond. As we all known, porous materials are widely used in catalysis [1-3], gas storage [4-7], drug delivery [8, 9] and magnetic properties [10, 11], owing to their high physical surface areas, robust porosity, adjustable structure, high thermal stability and chemical stability. However, in the 1990s, only inorganic carbon-based materials were widely applied in industry. For example, zeolites were thermally stable but degradable (or indeed dissolved) under certain chemical conditions. Activated carbons with good thermal and chemical stability were limited by scope for synthetic diversification. Until the 1960s, the first coordination polymer was synthesized, which bridged the gap between the inorganic chemistry and organic chemistry and overcome the shortcomings of the traditional materials. The rapid development occurred in 1990 after the Robson reported the first infinite three dimensional MOFs of which size and shape of cavities were determined by organic molecular [12]. In addition, this example supplied a new strategy to deliberate the design and construction of MOFs. Another new chapter was opened by Yaghi et al. In 1999, Yaghi et al. reported the structure of MOF-5 and defined the concept of reticular design [13]. From then on, numbers of publications in this field exponentially increased but MOFs were still synthesized by chance. It is demanding to have a general method for design and development of such materials.

Based on this point, O’Keeffe proposed a systematic terminology to classify the known structures based on the structures of the MOF’s [14]. R. Robson applied “node and spacer” viewpoint to generate coordination polymers and predict the structure but this approach could only be applied to be simple MOFs [15]. This challenge came from the intricate coordination mode of metal ions and ligands, especially the polydentate metal and organic ligand. What’s more, the PH, solvent, temperature and

counter anions can also affect the final structure. Although it is difficult to predict and get the precise structure of the desired material, some strategies have been widely used to underpin this work. For example, we have established the secondary units (SBUs) by using extendable organic ligands to facilitate network design, inhibit interpenetration and enhance the framework against disintegration upon guest removal. This method is helpful to address the issue of network synthesis and robustness [13, 16]. Furthermore, structure-directed agents (SDA) were applied to hierarchical porous MOFs, guiding mesopore assembly and increasing mass transport [17-21]. Thirdly, precursors were used to form framework structures that can be modified to our desired MOFs by *in situ* deprotecting the functional groups of the precursors [22]. The deprotective strategy was applied to synthesize the phase-pure MOFs such as Al-MIL-100 reported by C. Volkringer [23]. Finally, molecular simulations can be simply and quickly used to calculate the geometric surface areas of MOFs. Many examples have shown that the calculated value matches well with the actual Brunner–Emmet–Teller (BET) areas, which suggest that molecular simulation is an effective and efficient way to judge the pores size and the adsorption capability of materials [24-26]. Those strategies help us obtain better structure as we expected.

In this chapter, we will give a brief account of the design, synthesis and application of metal-organic frameworks by reviewing a large number of examples.

SYNTHESIS

Diffusion Synthesis

Liquid diffusion is beneficial to obtain crystals consisting of two different reactants which are dissolved in two different solvents. The reactants react with each other by slow diffusion at the interface of the different solvents and give rise to crystals. The rate of crystallization is effectively reduced by solvent-liquid diffusion, which involves three

discrete layers: One layer of the product solution, another layer of the precipitant solvent, and the final layer which is applied to isolate the other two layers and slowly produces crystals at the interface. This method is also benefit to separate crystals for X-ray diffraction analysis [27-29].

Vapor Diffusion

The basic operation of vapor diffusion is that compound is dissolved in the bigger solubility of A, and then put solvent A and B in an airtight container. Solvent B spreads to the solution of A and at the same time solvent B spreads to the solution of A. The growth of crystals will be slowly formed as the solution becomes saturated by solution A turning into a mixed solution of A and B. The growth rate of crystals can be controlled by adjusting the diffusion velocity of solvents [30, 31]. Chen et al. synthesised the Zn(II) complex $\text{Zn}(\text{INA})_2(\text{H}_2\text{O})_4$ (INA = isonicotinate) at the air–water interface under kinetically control. $\text{Zn}(\text{NO}_3)_2 \cdot 6\text{H}_2\text{O}$, isonicotinic acid (HINA), and distilled H_2O were mixed in a vial. $\text{NH}_3 \cdot \text{H}_2\text{O}$ was placed in another vial. The two vials were connected by a rubber tube fitted with a clip, and they were fixed on a foam panel. On releasing the clip, a thin, single-crystal film of $\text{Zn}(\text{INA})_2(\text{H}_2\text{O})_4$ was grown over a period of 12 h, which was dehydrated at 100°C for 1 h to afford $\text{Zn}(\text{INA})_2$. Moreover, NH_3 , as a gaseous base, could catalyze the reaction through gas diffusion, instead of directly adding ammonia solution to the reaction mixture affording an appropriate environment for the rapid, catalytic-like growth of single crystals.

Hydrothermal (or Solvothermal) Synthesis

To attain the indissolvable compound crystals, hydrothermal method or solvothermal method is normally used to facilitate the self-assembly of products. The basic principle of hydrothermal synthesis is dissolution and crystallization again. The specific operation method is that indissolvable

compounds and solvents are put in a steel pressure vessel, also called Teflon vial, and heated to 60°C ~ 260°C, at the same time the pressure of steel pressure vessel is gradually increased, and then precursors are dissolved and crystallization again with slowly cooling. Although the hydrothermal method is used for exploring the formation of mineral in nature condition, it had been generally applied to the synthesis of MOFs [32-37].

Microwave-Reaction Synthesis

Microwave consists of an electromagnetic radiation, which lies between radio waves and infrared frequencies, with relatively large wavelengths of 1 mm to 1 m [38, 39]. Compared to traditional heating mode, MW irradiation will directly trigger molecules that possess a dipole, therefore the energy transfer occurs in less than a nanosecond, resulting in a highly instantaneous temperature (T_i) of the molecules. The instantaneous temperature is a function of MW power input, and greater MW power intensities will result in a higher and more consistent T_i . The MW-assisted reaction rates 1,000 times faster than conventional heating [40]. Microwave-reaction with the advantage of improving the reaction of phase-selective [41, 42], controlling the particle size of crystallization [43, 44] and shorter reactions time has been widely used for the synthesis of MOFs. The crystals made by microwave reaction have similar features as traditional methods.

Ionothermal Synthesis

The method of ionothermal synthesis has been used in many areas, such as polymer materials, traditional porous materials, etc. Recently, this way is also applied to synthesis of MOFs due to the advantage of low vapor pressure, high thermal stability, chemical stability and so on [45-48]. Furthermore, using different ions can obtain different MOFs in

ionothermal synthesis. Chen et al. used the biphenyltetracarboxylic sodium (Na_4BPTC) ligand and $\text{M}(\text{OOCCH}_3)_2$ ($\text{M} = \text{Co}$ and Mn), BMImBr (1-butyl-3-methyl-imidazole bromine) as ionic liquid to synthesis two magnetism MOFs: $[\text{Co}_3\text{Na}_5(\text{BPTC})_3(\text{H}_2\text{O})_2(\text{CH}_3\text{O})_2][\text{BMIm}]$ and $[\text{Mn}_2(\text{BPTC})(\text{CH}_3\text{COO})][\text{BMIm}]$. A series of 2D $[\text{RMI}]_2[\text{Co}_3(\text{BDC})_3\text{X}_2]$ frameworks through the ionothermal reactions of 1,4-benzenedicarboxylic acid (H_2BDC) with $\text{Co}(\text{NO}_3)_2 \cdot 6\text{H}_2\text{O}$ was reported by Zhang et al. In this work, Eight kinds of 1-methyl-3-alkylimidazolium halide $[\text{RMI}]\text{X}$ ($\text{R} =$ ethyl (E), propyl (P), butyl (B) and amyl (A); $\text{MI} =$ imidazolium; $\text{X} = \text{Cl}, \text{I}$) as ionic liquids (ILs) was used as reaction media [49].

Electrochemical Synthesis

In the traditional solvothermal synthesis, the metal ions exist as salt, but in electrochemical synthesis, the metal ions exist as oxidation of the electrode. Reaction time and temperature are obviously lower than regular hydro- or solvothermal synthesis protocols. Changing the metal source, kinetics of forming MOFs can be adjusted. Using $\text{Cu}(\text{NO}_3)_2$ vs $\text{Cu}(\text{OAc})_2$ in the synthesis of HKUST-1 is a typical case [50].

APPLICATION

Adsorptions and Separations

The process which a mixture is separated by difference in adsorption/desorption behavior of distinct components in the mixture is the adsorption separations playing significant roles in industry and daily life [51]. The major influence factors for the adsorption separation process is the size of the adsorbates and the pore of the adsorbents [52, 53]. For a long time, a large number of materials have been explored as adsorbents such as zeolites, activated carbon, carbon nanotubes, porous organic

materials, inorganic and polymeric resins etc. However, the applications of those adsorbents are limited by steric, kinetic and equilibrium effects. MOFs as a class of new materials with a high BET surface area of 1000-8000 m² g⁻¹. As the gas storage is based on physisorption, we believe that increasing the surface area can some extent enhance the adsorptions capacity of the porous materials. In 2010, Yaghi. O. M et al. reported the MOF-180, MOF-200, MOF-205 and MOF-210 [54]. The octahedral Zn₄O(CO₂)₆ as a secondary units (SBUs) linked one or two kinds of organic linkers ((4,4',4''-[benzene-1,3,5-triyl-trisethyne-2,1-diyl])tribenzoate (BTE), 4,4',44''-[benzene-1,3,5-triyl-tris(benzene-4,1-diyl)]tribenzoate (BBC), 4,4',44''-benzene-1,3,5-triyl-tribenzoate (BTB)/2,6-naphthalenedicarboxylate (NDC), and BTE/biphenyl-4,4'-dicarboxylate (BPDC)). The results showed that the surface area of MOF-180 and MOF-200 was 1.9 and 2.6 greater than MOF-177, respectively. MOF-210 had the Langmuir surface areas of 6240 and 10,400 m² g⁻¹ and its carbon dioxide storage capacity could reach 2870 mg g⁻¹. Farha et al. reported NU-110 with BET surface areas of 7140 m² g⁻¹ and the capacity of nitrogen uptakes could reach 2845 cm³ g⁻¹ [55].

The manageable and appropriate pore size of MOFs provide a highly efficient way of selective separation mixed gases based on the kinetic diameter of adsorbate (such as H₂ (2.89 Å), CO₂ (3.3 Å), N₂ (3.64 Å) and CH₄ (3.8 Å)) [56]. S.-J. Lee et al. reported the relative adsorption of Xe and Kr. The order of adsorbent was UiO-66(Zr) (8 Å) < MIL-101(Cr) (8.6 Å) < MIL-100(Fe) (25 Å) [57]. Interestingly, UiO-66(Zr) exhibits the highest Xe and Kr uptakes. The result can be attributed to the appropriate pore sizes (8 Å) of UiO-66(Zr) for Xe (4 Å)/Kr (8 Å). Ma et al. reported catenated PCN-6 and noncatenated PCN-6'. The result proved that the PCN-6 had a higher hydrogen adsorption compared to PCN-6' [58]. Q. Wang and J. K. Johnson discovered that the optimal pore size was around 6 Å, about twice the effective kinetic diameter of the hydrogen molecule [59]. As a consequence, the proper pore sizes and proper pore geometry of MOF shows efficient separation performance for mixed gases. Furthermore, these properties can be further explained by mixture adsorption selectivity (S_{ads}). S_{ads} defined as the ratio of adsorbed amounts

of components in their binary mixtures. The isotherm is calculated with the standard definition: $S_{\text{ads}}(i/j) = [c_i^{\text{mixture}}/c_j^{\text{mixture}}]/[y_i/y_j]$ and is usually used to predict adsorption selectivities at mixture conditions from experimental single-component isotherms [60], where c_i^{mixture} is the adsorbed loading of component i in the mixture calculated from GCMC simulations and y_i is the bulk composition of component i in the mixture.

Using the functional groups such as open acidic metal sites (or coordinatively unsaturated metal sites (CUMs), Lewis acid sites, $-\text{CF}_3$, $-\text{SO}_2$, and others can effectively promote the selective separation [61-70]. Fen Xu and co-workers reported the amine-decorated microporous metal-organic framework CAU-1 which showed high CO_2 uptake capacity (7.2 mmol g^{-1}) and an impressive selectivity for CO_2 over N_2 . The chiral hexagonal Mg-MOF-1 was constructed by helical assembly of Mg^{2+} ions with achiral 3,5-pyridine dicarboxylates showing selective hydrogen (H_2) adsorption (ca. 0.8 wt% at 77 K) and carbon dioxide (CO_2) uptake (ca. 0.7 mmol g $^{-1}$ at 298 K) over nitrogen at 1 atm [71]. Ghosh, S. K et al. foreseen the spatial configurational orientations for Bz (planar p-cloud entity) and Cy (chair or boat configurations), which might play a key role in their desired efficient separation. Therefore, M-MOF-74 as the best Bz-selective MOF sorbent was established by π -Complexation triggering Lewis acid-base interactions between open metal sites (OMS) of metal-organic frameworks (MOFs) and π -e $^{-}$ rich adsorptive benzene (Bz) and had been rationally chosen for comprehensive Bz/Cy selectivity analyses [72]. Due to these attractive features, MOFs have been made into effective adsorbents or membranes for adsorptions and separation, but there is still a doubt whether the adsorbents can be applied in industry, because the kinetic effects of MOF is flexible at high adsorbate loading and pelleting for industrial application.

Luminescence

Metal-organic frameworks (MOFs) with photoluminescence (PL) properties have received wide attention and is a type of viable luminescent

sensory material [73-78]. Unlike adsorption performance, the nature of porosity, original results and considerations are not necessary. The luminescence of MOFs mainly arises from (i) the fluorescent ligand which can constitute the complete process from excitation to the emission of light. (ii) metal-centered with photophysical which can completely metal-based processes from excitation to emission. (iii) the ligand which participate in a combined process with suitable metals ions such as the lanthanides. The mechanism has been illuminated in previous reports [79-81]. Therefore, combining different metals with different ligands can offer the sheer infinite number of possibilities to establish new luminescent MOFs. Furthermore, different types of the charge transfer processes have also been reported, including ligand-to-metal charge transfer (LMCT), ligand-to-ligand charge transfer (LLCT), metal-to-ligand charge transfer (MLCT), metal-to-metal charge transfer (MMCT) and ligand centre luminescence. The different energy transfer processes can allow us to generate luminescent MOF materials with systematically varied emission wavelengths as well as different applications. The inner cavity of a MOF provides ideal locations where interaction between the framework and absorbent can also influence the luminescence processes of the framework. This will lead to change in the luminescence and offer a basic observable, even available to the eye, suggesting a very attractive strategy of sensing/detection.

Currently, small organic molecules have received increasing concerns because of their environmental biological hazards and human health risks. Hence, there exists an extensive interest in the sensing and recognition of small organic molecules. Recently, Yang et al. reported two luminescent MOFs $[Zn_2(TPC_4A)(DMF)(H_2O)_4] \cdot 3H_2O$ and $[(CH_3)_2NH_2]_2[Zn-(TNC_4A)] \cdot 4H_2O$ by varying the fluorescent tags of resorcin arene based on tetracarboxylic acids from phenyl to naphthyl, showing the highly selective detection of small organic molecules [82]. The MOFs were soaked into different organic solvents such as methanol, ethanol, 1-propanol, 2-propanol, DMF, THF, acetone, and acetonitrile. The luminescent intensities were strongly dependent on the solvents. Particularly in the case of acetone, the material showed the most serious quenching effect. The

gradual decrease of the fluorescence intensity was observed upon the addition of acetone to the suspensions of MOFs. It was suggested that their free guest molecules were gradually replaced by acetone, leading to the luminescence intensities of their suspensions quenching. Most strikingly, the clear fluorescence “on-off” switch-functions toward small organic molecules were observed, which was exceeding rare. The fluorescence property of Ln-MOFs (Ln = Eu) in different solvent was reported by Wang et al. [83]. The strong fluorescence quenching was exhibited upon the presence of NB and CH₃CN and electron transfer from the antenna ligand to the analyte.

The reports of luminescent MOFs detecting the volatile organic compounds (VOCs) and semi-volatile organic compounds (SVOCs: volatile fatty acids (VFAs), phenolic, and indolic compounds) were increase day by day due to the potent role of metal organic frameworks (MOFs) which overcome the limited adsorption capacity, high energy costs, and toxic. Among VOCs, the detection of nitroaromatics had especially attracted a lot of attention as some kind of fast detection of explosives [84-86]. Yang et al. reported thin film sensor MOF Eu-TDC which could rapidly detect the nitroaromatic explosives (nitrobenzene (NB), 4-nitrotoluene (4-NT), 2,4-dinitrotoluene (2,4-DNT), 1,3-dinitrobenzene (1,3-DNB), 4-nitrophenol (4-NP), 2,4-dinitrophenol (2,4-DNP) and 2,4,6-trinitrophenol (TNP)), especially to nitrophenols (TNP/DNP/4-NP) [87]. The cathodic electrodeposition process of Eu-TDC thin film included (1) OH⁻ ion that was generated by reduction of nitrate; (2) deprotonation of ligands (H₂TDC) triggered by OH⁻ ion and (3) the assembly of Eu³⁺ and TDC²⁻ into MOF thin films. The results proved that the electron-deficient property of NACs. Upon excitation, electrons were typically transferred from the conduction band (CB) of MOFs to the lowest unoccupied molecular orbitals (LUMOs) of analytes, causing the quenching and resonance energy transfer from the ligand of Eu-TDC thin film site to nitrophenols. The quenching of metal-centered emission might be the reason. Developing MOFs thin film by electrodeposition offered a new avenue to design convenient and recyclable luminescent devices for sensing nitroaromatic explosives.

Another main interest is the sensing of cations and anions, especially of metal cations. Zhao et al. exemplified luminescent probes of Zn-MOFs ($[\text{Zn}(\text{btz})]_n$) (**1**) and $\{[\text{Zn}_2(\text{ttz})\text{H}_2\text{O}]_n\}$ (**2**) (1,5-bis(5-tetrazolo)-3-oxapentane (H_2btz) and 1,2,3-Tris-[2-(5-tetrazolo)-ethoxy] propane (H_3ttz)). Twelve different kinds of ions in solution were slowly dropped into suspension solution of MOFs. The vastly fluorescence quenching effect of $\text{Cr}_2\text{O}_7^{2-}/\text{CrO}_4^{2-}$ was observed and hardly influenced by introducing other anions. The Stern-Volmer equation, indicating of that the quenching mechanisms were assigned to dynamic quenching processes. This report provided a new way for the practical applications of MOFs in detecting pollutant anions [88]. Wang and co-worker prepared eleven water-stable isostructural mono/bimetallic lanthanide coordination polymers (Ln-CPs) $\{[\text{Eu}_x\text{Tb}_{1-x}(\text{HL})(\text{H}_2\text{O})_3]\cdot\text{H}_2\text{O}\}_n$ ($x = 1.0$ (**1**), 0.9 (**3**), 0.8 (**4**), 0.7 (**5**), 0.6 (**6**), 0.4 (**7**), 0.3 (**8**), 0.2 (**9**), 0.1 (**10**), 0.05 (**11**), 0 (**2**), $\text{H}_4\text{L} = 5,5'-(1\text{H}-2,3,5\text{-triazole-1,4-diyl})\text{diisophthalic acid}$) [89]. Ln-CPs represented by **1** showed a rapid and drastic emission quenching and a quick and high sensitivity for Fe^{3+} and Cr^{3+} cations in aqueous solution. The uncoordinated triazole group formed contacts with $\text{Fe}^{3+}/\text{Cr}^{3+}$ ions which diffused into the pores of **1**, resulting in a low efficiency of energy transfer from ligand to Eu^{3+} and the luminescent quenching of **1**. The bimetallic **3-11** exhibited tunable light emission colors controlled by enhancing and weakening the corresponding emission intensities of Eu^{3+} and Tb^{3+} ions. For example, bimetallic CP **8** could be used as ratiometric luminescent sensors for organic solvent molecules and the luminescent color changes of **8** could be clearly distinguished by the naked eye.

Catalysis

MOFs have received widespread interest as heterogeneous catalysts due to (i) MOFs possess large enough pores to facilitate diffusion of substrates and products. (ii) Metal can be acted as metal node and catalytic sites forming unsaturated coordination site. (iii) Ligands can construct the frameworks or as a catalytic site directly incorporate or post modification.;

and (iv) relatively mild synthesis condition such as solvothermal or diffusion crystallizations can be another strong point. Those advantages make them fulfill requirements such as chiral environment, stable framework, catalytic center and accessible pore so that they can be effectively applied in heterogeneous catalysts. Zhang et al. reported a highly active NMOFs by Pd nanoparticles that supported on nanoscale metal-organic frameworks (NMOFs). High activity and good recyclability was demonstrated in terms of catalytic the Suzuki cross-coupling reaction between aryl/heteroaryl halides and arylboronic acids⁹⁰. Gole B. reported a series of stable Pd NPs in different porous MOFs (Pd@MOF) which shown extremely efficient heterogeneous catalysts for hydrogenation reactions of aryl bromides or iodides and alkenes and Heck-coupling [91].

Magnetism

MMOFs (magnetic metal-organic frameworks) are widely applied in electromagnetism, sensing and devices. The modular chemistry is an effective strategy to construct multifunctional magnetic MOFs by modifying metal ions or constructing various organic ligands. A large number of such materials with 3d transition metals (e.g., Mn, Co, Ni, Fe and Cu) have been synthesized and their magnetic properties have been extensively studied [92-99]. Sui-Jun Liu reported three new antiferromagnetic metal-organic frameworks $\{[\text{Co}_3\text{Na}(\text{BTC})_2(\mu_3\text{-OH})(\text{H}_2\text{O})_3(\text{DMAc})] \cdot \text{H}_2\text{O} \cdot 0.5\text{DMAc}\}_n$ (**1**), $\{[\text{Ni}_3(\text{BTC})_2(\mu_3\text{-OH})(\text{H}_2\text{O})_3] \cdot 2\text{H}_2\text{O} \cdot \text{DMAc}\}_n$ (**2**) and $\{[\text{NH}_2(\text{CH}_3)_2]_2[\text{Mn}_3(\text{BTC})_2(\text{CH}_3\text{COO})_2] \cdot \text{DMAc}\}_n$ (**3**) (DMAc = N,N'-dimethylacetamide) using 3d transition metals (Co, Ni, Mn). The χMT value of **1** and **2** were 10.18 and 2.95 $\text{emu mol}^{-1} \text{K}$, which was much larger than expected spin-only value 5.63 and 2.38 $\text{emu mol}^{-1} \text{K}$ for three magnetically isolated metal ions spin-only value (5.63 $\text{emu mol}^{-1} \text{K}$). In this work, all the carboxylate groups with syn-syn mode also played the dominant role of antiferromagnetic interactions between metal centres [100]. Organic linkers controlling the shape and topology of MMOFs was importance in the building of magnetic

materials. In addition, these ligands had proven to provide good superexchange pathways [101-103].

Drug Delivery

Recently, MOFs have been scaled down to nanometer sizes. NMOFs exhibit higher surface areas, especially the structural diversity and physicochemical properties making them potential for drug molecules [104-107]. Ray C A fabricated the Fe_3O_4 nanoparticles into the porous isorecticular metal organic frameworks (IRMOF-3) and folic acid was conjugated to the surface, developing a magnetic nanoscale metal-organic frameworks (NMOFs) for potential targeted drug delivery. This NMOFs achieved excellent effectiveness for targeting and killing the cancer cells [108]. Tamames-Tabar et al. investigated the cytotoxicity of fourteen nanoscale porous metal organic frameworks with different compositions (Fe, Zn, and Zr; carboxylates or imidazolates) in different cell lines [109].

CONCLUSION

MOFs have become an area of interdisciplinary research. The SBUs is put forward to adjust the pore size and the functionality of MOFs. While the development of reliable and reproducible methods to achieve robust mesoporous MOFs with tailored structures and tunable properties is limited only by imagination and our ability of preparing and characterizing well designed structures. Despite of the challenges, more and more functional MOFs structures have been reported and applied to various domains. However, the correlation between structure and property still didn't get in-depth research. Especially the kinetic effects of MOF framework flexibility are not well explored which is definitely a direction we should devote to.

REFERENCES

- [1] Viklund C, Frantisek Svec A, Fréchet JMJ, Irgum K. Monolithic, "Molded," Porous Materials with High Flow Characteristics for Separations, Catalysis, or Solid-Phase Chemistry: Control of Porous Properties during Polymerization. *Chem Mater*. 1996;8(3).
- [2] Perego C, Millini R. Porous materials in catalysis: challenges for mesoporous materials. *Chem Soc Rev*. 2012;42(9):3956-76.
- [3] Parlett CM, Wilson K, Lee AF. Hierarchical porous materials: catalytic applications. *Chem Soc Rev*. 2012;42(9):3876-93.
- [4] Thomas KM. Hydrogen adsorption and storage on porous materials. *Catal Today*. 2007;120(3-4):389-98.
- [5] Mccanney B, Alain E, Yin YF, Mays TJ. Porous Carbons for Gas Storage and Separation: *Springer Netherlands*; 2001. 677-83 p.
- [6] Sun Y, Zhou L. Gas Storage in Porous Materials. *Oil & Gas Storage & Transportation*.
- [7] Takagi H. Hydrogen Storage in Carbon and Porous Materials (Technology Status of Hydrogen and Natural Gas Storage). *Journal of the Japan Institute of Energy*. 2012;91:461-6.
- [8] Zhao D, Tan S, Yuan D, et al. Surface functionalization of porous coordination nanocages via click chemistry and their application in drug delivery. *Adv Mater*. 2011;23(1):90-3.
- [9] Hou Z, Li C, Ma P, et al. Electrospinning Preparation and Drug-Delivery Properties of an Up-conversion Luminescent Porous $\text{NaYF}_4:\text{Yb}^{3+}, \text{Er}^{3+}$ @Silica Fiber Nanocomposite. *Adv Funct Mater*. 2011;21(12):2356-65.
- [10] Corma A, Rey García F, Atienzar Corvillo P, García Gómez H, Harbuzaru BV. Highly hydrophobic lanthanide-organic porous material with fluorescence and magnetic properties. *Consejo Superior Investigacion*. 2009.
- [11] Xiang J, Chu YQ, Zhou GZ, Guo YT, Shen XQ. Structure and Magnetic Properties of Porous $\text{Ni}_{1-x}\text{Zn}_x\text{Fe}_2\text{O}_4$ Ultrafine Fibers Prepared by Electro spinning Technique. *J Inorg Mater*. 2012;27(4):363-8.

- [12] Hoskins BF, Robson R. Design and construction of a new class of scaffolding-like materials comprising infinite polymeric frameworks of 3D-linked molecular rods. A reappraisal of the $\text{Zn}(\text{CN})_2$ and $\text{Cd}(\text{CN})_2$ structures and the synthesis and structure of the diamond-related frameworks. *J Am Chem Soc.* 1990;112(4):1199-205.
- [13] Li H, Eddaoudi M, O'Keeffe M, Yaghi OM. Design and synthesis of an exceptionally stable and highly porous metal-organic framework. *Nature.* 1999;402(6759):276-9.
- [14] O'Keeffe M, Peskov MA, Ramsden SJ, Yaghi OM. The Reticular Chemistry Structure Resource (RCSR) database of, and symbols for, crystal nets. *Accounts Chem Res.* 2008;41(12):1782-9.
- [15] Braga D. Inorganic crystal engineering: a personal perspective. Journal of the Chemical Society, *Dalton Transactions.* 2000;01(21):3705-13.
- [16] Li H, Eddaoudi M, And TLG, Yaghi OM. Establishing Microporosity in Open Metal-Organic Frameworks: Gas Sorption Isotherms for $\text{Zn}(\text{BDC})$ ($\text{BDC} = 1,4\text{-Benzenedicarboxylate}$). *J Am Chem Soc.* 1998;120(33):8571-2.
- [17] Liu Y, Vch K, Larsen R, Eddaoudi M. Molecular building blocks approach to the assembly of zeolite-like metal-organic frameworks (ZMOFs) with extra-large cavities. *Chem Commun.* 2006;14(14):1488-90.
- [18] Fang QR, Zhu GS, Xue M, Sun JY, Qiu SL. Porous coordination polymers with zeolite topologies constructed from 4-connected building units. *Dalton T.* 2006;250(20):2399-402.
- [19] Zhao Y, Zhang J, Han B, Song J, Li J, Wang Q. Metal–Organic Framework Nanospheres with Well-Ordered Mesopores Synthesized in an Ionic Liquid/ CO_2 /Surfactant System. *Angewandte Chemie International Edition.* 2011;50:636-9.
- [20] Sun LB, Li JR, Park J, Zhou HC. Cooperative Template-Directed Assembly of Mesoporous Metal-Organic Frameworks. *J Am Chem SOC.* 2012;134(1):126-9.

- [21] Górka J, Fulvio PF, Pikus S, Jaroniec M. Mesoporous metal organic framework-boehmite and silica composites. *Chem Commun.* 2010;46(36):6798-800.
- [22] Mohideen MI, Xiao B, Wheatley PS, et al. Protecting group and switchable pore-discriminating adsorption properties of a hydrophilic-hydrophobic metal-organic framework. *Nat Chem.* 2011;3(4):304-10.
- [23] Volkringer C, Popov D, Loiseau T, et al. Synthesis, Single-Crystal X-ray Microdiffraction, and NMR Characterizations of the Giant Pore Metal-Organic Framework Aluminum Trimesate MIL-100. *Chem Mater.* 2009;21(24):5695-7.
- [24] Salles F, Ghoufi A, Maurin G, Bell RG, Mellotdrznieks C, Férey G. Molecular dynamics simulations of breathing MOFs: structural transformations of MIL-53(Cr) upon thermal activation and CO₂ adsorption. *Angewandte Chemie.* 2008;47(44):8487-91.
- [25] Kumar KV, Charalambopoulou G, Kainourgiakis M, Stubos A, Steriotis T. Insights on the physical adsorption of hydrogen and methane in UiO series of MOFs using molecular simulations. *Computational & Theoretical Chemistry.* 2015;1061:36-45.
- [26] Pillai RS. Highly selective CO₂ capture by small pore MOFs assessed by real coadsorption measurements and molecular simulations. *European Conference on Metal Organic Frameworks and Porous Polymers.* 2015.
- [27] Wang C, Lin W. Diffusion-controlled luminescence quenching in metal-organic frameworks. *J Am Chem Soc.* 2011;133(12):4232-5.
- [28] García E, Medina R, Lozano M, Hernández Pérez I, Valero M, Franco A. Adsorption of Azo-Dye Orange II from Aqueous Solutions Using a Metal-Organic Framework Material: Iron-Benzenetricarboxylate. *Materials.* 2014;7(12):8037-57.
- [29] Fujie K, Ikeda R, Otsubo K, Yamada T, Kitagawa H. Lithium Ion Diffusion in a Metal-Organic Framework Mediated by an Ionic Liquid. *Chem Mater.* 2015.

- [30] Chen Y, Yang C, Wang X, Yang J, Ouyang K, Li J. Kinetically controlled ammonia vapor diffusion synthesis of a Zn(II) MOF and its H₂O/NH₃ adsorption properties. *J Mater Chem A*. 2016;4(26).
- [31] Smith MK, Angle SR, Northrop BH. Preparation and Analysis of Cyclodextrin-Based Metal-Organic Frameworks: Laboratory Experiments Adaptable for High School through Advanced Undergraduate Students. *J Chem Educ*. 2015;92(2):368-72.
- [32] Fan L, Fan W, Li B, Zhao X, Zhang X. Hydrothermal syntheses, structural characterizations, and magnetic properties of five MOFs assembled from C₂-symmetric ligand of 1,3-di(2,4-dicarboxylphenyl) benzene with various coordination modes. *RSC ADV*. 2015;5(50):39854-63.
- [33] Z H, Y P, Z K, Y Q, D Z. A Modulated Hydrothermal (MHT) Approach for the Facile Synthesis of UiO-66-Type MOFs. *Inorg Chem*. 2015;54(10):4862-8.
- [34] Lai J, Niu W, Luque R, Xu G. Solvothermal synthesis of metal nanocrystals and their applications. *Nano Today*. 2015;10(2):240-67.
- [35] Zhou J, Chen Z, Sun Z. Hydrothermal synthesis and thermoelectric transport properties of PbTe nanocubes. *Mater Res Bull*. 2015;61:404-8.
- [36] Saha S, Chhetri S, Khanra P, et al. In-situ hydrothermal synthesis of MnO₂/NiO@Ni hetero structure electrode for hydrogen evolution reaction and high energy asymmetric supercapacitor applications. *Journal of Energy Storage*. 2016;6:22-31.
- [37] Zhang Y, Zhong L, Duan D. Single-step hydrothermal synthesis of strontium titanate nanoparticles from crystalline anatase titanium dioxide. *Ceram Int*. 2015;41(10):13516-24.
- [38] Baig RB, Varma RS. Alternative energy input: mechanochemical, microwave and ultrasound-assisted organic synthesis. *ChemInform*. 2012;41(21):1559-84.
- [39] Lidström P, Tierney J, Wathey B, Westman J. Corrigendum to “Microwave assisted organic synthesis-a review” [*Tetrahedron* 57 (2001) 9225-9283]. *Tetrahedron*. 2001;57(51):10229.
- [40] Hayes BL. Recent advances in microwave-assisted synthesis. 2004;3.

- [41] Jhung SH, Jin T, Kim YH, Chang JS. Phase-selective crystallization of cobalt-incorporated aluminophosphate molecular sieves with large pore by microwave irradiation. *Microporous & Mesoporous Materials*. 2008;109(1):58-65.
- [42] Surati MA, Jauhari S, Desai KR. A brief review: Microwave assisted organic reaction. *Archives of Applied Science Research*. 2012;4(1):645-61.
- [43] Stock N, Biswas S. ChemInform Abstract: Synthesis of Metal-Organic Frameworks (MOFs): Routes to Various MOF Topologies, Morphologies, and Composites. *ChemInform*. 2012;43(16):933-69.
- [44] Gawande MB, Shelke SN, Zboril R, Varma RS. Microwave-Assisted Chemistry: Synthetic Applications for Rapid Assembly of Nanomaterials and Organics. *Accounts Chem Res*. 2014;47(4):1338-48.
- [45] Li SY, Liu ZH. Ionothermal synthesis, thermal behavior, and fluorescence of two gallium-1,4-benzenedicarboxylate-based MOFs. *J Coord Chem*. 2015;68(10):1-11.
- [46] Chen WX, Bai JQ, Yu ZH, Liu QP, Zeng GN, Zhuang GL. Ionothermal synthesis, fluorescence, and DFT calculation of three lanthanide-based metal-organic frameworks. *Inorg Chem Commun*. 2015;60:4-7.
- [47] And ERP, Morris RE. 1-Alkyl-3-methyl Imidazolium Bromide Ionic Liquids in the Ionothermal Synthesis of Aluminium Phosphate Molecular Sieves. *Chem Mater*. 2006;18(20):4882-7.
- [48] Xu H, Gao J, Jiang D. Stable, crystalline, porous, covalent organic frameworks as a platform for chiral organocatalysts. *Nat Chem*. 2015;7(11).
- [49] Chen WX, Tan L, Liu QP, Qiang GR, Zhuang GL. The ionothermal synthesis, structure, and magnetism-structure relationship of two biphenyl tetracarboxylic acid-based metal-organic frameworks. *Dalton T*. 2014;43(43):16515-21.
- [50] Yang HM, Song XL, Yang TL, Liang ZH, Fan CM, Hao XG. Electrochemical synthesis of flower shaped morphology MOFs in an

- ionic liquid system and their electrocatalytic application to the hydrogen evolution reaction. *RSC Adv.* 2014;4(30):15720-6.
- [51] Yang RT. Adsorbents: Fundamentals and applications. Belgeler Com. 2003;2004(5):404.
- [52] Li JR, Kuppler RJ, Zhou HC. Selective gas adsorption and separation in metal-organic frameworks. *ChemInform.* 2009;38(29):1477-504.
- [53] Pires J, Pinto ML, Saini VK. Ethane Selective IRMOF-8 and Its Significance in Ethane-Ethylene Separation by Adsorption. *ACS Appl Mater Inter.* 2014;6(15):12093-9.
- [54] Furukawa H, Ko N, Go YB, et al. Ultrahigh Porosity in Metal-Organic Frameworks. *Science.* 2010;329(5990):424-8.
- [55] Farha OK, Eryazici I, Jeong NC, et al. Metal-organic framework materials with ultrahigh surface areas: is the sky the limit? *J Am Chem Soc.* 2012;134(36):15016-21.
- [56] Bozbiyik B, Lannoeye J, De Vos DE, Baron GV, Denayer JF. Shape selective properties of the Al-fumarate metal-organic framework in the adsorption and separation of n-alkanes, iso-alkanes, cyclo-alkanes and aromatic hydrocarbons. *Phys Chem Chem Phys.* 2016;18(4):3294-301.
- [57] Lee SJ, Yoon TU, Kim AR, et al. Adsorptive separation of xenon/krypton mixtures using a zirconium-based metal-organic framework with high hydrothermal and radioactive stabilities. *J Hazard Mater.* 2016;320:513-20.
- [58] Sun D, Ma S, Yanxiong Ke, And DJC, Zhou HC. An Interweaving MOF with High Hydrogen Uptake. *J Am Chem Soc.* 2006;128(12):3896-7.
- [59] Wang Q, Johnson JK. Molecular simulation of hydrogen adsorption in single-walled carbon nanotubes and idealized carbon slit pores. *J Chem Phys.* 1999;110(110):577-86.
- [60] Crittenden JC, Luft P, Hand DW, Oravitz JL, Loper SW, Ari M. Correction. Prediction of Multicomponent Adsorption Equilibria Using Ideal Adsorbed Solution Theory. *Environ Sci Technol.* 1985;19(11):1037-43.

- [61] Xiang Z, Cao D, Lan J, Wang W, Broom DP. Multiscale simulation and modelling of adsorptive processes for energy gas storage and carbon dioxide capture in porous coordination frameworks. *Energy Environ Sci.* 2010;3(10):1469-87.
- [62] Liang Z, Marshall M, Chaffee AL. CO adsorption-based separation by metal organic framework (Cu-BTC) versus zeolite. *Energ Fuel.* 2009;23(2):2785-9.
- [63] Dietzel PDC, Besikiotis V, Blom R. Application of metal-organic frameworks with coordinatively unsaturated metal sites in storage and separation of methane and carbon dioxide. *Journal of Materials Chemistry.* 2009;19(39):7362-70.
- [64] Yao Z, Zhang Z, Liu L, et al. Extraordinary Separation of Acetylene-Containing Mixtures with Microporous Metal-Organic Frameworks with Open O Donor Sites and Tunable Robustness through Control of the Helical Chain Secondary Building Units. *Chemistry.* 2016;22(16):5676-83.
- [65] Pentyala V, Davydovskaya P, Ade M, Pohle R, Urban G. Metal-organic frameworks for alcohol gas sensor. *Sensors & Actuators B Chemical.* 2016;222:904-9.
- [66] Neofotistou E, X CD, Dr. Malliakas, X PN, Prof. Dr. Trikalitis. Unprecedented Sulfone-Functionalized Metal-Organic Frameworks and Gas-Sorption Properties. *Chemistry (Weinheim an der Bergstrasse, Germany).* 2009;15(18):4523-7.
- [67] Bae YS, Farha OK, Hupp JT, Snurr RQ. Enhancement of CO₂/N₂ selectivity in a metal-organic framework by cavity modification. *Journal of Materials Chemistry.* 2009;19(19):2131-4.
- [68] An J, Geib SJ, Rosi NL. High and selective CO₂ uptake in a cobalt adeninate metal-organic framework exhibiting pyrimidine- and amino-decorated pores. *J Am Chem Soc.* 2010;132(1):38-9.
- [69] Si X, Jiao C, Li F, et al. High and selective CO₂ uptake, H₂ storage and methanol sensing on the amine-decorated 12-connected MOF CAU-1. *Energ Environ Sci.* 2011;4(11):4522-7.
- [70] Chen Z, Xiang S, Arman HD, et al. Three-Dimensional Pillar-Layered Copper(II) Metal-Organic Framework with Immobilized

- Functional OH Groups on Pore Surfaces for Highly Selective CO₂/CH₄ and C₂H₂/CH₄ Gas Sorption at Room Temperature. *Inorg Chem.* 2011;50(8):3442-6.
- [71] Mallick A, Saha S, Pachfule P, Roy S, Banerjee R. Selective CO₂ and H₂ adsorption in a chiral magnesium-based metal organic framework (Mg-MOF) with open metal sites. *Journal of Materials Chemistry.* 2010;20(41):9073-80.
- [72] Mukherjee S, Manna B, Desai AV, et al. Harnessing Lewis acidic open metal sites of metal-organic frameworks: the foremost route to achieve highly selective benzene sorption over cyclohexane. *Chem Commun.* 2016;52(53).
- [73] Zhao SS, Yang J, Liu YY, Ma JF. Fluorescent Aromatic Tag-Functionalized MOFs for Highly Selective Sensing of Metal Ions and Small Organic Molecules. *Inorg Chem.* 2016.
- [74] Z H, BJ D, J L. Luminescent metal-organic frameworks for chemical sensing and explosive detection. *ChemInform.* 2014;43(43):5815-40.
- [75] Ren XY, Lu LH. Luminescent nanoscale metal–organic frameworks for chemical sensing. *Chinese Chem Lett.* 2015;26(12):1439-45.
- [76] Zhou XH, Li L, Li HH, Li A, Yang T, Huang W. A flexible Eu(III)-based metal-organic framework: turn-off luminescent sensor for the detection of Fe(III) and picric acid. *Dalton T.* 2013;42(34):12403-9.
- [77] Weng H, Yan B. N-GQDs and Eu³⁺ co-encapsulated anionic MOFs: two-dimensional luminescent platform for decoding benzene homologues. *Dalton T.* 2016;45(21):8795-801.
- [78] Zhou ZY, Han YH, Xing XS, Du S. Microporous Ln-MOFs with multiple 1D channels: tunable colors, white light emission and luminescent sensing for Fe(II) and Fe(III). *Chempluschem.* 2016.
- [79] Müller-Buschbaum K. Luminescent MOFs and Frameworks; 2015.
- [80] Binnemans K. Lanthanide-Based Luminescent Hybrid Materials. *Chem Rev.* 2009;109(9):4283-374.
- [81] Sá GFD, Malta OL, Donegá CDM, et al. Spectroscopic properties and design of highly luminescent lanthanide coordination complexes. *Coord Chem Rev.* 2000;196(1):165-95.

- [82] Zhao SS, Yang J, Liu YY, Ma JF. Fluorescent Aromatic Tag-Functionalized MOFs for Highly Selective Sensing of Metal Ions and Small Organic Molecules. *Inorg Chem*. 2016.
- [83] Wang S, Shan L, Fan Y, Jia J, Xu J, Wang L. Fabrication of Ln-MOFs with color-tunable photoluminescence and sensing for small molecules. *J Solid State Chem*. 2017;132-7.
- [84] Cheng T, Hu J, Zhou C, Wang Y, Zhang M. Luminescent metal-organic frameworks for nitro explosives detection. *Science China Chemistry*. 2016;59(8):1-19.
- [85] Yang J, Wang Z, Hu K, et al. Rapid and Specific Aqueous-Phase Detection of Nitroaromatic Explosives with Inherent Porphyrin Recognition Sites in Metal-Organic Frameworks. *ACS Appl Mater INTER*. 2015;7(22).
- [86] Nagarkar SS, Desai AV, Ghosh SK. Engineering metal-organic frameworks for aqueous phase 2,4,6-trinitrophenol (TNP) sensing. *Crystengcomm*. 2016;18(17):2994-3007.
- [87] Zhang F, Wang Y, Chu T, Wang Z, Li W, Yang Y. A facile fabrication of electrodeposited luminescent MOF thin films for selective and recyclable sensing of nitroaromatic explosives. *Analyst*. 2016;141.
- [88] Cao CS, Hu HC, Xu H, Qiao WZ, Zhao B. Two solvent-stable MOFs as a recyclable luminescent probe for detecting dichromate or chromate anions. *Crystengcomm*. 2016;18(23):4445-51.
- [89] Liu W, Huang X, Xu C, et al. A Multiresponsive Regenerable Europium-Organic Framework Luminescent Sensor for Fe³⁺, Cr(VI) anions and Picric Acid. *Chemistry*. 2016.
- [90] Zhang L, Su Z, Jiang F, Zhou Y, Xu W, Hong M. Catalytic palladium nanoparticles supported on nanoscale MOFs: a highly active catalyst for Suzuki-Miyaura cross-coupling reaction. *Cheminform*. 2014;45(69):9237-44.
- [91] Gole B, Sanyal U, Banerjee R, Mukherjee PS. High Loading of Pd Nanoparticles by Interior Functionalization of MOFs for Heterogeneous Catalysis. *Inorg Chem*. 2016.

- [92] Liu Y, Li H, Han Y, Lv X, Hou H, Fan Y. Template-Assisted Synthesis of Co, Mn-MOFs with Magnetic Properties Based on Pyridinedicarboxylic Acid. *Cryst Growth Des.* 2012;12(7):3505-13.
- [93] Zhou X, Liu P, Huang W, Kang M, Wang Y, Shi Q. Solvents influence on sizes of channels in three fry topological Mn(ii)-MOFs based on metal-carboxylate chains: syntheses, structures and magnetic properties. *Crystengcomm.* 2013;15(40):8125-32.
- [94] Wang H, Zhang D, Sun D, et al. Co(II) Metal-Organic Frameworks (MOFs) Assembled from Asymmetric Semirigid Multicarboxylate Ligands: Synthesis, Crystal Structures, and Magnetic Properties. *Cryst Growth Des.* 2009;9(12):5273-82.
- [95] Yao RX, Qiao XH, Cui X, Jia XX, Zhang XM. Hexagonal Co₆ and zigzag Co₄ cluster based magnetic MOFs with a pcu net for selective catalysis. *Inorganic Chemistry Frontiers.* 2015;3(1):78-85.
- [96] Liu SJ, Han SD, Chang Z, Bu XH. Cluster- and chain-based magnetic MOFs derived from 3d metal ions and 1,3,5-benzenetricarboxylate. *NEW J CHEM.* 2016;40(3):2680-6.
- [97] Li Q, Tian C, Zhang H, Qian J, Du S. An alternative strategy to construct Fe(II)-based MOFs with multifarious structures and magnetic behaviors. *Crystengcomm.* 2014;16(39):9208-15.
- [98] Yang W, Chen H, Yun Z, Liu M. Magnetic Fe₃O₄@MOFs decorated graphene nanocomposites as novel electrochemical sensor for ultrasensitive detection of dopamine. *RSC Adv.* 2015;5(119):98260-8.
- [99] Hamida Y. Magnetism in a number of Metal Organic Frameworks (MOFs) with 1D and 3D characteristics: An experimental and analytical study. *Dissertations & Theses-Gradworks.* 2012.
- [100] Liu S, Han S, Chang Z, Bu X. Cluster- and chain-based magnetic MOFs derived from 3d metal ions and 1,3,5-benzenetricarboxylate. *New J Chem.* 2016;40(3):2680-6.
- [101] Liu SJ, Xue L, Hu TL, Bu XH. Two new Co(II) coordination polymers based on carboxylate-bridged di- and trinuclear clusters with a pyridinedicarboxylate ligand: synthesis, structures and magnetism. *Dalton T.* 2012;41(22):6813-9.

- [102] Díaz-Gallifa P, Fabelo Ó, Pasán J, et al. New copper based MOFs built up from 1,2,3,4-cyclobutanetetracarboxylate ligand. *Acta Crystallographica*. 2011;67(a1):C814.
- [103] Ge C, Du Y, Wang R, et al. A facile strategy to fabricate carboxyl-rich carbon spheres with copper-based MOFs through coordination bond. *J Porous Mat*. 2016:1-9.
- [104] An J, Geib SJ, Rosi NL. Cation-triggered drug release from a porous zinc-adeninate metal-organic framework. *J Am Chem Soc*. 2009;131(24):8376-7.
- [105] Horcajada P, Serre C, Maurin G, et al. Flexible porous metal-organic frameworks for a controlled drug delivery. *J Am Chem Soc*. 2008;130(21):6774-80.
- [106] Morris RE, Wheatley PS. Gas storage in nanoporous materials. *Angewandte Chemie International Edition*. 2008;47(27):4966-81.
- [107] Furukawa H, Ko N, Go YB, et al. Ultrahigh Porosity in Metal-Organic Frameworks. *SCIENCE*. 2010;329(5990):424-8.
- [108] Ray CA, Bhattacharya D, Sahu SK. Magnetic nanoscale metal organic frameworks for potential targeted anticancer drug delivery, imaging and as an MRI contrast agent. *Dalton T*. 2015;45(7):2963-73.
- [109] Tamamestabar C, Cunha D, Imbuluzqueta E, et al. Cytotoxicity of nanoscaled metal-organic frameworks. *Journal of Materials Chemistry*. 2013;2(3):262-71.

In: Crystal Growth
Editors: J. Li, J. Li and Y. Chu

ISBN: 978-1-53612-203-9
© 2017 Nova Science Publishers, Inc.

Chapter 7

**CONCEPT, PROPERTY AND APPLICABILITY
OF LIQUID CRYSTALS**

*Saswati Roy**

Department of Physics,
Birla Institute of Technology, Mesra, Ranchi, India

ABSTRACT

Liquid crystals have properties that are intermediate between the solid and liquid states. In the liquid crystalline state the three dimensional translational ordering of the centre of mass of the molecules is partially or entirely broken. The type of order retained characterises the type of liquid crystalline phase. In the liquid crystalline phase all molecules do not necessarily point along the same direction. They merely tend to point more in one direction than any other i.e., they have a preferred direction of orientation. This direction is referred to as the “director.”

A uniaxial (liquid) crystal has two principal refractive indices, no and ne associated with ordinary and extraordinary rays respectively. In liquid crystals the optic axis lies along the director direction and the vibration of the electric field vector is along it for extraordinary ray and perpendicular

* Saswati Roy Department of Physics, Birla Institute of Technology, Mesra, Ranchi, India, Pin-835215. Email Address: saswati_1976@yahoo.com.

to it for ordinary ray. Due to these anisotropy of molecular arrangement an internal electric field is generated and molecular polarisability can be estimated from it. The internal orientation of the molecules is measured by orientational order parameter. Different macroscopic properties of liquid crystals depend on it.

Keywords: birefringence, order parameter, mesogen, smectic, nematic

1. INTRODUCTION

The fundamental feature of liquid crystals is their anisotropy. This characteristic is basically due to the asymmetry in their molecular geometry leading to anisotropic molecular interaction and angular correlation. In the liquid crystal phase the 3-d positional ordering prevalent in the crystalline phase is entirely or partially destroyed, the order remaining be it only orientational or 2-dimensional positional or bond orientational etc. is determined by the nature of molecular interaction. The anisotropy in the bulk or macroscopic properties is a reflection of this asymmetry in molecular interaction and may be used as an index to evaluate the degree of order existing in the material. The degree of order is formally defined as the order parameter.

2. CLASSIFICATION OF LIQUID CRYSTALS

Liquid crystals have been broadly classified into two categories: lyotropic liquid crystal and thermotropic liquid crystal. Lyotropic liquid crystals are generally mixtures of amphiphilic compounds (having in the same molecule two groups: one hydrophilic and other liophilic) and a polar solvent; most frequently water. Due to this dual characteristic of amphiphilic compounds, interesting mesomorphic transitions are observed with an increase in solute concentration. Lyotropic liquid crystals occur abundantly in nature, particularly in living systems. DNA, certain viruses (e.g., TMV) and many synthetic polypeptides all form lyotropic

mesophases when dissolved in an appropriate solvent at suitable concentration and temperature.

The term thermotropic arises because transitions involving these mesophases are usually affected by change in temperature. Depending on the type of ordering, thermotropics are grouped into different classes; nematic, cholesteric and several types of smectics. Few commonly occurring phases are described below.

2.1. Nematics

Nematics are in general polarisable rod like organic molecules, normally of length of the order of 20-30 Å. Because of their tendency to organise themselves in a parallel fashion, they demonstrate interesting and useful optical properties. By decreasing the temperature from the isotropic phase, in which the molecules are randomly positioned and oriented, to the nematic phase the material gains an amount of orientational order but no positional order as shown in Figure 1. This reordering is thought to be due to the packing constraints of the molecules. This claim is supported by the fact that most liquid crystal molecules tend to be long (rod like) with a rigid central core.

2.2. Twisted Nematic or Cholesteric Mesophase

In this phase the molecules prefer to lie next to each other in a slightly skewed orientation (as shown in Figure 2). This induces a helical director configuration in which the director rotates through the material. If the helical axis be taken along the z axis, then

$$n_x = \cos(q_0z + \varphi)$$

$$n_y = \sin(q_0z + \varphi)$$

$$nz = 0$$

where the phase ϕ is arbitrary and q_0 is the pitch.

Chiral Nematics

When the molecules that make up a nematic liquid crystal are chiral (i.e., they are not symmetric when reflected) then chiral nematics phase will exist instead of the normal nematic. In this phase the molecules prefer to lie next to each other in a slightly skewed orientation. This induces a helical director configuration in which the director rotates through the material (Figure 3).

2.3. The Smectic Phases 1-2

The smectic phases 1-2, which generally exist at temperatures lower than nematic, form well-defined layers that can slide over one another like soap. The smectics are thus positionally ordered along one direction. Various types of smectic phases exist, the more common ones are described here.

In the smectic A phase, the molecules are parallel to one another and are arranged in layers (as shown in Figure 3), with the long axis perpendicular to the layer plane.

The structure of the smectic C phase is closely related to the structure of the smectic A phase. The molecules are arranged in layers, but with the long axes tilted to the layer normal (as shown in Figure 4).

*Smectic C**

In a manner similar to chiral nematics there are chiral forms of smectic phases. Figure 5 shows the molecular arrangement in a chiral smectic C phase, denoted by smectic C*. The tilted director rotates from layer to layer forming a helical structure.

This helix may be suppressed by placing the liquid crystal in a cell where the material is sandwiched between two glass plates. Such systems

are said to be surface stabilised. Once the helix is suppressed and the directors in each layer are forced to lie in the plane of the glass plates the chiral nature of the molecules creates a spontaneous polarization within each layer.

Chiral Smectic phase The chiral smectic C phase is by far the most important phase. The tilted director rotates layer to layer forming a helical structure. These systems can be surface stabilised in this case the helix may be decreased by liquid crystal in cell. This means the materials is effectively trapped between two glass plates. Once the helix is suppressed and the directors in each layer are forced to lie in the plane of the glass plates, this creates spontaneous polarisation within each other because of the chiral nature of the molecules. This is the basis of ferroelectric display devices. These ferroelectric liquid crystal displays and antiferroelectric liquid crystal displays operate by the application of an electric field which couples with the spontaneous polarisation and switches the director in the layers

The “discotic mesophase” was first synthesized and investigated by Chandrasekhar et al. 7. In this mesophase the molecules are disc- like and stack like coins to form columns of close pack arrays (as shown in Figure 6). Significant amount of research has been done on the discotic phase⁸⁻¹¹.

SmecticB

In the smecticB phase the molecules possess a three dimensional long range order as in a crystal, though with weak interlayer forces i.e., the layers may glide over one another. Within the layers, the centers of gravity of the molecules are arranged in a hexagonal¹²⁻¹⁴ face centred packing. The molecules are free to rotate around their long axes, and the structure is optically uniaxial. This type of smecticB phase is often referred to as crystal smecticB to distinguish it from hexatic smecticB which has three dimensional long range ‘bond orientational order’ but no long range positional order.



Figure 1. Schematic representation of molecules in nematic state.

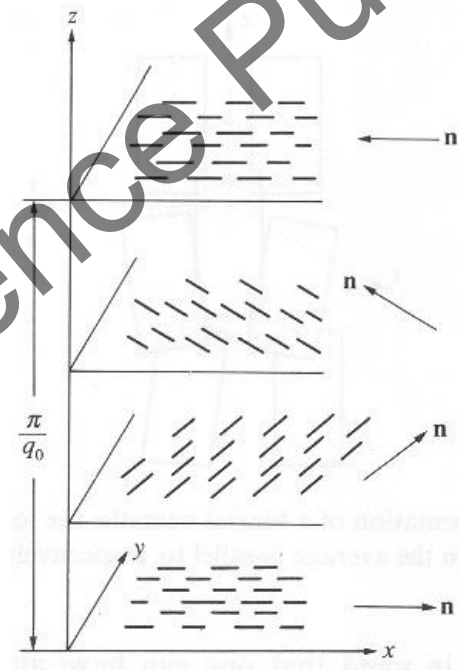


Figure 2. The arrangement of molecules in the cholesteric mesophase.

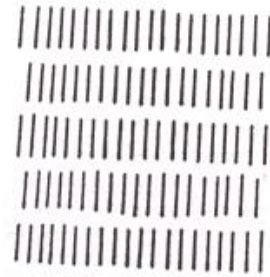


Figure 3. Schematic representation of smecticA.

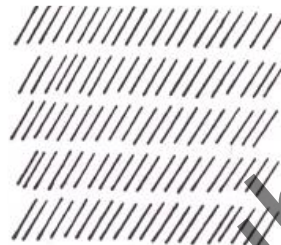


Figure 4. Schematic representation of smecticC



Figure 5. Schematic representation of smecticC*.

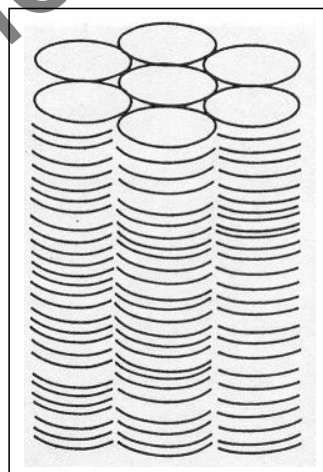


Figure 6. The structure of columnar phase of disc like molecules.

3. BIREFRINGENCE AND OPTICAL PROPERTY

A uniaxial (liquid) crystal has two principal refractive indices, n_o and n_e associated with ordinary and extraordinary rays respectively. In liquid crystals the optic axis lies along the director direction and the vibration of the electric field vector is along it for extraordinary ray and perpendicular to it for ordinary ray.

$$\begin{aligned} n_o &= n_{\perp} \\ n_e &= n_{\parallel} \end{aligned} \quad (1)$$

The anisotropy in refractive index is given by

$$\Delta n = n_e - n_o = n_{\parallel} - n_{\perp} \quad (2)$$

generally Δn is +ve and varies from values close to zero to 0.415. For a chiral nematic crystal, the uniaxial optic axis is the helix axis, which is perpendicular to the local director.

The polarisability \bar{P} within the liquid crystal may be written as

$$\bar{P} = N \langle \alpha \bar{E}_i \rangle \quad (3)$$

where the bracket denotes average over all possible orientations of the molecules. α is the molecular polarizability, N is the number of molecules per unit volume and \bar{E}_i is the internal field that acts on a molecule. \bar{E}_i , however is related to the macroscopic field \bar{E} and may be represented as

$$\bar{E}_i = \bar{k} \bar{E} \quad (4)$$

where \bar{k} is an ordinary second rank tensor. From equations (3) and (4) we have

$$\bar{P} = N \langle \alpha \bar{k} \bar{E}_i \rangle$$

The refractive index is related to the polarisability by the following relation.

$$n_{\parallel}^2 - n_{\perp}^2 = N \{ \langle \bar{\alpha} \cdot \bar{k} \rangle_{\parallel} - \langle \bar{\alpha} \cdot \bar{k} \rangle_{\perp} \} \tag{5}$$

To calculate the molecular polarisability from refractive index measurements, the internal field tensor \bar{k} must be known. Lorentz - Lorentz have derived equations relating polarizability and refractive indices for isotropic medium. This relation, however may not be used here due to the anisotropy of the liquid crystalline medium and is therefore replaced by Neugebauer’s relation¹⁶ or Vuks formula¹⁷.

Neugebauer’s relations to calculate the ordinary and extraordinary polarisabilities α_o and α_e are given by

$$\begin{aligned} n_o^2 - 1 &= 4N\pi\alpha_o(1 - N\alpha_o\gamma_o)^{-1} \\ n_e^2 - 1 &= 4N\pi\alpha_e(1 - N\alpha_e\gamma_e)^{-1} \end{aligned} \tag{6}$$

where γ_o and γ_e are internal fields constants for ordinary and extraordinary rays respectively with respective polarisabilities α_o and α_e . From equation (6), the equations for calculating the polarisabilities are

$$\frac{1}{\alpha_o} + \frac{1}{\alpha_e} = \frac{4\pi N}{3} \left[\frac{(n_e^2 + 2)}{(n_e^2 - 1)} + \frac{2(n_o^2 + 2)}{(n_o^2 - 1)} \right] \tag{7}$$

and

$$\alpha_e + 2\alpha_o = \frac{9}{4\pi N} \left[\frac{n^2 - 1}{n^2 + 2} \right] \tag{8}$$

where $n = \left[\frac{2n_o^2 + n_e^2}{3} \right]^{1/2}$ is the mean refractive index.

The Vuks formula relating the principal polarisabilities and the refractive indices may be written as

$$\frac{n_o^2 - 1}{n^2 + 2} = \frac{4\pi}{3} N\alpha_o$$

$$\text{and } \frac{n_e^2 - 1}{n^2 + 2} = \frac{4\pi}{3} N\alpha_e \quad (9)$$

The relation between the order parameter $\langle P_2 \rangle$ and polarisability (α_o , α_e) is given by¹⁸

$$\alpha_e = \alpha_{\text{ave}} + 2/3 \Delta\alpha \langle P_2 \rangle$$

$$\alpha_o = \alpha_{\text{ave}} - 1/3 \Delta\alpha \langle P_2 \rangle \quad (10)$$

where $\alpha_{\text{ave}} = (2\alpha_o + \alpha_e)/3$ is the mean polarizability and $\Delta\alpha = (\alpha_{\parallel} - \alpha_{\perp})$ is the molecular polarisability anisotropy.

We thus have

$$\langle P_2 \rangle = \frac{\alpha_e - \alpha_o}{\alpha_{\parallel} - \alpha_{\perp}} \quad (11)$$

The order parameter may be obtained from the above equation by determining α_e and α_o , provided $\alpha_{\parallel} - \alpha_{\perp}$ is known. To get an estimated value of $\alpha_{\parallel} - \alpha_{\perp}$, Haller's extrapolation procedure¹³ is followed. In this procedure $\ln(\alpha_e - \alpha_o)$ is plotted against $\ln(T_c - T)$ and a straight line obtained (T_c being the clearing temperature). The value of $(\alpha_{\parallel} - \alpha_{\perp})$ is determined by extrapolating the $\ln(\alpha_e - \alpha_o)$ versus $\ln(T_c - T)$ straight line to $T = 0$ where it may be assumed that $\langle P_2 \rangle = 1$.

4. ORDER PARAMETER AND ORIENTATIONAL DISTRIBUTION FUNCTION

In crystal, molecular order may be of various types; consequently there are various types of order parameters: orientational order parameter, translational order parameter, bond orientational order parameter or even a mixed order parameter coupling two types of orders. Nematics possess only orientational order and therefore may be characterised by a single order parameter – the orientational order parameter. In smectics, in addition to orientational order other types of order exist making it necessary to define other order parameters. However, orientational order is the common feature of all liquid crystalline phases.

In the liquid crystalline phase all molecules do not necessarily point along the same direction. They merely tend to point more in one direction than any other i.e., they have a preferred direction of orientation. This direction is referred to as the “director.” Ordering in the polar angle θ between the director direction \vec{n} and the molecular axis distinguishes the liquid crystalline phase from the isotropic liquid. However θ itself is not a convenient order parameter. By analogy with ferromagnetism, one might expect that the projection of molecules along ‘ \vec{n} ’ would be a natural parameter. This however is not quite correct. In magnetism, the electron spins have a definite polarity; the heads (north poles) being distinctly different from the tails (south poles). But in the mesophases the heads and tails are indistinguishable i.e., as many head ends point up as tail ends. Thus to prevent the order parameter from describing situations in which the mesomorphic phase becomes polarised, $\cos^2\theta$ rather than $\cos\theta$ is needed to describe the structure. Since one is interested in average behaviour representative of all molecules, the value of $\cos^2\theta$ averaged over all molecules i.e., $\langle \cos^2\theta \rangle$ is the relevant parameter. When all the molecules are orientated along \vec{n} , $\langle \cos^2\theta \rangle = 1$, whereas when the molecules are randomly distributed along all possible directions $\langle \cos^2\theta \rangle = 1/3$. However we require that the order parameter vanishes when there is

a random distribution of orientation. The orientational order parameter is thus defined as $\langle P_2(\cos\theta) \rangle = \frac{1}{2} (3 \langle \cos^2\theta \rangle - 1)$ which satisfies the required criteria i.e., $\langle P_2 \rangle = 0$ for a random distribution and equals unity when all molecules are aligned.

5. REMARKABLE PROPERTIES OF LIQUID CRYSTALS AND THEIR APPLICABILITY

Parallel to the growing worldwide research and development activities in the field of liquid crystal, the interest of the electronic industry in liquid crystals has enhanced remarkably. Liquid crystals find wide application in technological devices (especially display devices) as their physical properties are very sensitive, even to weak external perturbations. Liquid crystal display devices have the special advantage in that they operate at low voltage and therefore consume very little power. When twisted nematic liquid crystals are arranged in thin layers, their ability to transmit scattered or polarized light changes on the application of electric field. This property is utilised in analog devices, image converters and matrix type picture screens.

Smectic liquid crystals have also been used to advantage in liquid crystal displays (LCDs). They exhibit better viewing angle characteristics and contrast ratio as compared to nematics and can operate at high speed. In recent years chiral smectics (smecticC*), which have the property of spontaneous polarisation are finding wide application in display systems.

Cholesterics are very temperature sensitive, their pitch and colour change with slight variations in temperature. This is a very useful property in the manufacture of temperature sensitive devices. Detection of hot points in microcircuits, localisation of fractures and tumors, conversion of infrared images etc., are some of the applications of liquid crystals, to name only a few.

REFERENCES

- [1] G. Friedel, "Colloid Chemistry," Ed. J Alexander, Vol 1 p 102ff. The Chemical Catalogue Company, Inc., N. Y. (1926).
- [2] G. Friedel, *Ann. Physique*, 18, 273 (1922).
- [3] P. G. deGennes, "The Physics of Liquid Crystals," Calendron Press, Oxford, (1974).
- [4] T. R. Taylor, S. L. Arora and J. L. Ferguson, *Phys. Rev. Lett.*, 25, 722 (1970).
- [5] T. R. Taylor, J. L. Ferguson and S. L. Arora, *Phys. Rev. Lett.*, 24, 359 (1970).
- [6] deVries, *Acta Cryst.*, A25, 135 (1969).
- [7] S. Chandrasekhar, B. K. Sadashiva and K. A. Suresh, *Pramana*, 9, 471 (1977).
- [8] D. Guillon, A. Skoulios, C. Piechocki, J. Simson and P. Weber, *Mol. Cryst. Liq. Cryst.*, 100, 275 (1983).
- [9] J. Luz, *Tenth Int. Conf. On Liq. Crystals*, York, July, 1984, abstract no. H2.
- [10] A. C. Ribeiro and A. F. Martins, *Tenth Int. Conf. On Liq. Crystals*, York, July, 1984, abstract no. H6.
- [11] C. Destrade, H. Gasparoux, P. Foucher, N. H. Tinh, J. Malthete and J. Jacques, *J. Chem. Phys.*, 80, 137 (1983).
- [12] G. Chistyakov and W. M. Chaikowsky, *Mol. Cryst. Liq. Cryst.*, 7, 269 (1969).
- [13] M. Lambert and A. M. Levelut, "Anharmonic Lattices, Structural Transitions and Melting" (ed. T. Riste), Noordhoff, Leiden, 375 (1974).
- [14] M. Levelut and M. Lambert, *C. R. Acad. Sci.*, Paris, Ser. A. B., 272, 1018 (1971).
- [15] W. H. deJeu, "Physical Properties of Liquid Crystalline Materials," Gordon Breach, Science Publishers pg. 24 (1980).
- [16] H. E. J. Neugebauer, *Canad. J. Phys.*, 32, 1 (1954).
- [17] M. F. Vuks, *Optics and Spectroscopy*, 20, 193 (1971).
- [18] P. G. deGennes, *Mol. Cryst. Liq. Cryst.*, 12, 193 (1971).

Nova Science Publishing, Inc.

In: Crystal Growth
Editors: J. Li, J. Li and Y. Chu

ISBN: 978-1-53612-203-9
© 2017 Nova Science Publishers, Inc.

Chapter 8

**THE CORRELATION OF DENSITY,
REFRACTIVE INDEX
AND DIELECTRIC STUDIES ON TWO
PECULIAR LIQUID CRYSTALS**

*Debanjan Bhattacharjee and Ayon Bhattacharjee**
National Institute of Technology Meghalaya, Shillong, India

ABSTRACT

Liquid crystals, being anisotropic materials have aroused interest in the study of their optical and electrical properties. These properties have been harnessed for several applications. These properties are even more interesting when the structure of the liquid crystal becomes more complex. In the present work, we focus on two very interesting liquid crystalline compounds. The compound N(4-n-pentyloxybenzylidene) 4-n-alkylaniline, called 5O.16 in short, is an interdigitated liquid crystal having a bent shape with a high asymmetry in terms of its terminal alkyl chain length. The other compound reported in this work is commonly known as 7.O5O.7 and it is a liquid crystalline dimer. These dimers are the precursors to the liquid crystalline polymers and are formed by connecting two simple liquid crystalline segments with an alkyl chain

called the spacer group. The optical and electrical properties of the dimers depend on the constituent liquid crystals, as well as the length of the spacer group in term of odd or even number of carbon atoms. In this study, we report the density dependence of these compounds. The density studies are conducted by the capillary method. Liquid crystals being anisotropic exhibit optical birefringence in some of the liquid crystalline phases and therefore show two components of the refractive index, the ordinary refractive index and the extra-ordinary refractive index. These are obtained using the thin prism method with the 633.2 nm line from a HeNe laser. The results obtained were used to find a correlation between the density and refractive indices of the samples. Dielectric and impedance spectroscopy studies indicate the coupling between the liquid crystal and the electrical field. Studies were carried out as a function of temperature as well as frequency. Semicircular nature of the Cole-Cole plots indicates the reorientation of the molecules with the applied field. Using the experimental data and the theoretically fitted results, the effective equivalent model circuits for the two compounds were designed. These circuits were used to explain the behavior of the compound under the effect of external electric field and the influence of the electrodes. The effect of the conductivity with temperature and frequency are also discussed at the end of the chapter.

Keywords: liquid crystal, monomer, dimer, birefringence

1. INTRODUCTION

Generally, liquid crystals are neither crystals nor liquids, but they exhibit some properties of both these phases. Liquid crystalline compounds (LC) are intermediate between the fully ordered 3-dimensional crystals and disordered isotropic fluids. The liquid crystalline compounds exhibit a partially ordered fluid-like nature with spontaneous anisotropy that has a dependence of temperature. Due to the anisotropic properties, liquid crystals possess some typical optical characteristics which are harnessed in different technological applications. The formation of the packing order of the molecules influence the molecular shapes that help in determining the long-range attractive as well as repulsive forces. The long-range attractive and repulsive nature of the forces are responsible for the stability of liquid crystalline compounds. The polarizability of the molecules and dielectric

anisotropy of liquid crystals provide important information about the phases having different molecular compositions. Generally, the core and the terminal alkyl chain of the liquid crystals provide substantial information on the anisotropic behavior of the constituent molecules [1-7].

This chapter is dedicated to the detailed study of two different liquid crystals. One is a monomeric compound whose abbreviated name is 5O.16 monomeric and the other is a dimeric liquid crystalline compound named as 7.O5O.7. For the optical study, the refractive indices calculation of the compound is necessary because the refractive indices values help to measure the polarizability, order parameter, internal field factor and Lorentz field factor [2-4, 27-40].

Liquid crystals are optically very active and the anisotropic nature of the compounds helps to change the optical properties with the variation of temperature. The temperature dependence of the refractive indices is important for understanding the anisotropy and their molecular alignment. Due to the incident polarization of light, the liquid crystalline phase exhibits two refractive indices, the ordinary and the extraordinary refractive indices. When the incident ray is linearly polarized, parallel to the directors of the liquid crystal then we get the extraordinary ray and its extraordinary refractive index is n_e . On the other hand, when the incident light is linearly polarized, perpendicular to the director of the liquid crystal, then we get the ordinary ray and its ordinary refractive index is n_o . The difference between these two refractive indices is termed optical birefringence of the compounds and is expressed as

$$\Delta n = n_e - n_o \quad (1)$$

If the $n_e > n_o$ then the value of Δn is positive and the liquid crystalline compounds are said to be positively birefringent. On the other hand, if $n_e < n_o$ then the value of Δn is negative, and the liquid crystalline compounds are said to possess negative birefringence [1-5, 2, 4-11].

The most sensitive criteria that changes with the molecular orientation is the dielectric property and it helps us to understand the molecular dynamics of that material. In the liquid crystal, the director of the

molecules gets reoriented due to the externally applied field and resulting in the changes the behavior of the liquid crystals. The positive and negative dielectric anisotropic nature depends on the anisotropic distribution of the director and molecular dipole of liquid crystals. The behavior of the dielectric and its sign varies from compound to compound, and with the allocation of dipole moments.

Due to their highly anisotropic nature, liquid crystals and their response to an external applied field changes depending on dielectric anisotropy. Depending on the director, $\hat{\mathbf{n}}$ the dielectric permittivity shows different values. If the liquid crystalline compound is uniaxial, then it possesses two different dielectric constants, i.e., ϵ_{\parallel} and ϵ_{\perp} . When the director of the liquid crystals is normal to the axis of symmetry, it is measured as ϵ_{\parallel} and if the director is parallel to the axis, it is measured as ϵ_{\perp} . The separation between these two dielectric values provides the dielectric constants of the compounds and it is expressed as

$$\Delta\epsilon = \epsilon_{\parallel} - \epsilon_{\perp} \quad (2)$$

The positive values of dielectric anisotropy of the compounds are expressed as $\epsilon_{\parallel} > \epsilon_{\perp}$ in case of which the polarizability is greater along the molecular long axis. For negative dielectric anisotropy $\epsilon_{\parallel} < \epsilon_{\perp}$, the polarizability will be greater perpendicular to the long molecular axis. The positive or negative dielectric anisotropy of the compounds determine whether the liquid crystalline molecule will lie parallel to the long molecular axis or along the direction of the applied electric field [12-23, 24-29]. The anisotropic behavior of the liquid crystalline compounds is extremely useful in modern device applications, such as displays, storage devices and sensors. The Cole-Cole plots are constructed with the frequency dependence of complex dielectric permittivity in the complex plane. The dielectric relaxation of the liquid crystals obey the empirical nature Cole-Cole arc law. In this chapter, we discuss and provide an analysis of the Cole-Cole plots with different external DC bias voltages and temperatures.

1.1. 5O.m Series of Liquid Crystal

One of the most popular and interesting classes of the liquid crystalline family is formed by the N-(4-n-alkyl-oxybenzylidene)-4/-n-alkylanilines [30, 31-36]. Popularly this group of compounds are known as nO.m homologous series, where n and m represent the number of carbon atoms in both the terminal alkyl chains. These liquid crystalline compounds also contain a Schiff's base and are thermotropic in nature. The generalised molecular structure of nO.m is given below.

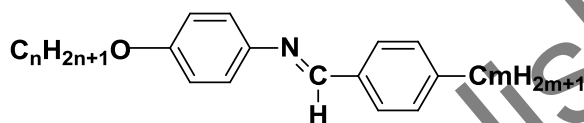


Figure 1. Molecular structure of the nO.m liquid crystal. (for the 5O.m series, n = 5, O represents oxygen).

Although the molecular structure of these compounds is simple, they exhibit smectic polymorphism. With the changes in the values of n or m, the molecular structure gets modified and it results in significant changes in different optical as well as physical properties. This makes the nO.m series of compounds very interesting in the field of liquid crystal research.

1.1.1. The 5O.16 monomeric compound: In the 5O.m series of the liquid crystalline compounds, various interesting phase sequences are observed. N-Sc (m=2), N-S_A-S_C-S_F-S_G (m=5), N-S_A-S_C-S_B-S_F-S_G, (m=6) and N-S_A-S_B or N-S_A for the higher homologs. For higher homologs 5O.m (14, 16), the compounds have unsymmetrical alkyl chain length distribution and they exhibit only the SmA-N phase.

In optical studies, the experimental birefringence of this compound could be observed only in the nematic phase [30, 31, 37]. Therefore, studies on optical properties are mainly concentrated in the nematic phase. 5O.16 compound has shown high values of refractive indices which is similar to the trend shown by other members of the 5O.m series. However, the optical studies of this compound reveals that the birefringence is

optically negative unlike the lower homologs of the 5O.m series. In addition negative birefringence, this compound is also optically negative in molecular polarizability, internal and Lorentz field factors. From the reported literature [38], the values of d-spacing of the compound are less than the expected measured value. Moreover, studies have also revealed that the compound also exhibits interdigitated phases [30, 31]. The negative birefringence is attributed to the fact that the d-spacing of the compound is decreased with the decreasing temperature, which results in decreasing in the molecular ordering. The long terminal chain at one end of the compound results in it having a skewed geometry, which further explains the unique behavior of 5O.16. Since this molecule is reported to be interdigitated, the probability is that the compound attains an energetically suitable arrangement at a higher temperature and gets strained with the lowering of temperature. This is the possible reason for the increase of polarizability of the molecule with increasing temperature [30, 31].

In terms of the molecular weight of the compound, the weight of core is lower than the longer terminal chain in the case of 5O.16. Therefore, bending of the molecule is a finite probability leading to a reorientation of the compound in the liquid crystalline phase. The lack of uniaxiality of the compound structure helps the perpendicular component of light to become slower relative to the parallel component. This is the reason for optically negative anisotropy in this case.

In the case of correlation between density and refractive indices of the 5O.16 compound, it is reported in literature [38] that, with the increase of density the birefringence of the compound decreases. From the literature survey, it is also known that the compound 5O.16 is interdigitated and the d-spacing of this compound decrease with the lowering of temperature. This, in turn, leads to the lowering of molecular ordering. Moreover, with the increasing density, the d-spacing also decreases and therefore the birefringence decreases with increasing density in 5O.16 [30, 31, 37].

In order to understand the dielectric behavior of the compound, it was confined in specially designed cells and the Cole-Cole plots were drawn. These Cole-Cole plots provide an idea for the relaxation process in the dielectric spectrum. These plots reveal that there is a monodisperse nature of the cell in our compound. The nature of the Cole-Cole plot of the compound is semi-circular but the center does not appear exactly on the axis. This clearly shows that the relaxation process in 5O.16 compound is non-Debye type. This happens when the orientation of the molecules change from perpendicular alignment to the parallel alignment in the presence of an externally applied electric field [39, 40].

1.2. Dimer: A dimeric liquid crystalline compound is formed when the two mesogenic rigid groups are connected by a linkage atom or spacer. This structure of the liquid crystal dimers has attracted remarkable attention in the field of experimental as well as theoretical research. In dimers, the different types of molecular conformation occur due to the flexibility of the linking atom or alkyl chain as compared to the conventional liquid crystal monomeric compounds where the conformation is governed mainly by the rigid core. In dimers, every thermodynamic observed in the compounds is due to the different structural conformations of the different molecular segments. These molecular conformations not only change the intramolecular and intermolecular forces, but also change the average molecular composition of these liquid crystalline compounds. This can happen due to the presence of the flexible terminal alkyl chains in the compounds. These structural and conformational changes also result in the reverse phase sequence in dimeric liquid crystals, as the phases change from crystal to isotropic. The extra flexibility that is imparted by the presence of the spacer not only changes the properties as compared to the constituent monomers, sometimes completely new phases are also observed in such dimers [41, 42].

Generally, the dimeric liquid crystalline compounds are categorised into two types: the symmetric and the non-symmetric dimers. When the mesogens on either end of the spacer are identical, the dimer is a symmetric dimer and when these groups are not identical, then the dimer is

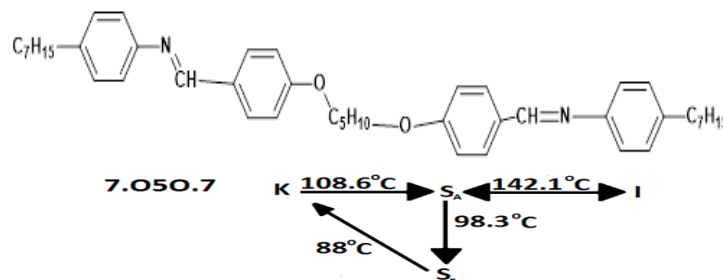


Figure 2. Molecular structure and phase transition temperature of the dimeric compound, where K is the crystalline state, S_A is the smectic A phase, S_F is the smectic F phase and I is the isotropic phase.

non-symmetric. The number of carbon atoms in the spacer group connecting the two segments plays an important role in determining the shape of the molecule. An odd number of carbon atoms in the spacer or an even number may change the shape of the dimeric molecule from straight to bent. The alternation of the behavior of the dimeric liquid crystalline compounds decrease with the increasing spacer length. This behavior, explain the changes in the molecular polarizability, order parameter, transitional entropies, different field factors and the average molecular compositions. If the chain length of the compound is short, then the two mesogenic groups are strongly coupled with each other and the dimer behaves as a rigid molecule.

1.2.1. The 7.050.7 dimer: The dimeric liquid crystalline compound 7.050.7 belongs to the homologous series of (α - ω -bis)4-alkylanilinebenzylidene-4/-oxy) alkanes, commonly referred to as m.OnO.m series of compounds. As seen from the Figure 2, the SmF phase is observed only in the cooling cycle whereas the SmA phase appears both in the cooling as well as the heating cycles. In other words, the SmF phase has a monotropic transition nature. The SmA phase is orthogonal with the short-range ordering and the molecules are oriented in a nematic-like nature with averaged alignment in the direction of the director. The SmF phase is a tilted phase and the molecules are packed in a hexagonal-like ordering. This kind of ordering with the tilted orientation is the key reason for not exhibiting the optical birefringence in the SmF phase [41, 42].

The primary focus of this study was to observe the different physical behavior in the SmA phase within the temperature range (140-100)°C. From the literature, it has already been known that the liquid crystalline dimers show the odd or even effect. Since the spacer is odd in the case of 7.O5O.7 dimer, the shape is not bent and therefore it can be aligned properly after repeated heating and cooling cycles. From the optical study, it is observed that the compound exhibit positive birefringence in SmA phase only and with the increasing temperature the values of birefringence decreases and it vanishes at isotropic temperature [41].

In the case of correlation between density and refractive indices of 7.O5O.7 compound, it is observed that with the decreasing density, the birefringence of the compound decreases. The ordering of the molecules decreases with the increasing temperature This is the probable reason for increasing the birefringence with the increasing density in the 7.O5O.7 dimeric compound.

For the electrical properties, the nature of the Cole-Cole plots indicate the variation of dielectric function with different temperature for fixed DC bias voltage. For the experimental purpose, homogeneous (HG) and homeotropic (HT) alignments of the different cells were used. The observed nature of the of the curves is semi-circular and it also passing through the origin of the axis, which clearly indicates that the behavior of the relaxation process is considered as a good approximation [41]. A comparison of these plots with that in literature [41,42] indicates that the observed relaxation phenomenon is in the low-frequency range, i.e., within the range of 20-100 kHz and that the nature of the dimeric liquid crystal is monodisperse. The Cole-Cole nature of the plots is semi-circular but the axis doesn't appear in the centre. This clearly suggests that the relaxation process of the compound behave as a non-Debye type. This happens due to the molecular alignment changes from perpendicular to parallel direction on application of external bias voltage [41]. From the dielectric results, the electrical equivalent circuit was also designed and it was reported in [41]. This equivalent circuit can easily replicate the experimentally measured data.

2. METHODS

2.1. Refractive Indices Measurement Method

2.1.1. Thin Prism Technique for Refractive Indices Study

The anisotropic nature of liquid crystals is very much responsible for some unique optical properties that are exploited in several advanced technical applications. Generally, the polarizability of the compounds, birefringence and order parameter are very important studies in the field of liquid crystal research and these values are mainly determined from the refractive indices data [2, 4-8, 44, 2, 5, 9-11, 18, 44, 45].

The refractive indices measurements of liquid crystal compounds are used to determine the birefringence of the liquid crystals. Various experimental techniques have been established to investigate the temperature dependence of the liquid crystal refractive indices [2, 4-11].

The temperature dependent refractive indices study of the liquid crystal are important for understanding their anisotropic nature and their alignment. Depending on the incident polarization of light in a homogeneous cell, the liquid crystal exhibits two refractive indices, i.e., ordinary and extraordinary refractive indices [2, 4, 5].

For the measurements of the refractive indices, various experimental techniques have been developed but thin prism technique is mostly used nowadays. Because this technique is simple and it gives refractive indices data up to the 4th decimal result, so it gives more corrected results. The measurement of the refractive indices was conducted using the thin prism technique with the help high power laser. The prism is made with a refracting angle less than 2° and is constructed with glass slides treated with 1% PVA solution. The PVA coated slides are rubbed unidirectionally to make the prism unidirectional that facilitates the alignment of liquid crystals.

Ordinary ray and extraordinary ray are the two components of split-refracted rays whenever light passes through an anisotropic crystal. Since the velocity of the ordinary ray is all most constant and the position of the image of the ordinary light remains stationary. In the case of the

extraordinary light, the position of the extraordinary light rotates in the direction of rotation of the crystal. In liquid crystalline compounds, the image of extraordinary ray revolves around the ordinary ray if seen through a proper polariser. From the polarizer, it is easy to verify the spots for the ordinary and extraordinary rays.

The observed refracted images of the spots were recorded using a high-resolution digital camera. The images were processed in the computer to locate the center of the spots of ordinary (n_o) and extraordinary (n_e) rays. From the captured spots, we can find the distance of the spots, such as d_1 , d_2 , and d_3 , and use these values are used in equation 3 and 4 to calculate the refractive indices of the compounds.

A schematic diagram of the thin prism setup is shown in Figure [2, 5, 9-11, 18, 44, 45, 46].

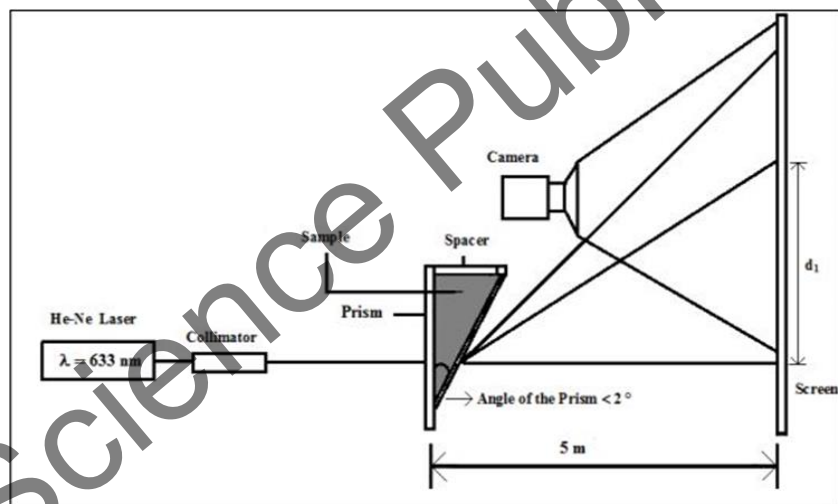


Figure 3. Schematic diagram of the thin prism setup.

The experimentally measured ordinary (n_o) and extraordinary (n_e) refractive indices were calculated using the following equations [47].

$$n_e = \left(1 + \frac{2d_2^e}{d_1} \right) \quad (3)$$

$$n_o = \left(1 + \frac{2d_2^o}{d_1} \right) \quad (4)$$

where d_2^o and d_2^e are respectively the distance of the ordinary spot and the extraordinary spot from the direct spot on the screen and d_1 is the distance between the position of the direct spot and the spots formed by the reflected beams from the two reflecting surfaces when the prism is placed symmetrically with its apex facing the direct beam from the laser [2, 30, 41].

2.2. Density Measurement Technique

The densities of liquid crystal as a function of temperature were measured by using a capillary type dilatometer. Weighed samples of liquid crystals were put into the dilatometer and then the dilatometer was dipped in a liquid bath containing water or glycerol. The liquid bath was heated and its temperature was controlled manually. The variation of the length of the compound column was then measured at different temperatures with the help of a high precision traveling microscope. The densities of the liquid crystals were calculated by correcting for the expansion of the glass capillary tube. Experimental uncertainty in density measurements is 0.1%.

A schematic diagram of the experimental setup for the measurement of the density of liquid crystal samples is shown in Figure 4.

2.3. Dielectric Measurements

The two-cell method is used for the dielectric measurement of real and complex dielectric permittivity of the compound. The samples are filled in homogeneous (HG) and homeotropic (HT) cells in this method and then

fixed thickness and various dielectric parameters. The measurements of the compounds were initially conducted for the empty cells at the given temperature and at the desired range of frequency. The liquid crystalline compounds were heated to their isotropic state and the cells were filled up by capillary action [41, 42]. In HG cell, the molecular orientation is a planner to the substrate surface and in the case of HT cell, the orientation of the molecules is perpendicular to the substrate surface. For the dielectric study, the value of capacitance and dissipation factor of the empty, as well as filled cell, were determined by the impedance analyzer.

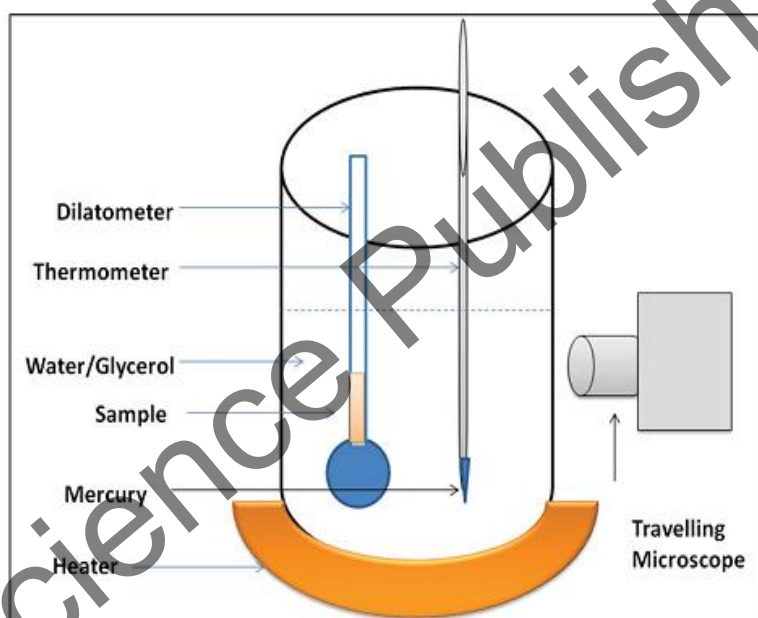


Figure 4. A schematic diagram of the experimental setup for the measurement of the density of liquid crystal.

The real part of the dielectric permittivity is obtained from the capacitance value [48]

$$\varepsilon' = \frac{\Delta C}{C_G} + 1 \quad (5)$$

$$\Delta C = C_p - C_o \quad (6)$$

where ΔC , capacitance change with the filled cell, C_p is the capacitance of the filled cell with the sample and C_o is the capacitance of the empty cell. C_G is the geometrical capacitance.

The dissipation (D) factor of the sample was derived from [48]

$$\tan \delta = \frac{C_p D_p - C_o D_o}{C_p - C_o} \quad (7)$$

where D_p is the dissipation factor of the sample filled cell and D_o is the dissipation factor of an empty cell.

The loss factor of the sample is given by,

$$\varepsilon'' = \varepsilon' \tan \delta$$

Slater's perturbation equations were used to find the relaxation time and activation energy is from [49-51].

$$\tau = \frac{\tan \delta}{\omega} \quad (8)$$

$$\Delta G = 2.303RT \log \left(\frac{\tau KT}{h} \right) \quad (9)$$

where R is the molar gas constant, h is the Planck's constant and k is the Boltzmann's constant.

For analysis of the dielectric spectra, Cole-Cole were providing information about the relaxation mechanism of the liquid crystal. The equation used [48, 52].

$$\varepsilon^* = \varepsilon_\infty + \frac{\varepsilon_0 - \varepsilon_\infty}{1 - (i\omega\tau)^{1-\alpha}} \quad (10)$$

where, ε_∞ is the permittivity at a higher frequency, τ is the relaxation time.

In the case of our experiments, we used HG alignments and in that case, the applied field was perpendicular to the molecular alignment. In the Debye model $\alpha = 0$, the the Cole-Cole plot is a semi-circular and center on ε' -axis. In the non-Debye case, $\alpha > 0$.

REFERENCES

- [1] Thingujam, K., et al., Effect of Temperature on the Refractive Indices of Liquid Crystals and Validation of a Modified Four-Parameter Model. 2012.
- [2] Devi, T., et al., Study of optical parameters of two fluorinated isothiocyanato nematic liquid crystals exhibiting high birefringence. *Opto-Electronics Review*, 2014. 22(1): p. 24-30.
- [3] Thingujam, K. D., et al., Optical studies of a liquid crystalline compound 6O.6. *Liquid Crystals*, 2013. 40(6): p. 810-816.
- [4] Kumar, A., Calculation of optical parameters of liquid crystals. *Acta Physica Polonica Series A*, 2007. 112(6): p. 1213.
- [5] Soorya, T., et al., Temperature dependent optical property studies of nematic mixtures. *Indian Journal of Pure and Applied Physics*, 2006. 44(7): p. 524-531.
- [6] Wu, S.-T., Birefringence dispersions of liquid crystals. *Physical Review A*, 1986. 33(2): p. 1270.
- [7] Wu, S.-T., et al., Refractive index dispersions of liquid crystals. *Optical Engineering*, 1993. 32(8): p. 1775-1780.
- [8] Li, J., S. Gauza, and S.-T. Wu, Temperature effect on liquid crystal refractive indices. *Journal of Applied Physics*, 2004. 96(1): p. 19.

- [9] Zeminder, A., S. Paul, and R. Paul, Refractive indices and orientational order parameter of five liquid crystals in nematic phase. *Molecular Crystals and Liquid Crystals*, 1980. 61(3-4): p. 191-206.
- [10] Chakraborty, A., et al., Optical, dielectric and visco-elastic properties of a few hockey stick-shaped liquid crystals with a lateral methyl group. *Journal of Materials Chemistry C*, 2013. 1(44): p. 7418.
- [11] Pramanik, A., et al., Mesomorphic, optical, dielectric, elastic and viscous properties of multi-component isothiocyanato mixtures. *Liquid Crystals*, 2013. 40(2): p. 149-158.
- [12] Sunanda, D., et al., Refractive Indices, Lorentz Field Factors, Order Parameters in Pure and Binary Nematic Mixtures. *Molecular Crystals and Liquid Crystals*, 2004. 409(1): p. 163-174.
- [13] Kuczyński, W., The orientational order in nematic liquid crystals from birefringence measurements. *Dielectrics and Electrical Insulation, IEEE Transactions on*, 2001. 8(3): p. 512-515.
- [14] Das, M.K., et al., Determination of the orientational order parameter of the homologous series of 4-cyanophenyl 4-alkylbenzoate (n. CN) by different methods. *Journal of Physics: Condensed Matter*, 2012. 24(11): p. 115101.
- [15] Chirtoc, I., et al., Determination of the order parameter and its critical exponent for n CB (n = 5–8) liquid crystals from refractive index data. *Liquid crystals*, 2004. 31(2): p. 229-240.
- [16] Chandel, V., R. Manohar, and J. Shukla, Refractive indices, order parameter and density study of BKS/B07 nematic liquid crystal. *Analele Universitatii in Bucuresti Chime*, 2011. 20: p. 155-163.
- [17] Singh, A., et al., Refractive indices, order parameter and optical transmittance studies of a nematic liquid crystal mixture. *Acta Physica Polonica Series A*, 2006. 110(4): p. 485.
- [18] Basak, S., et al., Determination of orientational order parameters of two tri-component mixtures from optical birefringence and x-ray diffraction measurements. *Acta Physica Pol A*, 2011. 120: p. 1037-1042.

- [19] Roy, P. D., B. Das, and M. K. Das, Determination of the orientational order parameter of a binary mixture showing an induced smectic A(d) phase from magnetic susceptibility measurements. *J Phys Condens Matter*, 2009. 21(33): p. 335108.
- [20] Sarna, R., V. Bhide, and B. Bahadur, Refractive indices, density and order parameter of some liquid crystals. *Molecular crystals and liquid crystals*, 1982. 88: p. 65-79.
- [21] De Gennes, P. and J. Prost, The physics of liquid crystals, 1993. Oxford University Press, New York, Olbrich E., Marinov O., Davidov D., *Phys. Rev. E*, 1993. 2713: p. 48.
- [22] Murthy, Y. N. and V. Murthy, Molecular Polarizabilities and orientational order parameters of binary mesophase mixtures of nematic compounds. *Asean Journal on Science and Technology for Development*, 2000. 17(1): p. 109-116.
- [23] Pandey, A. S., et al., Dielectric spectroscopy of unsymmetrical liquid crystal dimers showing wide temperature range TGBA and TGBC* phases. *Liquid Crystals*, 2009. 36(1): p. 13-19.
- [24] Alapati, P. R., et al., Study of Molecular Polarizabilities and Orientational Order Parameter in the Nematic Phase of 6.O12O.6 and 7.O12O.7. *World Journal of Condensed Matter Physics*, 2011. 01(04): p. 167-174.
- [25] Bhuyan, D., et al., Phase Transition Studies of 6.O12O.6 and 7.O6O.7 Using Density Measurements. *Molecular Crystals and Liquid Crystals*, 2011. 540(1): p. 205-212.
- [26] Misra, A. K., et al., Dielectric relaxation study of a H shaped liquid crystal dimer. *Physics and Chemistry of Liquids*, 2012. 50(5): p. 605-616.
- [27] Gogoi, B., T. K. Ghosh, and P. R. Alapati, Experimental investigation of phase transitions exhibited by symmetric liquid crystal dimers. *Crystal Research and Technology*, 2005. 40(7): p. 709-712.
- [28] Mrukiewicz, M., et al., Dielectric Properties of Compounds Creating Dual-Frequency Nematic Liquid Crystals. *Acta Physica Polonica, A*, 2013. 124(6).

- [29] Dunmur, D. A., et al., Dielectric relaxation in liquid crystalline dimers. *The Journal of Chemical Physics*, 2001. 115(18): p. 8681.
- [30] Bhattacharjee, D., P. R. Alapati, and A. Bhattacharjee, Negative Birefringence in the Higher Homologues of 5O. m Series of Liquid Crystals. *The Journal of Physical Chemistry B*, 2016.
- [31] Bhattacharjee, D., P. R. Alapati, and A. Bhattacharjee, Negative optical anisotropic behaviour of two higher homologues of 5O. m series of liquid crystals. *Journal of Molecular Liquids*, 2016. 222: p. 55-60.
- [32] Latha, D. M., V. G. K. M. Pisipati, and P. V. D. Prasad, Thermodynamic Parameters of nO.m Liquid-Crystal Compounds—A Dilatometric Study. *Molecular Crystals and Liquid Crystals*, 2010. 524(1): p. 144-165.
- [33] Alapati, P., et al., Phase transition and structural investigations in 5O.5, 5O.6 and 5O.7. *Liquid Crystals*, 1988. 3(11): p. 1461-1479.
- [34] Bhattacharjee, A., P. Alapati, and A. Verma, A comparative study of the properties of the liquid crystalline compounds 5O. 5 and 5O. 6 in solid, solution and thin film forms by laser Raman spectroscopy. *Liquid crystals*, 2002. 29(5): p. 725-731.
- [35] Gautam, S., et al., Phase transitions in liquid crystal 6O. 4 (pn-hexyloxybenzylidene-p'-n-butylaniline). *Pramana*, 2008. 71(5): p. 1159-1164.
- [36] Leadbetter, A., et al., Structure of the Smectic-B Phase and the Nature of the Smectic-B to-H Transition in the N-(4-n-Alkoxybenzylidene)-4'-Alkylanilines. *Physical Review Letters*, 1979. 43(9): p. 630.
- [37] Pisipati, V. and S. B. Ranavare, Interdigitated smectic A and B mesophases in higher homologues of the 5O. m series. *Liquid Crystals*, 1993. 13(6): p. 757-764.
- [38] Bhattacharjee, D., S. P. Choudhury, and A. Bhattacharjee, Correlation between the density and refractive index with higher homologues 5O. m series. *Molecular Crystals and Liquid Crystals*, 2016. 631(1): p. 69-73.

- [39] Chaudhary, A., et al., Electro-optic and dielectric studies of silica nanoparticle doped ferroelectric liquid crystal in SmC* phase. *Phase Transitions*, 2012. 85(3): p. 244-254.
- [40] DöS, A., et al., Dielectric relaxation in the fragile viscous liquid state of toluene. *The Journal of Chemical Physics*, 1997. 107(6): p. 1740.
- [41] Bhattacharjee, D., P. R. Alapati, and A. Bhattacharjee, Molecular polarization, order parameter and dielectric study of a dimeric compound. *Journal of Molecular Liquids*, 2016. 224: p. 507-514.
- [42] Bhattacharjee, D., et al., Dielectric relaxation and birefringence study of 7.O5O.7 dimeric liquid crystal compound. 2016. 1728: p. 020155.
- [43] Gauza, S., et al., Super High Birefringence Isothiocyanato Biphenyl-Bistolane Liquid Crystals. *Japanese Journal of Applied Physics*, 2004. 43(11A): p. 7634-7638.
- [44] Das, M., et al., A comparative study of the mesomorphic properties of fluoro-isothiocyanated and fluorinated terphenyl liquid crystals from birefringence, static dielectric permittivity, splay elastic constant and rotational viscosity measurements. *Journal of Physics D: Applied Physics*, 2012. 45(41): p. 415304.
- [45] Das, M. and R. Paul, Optical birefringence, density and order parameter of an ester-biphenyl mixture exhibiting an injected smectic phase. *Phase Transitions: A Multinational Journal*, 1994. 46(3): p. 185-197.
- [46] Patari, S., T. Devi, and A. Nath, Studies of optical texture, birefringence, order parameter, normalized polarizability and validation of the four-parameter model of a thermotropic mesogen 7OAOB. *Journal of Molecular Liquids*, 2016. 215: p. 244-252.
- [47] Yakhml, J., et al., Temperature dependence of refractive indices and order parameter of pn-butoxy-and pn-amyloxy benzoic acids. *Molecular crystals and liquid crystals*, 1979. 53(1-2): p. 55-62.
- [48] Singh, A. K., et al., Dielectric relaxation and anisotropy of nematic mixture E-24. *Journal of Physics and Chemistry of Solids*, 2005. 66(7): p. 1183-1186.
- [49] Slater, J. C., Microwave electronics. *Reviews of Modern Physics*, 1946. 18(4): p. 441.

- [50] Van Bladel, J., *Electromagnetic fields*. 1964. New York: p. 193.
- [51] Sastry, S. S., L. T. Kumar, and H. S. Tiong, Dielectric Studies on Benzothiazole Based Liquid Crystals at Radio Frequency Region.
- [52] Cole, K. S. and R. H. Cole, Dispersion and absorption in dielectrics I. Alternating current characteristics. *The Journal of Chemical Physics*, 1941. 9(4): p. 341-351.

Nova Science Publishing, Inc.

In: Crystal Growth
Editors: J. Li, J. Li and Y. Chu

ISBN: 978-1-53612-203-9
© 2017 Nova Science Publishers, Inc.

Chapter 9

**X-RAY, SPECTROSCOPIC
AND COMPUTATIONAL STUDIES OF
[N'-(2-HYDROXY-3-ETHOXYBENZYLIDENE)-
4-METHYLBENZENESULFONOHYDRAZIDE]
COPPER(II)**

Çiğdem Yüksektepe Ataol^{1,}, Nuray Şenyüz²,
Feyizan Güntepe³, Murat Taş⁴ and Hümevra Batı²*

¹Department of Physics, Faculty of Science,
Cankiri Karatekin University, Uluyazi, Cankiri, Turkey

²Department of Chemistry, Faculty Arts and Sciences, Ondokuz Mayıs
University, Kurupelit, Samsun, Turkey

³Department of Physics, Faculty of Science, Ondokuz Mayıs
University, Kurupelit, Samsun, Turkey

⁴Department of Science Education, Faculty of Education, Ondokuz
Mayis University, Kurupelit, Samsun, Turkey

* Corresponding author: ÇiğdemYüksektepeAtaol.E-mail: yuksektepe.c@karatekin.edu.tr;
yuksekc85@gmail.com.

ABSTRACT

The $C_{30}H_{30}CuN_4O_8S_2$ (*I*) complex has been investigated and characterized by single crystal X-ray diffraction (CIF file CCDC no. 955436), Infrared (IR), Ultraviolet-visible (UV-vis) and Density Functional Theory (DFT) from spectroscopic and computational chemistry methods. Cu (II) forms a 1: 2 (metal/ligand) complex. The mononuclear Cu (II) complex crystallized in the monoclinic crystal system has a $P2_1/n$ space group. In the title structure, $[C_{30}H_{30}CuN_4O_8S_2]$, coordination around Cu atom is distorted square planar. In addition to the results obtained from X-ray, the molecular structure, vibrational assignments and molecular electrostatic potential map of the title compound have been investigated by using the B3LYP/6-311G and B3LYP/3-21G methods. Nonlinear optical (NLO) properties of the molecule such as the polarizability ($\langle\alpha\rangle$), the anisotropy of the polarizability ($\langle\Delta\alpha\rangle$), ground state dipole moment (μ) and the first-order hyperpolarizability (β) of molecule are studied at the Density Functional Theory (DFT/B3LYP) with 3-21G and 6-311G basis sets. Also, E_{HOMO} (the highest occupied molecular orbital energy), E_{LUMO} (the lowest unoccupied molecular orbital energy), HOMO-LUMO energy gap (ΔE), electron affinity (A), ionization potential (I), global hardness (η), softness (σ), electronegativity (χ), chemical potential (Π), global electrophilicity index (ω) are investigated by quantum chemical methods.

Keywords: copper (II), crystal structure, nonlinear optics, sulfonohydrazide, DFT

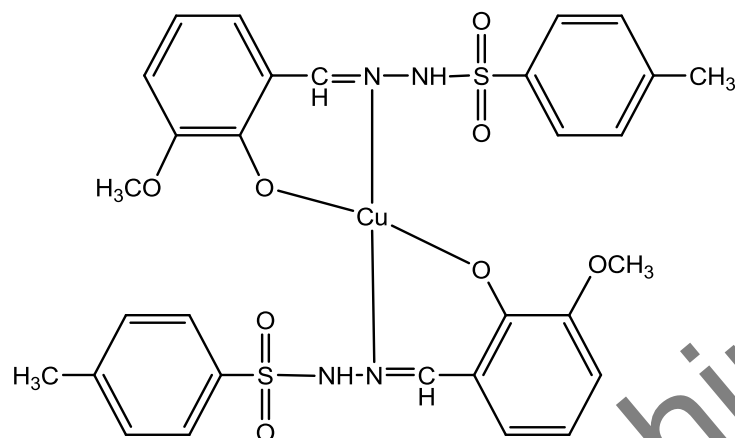
INTRODUCTION

Many Schiff base complexes have potential biological interest in an attempt to mimic the structural and functional features of multimetal active sites. It is found that Schiff bases have many applications in physics and chemistry [1]. In coordination chemistry, Schiff bases are easily coordinated with metal ions in order to form mono or poly nuclear metal complexes [2, 3]. Besides these applications, they can be used also in analytical chemistry and biochemical models [4, 5]. Schiff bases have biological activities such as anti-bacterial, anti-cancer, anti-inflammatory and anti-toxic[6]; in particular, sulfur-containing Schiff bases are very

effective. Schiff bases have played an important role in the development coordination chemistry and Schiff bases ligands are well known their wide range of application in pharmaceutical and industrial field [7, 8]. The coordination compounds derived from Schiff bases with transition metals have been studied with wide scope of their applications [9].

Some studies show that hydrazone compounds are used in organic or metal organic structures [10-13] and particularly in hydrazone Schiff base ligands [14-17], which are among others employed in dinuclear catalysts [18]. In addition, medicines containing hydrazone compound have been used in the treatment of many diseases. Hydrazone compounds having physiological activity constitute stable chelate complexes with transition metals which catalyze physiological processes [19-21]. Hydrazones find applications as multidentate ligands for transition metals in colorimetric or fluorimetric determinations [22, 23].

We have prepared a new sulfonylhydrazone Cu(II) complex-[N'-(2-hydroxy-3-methoxybenzylidene)-4-methylbenzenesulfonylhydrazone]copper(II) ($C_{30}H_{30}CuN_4O_8S_2$) (*I*) which has been identified by a combination of FT-IR spectra, UV-Vis spectra, magnetic susceptibility measurements, and single crystal X-ray diffraction. Density Functional Theory (DFT) is used to optimize the Cu II complex molecule. Later, using the optimized structures, its vibration frequencies were calculated with different base sets. In addition, the potential map of the complex molecule was obtained with the same base function and 6-311G basis set. Frontier molecular orbital (FMO) analysis including spin transitions have been explained in detail by using TD-UB3LYP. The calculated ionization potential (I), electron affinity (A), electronegativity (χ), chemical potential (Pi), chemical hardness (η), chemical and global softness (s , σ) and global electrophilicity index (ω) have been obtained from molecular frontier orbital energies using ab initio methods at different basis sets. Also, the nonlinear optical (NLO) parameters such as the polarizability ($\langle\alpha\rangle$), the anisotropy of the polarizability ($\langle\Delta\alpha\rangle$), ground-state dipole moment (μ) and the first-order hyperpolarizability (β) of molecule have been by DFT with 3-21G and 6-311G basis sets.



Scheme 1. The chemical diagram of [N'-(2-hydroxy-3-methoxybenzylidene)-4-methylbenzenesulfonylhydrazide]copper(II).

The first aim of this study is to understand its crystal and molecular structures by X-ray analysis and quantum chemical method, comparing experimental and theoretical results. The chemical diagram of 1 is the following:

EXPERIMENTAL

Physical measurements and theoretical methods. The optical absorption spectra of complex 1 was obtained at room temperature in solvent environment on a Unicam UV2 UV-vis spectrometer between 200-900 nm. IR spectra were recorded on a Vertex 80v Bruker FTIR spectrophotometer in 4000-400 cm^{-1} using KBr pellets. Magnetic measurements MX SHERWOOD SCIENTIFIC model was made according to one embodiment of the method of Evansim proved method of Gouy magnetic susceptibility balance.

Starting geometries of compound 1 were taken from X-ray refinement data for computing procedure. The molecular structures of compound 1 in the ground state (*in vacuo*) were optimized by DFT methods to include correlation corrections with the 3-21G and 6-311G basis sets. DFT forms

hybrid functionals, including B3 [24], which defines the exchange functional as the linear combination of Hartree-Fock, local, and gradient-corrected exchange terms. The B3 hybrid functional was used in combination with the correlation functionals [25].

Then vibrational frequencies for optimized molecular structures have been calculated by using DFT/B3LYP with 3-21G and 6-311G basis sets. Besides of this, the lowest unoccupied molecular orbital (*LUMO*) highest occupied molecular orbital (*HOMO*) energy differences were calculated with Time-Dependent Density Functional Theory (*TD-DFT*). All the calculations were performed using Gaussian 09 program [26].

Polarizabilities were calculated at the same level of theory using the standard GAUSSIAN-09 keyword 'Polar' [27]. This keyword means that the polarizabilities were obtained analytically rather than by numerical differentiation. The energy of an uncharged molecule under a weak, general electric field can be expressed by Buckingham type expansion [28-30]

$$E = E_0 - \mu_i F_i - (1/2)\alpha_{ij} F_i F_j - (1/6)\beta_{ijk} F_i F_j F_k + \dots \quad (1)$$

where E is the energy of a molecule under the electric field F , E_0 is the unperturbed energy of a free molecule, F_i is the vector component of the electric field in the i direction, and μ_i , α_{ij} , β_{ijk} are the dipole moment, linear polarizability and first-order hyperpolarizability, respectively. Here, each subscript of i , j and k denotes the indices of the Cartesian axes x , y , z , and a repeated subscript means a summation over the Cartesian indices x , y , z . The ground state dipole moment μ , the polarizability $\langle \alpha \rangle$, the anisotropy of the polarizability $\langle \Delta \alpha \rangle$ and the first-order hyperpolarizability β , using the x , y , z components they are defined as [31, 32].

$$\mu = (\mu_x^2 + \mu_y^2 + \mu_z^2)^{1/2} \quad (2)$$

$$\langle \alpha \rangle = \frac{\alpha_{xx} + \alpha_{yy} + \alpha_{zz}}{3} \quad (3)$$

$$\langle \Delta \alpha \rangle = \left[\frac{(\alpha_{xx} - \alpha_{yy})^2 + (\alpha_{yy} - \alpha_{zz})^2 + (\alpha_{zz} - \alpha_{xx})^2 + 6(\alpha_{xy}^2 + \alpha_{xz}^2 + \alpha_{yz}^2)}{2} \right]^{1/2} \quad (4)$$

$$\beta = \sqrt{(\beta_{xxx} + \beta_{yyy} + \beta_{zzz})^2 + (\beta_{yyy} + \beta_{zzz} + \beta_{yxx})^2 + (\beta_{zzz} + \beta_{zzx} + \beta_{zyy})^2} \quad (5)$$

Since the values of the polarizabilities (α) and first-order hyperpolarizability (β) of GAUSSIAN-09 output [33] are reported in atomic units (a.u.), the calculated values have been converted into electrostatic units (esu) (α : 1 a.u. = 0.1482×10^{-24} esu; β : 1 a.u. = 8.6393×10^{-33} esu) [34].

Synthesis of complex 1. An ethanolic solution (15 mL) of *o*-vanillin (2 mmol, 0.304g) was added to a solution of the 4-methylbenzenesulfonylhydrazine (2 mmol, 0.372g), in ethanol (15 mL). There sulting solution was stirred for half an hour, and then Cu(CH₃COO)₂.2H₂O (1mmol, 0.199g) in 10 mL ethanol was added. The solution was refluxed for 48 h, with stirring. The mixture was then cooled to room temperature and a brown powder was precipitated. The product was filtered and washed with ethanol. Crystals of suitable for X-ray diffraction were grown from an acetonitrille solution and slowly evaporated for 6 days. (mp: 227°C and yield 65%).

X-ray crystallography. Data collection was carried out on a Oxford Diffraction SuperNova (single source at offset) Eos diffractometer equipped with a graphite monochromated MoK α radiation ($\lambda = 0.7107 \text{ \AA}$) at 293 K. The structure was solved by direct methods using SHELXS [35] implemented in the WinGX software system [36] and refined by full-matrix least-squares procedure on F^2 using SHELXL [37]. All other atoms except hydrogen atoms are anisotropically refined and later, hydrogen atoms are isotropically refined with C–H = 0.93–0.97 and N–H = 0.86 \AA . $U_{\text{iso}}(\text{H}) = 1.2U_{\text{eq}}(\text{C}, \text{N})$, $U_{\text{iso}}(\text{H}) = 1.5U_{\text{eq}}$ (for methyl group). Crystals of 1 were found approximately 0.25:0.75 ratio to be twinned. Data

collection, CrysAlisPro [38]; cell refinement, CrysAlisPro; data reduction, CrysAlisPro. The molecular structure plots were prepared by using the ORTEP-3 for *Windows*[36]. Crystallographic data, details of the data collection and structure refinements are listed in Table 1, the selected geometric parameters are given in Table 2.

Supplementary material for structure 1 has been deposited with the Cambridge Crystallographic Data Centre (no. 955436; deposit@ccdc.cam.ac.uk or <http://www.ccdc.cam.ac.uk>).

Table 1. Crystallographic data and structure refinement for complex 1

Parameter	Value
Empirical formula	C ₃₀ H ₃₀ CuN ₄ O ₈ S ₂
F _w	702.27
Crystal system	Monoclinic
Space group	P2 ₁ /n
Unit cell dimensions:	
<i>a</i> , Å	9.0397(3)
<i>b</i> , Å	21.0694(8)
<i>c</i> , Å	16.5707(6)
β	93.189(3)
Volume, Å ³	3151.2(2)
<i>Z</i>	4
ρ_{calcd} , mg m ⁻³	1.480
μ , mm ⁻¹	0.882
Absorption correction	Multi-scan
Diffractometer/measurement	SuperNova (Single source at offset), Eos diffractometer/rotation (ω scan)
Index ranges (<i>h</i> , <i>k</i> , <i>l</i>)	-9 ≤ <i>h</i> ≤ 11, -25 ≤ <i>k</i> ≤ 17, -20 ≤ <i>l</i> ≤ 15
θ Range for data collection, deg	3.26-26.00
Reflections collected	12775
Independent reflections	6184
Observed reflections (<i>I</i> > 2 σ (<i>I</i>))	4450
<i>R</i> _{int}	0.036
Goodness-of-fit on <i>F</i> ²	1.045
Final <i>R</i> indexes (<i>I</i> > 2 σ (<i>I</i>))	<i>R</i> ₁ = 0.048, <i>wR</i> ₂ = 0.108
$\Delta\rho_{\text{max}}, \Delta\rho_{\text{min}}$, e Å ⁻³	0.56, -0.52
Extinction coefficient	0.0014(3)

Table 2. Selected geometrical parameters of 1 with X-ray structure and the DFT method

Bond	Experimental	B3LYP 3-21G	B3LYP 6-311G
		<i>d</i> , Å	
Cu–O(1)	1.875(2)	1.825	1.897
Cu–O(1a)	1.875(2)	1.823	1.897
Cu–N(1)	1.960(2)	1.888	1.979
Cu–N(1a)	1.961(2)	1.888	1.980
S(1)–O(4)	1.428(3)	1.594	1.640
S(1)–O(3)	1.426(3)	1.589	1.634
S(1)–N(2)	1.680(3)	1.887	2.002
S(1a)–O(3a)	1.431(3)	1.589	1.634
S(1a)–O(4a)	1.426(3)	1.595	1.640
S(1a)–N(2a)	1.666(3)	1.899	2.001
N(1a)–N(2a)	1.432(3)	1.461	1.407
N(1)–N(2)	1.432(4)	1.462	1.406
N(1a)–C(1a)	1.289(4)	1.317	1.324
N(1)–C(1)	1.298(4)	1.318	1.329
Bond angles		deg	
O(1)CuO(1a)	177.77(11)	164.68	179.88
O(1)CuN(1)	92.01(10)	91.96	91.39
O(1a)CuN(1)	88.27(10)	91.02	88.62
O(1)CuN(1a)	88.39(10)	90.38	88.58
O(1a)CuN(1a)	91.37(10)	92.68	91.41
N(1)CuN(1a)	178.66(11)	157.17	179.82
O(4a)S(1a)O(3a)	120.88(16)	120.51	122.90
O(4a)S(1a)N(2a)	106.81(16)	105.86	103.69
O(3a)S(1a)N(2a)	103.64(16)	104.68	104.83
O(3)S(1)O(4)	121.06(16)	121.64	122.95
O(3)S(1)N(2)	103.90(16)	105.94	104.84
O(4)S(1)N(2)	106.59(17)	105.79	103.64
C(1a)N(1a)N(2a)	115.86(2)	114.83	115.41
C(1a)N(1a)Cu	125.89(2)	127.94	126.22
N(2a)N(1a)Cu	118.24(19)	117.23	118.30
C(3a)O(1a)Cu	126.51(18)	129.16	130.57
C(3)O(1)Cu	128.36(2)	129.76	130.59
C(1)N(1)N(2)	115.82(3)	113.89	115.37

Bond	Experimental	B3LYP 3-21G	B3LYP 6-311G
C(1)N(1)Cu	125.68(2)	128.05	126.24
N(2)N(1)Cu	118.37(2)	117.84	118.33
N(1)N(2)S(1)	112.13(19)	109.34	111.32
N(1a)N(2a)S(1a)	113.8(2)	110.99	111.44
Torsion angles		deg	
O(1)CuN(1a)N(2a)	18.8(2)	-13.1	-3.5
O(1a)CuN(1a)N(2a)	-163.4(2)	-178.1	176.6
N(1)CuN(1a)N(2a)	-89.0(5)	82.8	76.6
O(1)CuN(1)N(2)	160.9(2)	-166.4	-176.8
O(1a)CuN(1)N(2)	-16.9(2)	-1.6	3.0
N(1a)CuN(1)N(2)	-91.2(5)	97.9	103.0
CuN(1)N(2)S(1)	96.0(2)	-109.4	-106.0
CuN(1a)N(2a)S(1a)	96.2(2)	112.66	106.5

RESULTS AND DISCUSSION

The X-ray structure of [N²-(2-hydroxy-3-methoxybenzylidene)-4-methylbenzenesulfonylhydrazide]copper(II) was determined in order to confirm the assigned structure and to establish conformation of the molecule. ORTEP drawing of the structure with atomic numbering is shown in Figure 1(a). The single crystal structure of the mononuclear Cu (II) has a monoclinic crystal system and a space group P2₁/n. Complex 1 is centrosymmetric where the Cu (II) is coordinated to two sulfonylhydrazide ligands *via* hydrazone nitrogens (N(1) and N(1a)) and hydroxyl oxygens (O(1) and O(1a)). The coordination around Cu atom is distorted square planar. Deviation from idealized square planar arrangement evident from the values of both *cis*- and *trans* bond angles around the central Cu (II) atom in Table 2. The ligand: metal ratio was 2: 1 in the case of complex 1. The Cu-N(1)-O(1)-N(1a)-O(1a) atoms is nearly planar with a mean deviation of 0.0306(13) Å for O(1a). The dihedral angle between the coordination O(1)/N(1)/O(1a)/N(1a)/Cu(1) and C(2)-C(7) planes is 13.52(16)° while the C(2a)-C(7a) deviate from the Cu coordination plane by 21.16(14)°. The C(9)-C(14) and C(9a)-C(14a) planes also form dihedral angles of 23.54(14)° and 28.90(15)° with the Cu coordination plane,

respectively. The average Cu–N bond distances of 1.960(2) is within the range 2.015(5)–1.922(3) Å reported for related compound [39–41]. As can be seen in [42], the C–S–N(H)–N sulfonohydrazide linkage is non-planar, the torsion angles are $-51.7(2)^\circ$ and $57.0(2)^\circ$ for C(9a)–S(1a)–N(2aH)–N(1a) and C(9)–S(1)–N(2H)–N(1), respectively, the S atom showing a tetrahedral environment suggests a sp^3 hybridization for the S atom. The C–N bond lengths in compound 1 are 1.298(4) and 1.289 (4) Å for N(1)–C(1) and N(1a)–C(1a), respectively, which shorter than a C–N single bond length 1.443 Å [43], but longer than a typical C=N bond length 1.269 Å [44], indicating delocalization.

In order to investigate the aromaticity of rings, (HOMA) indices for rings by using following equation:

$$HOMA = 1 - \left[\frac{\alpha}{n} \sum_{i=1}^n (R_i - R_{opt})^2 \right] \quad (6)$$

n is the number of bonds in ring, α is the constant equal to 257.7 and R_{opt} is equal to 1.388 Å for C–C bonds. For the purely aromatic compounds HOMA (harmonic oscillator model of aromaticity) index is equal to 1 but, for non-aromatic compounds it is equal to 0 [45, 46]. The calculated HOMA indices for C2–C7, C2a–C7a, C9–C14 and C9a–C14a rings are 0.8642, 0.8456, 0.9795 and 0.9495, respectively. These results also indicate that the titled compound exists rings are the aromatic.

In the molecular structure of title compound 1, it is observed that the sulfonyloxygens O(3) and O(4a) involved in intramolecular hydrogen bonds with the C(10)–H and C(14a)–H proton, respectively. These hydrogen bonds motif of graph set descriptors S(5) form five membered rings. The sulfonyl oxygen O(3) forms inter molecular C–H...O hydrogen bonding with the C(7a)–H proton at $(1 + x, y, z)$. This hydrogen bond of graph set descriptor C(10) [47] forms a chain propagating along the x -axis as shown in Figure 2(a). The crystallographically independent chains interconnected by edge to face C–H ... π interactions along the [101]

directions as shown in Figure 2(b). The details of hydrogen bonds are given in Table 3.

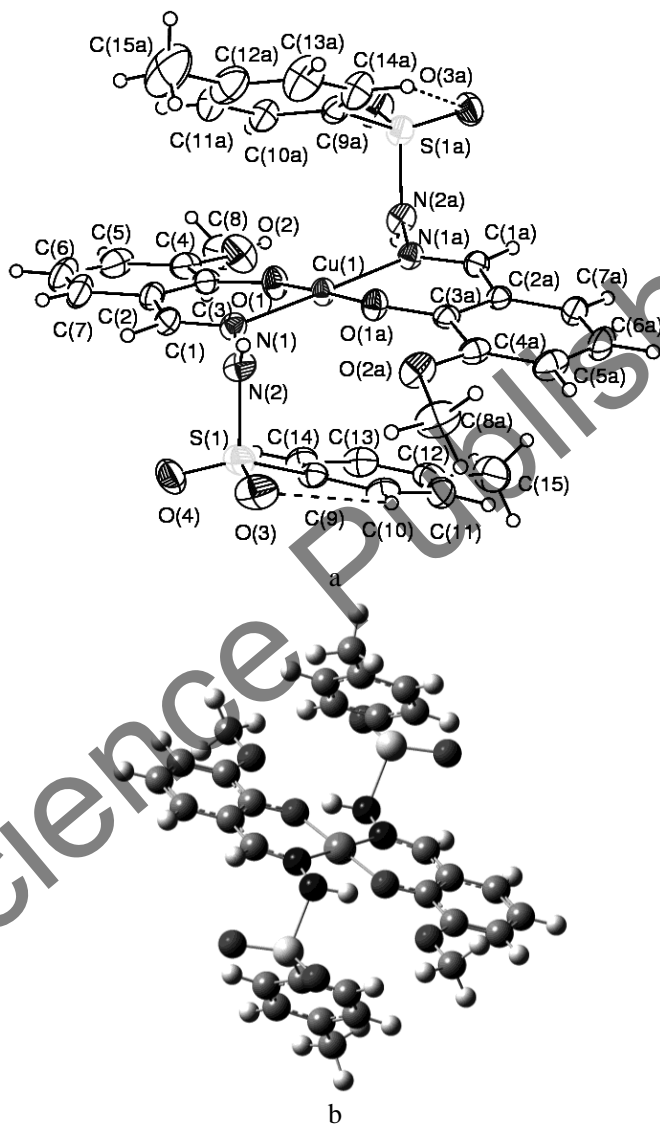


Figure 1. ORTEP-3 drawing of the basic crystallographic unit of the title compound, showing the atom-numbering scheme (a) (displacement ellipsoids are drawn at the 30% probability level and all H atoms are shown as small spheres of arbitrary radii); optimized structure of 1 (b).

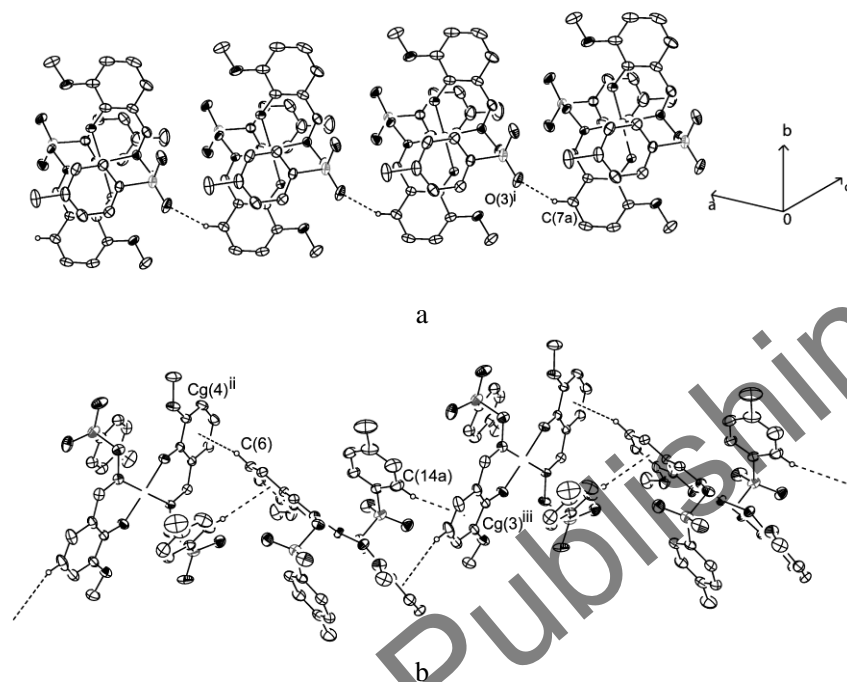


Figure 2. Intermolecular C(7a)–H(22) ... O(3)ⁱ hydrogen bonding extending along a-axis. Symmetry code: ⁱ 1 + x, y, z (a); C(6)–H(6) ... Cg(4)ⁱⁱ and C(14a)–H(25) ... Cg(3)ⁱⁱⁱ interactions. Symmetry codes: ⁱ -1/2 + x, 1/2 - y, -1/2 + z; ⁱⁱⁱ 1/2 + x, 1/2 - y, 1/2 + z (b).

The optimized molecular structure is shown in Figure 1(b). Some selected geometric parameters experimentally obtained and theoretically calculated by B3LYP/3–21G and B3LYP/6–311G methods are listed in Table 2. Experimental results are solid phase and theoretical calculations are gaseous phase. In solid state, intermolecular interactions combine molecules and cause differences in the bonds between calculated and experimental values. DFT optimized geometric parameters are usually in good agreement with experimental values and more accurate than Hartree-Fock and semi-empirical methods, due to inclusion of electron correlation.

Optimized bond lengths and torsion angles provided by B3LYP/3-21G method are closer to the X-ray results (see Table 2) whereas the bond angles are provided by B3LYP/6-311G show the best agreement with the experimental values.

Table 3. Hydrogen bonding geometries for the title compound

D-H ... A	D-H	Distance, Å		
		H ... A/Cg	D ... A/Cg	D-H ... A/Cg, deg
C(10)–H(10) ... O(3)	0.93	2.58	2.946(5)	104
C(14a)–H(25) ... O(4a)	0.93	2.55	2.918(4)	104
C(7a)–H(22) ... O(3) ⁱ	0.93	2.57	3.300(4)	136
C(6)–H(6) ... Cg(4) ⁱⁱ	0.93	2.8846	3.652(4)	140.64
C(14a)–H(25) ... Cg(3) ⁱⁱⁱ	0.93	2.8886	3.759(5)	156.58

Symmetry codes: ⁱ 1 + x, y, z; ⁱⁱ -1/2 + x, 1/2 -y, -1/2 + z; ⁱⁱⁱ 1/2 + x, 1/2 -y, 1/2 + z; Cg(3) centroid of (C(2)–C(7)) ring, Cg(4) centroid of (C(2a)–C(7a)) ring.

Vibrational frequencies are calculated at the B3LYP/3-21G and B3LYP/6-311G levels for 1. Some primary calculated harmonic frequencies are listed in Table 4 and compared with experimental data; assignments are also indicated in Table 4. Gaussview molecular visualization program was used to assign the calculated harmonic frequencies. IR spectra of 1 has been studied to characterize its structure. Experimental and theoretical IR spectra is shown in Figure 3.

In the experimental IR spectrum of complex 1, a sharp band observed at 3116 cm⁻¹ is assigned to the $\nu(\text{NH})$ group. The characteristic phenolic $\nu(\text{OH})$, due to the presence of an hydroxy group at the *o*-position, was observed in ligand at 3148 cm⁻¹. In IR spectrum of the complex, these peaks $\nu(\text{OH})$ have disappeared after deprotonation, and the phenolic oxygen coordinates with the Cu atom. However, such coordination is supported by the shifting of the phenolic $\nu(\text{C}=\text{O})$ to lower wavenumber in the complex. In IR spectra of the Schiff base ligand, a sharp band at 1610 cm⁻¹ is assigned to the $\nu(\text{C}=\text{N})$ mode of the azomethine group. These shifts to lower wavenumbers in CuL complex suggest the coordination of the azomethine nitrogen to the Cu atom. This is further substantiated by the presence of a new band at 471 cm⁻¹ is assigned to $\nu(\text{M}=\text{N})$. In IR spectrum of complex, the two bands at 1322, 1166 cm⁻¹ are attributed to $\nu_s(\text{SO}_2)$, $\nu_{as}(\text{SO}_2)$ vibrations.

Table 4. Vibrational frequencies of 1 with experimental and DFT/B3LYP methods

Frequencies	Experimental	B3LYP/3-21G	B3LYP/6-311G
$\nu(\text{CH})$ aromatic		3253-3218	3212-3208
$\nu_{\text{as}}(\text{CH})$ aromatic		3214-3185	3192/3173
$\nu(\text{CH})$		3185-3182	3167
$\nu_{\text{as}}(\text{CH}_3)$	2975	3181-3097	3161-3073
$\nu_{\text{as}}(\text{NH})$	3116	3075-3059	3204
$\nu(\text{CH}_3) + \nu(\text{NH})$		3052-3035	3019-3006
$\nu(\text{CC})$		1635	1641
$\nu(\text{CC}) + \delta(\text{NH}) + \nu(\text{C} = \text{N})$	1610	1601	1608/1572
$\delta(\text{CH}_3)$		1570	1536
$\rho_r(\text{CH}_3) + \delta(\text{CH}) + \delta(\text{NH})$		1561/1480	1531/1497
$\delta(\text{CH})$ aromatic	1544	1554-1543	1517/1494
$\delta(\text{NH})$	1470	1531/1514/1503	1524/1494
$\omega(\text{CH}_3)$	1451	1494/1492	1528
$\rho_s(\text{CH})$	1461/1367	1448/1445	1497
$\nu(\text{CC}) + \delta(\text{NH}) + \delta(\text{CH}) + \delta(\text{CCO}) + \delta(\text{CCN})$	1358	1364/1352	1463
$\delta(\text{NH})$ out of plane		1326	1370-1344
$\nu(\text{CO})$ linked methyl	1293	1261	1268/962
$\nu(\text{CO}) + \nu(\text{CN})$	1320	1470	1266
$\theta(\text{phenyl})$	1251	1225-1107	1341/1266/1089
$\rho_r(\text{NH}) + \nu(\text{SO})$	1117	1171/1079	1226/1146
$\rho_s(\text{CH})$ aromatic	1226/1183	1122/1093	1225/1098
$\tau(\text{CH})$ aromatic	1088-1104	1047-1018	995
$\nu(\text{NN})$	1031	988/937/928	1013/973
$\nu(\text{CH})$	962	1026	978
$\nu_{\text{as}}(\text{OSO})$	1166	1093/1081-1077	887/793
$\rho_r(\text{CH})$		983	826
$\omega(\text{CH})$ aromatic	774/902	887/783	874/795
$\nu(\text{OCuO})$		901/898/764	887/883
$\delta(\text{OCuO})$		727	881
$\nu(\text{NCuN})$	471	647	762
$\delta(\text{NNC})$		639	962/759/658
$\nu(\text{OSO})$	1322	905-901	747

These values are in accord with reported structure in [42]. In addition to these, the calculated vibrational frequencies can be seen in Table 4. In general, when the calculated IR frequencies are compared with the experimental data of 1, approximately all data agree with calculated vibrations. Because experimental results are solid phase and theoretical

calculations are gaseous phase, there is a minor difference between the data.

The molecular electrostatic potential (MEP) is a technique of mapping electrostatic potential onto the iso-electron density surface [48]. MEP is related to electron density and is a very useful descriptor in understanding sites for electrophilic (electron-deficient, positively charged species) attack and nucleophilic (an electron rich, negatively charged species) reactions as well as hydrogen-bonding interactions [49]. To predict reactive sites for electrophilic attack for **1**, MEP was calculated at the B3LYP/6-311G optimized geometry. Negative regions of MEP are rich in electrons and positive regions are not of electrons (Figure 4). This molecule has a possible site for electrophilic attack. The negative regions are mainly over oxygen atoms with O(3), O(4), O(3a), and O(4a) atoms. Total density, contour of total density, alpha density, electrostatic potential, the contour of electrostatic potential and molecular electrostatic potential are shown in Figure 4.

Because the complex has a paramagnetic feature, the electronic transition energies including α (spin up) and β (spin down) electron spins have been calculated both gas phase and acetonitrile (solvent) phase by the TD-UB3LYP/3-21G and TD-UB3LYP/6-311G methods from the optimized geometries to reproduce UV-Vis spectroscopic transitions for 45 states. According to the restricted shell calculations, the results indicate that **1** has 182 occupied molecular orbitals (MOs). Besides of this, the unrestricted shell calculations indicate that **1** has 182 and 181 occupied molecular orbitals (MOs) for α and β spins, respectively. The DOS (density of states) plot provided a diagrammatic view of the molecular orbital contributions, computed by the Gauss-Sum 3.0 program [50] at UB3LYP/3-21G. The bonding highest-occupied MO (HOMO) energies, the antibonding lowest-unoccupied MO (LUMO) (Figure 5) energies, total energies, the energy gaps, dipol moment and metal and ligand percentage distribution to MOs are given in Table 5 for gas and solvent phases. The frontier MOs play an important role in electrical and optical properties, as well as in UV-Vis spectra and chemical reactions [51]. Based on the TD-DFT UB3LYP/3-21G and UB3LYP/6-311G optimized geometries, the

total energy of 1 has been calculated by these methods, as -4395.970(gas), -4395.996(solvent) and -4418.482(gas), -4418.520(solvent) a.u. respectively. It can be said that the narrower HOMO-LUMO gap of the molecule, it will be the more chemically reactive [52]. In this study, the lowest HOMO-LUMO gaps of the molecule for α and β are calculated such as 2.762 eV and 2.664 eV by UB3LYP/6-311G(acetonitrile) methods, respectively (Table 5), and this energy gap indicates that the structure is very stable. As can be seen, the electrons of the copper atom have mostly occupied to HOMO-4 β , HOMO-5 β and HOMO-20 β . The total spin transitions, MO \rightarrow MO transition and its percentage contributions corresponding to some wavelengths are shown in Table 6 by using different basis sets together gas and solvent phases for 45 states. HOMO and LUMO are shown in Figure 5. A UV diagram including experimental and theoretical results is shown in Figure 6. Also, the density of the states (DOS) is shown in Figure 7.

The dipole moment in a molecule is an important property, which is mainly used to study the intermolecular interactions involving the nonbonded type dipole-dipole interactions, because the higher the dipole moment, the stronger the intermolecular interactions will be. The dipole moments of the studied structure obtained using DFT calculations are summarized in Table 5. Results show that there is approximately increase in μ when the calculation is done at 3-21G and 6-311G basis sets when compared to other basis sets.

The experimental UV-Vis spectrum of complex 1 is complicated by the presence of intense absorption 262 and 361 nm due to the Schiff base ligand. The absorption bands 262 and 361 nm can be assigned to $\pi \rightarrow \pi^*$ and $n \rightarrow \pi^*$ transitions of the ligand. There is two absorption bands at 401 and 691 nm in the spectrum of complex 1. The first band of relatively high intensity is assigned as ligand \rightarrow metal charge transfer transition.

The second weak band corresponds to the $d \rightarrow d$ transitions. It is seen that the wavelengths of HOMO-LUMO gap calculated by using UB3LYP/3-21G and UB3LYP/6-311G methods are consistent experimentally ligand \rightarrow metal charge transfer transition.

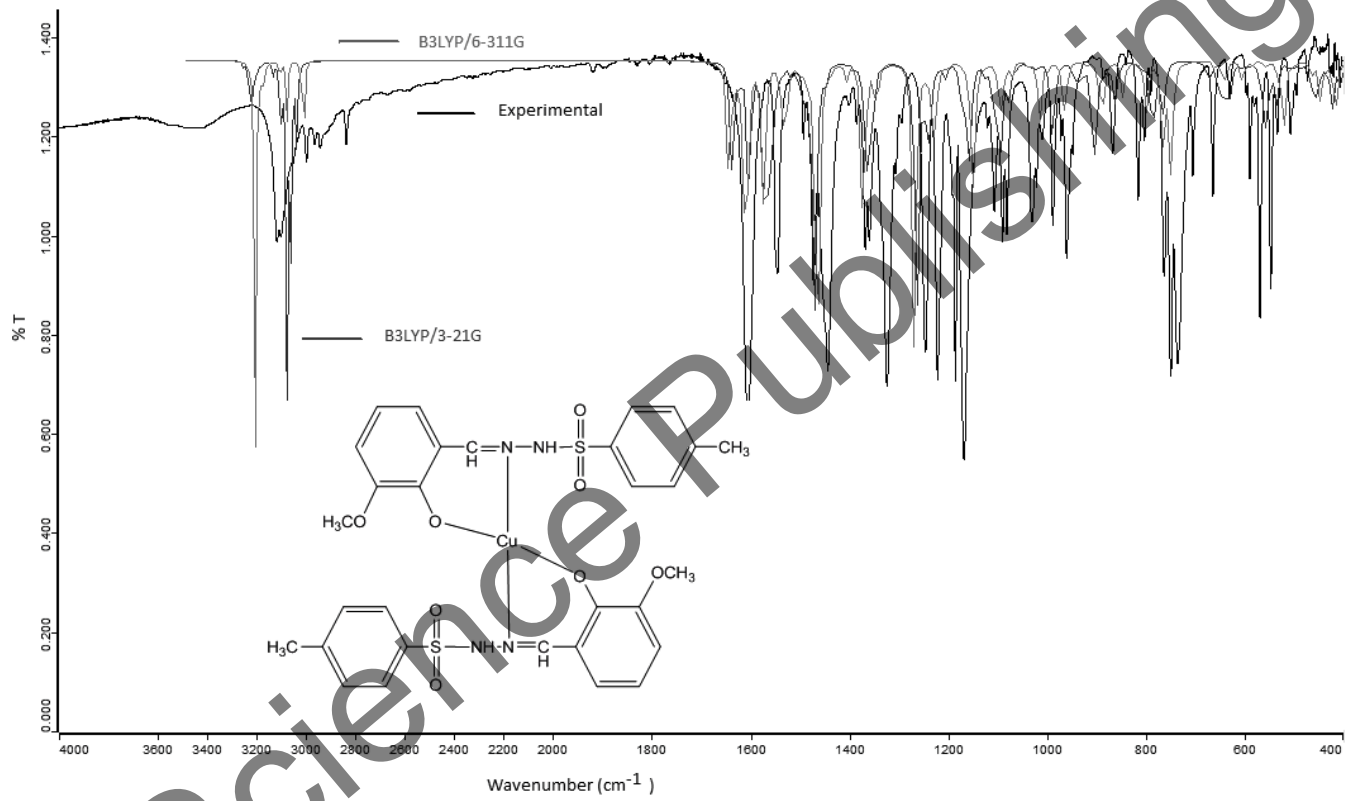


Figure 3. Experimental and theoretical IR spectra.

Table 5. MO energies of 1 with DFT method

MO Energies (Metal % + Ligand %) Fragmentation to MOs	UB3LYP 3-21G Gas	UB3LYP 3-21G Acetonitrile	UB3LYP 6-311G Gas	UB3LYP 6-311G Acetonitrile
LUMO+6 α , a.u.	-0.0113 (1%+99%)	-0.0188 (1%+99%)	-0.0337(0%+100%)	-0.0321(0%+100%)
LUMO+5 α , a.u.	-0.0147 (2%+98%)	-0.0208 (2%+98%)	-0.0458(1%+99%)	-0.0553(0%+100%)
LUMO+4 α , a.u.	-0.0211 (1%+99%)	-0.0233 (1%+99%)	-0.0480(0%+100%)	-0.0576(0%+100%)
LUMO+3 α , a.u.	-0.0384 (1%+99%)	-0.0441 (1%+99%)	-0.0578(0%+100%)	-0.0621(0%+100%)
LUMO+2 α , a.u.	-0.0411 (1%+99%)	-0.0461 (1%+99%)	-0.0581(0%+100%)	-0.0623(0%+100%)
LUMO+1 α , a.u.	-0.0738 (2%+98%)	-0.0803 (2%+98%)	-0.1059(0%+100%)	-0.1138(0%+100%)
LUMO α , a.u.	-0.0749 (2%+98%)	-0.0811 (2%+98%)	-0.1085(1%+99%)	-0.1166(1%+99%)
HOMO α , a.u.	-0.1919 (28%+72%)	-0.1970 (28%+72%)	-0.2178(3%+97%)	-0.2181(3%+97%)
HOMO-1 α , a.u.	-0.2034 (9%+91%)	-0.2070 (9%+91%)	-0.2234(0%+100%)	-0.2236(0%+100%)
HOMO-2 α , a.u.	-0.2157 (10%+90%)	-0.2191 (10%+90%)	-0.2338(15%+85%)	-0.2377(16%+84%)
HOMO-3 α , a.u.	-0.2317 (15%+85%)	-0.2366 (15%+85%)	-0.2475(0%+100%)	-0.2519(6%+94%)
HOMO-4 α , a.u.	-0.2382 (5%+95%)	-0.2450 (5%+95%)	-0.2482(6%+94%)	-0.2526(0%+100%)
HOMO-5 α , a.u.	-0.2622 (5%+95%)	-0.2682 (5%+95%)	-0.2752(0%+100%)	-0.2772(0%+100%)
$\Delta\alpha$, a.u. (eV)	0.1170 (3.185)	0.1159 (3.154)	0.1093(2.974)	0.1015(2.762)
LUMO+4 β , a.u.	-0.0265 (30%+70%)	-0.0314(30%+70%)	-0.0570(0%+100%)	-0.0615(0%+100%)
LUMO+3 β , a.u.	-0.0382 (1%+99%)	-0.0438(1%+99%)	-0.0573(0%+100%)	-0.0616(0%+100%)
LUMO+2 β , a.u.	-0.0414 (3%+97%)	-0.0464(3%+97%)	-0.0938(37%+63%)	-0.0940(40%+60%)
LUMO+1 β , a.u.	-0.0733 (2%+98%)	-0.0800(2%+98%)	-0.1057(0%+100%)	-0.1137(0%+100%)
LUMO β , a.u.	-0.0745 (3%+97%)	-0.0808(3%+97%)	-0.1107(5%+95%)	-0.1186(3%+97%)

MO Energies (Metal % + Ligand %) Fragmentation to MOs	UB3LYP 3-21G Gas	UB3LYP 3-21G Acetonitrile	UB3LYP 6-311G Gas	UB3LYP 6-311G Acetonitrile
HOMO β , a.u.	-0.1992 (14% + 86%)	-0.2032 (14% + 86%)	-0.2162 (3% + 97%)	-0.2165 (3% + 97%)
HOMO-1 β , a.u.			-0.2224 (0% + 100%)	-0.2227 (0% + 100%)
HOMO-2 β , a.u.	-0.2118 (5% + 95%)	-0.2148 (5% + 95%)	-0.2442 (3% + 97%)	-0.2479 (3% + 97%)
HOMO-3 β , a.u.	-0.2273 (28% + 72%)	-0.2316 (28% + 72%)	-0.2462 (0% + 100%)	-0.2514 (0% + 100%)
HOMO-4 β , a.u.			-0.2747 (0% + 100%)	-0.2770 (0% + 100%)
HOMO-5 β , a.u.	-0.2359 (11% + 89%)	-0.2423 (11% + 89%)	-0.2761 (1% + 99%)	-0.2777 (0% + 100%)
HOMO-6 β , a.u.		-0.2586 (76% + 24%)	-0.2824 (1% + 99%)	-0.2821 (0% + 100%)
HOMO-20 β , a.u.	-0.2550 (76% + 24%)	-0.3013 (9% + 91%)	-0.3240 (59% + 41%)	-0.3231 (57% + 43%)
$\Delta\beta$, a.u. (eV)	-0.2560 (76% + 24%)	-0.2605 (76% + 24%)	0.1055 (2.871)	0.0979 (2.664)
Total energies, a.u.	-4395.9701	-4395.9961	-4418.4821	-4418.5203
μ (Debye)	-0.2571 (43% + 57%)	-0.2623 (43% + 57%)	0.2022	0.2695
	-0.2920 (9% + 91%)	-0.3013 (9% + 91%)		
	0.1247 (3.393)	0.1224 (3.331)		
	1.3350	1.8014		

1 a.u. = 27.2116 eV.

Table 6. The total spin transitions, MO→MO transition and its percentage contributions corresponding to some wavelengths of the optimized molecule with TD-UB3LYP/3-21G (gas and solvent) and 6-311G (gas and solvent). The values 10 percent and its above are considered

TD-UB3LYP	Wavelengths(nm/eV)	Total Spin Transition	MO→MO	% Contributions
3-21G (Gas)	647.542 (1.915)	13 β	HOMO-5 β →LUMO+4 β HOMO β →LUMO+4 β	28% 27%
	590.011 (2.011)	3 α + 4 β	HOMO α →LUMO α HOMO α →LUMO+1 α	55% 18%
3-21G (Gas)	426.813 (2.905)	3 α + 4 β	HOMO β →LUMO β HOMO-1 α →LUMO α HOMO β →LUMO β	10% 36% 33%
	378.487 (3.276)	4 α + 2 β	HOMO β →LUMO+1 β HOMO-2 α →LUMO+1 α	14% 46%
	342.093 (3.624)	4 α + 8 β	HOMO-1 β →LUMO+1 β HOMO-3 α →LUMO+1 α	30% 10%
	323.054 (3.838)	4 α + 8 β	HOMO-2 β →LUMO+1 β HOMO-4 α →LUMO α	45% 30%
	313.552 (3.954)	4 α + 7 β	HOMO-1 α →LUMO+3 α HOMO-3 β →LUMO β	10% 12%
	299.170 (4.144)	10 α + 8 β	HOMO β →LUMO+3 β HOMO-4 α →LUMO+1 α HOMO-4 β →LUMO β	11% 12% 27%
			HOMO α →LUMO+6 α HOMO α →LUMO+5 α	22% 10%

TD-UB3LYP	Wavelengths(nm/eV)	Total Spin Transition	MO→MO	% Contributions
3-21G (Acetonitrile)	654.792 (1.894)	14β	HOMOβ→LUMO + 4β	24%
	594.595 (2.085)	3α + 5β	HOMO-5β→LUMO + 4β	20%
			HOMOα→LUMOα	53%
			HOMOα→LUMO + 1α	18%
			HOMOβ→LUMOβ	10%
436.813 (2.838)	5α + 5β	HOMO-1α→LUMOα	28%	
390.590 (3.174)	3α + 4β	HOMOβ→LUMOβ	20%	
		HOMOβ→LUMO + 1β	19%	
		HOMO-2α→LUMO + 1α	44%	
		HOMO-2α→LUMOα	16%	
3-21G (Acetonitrile)	349.627 (3.546)	6α + 7β	HOMO-1β→LUMO + 1β	20%
	334.173 (3.710)	3α + 4β	HOMO-2β→LUMO + 1β	30%
			HOMOβ→LUMO + 2β	20%
			HOMO-3α→LUMOα	19%
			HOMO-3β→LUMO + 1β	24%
			HOMOβ→LUMO + 2β	14%
			HOMO-4β→LUMO + 1β	14%
315.491 (3.930)	4α + 7β	HOMO-4α→LUMOα	21%	
313.529 (3.955)	2α + 8β	HOMO-4β→LUMOβ	38%	
		HOMO-4α→LUMO + 1α	21%	
		HOMO-4β→LUMO + 1β	31%	
		HOMO-3β→LUMO + 1β	14%	
301.990 (4.106)	7α + 12β	HOMOα→LUMO + 6α	23%	
		HOMO-6β→LUMO + 1β	17%	

Table 6. (Continued)

TD-UB3LYP	Wavelengths (nm/eV)	Total Spin Transition	MO→MO	% Contributions	
6-311G(Gas)	697.328 (1.778)	2 α + 9 β	HOMO β →LUMO β HOMO β →LUMO + 2 β HOMO-20 β →LUMO + 2 β	38% 29% 10%	
	496.476 (2.497)	5 α + 3 β	HOMO α →LUMO+1 α HOMO β →LUMO+1 β	55% 22%	
	455.208 (2.724)	3 α + 3 β	HOMO-1 α →LUMO α HOMO-1 β →LUMO + 2 β HOMO-1 β →LUMO β	13% 50% 17%	
	390.516 (3.175)	7 α + 10 β	HOMO-3 β →LUMO β	49%	
	376.111 (3.297)	3 α + β	HOMO-3 α →LUMO α HOMO-2 β →LUMO + 1 β	56% 32%	
	362.095 (3.424)		6 α + 6 β	HOMO-4 α →LUMO + 1 α HOMO-3 β →LUMO + 2 β	13% 45%
6-311G (Acetonitrile)	693.466 (1.788)	3 α + 4 β	HOMO α →LUMO + 1 α HOMO-1 α →LUMO α HOMO β →LUMO + 1 β HOMO-1 β →LUMO β	25% 16% 27% 20%	
	536.847 (2.310)523.033 (2.370)	4 α + 4 β α + 3 β	HOMO α →LUMO + 1 α HOMO-1 α →LUMO α	71% 69%	
			HOMO β →LUMO + 1 β HOMO-1 β →LUMO + 2 β HOMO-3 β →LUMO β	15% 11% 24%	
	384.747 (3.223)	10 α + 13 β 2 α + β	HOMO-4 α →LUMO α HOMO-2 β →LUMO + 1 β	37% 53%	
			HOMO-3 α →LUMO + 1 α HOMO-3 β →LUMO + 1 β HOMO-3 β →LUMO + 2 β	57% 24% 75%	
	355.655 (3.486) 334.615 (3.705)	3 α + β 4 α + 5 β 5 α + 2 β	HOMO-5 α →LUMO α HOMO-5 β →LUMO + 2 β HOMO-4 β →LUMO β	29% 13% 31%	

Table 7. Calculated components of the polarizability tensor α , the polarizability $\langle\alpha\rangle$ and the anisotropy of the polarizability $\langle\Delta\alpha\rangle$, The electric dipole moments, μ (D) and first order hyperpolarizability of studied molecule using different basis sets from DFT/B3LYP calculations

Basis Sets	α_{xx} (a. u.)	α_{xy} (a. u.)	α_{yy} (a. u.)	α_{xz} (a. u.)	α_{yz} (a. u.)	α_{zz} (a. u.)	$\langle\alpha\rangle$ (a. u.)	$\langle\Delta\alpha\rangle$ (a. u.)	$\langle\Delta\alpha\rangle \times 10^{-24}$ (esu)	$\langle\alpha\rangle \times 10^{-24}$ (esu)	
3-21G	459.9633	-85.9387	458.6670	-46.7691	-26.6509	356.9069	425.1791	203.32	30.13	63.01	
6-311G	582.3440	-95.8807	487.6337	-42.3175	-28.2399	422.8304	497.6027	223.99	33.19	73.74	
	μ_x	μ_y	μ_z	μ (D)							
3-21G	-0.3672	-0.3376	0.1645	0.5253							
6-311G	-0.0208	-0.0683	-0.0352	0.0794							
	β_{xxx} (a. u.)	β_{xxy} (a. u.)	β_{xyy} (a. u.)	β_{yyy} (a. u.)	β_{xxz} (a. u.)	β_{xyz} (a. u.)	β_{yyz} (a. u.)	β_{xzz} (a. u.)	β_{yzz} (a. u.)	β_{zzz} (a. u.)	$\beta \times 10^{-33}$ (esu)
3-21G	-81.3782	-3.5390	-3.8516	81.0510	-21.6492	-37.9355	-29.6183	55.9766	16.9757	83.0195	897.48
6-311G	20.0547	-22.3398	-9.7632	2.5425	11.7923	6.2552	1.2755	7.6057	9.4558	16.2660	309.98

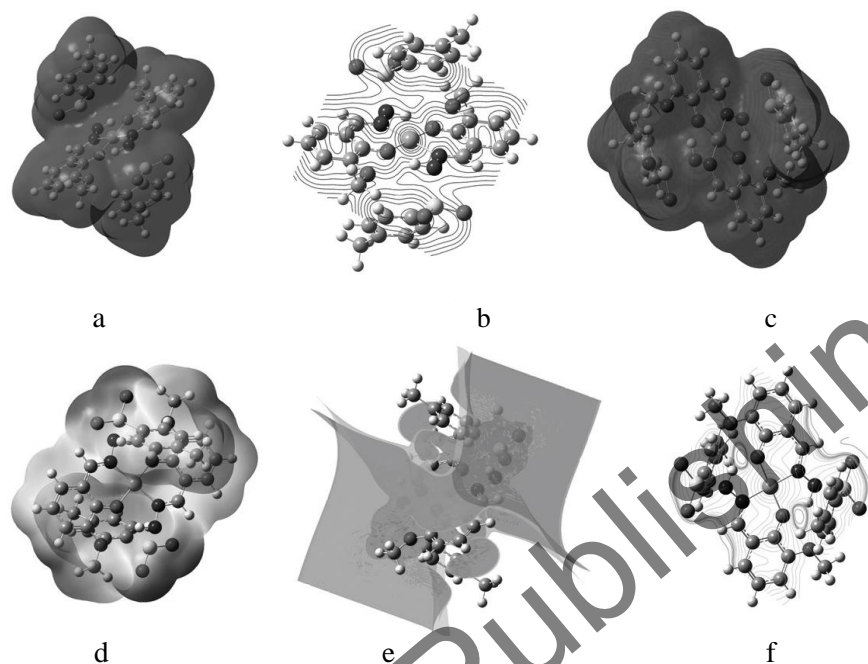


Figure 4. a - total density, b - contour (total density), c - alpha density, d - MEP, e - ESP, f - contour (ESP) map (in a.u.) of 1 with the DFT/B3LYP/6-311G method (with an isodensity value of 0.0004 a.u.).

Besides of these properties of the molecule, we have calculated ionization potential (I), electron affinity (A), electronegativity (χ), chemical potential (μ), chemical hardness (η), chemical and global softness (s , σ) and global electrophilicity index (ω) of the molecule with DFT. The ionization potential of the molecule corresponds to negative value of HOMO while the electron affinity corresponds to negative of LUMO. The low I creates a better electron donor, and the large A makes a better electron acceptor. The ionization potentials ($I = -\text{HOMO}$) of the molecule are 5.222 and 5.927 eV for B3LYP/3-21G and B3LYP/6-311G basis sets, respectively. The electron affinity ($A = -\text{LUMO}$) of the molecule are 2.037 and 2.953 eV for B3LYP/3-21G and B3LYP/6-311G basis sets, respectively. The electronegativity ($\chi = (I + A)/2$) and chemical potential ($\mu = -(I + A)/2$) of the molecule are 3.630, 4.400 eV and -3.630, -4.400 eV for B3LYP/3-21G and B3LYP/6-311G basis sets, respectively. A hard

molecule has a large energy gap, and a soft molecule has a small one. Hard molecules are lesser reactive than soft molecules. For the simplest transfer of electrons, absorption could occur at the part of the molecule where softness, which is a localised, has the highest value. The chemical hardness ($\eta = (I-A)/2$) of the molecule are 1.592 and 1.487 eV for B3LYP/3-21G and B3LYP/6-311G basis sets, respectively. The chemical softness ($s = 1/2\eta$) of the molecule and global softness ($\sigma = 1/\eta$) which a measure of the electrophilic power of a molecule are 0.314, 0.336 eV and 0.628, 0.672 eV⁻¹ for B3LYP/3-21G and B3LYP/6-311G basis sets, respectively. Lower values of hardness and softness are supported that complex is more stable and more lower chemical activity. Also, the global electrophilicity index ($\omega = (\mu)^2/2\eta$) are 4.125 and 6.510 eV for B3LYP/3-21G and B3LYP/6-311G basis sets, respectively. The electrophilicity index, ω , encompasses both; the propensity of the electrophile to acquire an additional electronic charge driven by μ^2 (the square of chemical potential) and the resistance of the system to exchange an electronic charge with the environment described by η simultaneously. Therefore, a good electrophile is characterized by a high value of μ and a low value of η [53].

NLO is at the forefront of current research because it provides the key functions of frequency shifting, optical modulation, optical switching, optical logic, and optical memory for the emerging technologies in areas such as telecommunications, signal processing, and optical interconnections [54, 55]. Nonlinear optical properties of the complex having paramagnetic feature are calculated by using DFT and reported in atomic units (a.u.), the calculated values have been converted into electrostatic units (esu) (α : 1 a.u. = 0.1482×10^{-24} esu; β : 1 a.u. = 8.6393×10^{-33} esu). The polarizability of the molecule is also included in the top of its electronic properties. The calculated components of the polarizability tensor α , the polarizability $\langle\alpha\rangle$ and the anisotropy of the polarizability $\langle\Delta\alpha\rangle$ for studying the molecules are listed in Table 7. The concepts of hardness and softness of atoms and molecules are however, intimately linked with their polarizabilities and also the sizes. That is, soft molecules can be more polarized because they have great values of the polarizability [56].

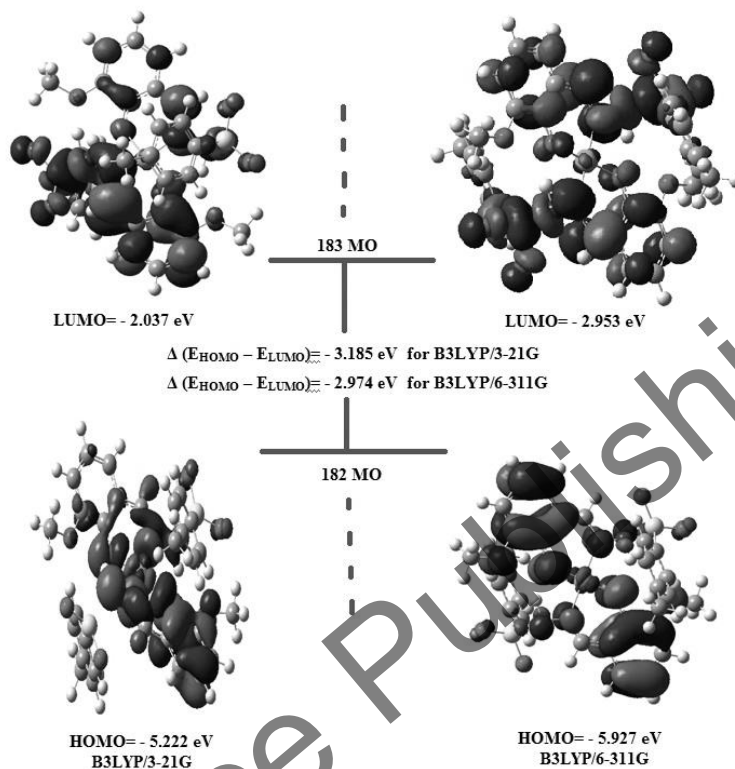


Figure 5. Patterns of the HOMO, LUMO of 1 obtained with TDDFT/B3LYP/3-21G and B3LYP/6-311G methods.

The investigation of the first static hyperpolarizability is explained by the calculation of the frontier molecular orbital energies, which helps to use intramolecular charge transfer to explain the hyperpolarizability. Therefore previous and present calculations show the inverse relationship between the polarizability and HOMO-LUMO energy gaps [57]. Non-linear optical parameters are listed in Table 7.

The magnetic susceptibility measurement of 1 indicates paramagnetism.

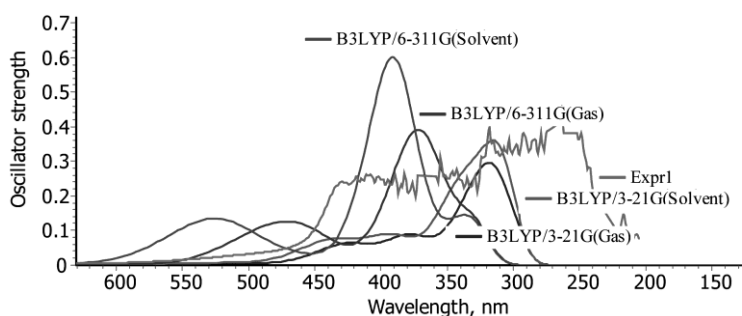


Figure 6. A UV diagram including experimental and theoretical results.

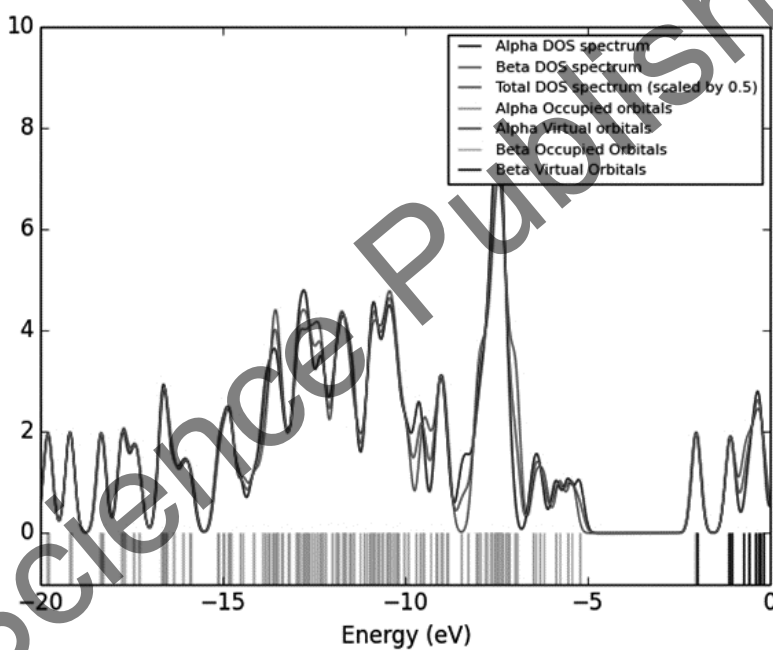


Figure 7. Calculated total electronic density of states diagram of the title compound.

CONCLUSION

Compound of title of [N'-(2-hydroxy-3-methoxybenzylidene)-4-methylbenzenesulfonohydrazide]copper(II) has been synthesized and

thoroughly characterized. A complete vibrational analysis of mononuclear Copper (II) complex has been performed by DFT method with B3LYP/3-21G and 6-311G basis sets. The experimental parameters with the bond parameters and of the optimized structure of the molecule were compared and found to be close to its the experimental data. The frontier molecular orbital energies of the structure and its NLO properties were investigated by DFT. To predict the reactive sites for electrophilic and nucleophilic attack for the complex molecule, the MEP at the B3LYP/6-311G optimized geometry was calculated. Because of the complex's paramagnetic feature, the electronic transition energies including α (spin up) and β (spin down) electron spins have been calculated both gas phase and acetonitrile (solvent) phase by the TD-UB3LYP/3-21G and TD-UB3LYP/6-311G methods from the optimized geometries to reproduce UV-Vis spectroscopic transitions for 45 states. We found that total energies and HOMO-LUMO energy gap of the complex have lower values in the acetonitrile media by TDDFT/UB3LYP/6-311G. The other molecular properties such as ionization potential (I), electron affinity (A), electronegativity (χ), chemical potential (μ), chemical hardness (η), chemical and global softness (s , σ) and global electrophilicity index (ω) were described. Eventually, the theoretical results showed an acceptable general agreement with the experimental record.

REFERENCES

- [1] N. Şenyüz, C. Yuksektepe, H. Batı, N. Çalışkan, O. Büyükgüngör. *Acta Crystallogr.*, E62, m3163 (2006).
- [2] M.T.H. Tarafder, K.T. Jin, K.A. Crouse, A.M. Ali, B.M. Yamin, H.-K. Fun. *Polyhedron*, 21, 2547 (2002).
- [3] P. Guerriero, S. Tamburini, P.A. Vigato, *Coord. Chem. Rev.*, 139, 17 (1995).
- [4] R. Sreekala, K.K.M. Yusuf. *React. Kinet. Catal. Lett.*, 48, 575 (1992).
- [5] N.N. Das, A.C. Dash. *Polyhedron*, 14, 1221 (1995).
- [6] D.R. Williams. *Chem. Rev.*, 72, 203 (1972).

- [7] Babahan, E.P. Coban, H. Bıyık. *Maejo Int. J. Sci. Techno.*, 7,26 (2013).
- [8] E. Assayehegn. *Thesis*, Addis Ababa University Schooll of Graduate Studies Department of Chemistry Graduate Program, August, (2007).
- [9] M. Kumar, P.N. Saxena. *Ori. J. Chem.*, 28(4), 1927 (2012).
- [10] F. Armbruster, U. Klingebiel, M. Noltemeyer. *Z. Naturforsch.*, B61, 225 (2006).
- [11] O.S. Senturk, S. Sert, U. Ozdemir. *Z. Naturforsch.*, B58, 1124 (2003).
- [12] A.E.G.E. Amr, A.M. Mohamed, A.A. Ibrahim. *Z. Naturforsch.*, B58, 861 (2003).
- [13] H. Mohrle, G. Keller. *Z. Naturforsch.*, B58, 885 (2003).
- [14] J. Chakraborty, R.K.B. Singh, B. Samanta, C.R. Choudhury, S.K. Dey, P. Talukder, M.J. Borah, S. Mitra. *Z. Naturforsch.*, B61, 1209 (2006).
- [15] V. Lozan, P.-G. Lassahn, C. Zhang, B. Wu, C. Janiak, G. Rheinwald, H. Lang. *Z. Naturforsch.*, B58, 1152 (2003).
- [16] C.T. Zeyrek, A. Elmali, Y. Elerman, *Z. Naturforsch.*, B61, 237 (2006).
- [17] D.K. Dey, B. Samanta, A. Lycka, L. Dahlenburg. *Z. Naturforsch.*, B58, 336 (2003).
- [18] C. Janiak, P.-G. Lassahn, V. Lozan. *Macromol. Symp.*, 236, 88 (2006).
- [19] M. Katyal, Y. Dutt, *Talanta*, 22, 151 (1975).
- [20] M. Mohan, M.P. Gupta, L. Chandra, N.K. Jha. *Inorg. Chim. Acta*, 151, 61 (1988).
- [21] R.B. Sinh, P. Jain. *Talanta*, 29, 77 (1982).
- [22] Suez, S.O. Pehkonen, M.R. Hoffmann. *Sci. Technol.*, 28, 2080 (1994).
- [23] L.H. Terra, A.M.C. Areias, I. Gaubeur, M.E.V. Suez-Iha. *Spectrosc. Lett.*, 32, 257 (1999).
- [24] A.D. Becke, *J. Chem. Phys.*, 98, 5648 (1993).
- [25] C. Lee, W. Yang, R.G. Parr, *Phys. Rev.*, B37, 785 (1988).

- [26] M.J. Frisch, G.W. Trucks, H.B. Schlegel, G.E. Scuseria, M.A. Robb, J.R. Cheeseman, G. Scalmani, V. Barone, B. Mennucci, G.A. Petersson, H. Nakatsuji, M. Caricato, X. Li, H.P. Hratchian, A.F. Izmaylov, J. Bloino, G. Zheng, J.L. Sonnenberg, M. Hada, M. Ehara, K. Toyota, R. Fukuda, J. Hasegawa, M. Ishida, T. Nakajima, Y. Honda, O. Kitao, H. Nakai, T. Vreven, J.A. Montgomery, Jr., J.E. Peralta, F. Ogliaro, M. Bearpark, J.J. Heyd, E. Brothers, K.N. Kudin, V.N. Staroverov, R. Kobayashi, J. Normand, K. Raghavachari, A. Rendell, J.C. Burant, S.S. Iyengar, J. Tomasi, M. Cossi, N. Rega, J.M. Millam, M. Klene, J.E. Knox, J.B. Cross, V. Bakken, C. Adamo, J. Jaramillo, R. Gomperts, R.E. Stratmann, O. Yazyev, A.J. Austin, R. Cammi, C. Pomelli, J.W. Ochterski, R.L. Martin, K. Morokuma, V.G. Zakrzewski, G.A. Voth, P. Salvador, J.J. Dannenberg, S. Dapprich, A.D. Daniels, Ö. Farkas, J.B. Foresman, J.V. Ortiz, J. Cioslowski, and D.J. Fox. *Gaussian 09*, Wallingford (CT, US): Gaussian, Inc., (2009).
- [27] Hinchliffe, B. Nikolaidi, H.J.S. Machado. *Int. Journal of Mol. Sci.*, 5(8), 224 (2004).
- [28] A.D. Buckingham. *Adv. in Chem. Phys.*, 12, 107 (1967).
- [29] A.D. McLean, M. Yoshimine. *The Journal of Chem. Phys.*, 47, 1927 (1967).
- [30] C. Lin, K. Wu. *Chem. Phys. Lett.*, 321(1-2), 83 (2000).
- [31] J.P. Abraham, D. Sajan, I. Hubert Joe, V.S. Jayakumar. *Spectr. Acta Part A* 71(2), 355 (2008).
- [32] P. Karamanis, C. Pouchan, G. Maroulis. *Phys. Rev. A* 77, 013201 (2008).
- [33] R. Krishnan, J.S. Binkley, R. Seeger, J.A. Pople. *Journal of Chem. Phys.*, 72, 650 (1980).
- [34] Ben Ahmed, H. Feki, Y. Abid, H. Boughzala, A. Mlayah. *Journal of Mol. Struc.*, 888(1-3), 180 (2008).
- [35] G.M. Sheldrick, *Acta Cryst.*, A71, 3 (2015).
- [36] L.J. Farrugia, *J. Appl. Crystallogr.*, 45, 849 (2012).
- [37] G.M. Sheldrick, *Acta Cryst.*, C71, 3 (2015).

- [38] *Oxford Diffraction. CrysAlis PRO*, Abingdon (England): Oxford Diffraction Ltd., (2007).
- [39] N. Senyuz, B. Yılmaz, H. Batı, E. Bozkurt, O. Büyükgüngör. *Spectrochim. Acta*, A101, 167 (2013).
- [40] M.R. Bermejo, A. Sousa. *New J. Chem.*, 25, 647 (2001).
- [41] P.J. Naskar, C. Biswas, L. Lu, M. Zhu. *J. Chem. Crystallogr.*, 41(4), 502 (2011).
- [42] N. Şenyuz, Ç. YüksektepeAtaol, H. Bati. *Russian J. Coord. Chem.*, 40(11), 849 (2014).
- [43] F.H. Allen, O. Kennard, D.G. Watson, L. Brammer, A.G. Orpen, R. Taylor. *J. Chem. Soc., Perkin Trans.*, 2, 1 (1987).
- [44] G. Koz, N. Ozdemir, D. Astley, M. Dincer, S.T. Astley. *J. Mol. Struct.*, 966, 39 (2010).
- [45] S. Demir, S. Cakmak, N. Dege, H. Kutuk, M. Odabasoglu, R.A. Kepekci. *J. Mol. Struct.*, 1100, 582 (2015).
- [46] S. Demir, F. Tinmaz, N. Dege, I.Ö. İlhan. *J. Mol. Struct.*, 1108, 637 (2016).
- [47] J. Bernstein, R.E. Davis, L. Shimon, N.L. Chang. *Angew. Chem. Int. Ed.*, 34, 1555 (1995).
- [48] Z. Demircioğlu, C. KaştaşAlbayrak, O. Büyükgüngör. *Spectrochim. Acta*, A139, 539 (2015).
- [49] C. Yuksektepe, H. Saracoğlu, N. Çalışkan, I. Yılmaz, A. Cukurovali. *Bull. Korean Chem. Soc.*, 31, 3553 (2010).
- [50] N.M. O'Boyle, A.L. Tenderholt, K.M. Langer. *J. Comput. Chem.* 29, 839 (2008).
- [51] Fleming, *Frontier Orbitals and Organic Chemical Reactions*, London: Wiley, (1976).
- [52] R. Kurtaran, S. Odabaşoğlu, A. Azizoğlu, H. Kara, O. Atakol. *Polyhedron*, 26(17), 5069 (2007).
- [53] Eşme, G.S. Sağdınç. *Journal of Balikesir Uni. Inst. of Sci. And Tech.*, 16(1), 47 (2014).
- [54] V.M. Geskin, C.J. Lambert, L. Bredas. *J. Am. Chem. Soc.*, 125, 15651 (2003).

- [55] D. Sajan, H. Joe, V.S. Jayakumar, J. Zaleski. *Journal of Mol. Struct.*, 785, 43 (2006).
- [56] Ghanadzadeh, H. Ghanadzadeh, G. Ghasmi. *Journal of Mol. Liq.*, 88(2-3), 299 (2000).
- [57] Hinchliffe, H.J. Soscun Machado. *Journal of Mol. Struct. (Theochem)*, 312(1), 57 (1994).

In: Crystal Growth
Editors: J. Li, J. Li and Y. Chu

ISBN: 978-1-53612-203-9
© 2017 Nova Science Publishers, Inc.

Chapter 10

**FENAMATE CRYSTALS AND COCRYSTALS:
STRUCTURAL AND
THERMODYNAMIC ASPECTS**

German L. Perlovich and Artem O. Surov*

Institution of Russian Academy of Sciences
G. A. Krestov Institute of Solution Chemistry
Ivanovo, Russia

ABSTRACT

Crystal structures of different polymorphic forms of nonsteroidal anti-inflammatory drug fenamates (niflumic (**NFA**), flufenamic (**FFA**), tolfenamic (**TFA**), mefenamic (**MFA**) acids) and structurally related compounds (N-phenylanthranilic acid (**N-PA**) and diphenylamine (**DPA**)) were studied and compared. Conformational features, packing arrangements and hydrogen bonds were investigated. Thermodynamic aspects of sublimation processes of the selected class of compounds were analyzed. A thermochemical comparison of different polymorphic forms

* Corresponding Author Address: Institution of Russian Academy of Sciences, G.A. Krestov Institute of Solution Chemistry RAS, 153045, Ivanovo, Russia Tel: +7 4932 533784; Fax: +7 4932 336237; E-mail: glp@isc-ras.ru.

was carried out. The absolute values of the crystal lattices energies of the polymorphic modifications of mefenamic, flufenamic and tolfenamic acids were calculated based on the sublimation and solution calorimetric experiments. Relationships between the sublimation thermodynamic functions and structural features of fenamate polymorphic forms were revealed. Dependences between the sublimation thermodynamic functions and thermochemical characteristics (enthalpies and temperatures of fusion) were observed. A correlation was found between the fusion entropies and the free volume per molecule in the crystal lattices.

Cocrystallization of **N-PA**, **NFA**, **FFA**, **TFA** and **MFA** with 4,4'-bipyridine (**BP**) resulted in the formation of cocrystals with a (2:1) molar ratio. The relationships between packing arrangements in the crystals of pure fenamates and their cocrystals with **BP** were found via The Crystal Packing Similarity analysis. Analysis of the cocrystals melting points and individual components shows a good correlation and this fact allows predicting similar cocrystals with specified characteristics. Cocrystal formation enthalpies for the considered two-component crystals were obtained and discussed. The enthalpies of cocrystal formation are small, which indicates that the packing energy gain is only achieved by weak van der Waals interactions between the API and **BP** molecules.

1. INTRODUCTION

Fenamates (N-phenylanthranilic acid, niflumic acid, flufenamic acid, tolfenamic and mefenamic acids) belong to an important class of nonsteroidal anti-inflammatory drugs (NSAIDs), widely used as analgesic, antipyretic and anti-inflammatory agents [1] (Figure 1). The major mechanism mediating the anti-inflammatory effects of fenamate and other NSAIDs is inhibition of cyclooxygenase (COX-1 and COX-2) that catalyzes the biosynthesis of prostaglandins from arachidonic acid in both peripheral and central tissues [2-4]. In recent decades, fenamates have been recognized as potent therapeutic agents with a broad spectrum of biological activity. For example, fenamates affect various types of membrane channels, and their effects on different types of ion channels have been studied widely [5-7]. It has been reported that inflammatory processes are associated with the pathophysiology of Alzheimer's disease and that treatment with some fenamates may help to reduce the progression of

Alzheimer's disease [8-10]. In addition, it has been discovered that the members of fenamate family can be also used as novel anticancer therapeutic agents against different types of cancers [11-12].

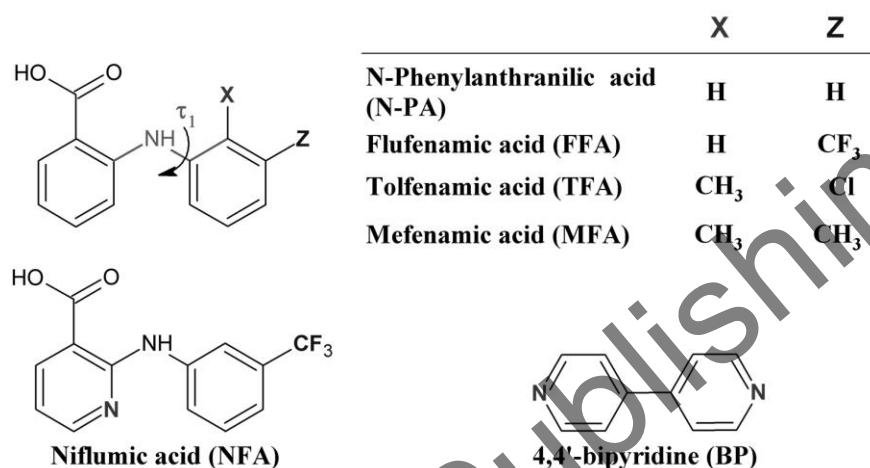


Figure 1. Molecular structures of fenamates.

In the field of solid-state chemistry, fenamates are well known as highly polymorphic compounds, and many of them exhibit the so-called conformational polymorphism [13]. This strong tendency of fenamate molecules to form polymorphs in a crystal state has been considered in terms of the polymorphophore concept [14] (analogous to “pharmacophore” as a structure which is especially useful in finding new leads in drug discovery, introduced and defined by Matzger as “a structural element that, when incorporated into a molecule, favours the formation of polymorphic crystal forms.” According to this concept, there are families of related molecules containing a common substructure which is responsible for propensity of a compound to display multiple crystalline phases. Thus, the fenamate fragment is a polymorphophore, rationalizing the polymorphism of many fenamates [15, 16].

Besides polymorphs, a range of multi-component crystalline forms of fenamates, including cocrystals, salts and solvates, have been described in the literature. Pharmaceutical cocrystals of fenamates (except **N-PA**) with

nicotinamide have been reported by Fábíán et al. [17]. For **MFA**, DMF solvate and cytosine salt have been isolated during preparation of its different polymorphic forms [18]. A comprehensive study of the crystal structures of various complexes of **MFA** with cyclic and acyclic amines were reported by Antipin et al. [19] In turn, co-crystals of **FFA** with the asthma-therapy drug theophylline and 2-pyridone were obtained by Aitipamula et al. [20] We have also made a contribution to extending the range of fenamate cocrystals through cocrystallization with 4,4'-bipyridine [21].

The first part of the chapter is devoted to various aspects of polymorphism of individual fenamates. Special attention is paid to studying fusion and sublimation processes and analyzing thermodynamic stability of polymorphic phases of the selected class of substances. The second part deals with the crystal structures of two-component cocrystals based on fenamates with 4,4'-bipyridine (**BP**). A comparative analysis of molecular conformational states has been done on molecular crystals of different polymorphic modifications of the individual compounds and cocrystals. In this paper we attempt to estimate cocrystal formation enthalpies. We have also obtained relationships between the melting points of cocrystals based on fenamates with **BP** and the melting points of individual fenamates.

2. STRUCTURAL AND PHYSICOCHEMICAL PROPERTIES OF INDIVIDUAL FENAMATES

2.1. Crystal Structures and Polymorphism of Fenamates

The crystal structures of all the fenamates are based on the same $R_2^2(8)$ hydrogen bonded dimer (Figure 2a), and differ in the packing of the phenyl rings. As the molecules are conformationally mobile, nucleation and new phase growth can have various conformations which are sufficiently trapped kinetically and are favorable thermophysically, and

thus become crystalline polymorphs. The most basic fenamate molecule is *N*-phenylanthranilic acid (**N-PA**) which has no substitutions in the second (noncarboxylated) phenyl ring (Figure 1). It crystallizes in P-1 space group with two molecules in an asymmetric unit (Figure 2b). It is remarkable that **N-PA**, which can be considered a bare polymorphophore, is the only compound in the fenamate family that has no known polymorphs [22]. The explanation of this contradiction has been found by Uzoh et al. who have shown that for *N*-phenylanthranilic acid, the known structure is more thermodynamically favored than all other alternatives, limiting the range of potential polymorphism [23]. Based on crystal structure prediction (CSP) results, Uzoh et al. have concluded that it is the phenyl ring substitutions that determine the relative energies of fenamate crystal structures and, therefore, enable polymorphism.

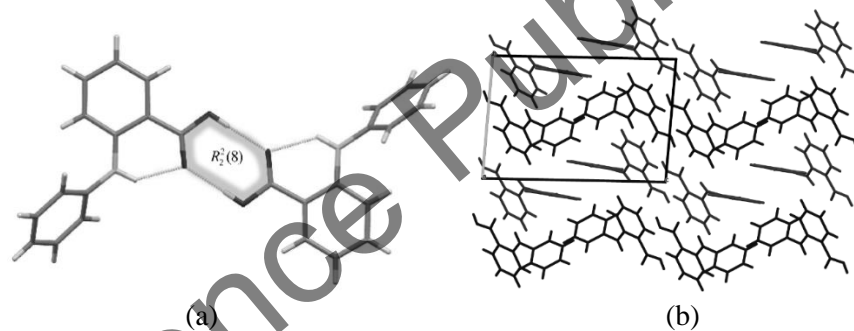


Figure 2. (a) Illustration of hydrogen bonded dimer formed by fenamate molecules; (b) molecular packing projections for *N*-phenylanthranilic acid.

Niflumic acid (**NFA**) has also been viewed as a monomorphic compound for a long time. The crystal structure of **NFA** was first obtained in the late 1970-s [24] (Figure 3a). Since then no evidences of polymorphism of **NFA** have been reported. However, in 2012, a second polymorphic form of **NFA** was observed by Bag and Reddy [25] by applying the fast evaporation approach to screening kinetic forms of several APIs, including niflumic acid. Unfortunately, the authors could not obtain a single crystal of the new form, so its crystal structure remains unknown. It is interesting to note that the unsubstituted analog of **NFA**,

i.e., 2-(phenylamino)nicotinic acid (Figure 3b), is found to exist in four polymorphic forms: α , β , γ and δ [26]. The crystal structures of forms α and β consist of discrete hydrogen bonded dimers similar to those in **NFA** structure. In forms γ and δ , however, the conventional acid-acid dimer is replaced by acid-pyridine heterosynthon, indicating the so-called synthon polymorphism. The fact that 2-(phenylamino)nicotinic acid has four polymorphs and *N*-phenylanthranilic acid has none suggests that the substituents in the phenyl ring of the fenamate molecule are not the only factor influencing polymorphism propensity. A similar effect can be achieved by introducing aromatic nitrogen into the molecular structure. In some cases, the combination of these two molecular changes may have the opposite effect, decreasing the number of polymorphs, as it is seen for niflumic acid. However, each of the mentioned structural changes applied separately has the potential to give rise to multiple packing arrangements. The latter statement can be exemplified by introducing a CF₃-group into the second (noncarboxylated) phenyl ring on the *N*-phenylanthranilic acid molecule, which leads to formation of one of the most polymorphic drug compounds ever known, namely flufenamic acid (**FFA**) (Figure 1).

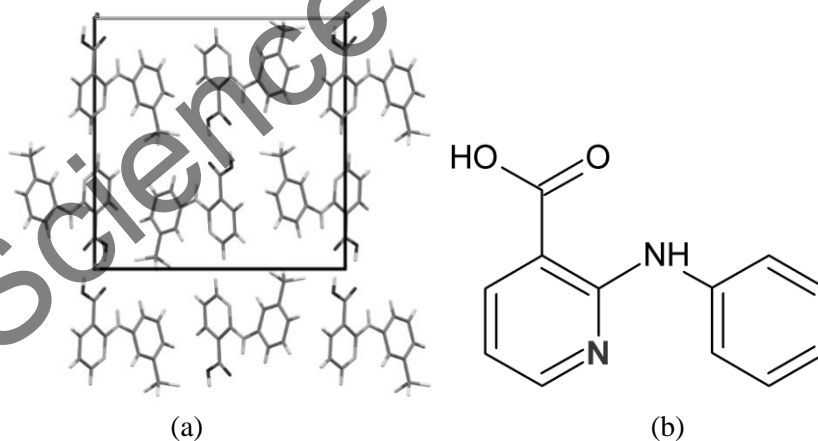


Figure 3. (a) Molecular packing projections for niflumic acid and (b) molecular structure of 2-(phenylamino)nicotinic acid.

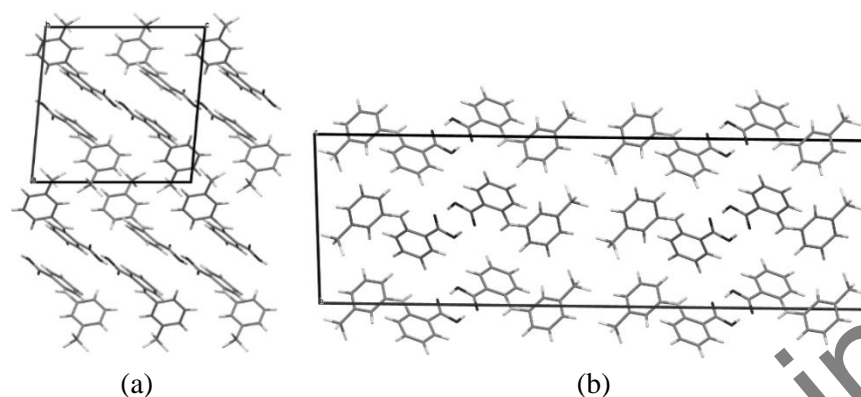


Figure 4. Molecular packing projections for (a) form I and (b) form III of flufenamic acid.

The existence of polymorphism in **FFA** has been known for more than 40 years. The crystal structure of **FFA** form III was first reported in 1973 [27], while the structure of form I was obtained nearly 10 years later [28]. In addition, the existence of other five polymorphs of **FFA** (II, IV, V, VI, VII) and their morphology were confirmed and described by Krc [29]. In 2012, two additional polymorphs of the compound (forms VIII and IX) were discovered and the crystal structures of forms II, IV-VIII were disclosed for the first time by Matzger et al. [16] using the polymer-induced heteronucleation technique of crystal growth. This breakthrough made **FFA** a compound with one of the largest structurally characterized number of polymorphs in the CSD. Although nine polymorphs are able to coexist at room temperature and atmospheric pressure, only form I and form III (Figure 4) possess long-term stability and, therefore, can be used in pharmaceutical formulations. The low temperature form III is stable at room temperature, and forms III and I are enantiotropic, with a transition temperature of *ca.* 42°C.

The next member of fenamate family, tolfenamic acid (**TFA**) (Figure 1), is also found to be a highly polymorphic compound. Similar to **FFA**, two polymorphs of **TFA** (form I – white, form II – yellow) have been known for a long time [30], and three novel phases of the drug have become accessible by applying a sophisticated polymer-induced screening technique [15]. According to the experimental data collected from different

sources [15, 30, 31], form I and form II of **TFA** (Figure 5) are closely comparable in terms of both free and lattice energies. However, forms III-V are apparently metastable polymorphs.

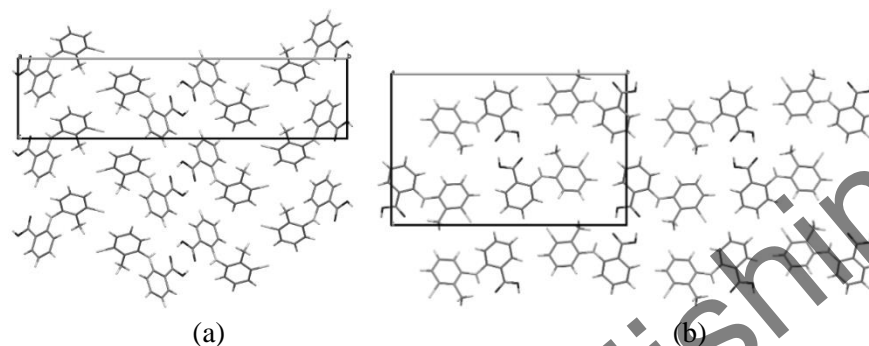


Figure 5. Molecular packing projections for (a) form I and (b) form II of tolfenamic acid.

Among the fenamates, the polymorphic behavior of mefenamic acid (MFA) has probably been studied best of all. For decades, MFA has been known to exist as enantiotropically related dimorphs (form I and form II). The crystal structure of stable form I, crystallizing from the common solvents, was reported in 1976 [32], although the crystal data for form II was first published by Lee et al. in 2006 [33] and was later revised by other researchers [34]. In the crystal of form II, the amino-group and the alkylated phenyl ring are disordered with a population distribution of 55:45. Since the disorder remains even at low temperature (100 K), it could be of static nature (Figure 6).

The third MFA polymorph was discovered in 2012 during an attempt to cocrystallize mefenamic acid with adenine [18]. Form III is found to be the least thermodynamically stable at ambient conditions and enantiotropically related with form II. The thermodynamic and kinetic aspects of the form I→form II polymorphic transformation of MFA are well documented in the literature. Umeda et al. [35] and Gilpin & Zhou [36] investigated the kinetics of the polymorphic conversion from form I to form II of MFA in the solid state and obtained the activation energy for the process. In addition, the kinetics of the transformation process of form II to form I

under various conditions was extensively investigated by Kato et al. [37, 38].

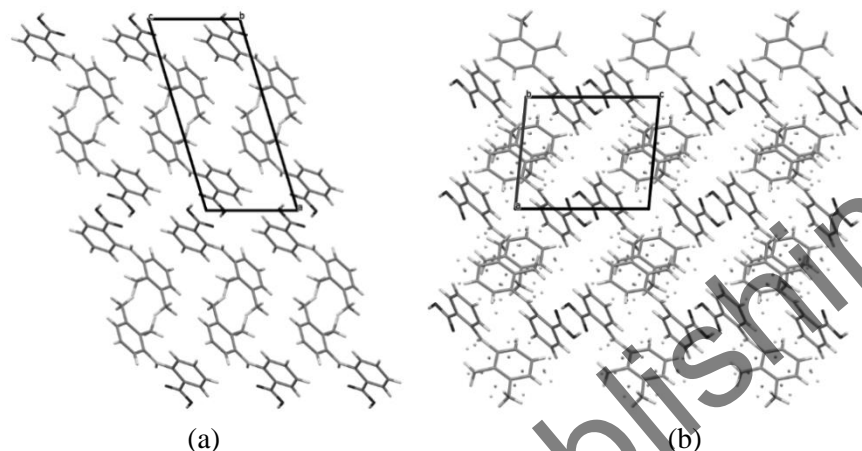


Figure 6. Molecular packing projections for (a) form I and (b) form II of mefenamic acid.

2.2. Thermodynamic aspects of fenamate polymorphism

The stability relationship between polymorphic forms (I and II) at particular temperature and pressure can be described in terms of the following fundamental thermodynamic functions: $\Delta G_{I \rightarrow II}^0$ which shows the free energy difference between the polymorphs, $\Delta H_{I \rightarrow II}^0$ which corresponds to the difference in crystal lattice energy of the polymorphic forms and $\Delta S_{I \rightarrow II}^0$ which provides information about the entropy change in the polymorphic system. The Gibbs energy difference between the two polymorphs ($\Delta G_{I \rightarrow II}^0$) is directly proportional to the ratio of their solubility values (assuming that the activities are approximated by the concentrations). The value of $\Delta H_{I \rightarrow II}^0$ can be derived from the solution enthalpy difference between different polymorphs obtained in the same solvent. The polymorph solution enthalpy, in turn, can be measured

directly by solution calorimetry experiments, or it may be calculated from the temperature dependence of a polymorph's solubility in the chosen solvent. Although solubility and heat of polymorphs solution are functions of the solvent, their ratio and difference are independent of the solvent used. There is experimental data about solubility and solution enthalpy of form I and form II of mefenamic acid in the literature (Table 1). Table 1 shows that the $\Delta G_{I \rightarrow II}^0$ values calculated from the solubility values of the polymorphs in different solvents are consistent. The average value of the free energy difference between form I and form II is found to be 0.7 kJ·mol⁻¹. However, certain inconsistency is observed in the $\Delta H_{I \rightarrow II}^0$ values. It is evident that the enthalpies of the polymorphic transition calculated from the temperature dependences of solubility show a poor agreement with each other and with the values obtained from the solution calorimetry experiments. However, the $\Delta H_{I \rightarrow II}^0$ values derived from the solution calorimetry measurements and reported by us [43] and Urakami et al. [41] are closely comparable. It can be assumed that the mentioned inconsistency may be associated with the partial conversion of one polymorph to another during a long-term solubility experiment which affects the solution enthalpies.

The solution calorimetry technique, however, does not have this drawback, so the values obtained by this method should be more reliable for polymorphic systems. Despite the modest values of $\Delta G_{I \rightarrow II}^0$ and $\Delta H_{I \rightarrow II}^0$, both experiments suggest that form I is thermodynamically more stable than form II at ambient conditions. The entropy change of the polymorphic transition ($\Delta S_{I \rightarrow II}^0$) is found to be *ca.* 9.7 J·mol⁻¹·K⁻¹. However, the calculated densities of the corresponding crystals at room temperature (283-303K) are virtually identical (1.268 g·cm⁻³ for form I and 1.267 g·cm⁻³ for form II).

In case of flufenamic and tolfenamic acids, there are only a few studies that address solubility and thermochemical study of polymorphic forms (Table 2). The experimental data collected in Table 2 suggests that the

$\Delta G_{I \rightarrow II,III}^0$ values for the **FFA** and **TFA** polymorphs are close to zero, indicating a minor stability difference between the corresponding polymorphs. The enthalpy of the polymorphic transition from form I to form III of **FFA**, obtained by solution calorimetry, equals -2.7 ± 1.1 $\text{kJ}\cdot\text{mol}^{-1}$. Therefore, these two enantiotropic polymorphs are practically isoenergetic. The difference in the crystal lattice energies between form I and form II of **TFA** at 298K reaches 6.7 ± 1.2 $\text{kJ}\cdot\text{mol}^{-1}$. In both cases, the polymorphic transition from stable to metastable form is accompanied by a decrease in the system entropy ($\Delta S_{I \rightarrow II,III}^0$).

2.3. Thermodynamics of Sublimation and Melting Processes

Vapor pressure and sublimation enthalpy of drug compounds are important thermodynamic parameters which are relevant to the pharmaceutical industry. In addition, experimental sublimation enthalpies are in many cases used as the reference values for development and adjustment of theoretical models for calculating crystal lattice energies [47]. The thermodynamic parameters of sublimation and melting processes of the fenamates are summarized in Table 3.

As mentioned above, the difference between the heats of polymorphs solutions is equal to the difference of their crystal lattice energies. Thus, if the lattice energy (sublimation enthalpy) of polymorph I and the $\Delta H_{I \rightarrow II}$ value are known, it is possible to calculate the crystal lattice energy of polymorph II. According to the experimental data in Tables 1, 2 and 3, the sublimation enthalpy of metastable form II of **MFA** equals:

$$\Delta H_{sub}^{298}(II) = 136.2 - 3.6 = 132.6 \text{ kJ}\cdot\text{mol}^{-1}.$$

In case of low-temperature form III of **FFA**, the lattice energy is estimated to be $\Delta H_{sub}^{298}(III) = 121.2 + 2.7 = 123.9$ $\text{kJ}\cdot\text{mol}^{-1}$. And for form II of **TFA**: $\Delta H_{sub}^{298}(II) = 128.4 + 6.7 = 135.1$ $\text{kJ}\cdot\text{mol}^{-1}$.

Table 1. Solubility (S_2), solution enthalpies (ΔH_{sol}^0) of MFA polymorphs in different solvents at 298.2 K and thermodynamic parameters of polymorphic transitions

Solvent	Polymorph	S_2 mol·l ⁻¹	ΔH_{sol}^0 kJ·mol ⁻¹	$\Delta G_{I \rightarrow II}^0$ kJ·mol ⁻¹	$\Delta H_{I \rightarrow II}^0$ kJ·mol ⁻¹	$\Delta S_{I \rightarrow II}^0$ J·mol ⁻¹ ·K ⁻¹
Ethyl acetate	Form I	0.039 ^a	31.9 ± 1.2 ^{b*}	0.6	6.5 ± 1.9	19.8
	Form II	0.050 ^a	25.4 ± 0.7 ^{b*}			
Ethanol	Form I	0.031 ^a		0.8		
	Form II	0.043 ^a				
Dodecyl alcohol	Form I	0.025 ^c	28.0 ^{d*}	0.7	4.2	11.7
	Form II	0.033 ^c	23.8 ^{d*}			
DMF	Form I		17.8 ^{c**}		3.7	
	Form II		14.1 ^{e**}			
Methanol	Form I		25.6 ± 0.5 ^{e**}		3.6 ± 1.0	
	Form II		22.0 ± 0.5 ^{e**}			

*calculated from the temperature dependence of solubility.

**measured by solution calorimetry.

^adata taken from ref. [39].

^bdata taken from ref. [40].

^cdata taken from ref. [41].

^ddata taken from ref. [42].

^edata taken from ref. [43].

Table 2. Solubility ratios ($S_2(I)/S_2(II, III)$), solution enthalpies ($\Delta H_{sol}^{0,298}$) of FFA and TFA polymorphs in different solvents and thermodynamic parameters of polymorphic transitions

Solvent	Temp. K	Solubility ratio $S_2(I)/S_2(II, III)$	$\Delta H_{sol}^{0,298}$ kJ·mol ⁻¹	$\Delta G_{I \rightarrow II, III}^{0, T}$ kJ·mol ⁻¹	$\Delta H_{I \rightarrow II, III}^{0, 298}$ kJ·mol ⁻¹	$\Delta S_{I \rightarrow II, III}^{0, T}$ J·mol ⁻¹ ·K ⁻¹
Flufenamic acid						
Ethanol/water (70:30 v/v)	298.2	1.07 ^a		-0.2		
Diacetone alcohol/water (40:60 v/v)	303.2	1.04 ^b		-0.1		
Water	300.0	≈ 1.0 ^c		0.0		
Methanol	298.2		18.9 ± 0.5 ^d (Form I)		-2.7 ± 1.0	-9.1
			21.6 ± 0.5 ^d (Form III)			
Tolfenamic acid						
Ethanol	310.2	0.91 ^e		0.3		
Isooctane	300.0	≈ 1.0 ^f		0.04		
Buffer pH7.4	298.2	≈ 1.0 ^g		0.0		
Methanol	298.2		27.1 ± 0.5 ^g (Form I)		-6.5 ± 1.0	-21.8
			33.6 ± 0.5 ^g (Form II)			

^adata taken from ref. [44].

^bdata taken from ref. [45].

^cdata taken from ref. [16].

^ddata taken from ref. [43].

^edata taken from ref. [46].

^fdata taken from ref. [15].

^gdata taken from ref. [31].

Table 3. Thermodynamic parameters of sublimation and melting processes of fenamates

	N-PA	NFA	FFA (Form I)	TFA (Form I)	MFA (Form I)
ΔG_{sub}^{298} , kJ·mol ⁻¹	58.9 ± 0.5	61.3 ± 0.4	54.3 ± 0.4	53.9 ± 0.4	59.2 ± 0.1
ΔH_{sub}^T , kJ·mol ⁻¹	123.0 ± 1.3	127.7 ± 0.8	119.4 ± 0.7	125.7 ± 0.8	132.7 ± 0.8
ΔH_{sub}^{298} , kJ·mol ^{-1a}	126.0 ± 1.3	130.2 ± 0.8	121.2 ± 0.7	128.4 ± 0.8	136.2 ± 0.8
$T\Delta S_{sub}^{298}$, kJ·mol ⁻¹	68.0 ± 1.8	68.9 ± 1.2	66.9 ± 1.1	74.8 ± 1.2	76.2 ± 0.9
ΔS_{sub}^{298} , J·mol ⁻¹ ·K ⁻¹	193 ± 6	231 ± 4	224 ± 4	216 ± 4	213 ± 3
T _m , K	458.2 ± 0.2	478.5 ± 0.2	405.3 ± 0.2	484.3 ± 0.2	503.5 ± 0.2
ΔH_{fus}^T , kJ·mol ⁻¹	39.7 ± 0.5	36.5 ± 0.5	26.7 ± 0.5	38.6 ± 0.5	38.7 ± 0.5

^aCalculated according to the procedure developed by Chickos and Acree using the isobaric molar heat capacities of the solid compounds [48].

The thermodynamic functions of the sublimation process depend on a number of parameters, among which are: structure and topology of molecules studied, nature of atoms, molecular packing architecture in the crystal lattice, molecular conformational state, and topology of hydrogen bond networks. It is, therefore, very difficult to pick a single descriptor to describe the thermodynamic functions. On the other hand, it appears inappropriate to search for multiparameter equations due to the restricted number of the compounds studied. Therefore, we tried to find regularities between the thermodynamic functions and some structural characteristics of the crystals. As the X-ray diffraction experiments show, all the considered molecules create dimers in the respective crystal lattices between the coplanar carboxylic groups at the first benzene rings. The second benzene ring may have restricted conformational mobility depending on the size of the substituents. In this case, the benzene motives twist to compensate for strains of the steric hindrances and to minimize the molecular packing energy of the crystal lattices. Therefore, it can be assumed that it is the angle between the least-squares planes of phenyl rings (α) in a fenamate molecule (Figure 7) that will be connected to the molecular packing density and thermodynamic sublimation functions.

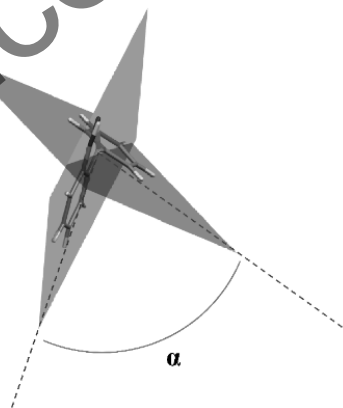


Figure 7. Illustration of dihedral angle between mean-square planes of phenyl rings in fenamate.

The dependence of the sublimation enthalpies of fenamates versus α is shown in Figure 8. ΔH_{sub}^0 obtained by sublimation measurements are marked by filled squares and the values derived from the solution calorimetry experiments are marked by empty squares. It is evident that for the same compound a higher value of the crystal lattice energy corresponds to the polymorphic form with a lower value of the α parameter.

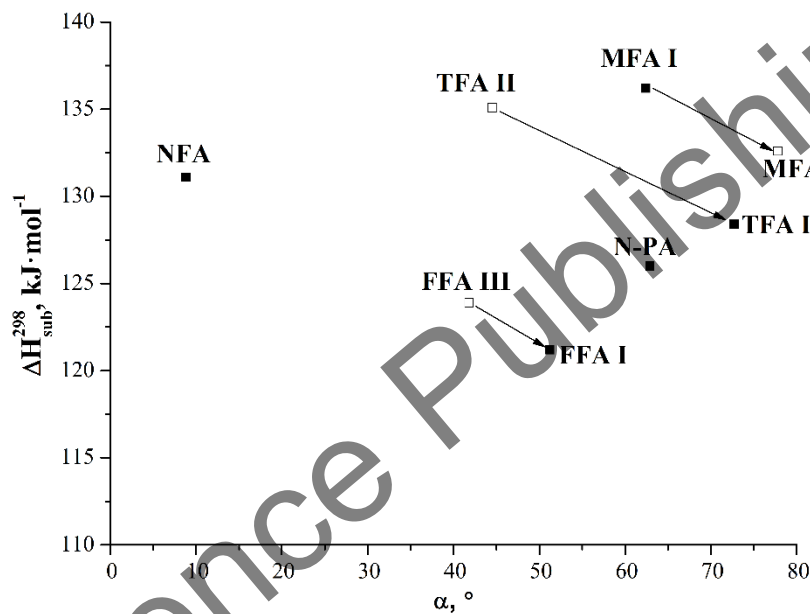


Figure 8. Dependence of ΔH_{sub}^{298} versus the angle between phenyl rings (α) for fenamates and their polymorphic forms.

The next step was to analyze the impact of various substituents (introduced to the molecule N-phenyl-anthranilic acid) on the sublimation enthalpies and melting points. The presence of a carboxylic group in the molecules determines the formation of inter- and intra- molecular hydrogen bonds, and this fact produces increasing ΔH_{sub}^{298} and T_m values. For example, both the sublimation enthalpy and the melting point of N-phenylanthranilic acid are higher by, respectively, 30.8 kJ·mol⁻¹ and 132.1

K, compared to that of diphenylamine ($\Delta H_{sub}^{298} = 95.2 \pm 0.6 \text{ kJ}\cdot\text{mol}^{-1}$, $T_m = 326.1 \pm 0.2 \text{ K}$ [49]), which is the structural precursor of the studied molecules. Introducing a $-\text{CF}_3$ group into **N-PA** molecule (flufenamic acid) leads to a decrease in the melting point (by 52.9 K) and sublimation enthalpy (by $4.8 \text{ kJ}\cdot\text{mol}^{-1}$). As mentioned above, replacing the carbon atom of the flufenamic acid molecule by a nitrogen atom (i.e., niflumic acid) leads to essential changes in the molecular structure, packing density, and crystal lattice energies. The sublimation enthalpy of niflumic acid is $9.0 \text{ kJ}\cdot\text{mol}^{-1}$ higher than that of flufenamic acid, whereas their melting points differ by 73.2 K. Introducing two methyl groups into the **N-PA** molecule (i.e., mefenamic acid) increases the crystal lattice energy by $10.2 \text{ kJ}\cdot\text{mol}^{-1}$ and the melting point by 45.3 K. Probably, electron donor substituents (like methyl groups) increase the total molecular electron density and, as a consequence, lead to increased sublimation enthalpy and melting point. The opposite effect is observed for electron acceptor substituents (such as $-\text{CF}_3$ and $-\text{Cl}$), as it is seen for flufenamic and tolfenamic acids.

A good correlation between the sublimation enthalpies and the melting points of the studied compounds is observed (Figure 9). Therefore, the ΔH_{sub}^{298} value for this class of substances can be estimated using the following correlation equation:

$$\Delta H_{sub}^{298}(\text{calc}) = (75.2 \pm 7.4) + (0.11 \pm 0.01) \cdot T_m \quad (1)$$

$$R = 0.971; \text{SD} = 1.19; n = 5$$

New fenamate analogs have been recently synthesized by Lopez-Mejías and Matzger [50] and their propensity to polymorphism has been studied (Table 4). We estimate the sublimation enthalpies of the most stable polymorphs of new compounds using the correlation equation (1). Since the melting temperatures of compounds 1-4 are found to be within the range of the fenamates melting points (T_m), the ΔH_{sub}^{298} (calc.) values are reliable.

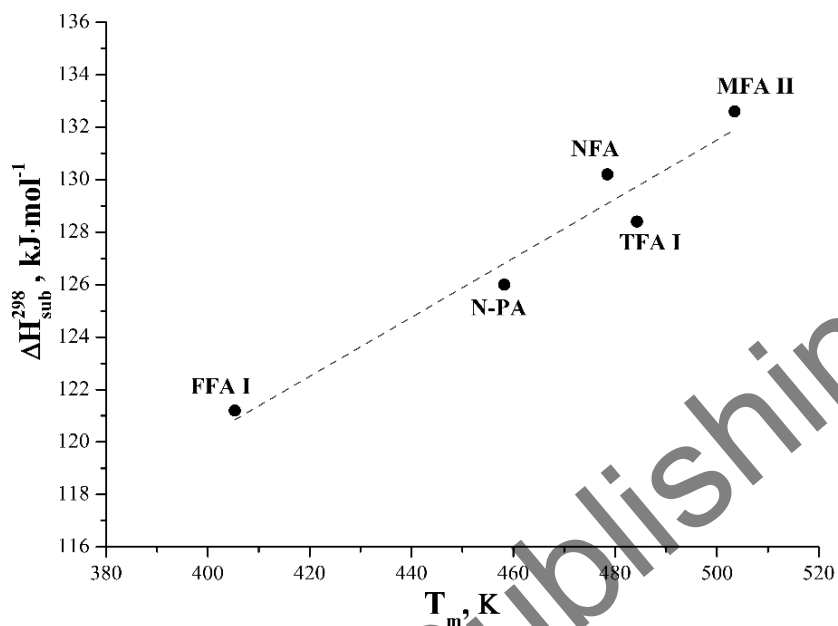
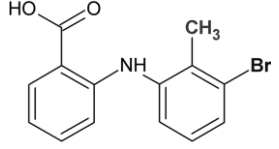
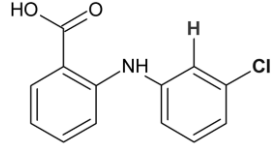
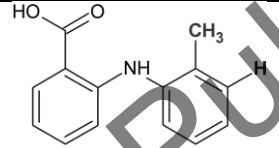
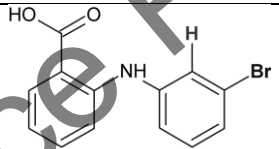


Figure 9. Dependence of sublimation enthalpies versus melting points of compounds studied.

Considering the experimental sublimation enthalpies for fenamates (Table 3) and the ΔH_{sub}^{298} (calc.) values for fenamate analogs (Table 4), the following regularities are observed: if there is a $-\text{CH}_3$ -group at the *ortho*-position of the noncarboxylated phenyl ring, the crystal lattice energy of the compound increases together with the increase in the volume of the substitution at the meta-position (compound 3 (128.0) \approx **TFA** (128.4) < compound 1 (130.6) < **MFA** (132.6)). However, if the *ortho*-position of the noncarboxylated phenyl ring is unsubstituted, the opposite relationship is observed: **N-PA** (126.0) > compound 2 (125.0) \approx compound 4 (125.5) > **FFA** (121.2). It should be also noted that crystals of **TFA** (form I) and compound 1 (form I) are found to be isostructural. Hence, the minor difference in lattice energies between those substances should be mainly due to the halogen interactions.

Table 4. Molecular structures, melting temperatures (T_m) and calculated sublimation enthalpies (ΔH_{sub}^{298} (calc.)) for fenamate analogs

	Molecular structure	T_m , K	ΔH_{sub}^{298} (calc.), kJ·mol ⁻¹
Compound 1 (form I)		490.2	130.6
Compound 2 (form I)		440.5	125.0
Compound 3 (form I)		466.9	128.0
Compound 4 (form I)		445.6	125.5

2.4. The Influence of Substitutions and Packing Arrangements on Fenamates Conformation

The main conformational variations in the fenamate molecules can be described by using the angle between the phenyl rings (α) (Figure 7). The α angle should be considered as an integral parameter, the value of which in the crystal is under the influence of two effects, namely supramolecular surroundings as well as the chemical nature and the position of substitutions in the noncarboxylated phenyl ring of the molecule. In order to separate and estimate those effects we propose the following scheme, shown in Figure 10.

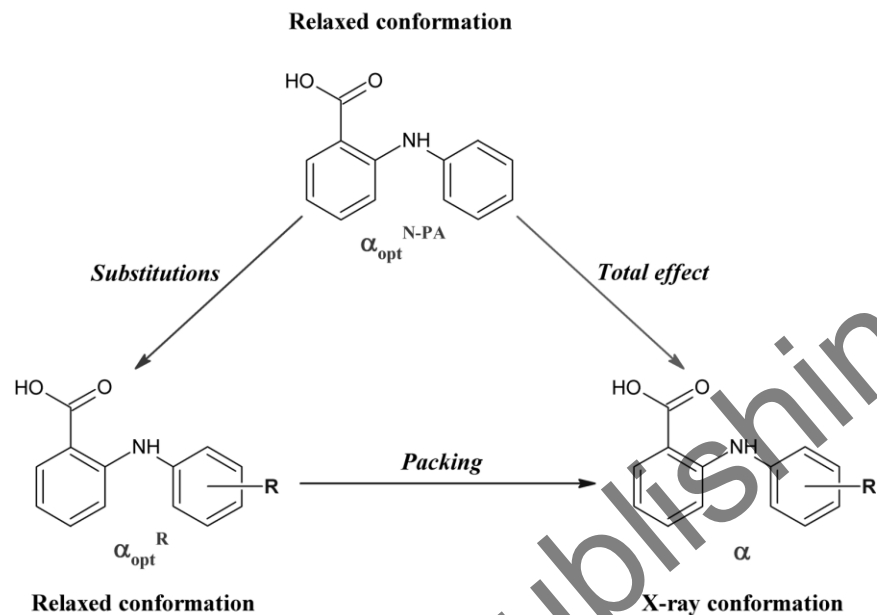


Figure 10. Schematic illustration of different effects responsible for conformation of fenamate molecules in the crystal.

As a molecule is released from a crystal, it adopts the conformation that corresponds to the minimum of its conformational energy. Therefore, the influence of packing on the conformational state of the fenamate molecules can be estimated by considering the difference between the α angles of the fully relaxed molecule (α_{opt}^R) and the same molecule with X-ray geometry (α). The influence of substitutions on the fenamate conformation can be deduced based on the difference between the α_{opt}^R value of the particular molecule and the angle between the phenyl rings in the fully relaxed molecule of N-phenylanthranilic acid (α_{opt}^{N-PA}).

Geometric optimization of the isolated fenamate molecules was carried out using the GAUSSIAN09 program at the B3LYP/6-311++G(d,p) level of theory [51]. The X-ray conformation of a fenamate molecule was used as the starting point of the optimization procedure. For optimized geometry, we calculated vibrational frequencies analytically to ensure that

it was the true local minimum (no imaginary frequencies). The results are shown in Table 5.

Table 5. Angles between least-squares planes of phenyl rings of fenamate molecules in the crystal and after optimization procedure at the B3LYP/6-311++G(d,p) level of theory

	α , °	α_{opt}^R , °	$\alpha - \alpha_{opt}^R$, °	$\alpha_{opt}^R - \alpha_{opt}^{N-PA}$, °
N-PA				
mol. A	52.9	44.6	8.3	–
mol. B	72.6	44.6	28.0	–
NFA^a	8.8	2.4	6.4	2.0
MFA				
form I	62.4	54.75	7.65	10.15
form II	77.8	80.2	-2.4	35.6
form III	80.3	80.2	0.1	35.6
FFA				
form I	51.2	45.3	5.9	0.7
form II	50.8	45.3	5.5	0.7
form III	41.8	41.0	0.8	-3.6
TFA	2.9	5.6	2.6	
form I	72.7	70.4	2.3	25.8
form II	44.5	51.3	-6.8	6.7
form III				
mol. A	53.5	51.3	2.2	6.7
mol. B	54.3	51.3	3	6.7
form IV				
mol. A	61.5	51.3	10.2	6.7
mol. B	63.8	51.3	12.5	6.7
mol. C	58.1	51.3	6.8	6.7
form V	76.9	70.4	6.5	25.8

^aIn case of **NFA**, the $\alpha_{opt}^R - \alpha_{opt}^{N-PA}$ parameter was calculated by using 2-(phenylamino)nicotinic acid as the unsubstituted analog (see Figure 3b).

For more convenient analysis, the results of calculations are presented in Figure 11 as a plot of $\alpha - \alpha_{opt}^R$ versus $\alpha_{opt}^R - \alpha_{opt}^{N-PA}$. The diagram is divided into five separate sectors, according to the values of the respective

$\alpha - \alpha_{opt}^R$ and $\alpha_{opt}^R - \alpha_{opt}^{N-PA}$ contributions. The dashed lines correspond to the $\alpha - \alpha_{opt}^R = \alpha_{opt}^R - \alpha_{opt}^{N-PA}$ condition.

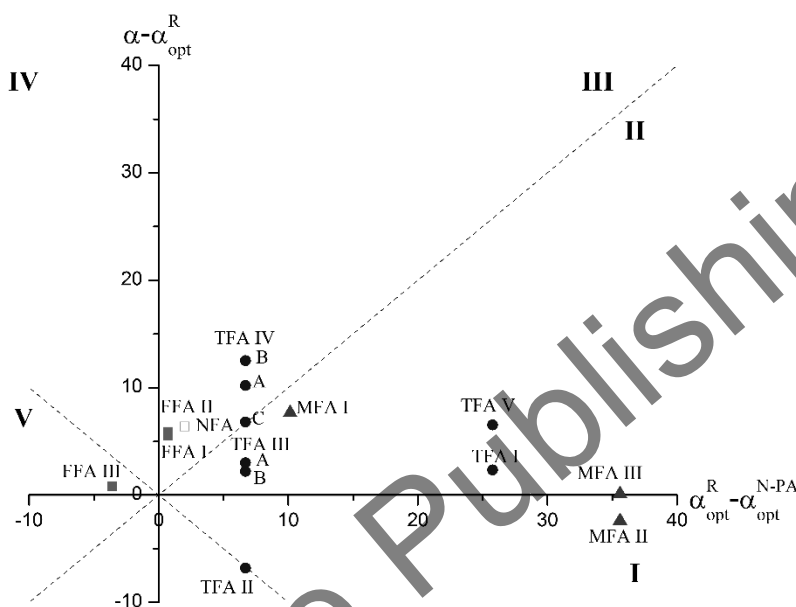


Figure 11. Relationship between $\alpha - \alpha_{opt}^R$ and $\alpha_{opt}^R - \alpha_{opt}^{N-PA}$ for fenamates.

Most of the compounds are located in sectors II and III. This indicates that both the packing and the substitution effects contribute to the molecular geometry. The conformation of molecules situated in sector II is mainly determined by the substitutions. For forms II and III of **MFA**, the $\alpha - \alpha_{opt}^R$ values are close to zero, suggesting that polymorphs II and III contain relatively low-energy molecular conformations. It is interesting to note that conformations of the **TFA** molecules in form IV are mainly dependent on supramolecular surroundings. However, in forms I, III and V of **TFA**, the packing influence on molecular conformations is less prominent. The conformation of **TFA** in form II may be seen as a result of the competition between the packing and substitution effects. In forms I and II of **FFA** and **NFA**, the relaxed molecular conformations are close to

those for N-phenylanthranilic acid and 2-(phenylamino)nicotinic acid, respectively, indicating that substitution has only a modest influence on the molecule geometry. The only case when $\alpha_{opt}^R - \alpha_{opt}^{N-PA}$ is negative is observed for form III of **FFA**. It might be reasonable to assume that the electron withdrawing of the $-CF_3$ group from the **FFA** molecule may decrease the repulsion between the hydrogen atoms in the conjunct phenyl rings, which makes a relatively flat conformation more favorable than that of N-phenylanthranilic acid.

3. STRUCTURAL AND PHYSICOCHEMICAL PROPERTIES OF FENAMATE COCRYSTALS WITH 4,4'-BIPYRIDINE

3.1. Materials

3.1.1. Compounds and Solvents

All the fenamates, 4,4'-bipyridine and solvents (>99% purity) were available commercially and were used without further purification. Before cocrystallization experiments, all the substances were characterized by X-ray powder diffraction (XRPD) and compared with the XRPD patterns calculated based on their single crystal structure data. Mefenamic acid and tolfenamic acid were identified as form I (ref. codes XYANAC and KAXXA101). The experimental XRPD pattern of flufenamic acid was found to be in well agreement with form I (FPAMCA11).

3.1.2. Crystallization Procedure

The fenamates and 4,4'-bipyridine in a (2:1) molar ratio were dissolved in a small amount of solvent and stirred at room temperature. The crystals were obtained by slow evaporation of saturated solutions. For N-phenylanthranilic acid, mefenamic acid and tolfenamic acid crystallization, acetone was used. In case of niflumic and flufenamic acids, diffraction quality crystals were obtained from methanol solution.

3.1.3. Solvent-Drop Grinding

Solvent-drop grinding experiments were performed using a Fritsch planetary micro mill, model Pulverisette 7. The experiments were carried out with the fenamates and 4,4'-bipyridine in a (2:1) molar ratio and a few drops of solvent (methanol or acetone) added with a micropipette.

3.2. Crystal Structures of the Cocrystals

Crystallographic data are summarized in Table 6, and the molecular units of the cocrystals are shown in Figure 12.

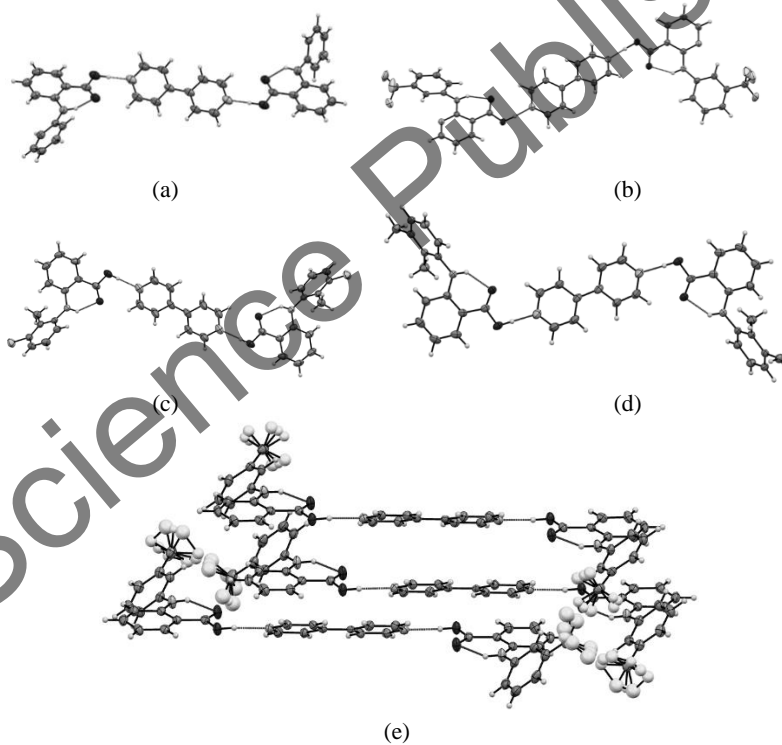


Figure 12. Molecular units in (a) [N-PA + BP]; (b) [NFA + BP]; (c) [TFA + BP]; (d) [MFA + BP]; (e) [FFA + BP]. Displacement ellipsoids are shown at 50% probability. For [FFA + BP], all $-\text{CF}_3$ groups are rotationally disordered over three positions.

Table 6. Crystallographic data for the fenamates cocrystals

	[N-PA + BP]	[NFA + BP]	[TFA + BP]	[MFA + BP]	[FFA + BP]
CCDC	1017637	1017636	1017633	1017635	1017634
Chemical formula	2(C ₁₃ H ₁₁ NO ₂)• C ₁₀ H ₈ N ₂	2(C ₁₃ H ₉ F ₃ N ₂ O ₂)• C ₁₀ H ₈ N ₂	2(C ₁₄ H ₁₂ ClNO ₂)• C ₁₀ H ₈ N ₂	2(C ₁₅ H ₁₅ NO ₂)• C ₁₀ H ₈ N ₂	2(C ₁₄ H ₁₀ F ₃ NO ₂)• C ₁₀ H ₈ N ₂
Crystal system	Triclinic	Monoclinic	Monoclinic	Triclinic	Triclinic
Space group	<i>P</i> $\bar{1}$	<i>C</i> 2/ <i>c</i>	<i>P</i> 21/ <i>c</i>	<i>P</i> $\bar{1}$	<i>P</i> $\bar{1}$
<i>a</i> /Å	7.7606(5)	26.000(4)	4.7315(12)	7.3302(4)	9.8384(11)
<i>b</i> /Å	9.7575(6)	6.7394(10)	45.263(12)	8.6992(5)	10.3962(11)
<i>c</i> /Å	20.0638(12)	19.854(3)	7.929(2)	13.6719(8)	25.015(3)
<i>α</i> /°	98.2930(10)	90.00	90.00	106.276(1)	84.632(2)
<i>β</i> /°	92.4230(10)	111.386(2)	106.911(3)	99.368(1)	81.353(2)
<i>γ</i> /°	104.5940(10)	90.00	90.00	98.738(1)	71.679(2)
Unit cell volume/Å ³	1450.01(16)	3239.3(8)	1624.6(7)	807.55(8)	2398.3(5)
Temperature/K	183(2)	173(2)	183(2)	183(2)	153(2)
No. of formula units per unit cell, <i>Z</i>	2	4	2	1	3
Absorption coefficient, μ/mm ⁻¹	0.088	0.122	0.249	0.086	0.122
No. of reflections measured	16156	13319	13525	8341	19730
No. of independent reflections	7681	3523	3508	3878	8504
<i>R</i> _{int}	0.0216	0.0384	0.0216	0.0151	0.0421
No. of variables	517	288	281	293	751
Final <i>R</i> ₁ values (<i>I</i> > 2σ(<i>I</i>))	0.0438	0.0423	0.0493	0.0406	0.0583
Final <i>wR</i> (<i>F</i> ²) values (all data)	0.1084	0.1115	0.1086	0.1137	0.1669
Goodness of fit on <i>F</i> ²	1.017	1.031	1.142	1.050	1.019
Largest diff. peak & hole, e•Å ⁻³	0.143 / -0.185	0.357 / -0.299	0.230 / -0.235	0.237 / -0.210	0.419 / -0.535

In the [N-PA + BP] structure, the 4,4'-bipyridine molecules occupy general positions, while in [MFA + BP], [NFA + BP] and [TFA + BP] they possess crystallographically imposed symmetry. As for specific case of [FFA + BP], one independent BP molecule occupies general position and another lies on inversion centre resulting in 1.5 crystallographically unique BP fragments. In each structure, fenamate and BP molecules connected by O-H...N hydrogen bonds involving API carboxylic acid and pyridine N atoms of BP to form a hetero-trimer unit (Figure 12). In addition, BP forms C-H...O contacts with the neighbouring API molecules.

In spite of similar organization of the cocrystals asymmetric units, the BP molecule shows considerable conformational variations and a different orientation relative to the anthranilic fragment of the fenamate molecule. The angles between the least-squares planes of the pyridine rings of BP (β) and the angles between the fenamate anthranilic fragment and the hydrogen-bonded pyridine ring of BP (θ) in the cocrystals (Figure 13) are summarized in Table 7.

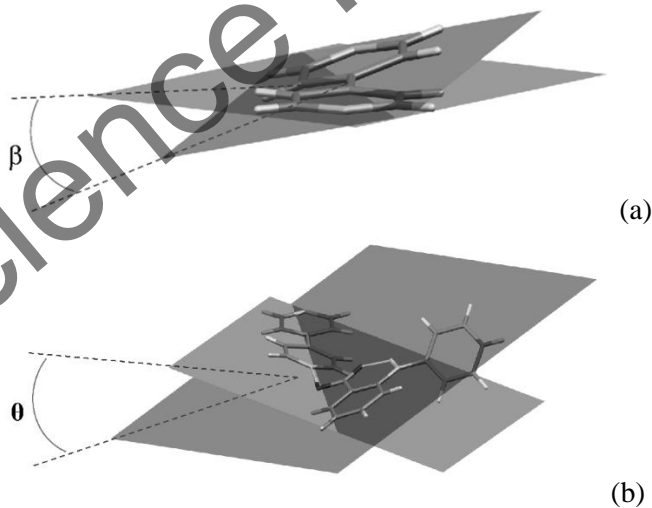


Figure 13. Illustration of different dihedral angles in the cocrystals: (a) the dihedral angle in BP molecule (β); (b) the dihedral angle between the anthranilic fragment of fenamate and the hydrogen-bonded pyridine ring of BP (θ).

Table 7. The dihedral angle in BP molecules, β , and the angle between the fenamate anthranilic fragment and the BP hydrogen-bonded pyridine ring, θ

Cocrystal	β , °	θ , °
[N-PA + BP]	14.83(6)	23.80(5), 39.43(4)
[NFA + BP]	26.65(3)	23.39(3)
[TFA + BP]	0.0	24.6(1)
[MFA + BP]	0.0	5.07(7)
[FFA + BP]		
<i>Molecule A</i>	0.0	30.86(9)
<i>Molecule B</i>	0.0	31.78(9)
<i>Molecule C</i>	0.9(1)	32.33(9)

It has been reported that the most of two-component cocrystals with **BP** contain the planar conformation of the molecule, which is a relatively higher-energy state. [52] A similar trend is also observed for fenamate cocrystals with **BP**. The molecular conformation of **BP** is considerably twisted from planarity only in two structures, namely [N-PA + BP] and [NFA + BP]. It should be noted that conformational diversity of the API molecule in [FFA + BP] has only a minor effect on **BP** conformation. In all other cases the **BP** molecules hold planar conformation. In contrast to β , angle θ , which characterizes orientation of the fenamate anthranilic fragment and the hydrogen-bonded pyridine ring of **BP**, is considerably greater than 0° for all the cocrystals.

The least value of angle θ is observed in [MFA + BP]. Probably, it is a consequence of the $\pi \dots \pi$ interactions between **BP** and the neighboring molecules of mefenamic acid. For the rest of the cocrystals, the θ value varies within a *ca.* 20° range, and it does not correlate with the **BP** conformation. It is evident that both angles (β and θ) reflect the influence of supramolecular surroundings on the **BP** orientation in a cocrystal. It is difficult, however, to highlight the influence of certain factors on the mentioned angles.

3.3. Conformational Analysis and Crystal Packing Similarity

Considering a diversity of polymorphic forms and a variety of conformational states of fenamates, it would be interesting to compare molecular conformations of fenamates in the cocrystals with **BP** and different polymorphs, the known cocrystals and solvates (Table 8).

Table 8. Selected torsion angle, τ_1 , and the dihedral angle between planes of phenyl rings, α , of the fenamate molecules in different crystal forms^a

	$\tau_1, ^\circ$	$\alpha, ^\circ$	<i>rmsd</i>	Ref. code/ CCDC
[N-PA + BP]	-139.5 (A'); -69.8 (B')	47.9 (A'); 70.1 (B')		1017637
N-PA	-136.6 (A); - 70.5 (B)	52.9 (A); 72.6 (B)	0.081 (A'A); 0.081 (B'B)	QQQBTY02
[NFA + BP]	-154.4	22.0		1017636
NFA	-176.3	8.8	0.250	
[NFA + Nicotinamide]	11.6	9.0	2.072	EXAQEA
[TFA + BP]	-76.3	69.9		1017633
TFA form I	-74.9	72.7	0.101	KAXXAI01
TFA form II	-142.6	44.5	0.905	KAXXAI
TFA form III	-138.4 (A); 126.8 (B)	54.3 (A); 53.5 (B)	0.756(A); 1.840(B)	KAXXAI02
TFA form IV	-115.9 (A); - 125.9 (B); -134.1	61.5 (A); 63.8 (B); 58.1 (C)	0.674(A); 0.624(B); 0.699(C)	KAXXAI03
TFA form V	-125.1 (50% of occupancy)	76.9	0.445	KAXXAI04
[TFA + Nicotinamide]	133.7	46.9	1.807	EXAQIE
[MFA + BP]	77.2	79.3		1017635
MFA form I	-119.9	62.4	1.787	XYANAC
MFA form II	68.2 (55% of occupancy)	77.8	0.121	XYANAC02
MFA form III	-80.2	80.3	1.813	XYANAC03
[MFA + DMF]	-75.6	75.3	1.788	ZAZGAK
[MFA + Nicotinamide]	137.1	50.4	0.664	EXAQOK

	$\tau_1, ^\circ$	$\alpha, ^\circ$	<i>rmsd</i>	Ref. code/ CCDC
[FFA + BP]	155.3(A'); 148.3 (B'); -44.1 (C')	40.8(A'); 43.2(B'); 47.2(C')		1017634
FFA form I	-130.1	53.0	1.128(A'); 1.488(B'); 1.252(C')	FPAMCA11
FFA form II	141.3	50.8	0.427(A') ; 0.326(B') ; 2.095(C')	FPAMCA17
FFA form III	8.7	43.0	1.538(A'); 1.487(B'); 0.384(C')	FPAMCA
[FFA + Nicotinamide]	135.4	54.8	0.537(A') ; 0.346(B') ; 2.050(C')	EXAQAW
[FFA + Theophylline] ^b	37.3	47.8	1.437(A'); 1.311(B'); 0.473(C')	
[FFA + 2-pyridone] ^b	54.4	53.4	1.343(A'); 1.249(B'); 0.290(C')	

^aMolecules corresponding to a cocrystal are indicated by stroke ('). ^b Ref [13].

The conformational state of the fenamate molecules can be described in terms of the most widely varying torsion angle, τ_1 , (Figure 1) and the angle between the least-squares planes of phenyl rings, α (Figure 7). For quantitative comparison of conformations, we used *rmsd* parameter, which is the root-mean-square deviation of all non-hydrogen atom positions in two molecules, calculated in Mercury [53]. The overlay of conformations of the fenamate molecules in different crystal forms is shown in Figure 14.

The results shown in Table 8 reveal that conformations of the fenamate molecules in the cocrystals with **BP** are similar to those in different polymorphs of pure fenamates. Moreover, for [**N-PA** + **BP**], both asymmetric molecules of **N-PA** show almost identical conformations to the ones in the pure compound. In [**NFA** + **BP**], the conformation of **NFA** is in good agreement with the known form of **NFA**, while the alternative conformer is observed in the nicotinamide cocrystal (EXAQEA).

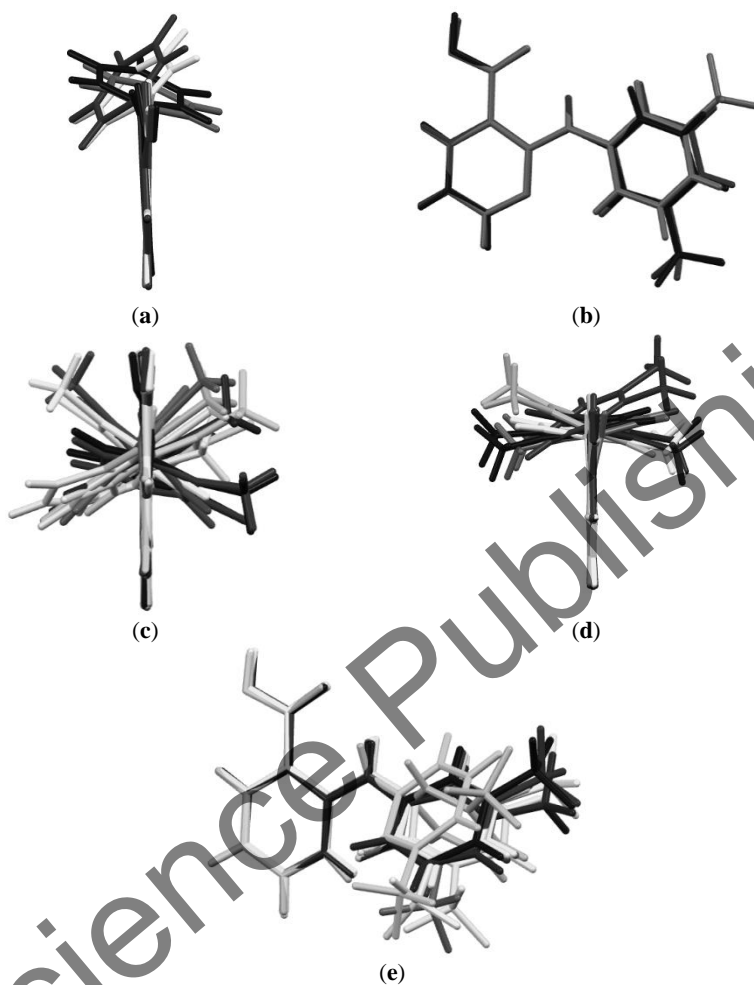


Figure 14. Overlay of the fenamate molecules conformations in different crystal forms shown in Table 8: (a) **N-PA**; (b) **NFA**; (c) **TFA**; (d) **MFA**; (e) **FFA**.

For the [**TFA** + **BP**] cocrystals, the conformation of the API molecule corresponds to form I of **TFA**. In case of [**MFA** + **BP**], the *rmsd* parameter indicates a large similarity between molecular conformation in the cocrystal and form II of pure **MFA**.

The [**FFA** + **BP**] structure is interesting as it contains three crystallographically independent molecules with distinct conformations. According to Cruz-Cabeza and Bernstein [54], a new conformation is considered to be a new conformer only if it corresponds to distinct energy minima of the gas-phase potential energy surface. Therefore, the asymmetric unit of [**FFA** + **BP**] contains two different conformers of **FFA** molecule, where one of the conformers adopts two conformations (Table 8, Figure 14e). It should be noted that similar phenomenon was found only in metastable polymorphic forms IV, VI, VIII of pure **FFA** [55]. Table 8 shows a comparison of the **FFA** conformations in the cocrystal with the most stable polymorphs I-III and the known cocrystals. The conformation of the molecules A' and B', which are two conformations of the first conformer, is comparable to that in **FFA** form II. Whereas the second conformer (molecule C') corresponds to the most thermodynamically stable form III of **FFA**. Figure 15 shows the distributions of the torsion angle, τ_1 , and the dihedral angle, α , in all known crystal forms of **FFA**.

Apparently, τ_1 values are distributed into two tight regions corresponding to two energy minima of the potential energy surface. Molecules A' and B' belong to the high-angle region, while the molecule C' is located in the low-angle region.

Conformational analysis clearly shows that the fenamate conformations are not influenced significantly by cocrystal formation. It might be reasonable to assume that a similar trend may be observed in the packing arrangement of the API molecules in the cocrystals. In order to test this assumption, the crystal structures of the fenamate cocrystals and their polymorphic forms were compared using the Crystal Packing Similarity module [56] implemented in Mercury [53]. Figure 16a shows the results of the Crystal Packing Similarity analysis between [**N-PA** + **BP**] and the only known form of pure **N-PA** (QQQBTY02). The crystal structures overlay 20 molecules with $rmsd_n$ of 0.377 Å. Therefore, a considerable similarity in large clusters of molecules between those two structures is observed. Comparison of the crystal structures of [**TFA** + **BP**] and **TFA** form I (KAXXAI01) resulted in a 20 molecule overlay with $rmsd_n$ of 0.426 Å (Figure 17a). For [**MFA** + **BP**] (Figure 18a,b), the best

results were obtained in **MFA** form II (XYANAC02) ($n = 16$, $rmsd_n = 0.703$) and DMF solvate (ZAZGAK) ($n = 13$, $rmsd_n = 0.670$). However, for **[NFA + BP]** and **[FFA + BP]**, the Crystal Packing Similarity search has not revealed clusters of molecules with $n > 10$ and $rmsd_n < 1$. In case of **[FFA + BP]**, crystal structures of all currently established polymorphic forms were considered. Therefore, the packing arrangement of the **NFA** and **FFA** molecules in the cocrystals with **BP** is unique, and it is not seen in any of the APIs polymorphs.

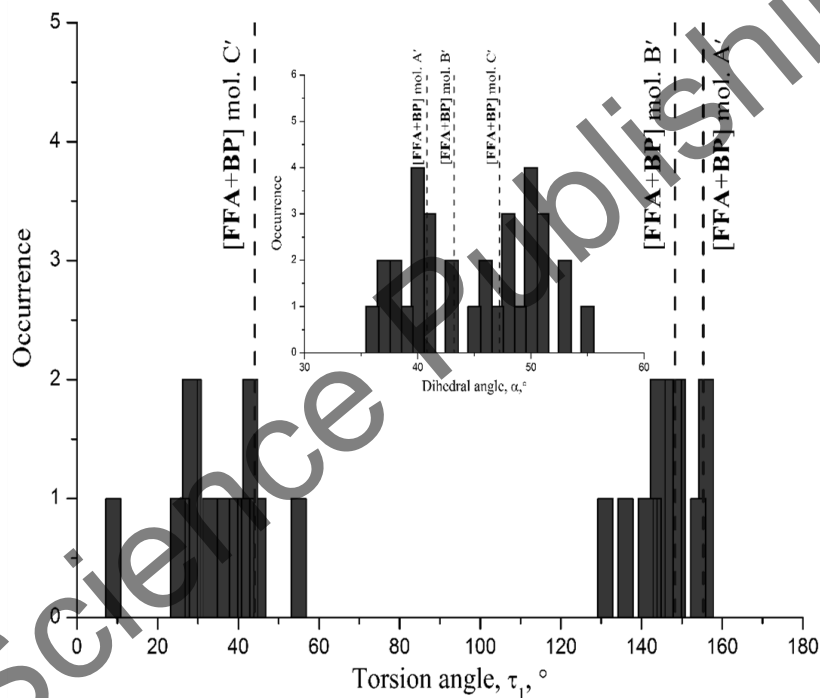


Figure 15. Distributions of the torsion angle, τ_1 , and the dihedral angle, α , in all known crystal forms of FFA. Conformations of A', B' and C' molecules in [FFA + BP] are indicated by dash lines.

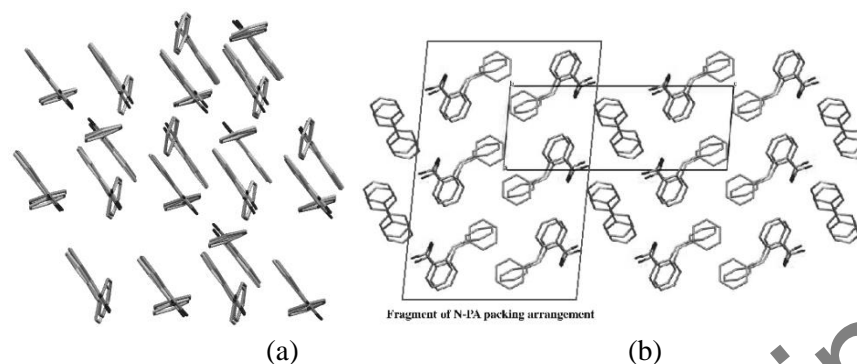


Figure 16. (a) Overlay of the [N-PA + BP] crystal structure and the only known form of N-PA ($n=20$, $rmsd_n = 0.377$); (b) molecular packing projection for [N-PA + BP]. Hydrogen atoms are omitted.

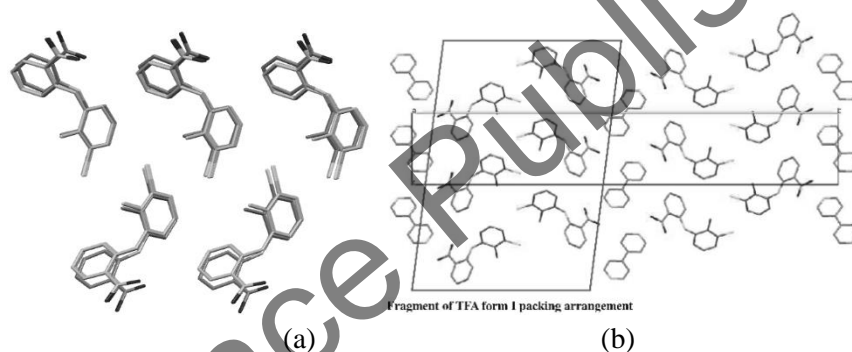


Figure 17. (a) Overlay of the [TFA + BP] crystal structure and form I of TFA ($n=20$, $rmsd_n = 0.426$); (b) molecular packing projection for [TFA + BP]. Hydrogen atoms are omitted.

The Crystal Packing Similarity analysis indicates clearly that the packing arrangement of the [N-PA + BP], [TFA + BP] and [MFA + BP] cocrystals consists of discrete fragments of the crystal structures of initial APIs connected to each other by BP molecules (Figures 16b, 17b, 18c). In [MFA + BP], the basis of the cocrystal structure is MFA form II, which is thermodynamically less stable than form I under ambient conditions. The fragments are segregated so that there are clear regions with interactions between API and BP and regions where only API or BP molecules interact.

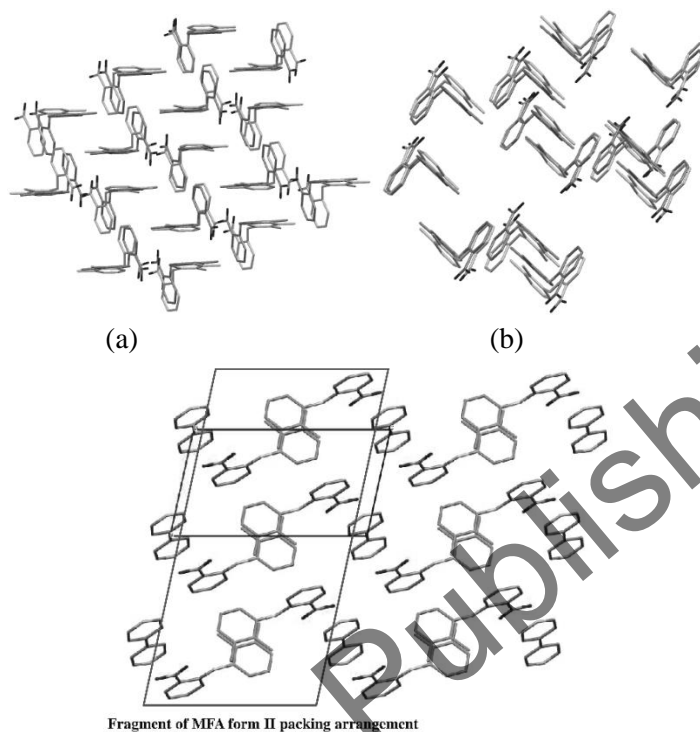
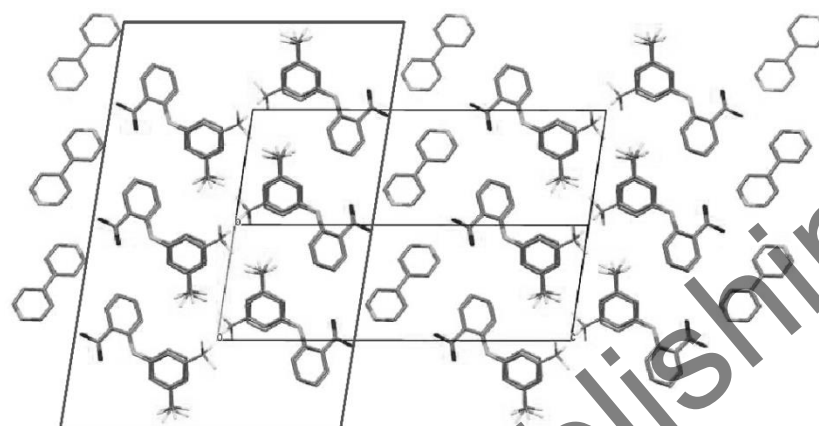


Figure 18. (a) Overlay of the [MFA + BP] crystal structure and form II of MFA ($n=16$, $rmsd_n = 0.703$); (b) Overlay of the [MFA + BP] crystal structure and DMF solvate of MFA ($n=13$, $rmsd_n = 0.670$); (c) molecular packing projection for [MFA + BP]. Hydrogen atoms are omitted.

It should be pointed out that the [FFA + BP] crystal structure consists of distinct alternating fragments, which contain either **FFA** or **BP** molecules (Figure 19a). This packing arrangement is essentially similar to that of [N-PA + BP], [TFA + BP] and [MFA + BP]. Based on the packing similarity analysis described above, it might be reasonable to assume that the packing arrangement of the **FFA** molecules in the cocrystal also corresponds to a stable or metastable configuration of molecules in a crystal of the pure compound. However, the Crystal Packing Similarity search does not show any satisfactory match between the cocrystal structure and the known crystal forms of **FFA**. Considering the highly polymorphic nature of **FFA** we speculate that the [FFA + BP] structure

contains fragments of new polymorphic form of **FFA** stabilized by the **BP** molecules due to weak van der Waals interactions.



Fragment of new packing arrangement
of the FFA molecules

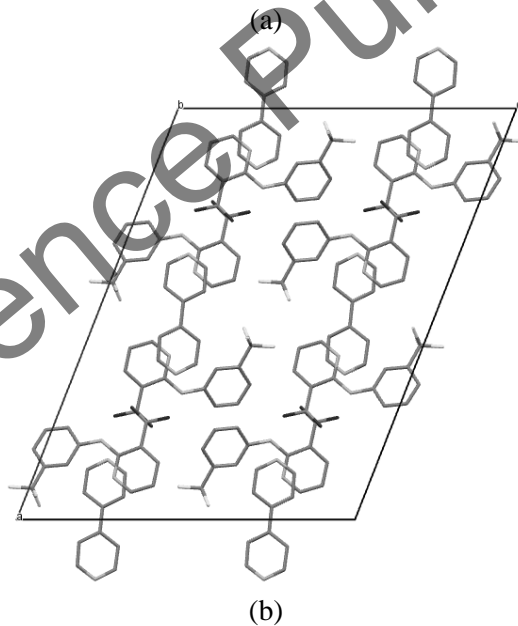


Figure 19. Molecular packing projection for (a) [FFA + BP]; (b) [NFA + BP].
Hydrogen atoms are omitted.

The [NFA + BP] structure is found to be different compared to the other fenamate cocrystals. In this structure the API and BP molecules are distributed uniformly in the bulk of the crystal, although the discrete fragments of the crystal structures of the components are not seen (Figure 19b). In addition, the Crystal Packing Similarity search does not show any satisfactory match between the cocrystal structure and the known NFA crystal forms. In order to highlight the difference between the [NFA + BP] crystal structure and the other fenamate cocrystals, the CLP (Coulomb–London–Pauli) calculations were carried out [57]. The calculation results are summarized in Table 9. For [FFA + BP], the calculations were not performed due to complex disorder of CF₃ group.

Table 9. Sums of the intermolecular interaction energies (kJ mol⁻¹) between the different types of molecules calculated using the CLP method

	API-API	API-BP	BP-BP	Total ^a
[N-PA + BP]	-59.4 (50.6%)	44.1 (37.5%)	-14.0 (11.9%)	-117.5
[MFA + BP]	-61.0 (47.3%)	-57.7 (44.8%)	-10.2 (7.9%)	-128.9
[TFA + BP]	-64.7 (52.9%)	-43.0 (35.2%)	-14.6 (11.9%)	-122.3
[NFA + BP]	-58.7 (46.9%)	-65.6 (52.4%)	-1.0 (0.8%)	-125.3

^a The total corresponds to the calculated energy change for formation of one mole of [API + BP] crystal from two moles of API and one mole of BP separated in the gas phase.

In [N-PA + BP], [MFA + BP] and [TFA + BP], the API-API interactions provide the largest contribution to the lattice energy ($\approx 50\%$), while the BP-BP interactions comprise *ca.* 8 - 12% of the total energy. This energy distribution reflects the alternation of the API and the BP molecular fragments in a crystal lattice of the cocrystals. The energy distribution of the intermolecular interactions for [NFA + BP] is substantially different compared to the other cocrystals. In this case, the API-BP interactions provide the largest contribution to the lattice energy.

In addition, API-API and API-BP interactions comprise more than 99% of the total energy, while the BP molecules do not seem to interact with each other.

It turns out that the packing fragment segregation phenomenon in a cocrystal is observed not only in fenamates. As an example, we used a BP cocrystal with Carbamazepine (XAQQUC). Carbamazepine (CBZ) is an important drug in treatment of epilepsy and trigeminal neuralgia, which is famous for its ability to form solvates [58-61], cocrystals [62-67] and polymorphs [68-71]. The Crystal Packing Similarity analysis of the [CBZ + BP] cocrystal shows a close resemblance in large clusters of molecules between this structure and form III of pure CBZ (CBMZPN01) ($n=12$, $rmsd_n = 0.684$), DMSO solvate (UNEYIV) ($n=12$, $rmsd_n = 0.495$), acetone solvate (CRBMZA01) ($n=12$, $rmsd_n = 0.370$).

3.4. Thermal Analysis

The thermal data for all the cocrystals and pure components are represented in Table 10. We have recently reported that the increase in the melting temperature of BP cocrystals with different APIs is accompanied by an increase in the melting temperature of the corresponding pure APIs [52]. Figure 20 shows the melting temperature of the fenamate cocrystals with BP as a function of the melting points of the corresponding pure fenamates. In the temperature range considered, the increase in T_m of the cocrystals is accompanied by an increase in the melting temperature of the pure API. It indicates that the intermolecular interactions, which are responsible for the thermal stability of the pure API crystals, are partially conserved in the fenamate cocrystal.

This fact is consistent with the Crystal Packing Similarity analysis. The average value of fusion heat for most of the cocrystals is found to be *ca* 81 kJ mol⁻¹, while [NFA + BP] is an exception. The increase in ΔH_{fus} in this case is probably caused by the difference in the energy distribution of the intermolecular interactions for [NFA + BP] compared to the other

cocrystals. The melting temperature of this cocrystal, however, is consistent with the general correlation.

Table 10. Thermophysical data for the fenamate cocrystals, pure APIs and 4,4'-bipyridine

	T_m , °C (onset)	ΔH_{fus} , kJ mol ⁻¹	ΔS_{fus} , J mol ⁻¹ K ⁻¹
[N-PA + BP]	145.7 ± 0.3	83.0 ± 0.9	198.1
[NFA + BP]	153.8 ± 0.3	96.1 ± 1.1	225.1
[TFA + BP]	157.0 ± 0.3	77.1 ± 0.7	201.2
[MFA + BP]	163.5 ± 0.3	83.1 ± 0.9	179.2
[FFA + BP]	128.0 ± 0.3	84.6 ± 0.5	190.3
N-PA	186.6 ± 0.3	39.7 ± 0.5	86.4
NFA	202.9 ± 0.3	36.5 ± 0.4	76.7
TFA (form I)	212.1 ± 0.2	41.0 ± 0.4	84.5
MFA (form II)	230.4 ± 0.2	38.7 ± 0.5	76.8
FFA (form III)	133.9 ± 0.2	26.7 ± 0.5	65.6
4,4'-bipyridine	111.8 ± 0.2	24.7 ± 0.5	64.1

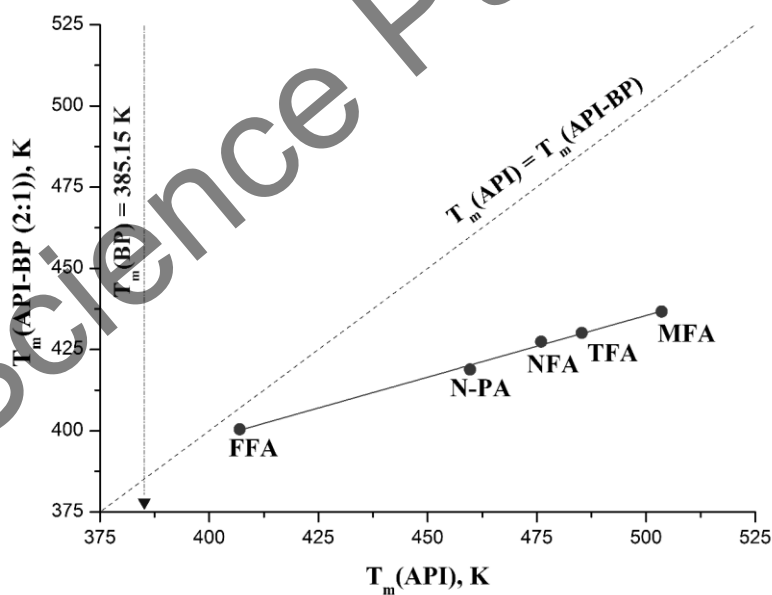


Figure 20. Plot of melting temperature of the fenamate co-crystals with BP vs the melting points of the corresponding pure fenamates.

3.5. Solution Calorimetry

Solution enthalpies were measured by using an ampoule-type isoperibolic calorimeter with a titanium reaction vessel volume of 50 cm³.

The enthalpy of formation, $\Delta H_f^T(AB)$, of a cocrystal with (1:1) stoichiometry can be calculated as [72]:

$$\Delta H_f^T(AB) = \Delta H_{sol}^T(A)_B + \Delta H_{sol}^T(B)_A - \Delta H_{sol}^T(AB)_B, \quad (2)$$

where $\Delta H_{sol}^T(A)_B$ and $\Delta H_{sol}^T(B)_A$ are the solution heat values for solid A in a solution containing B and for solid B in a solution containing A, respectively. For [API + BP] (2:1), the formation enthalpy was calculated in a similar manner with a proper account of the cocrystal stoichiometry. All experiments were conducted at 298.15 K. Methanol was chosen as a solvent as the cocrystals dissolve well with a large endothermic heat effect. The results of solution calorimetry experiments and calculated enthalpies of formation for the cocrystals are summarized in Table 11.

Table 11. Solution enthalpies, ΔH_{sol}^{298} , and calculated enthalpies of formation, ΔH_f^{298} , at 298 K (kJ mol⁻¹)

	$\Delta H_{sol}^{298}([API + BP])$	$\Delta H_{sol}^{298}(API)_{BP}$	$\Delta H_{sol}^{298}(BP)_{Fen}$	$\Delta H_f^{298}([API + BP])$
[N-PA + BP] (2:1)	68.9 ± 1.4	18.8 ± 0.2	25.8 ± 0.1	-5.6 ± 1.7
[NFA + BP] (2:1)	77.7 ± 0.2	23.6 ± 0.1	27.7 ± 0.1	-4.6 ± 0.4
[TFA + BP] (2:1)	75.1 ± 0.3	27.4 ± 0.3	16.4 ± 0.1	-3.9 ± 0.6
[MFA + BP] (2:1)	73.4 ± 0.1	28.2 ± 0.4	17.1 ± 0.3	0.2 ± 0.8
[FFA + BP] (2:1)	68.7 ± 0.2	23.1 ± 0.1	14.2 ± 0.2	-8.4 ± 0.5

Table 11 shows that the enthalpies of formation of the cocrystals are small. Moreover, for [MFA + BP], the ΔH_f^{298} value is of the same order of magnitude as the experimental error. It should be noted that enthalpy of formation is an integral parameter which indicates the difference between the crystal lattice energy of a cocrystal and individual components at certain stoichiometry. Therefore, for [MFA + BP], almost all intermolecular interactions (including hydrogen bonds) present in the crystals of pure components are energetically comparable to those in the cocrystal. As mentioned above, the basis of the [MFA + BP] crystal structure is form II of MFA, which is found to be *ca* 3.6 kJ mol⁻¹ less stable than form I [43]. Considering the difference in crystal lattice energy between MFA polymorphs, the formation enthalpy of [MFA + BP] from MFA form II as the starting polymorph is *ca* -7.0 ± 0.8 kJ mol⁻¹. For [N-PA + BP] and [TFA + BP], which also contain large clusters of molecules of initial API, the enthalpies of formation are -5.6 ± 1.4 kJ mol⁻¹ and -3.9 ± 0.6 kJ mol⁻¹, respectively. In this case, the packing energy gain for the cocrystals is mainly caused by weak van der Waals API-BP and BP-BP interactions as the energy of API-API intermolecular interactions inside the clusters should be comparable to that of the pure APIs. The formation enthalpy of the [NFA + BP] cocrystal is close to that of [N-PA + BP] и [TFA + BP]. However, according to CLP calculations, the packing energy gain in [NFA + BP] is expected to be the result of the API-BP and API-API interactions, and the latter should be energetically comparable to those in the pure NFA crystal. The [FFA + BP] cocrystal shows the largest value of ΔH_f^T . However, the formation enthalpy of [FFA + BP] from the most thermodynamically stable FFA form III, which is *ca* 2.7 kJ mol⁻¹ more stable than form I, is calculated to be *ca* -3.0 ± 0.6 kJ mol⁻¹ [43]. This estimate does not exceed the average ΔH_f^{298} value for the fenamate cocrystals and equals *ca* -5.2 kJ mol⁻¹. It was established above that the packing arrangement of [FFA + BP] is essentially similar to that in [N-PA + BP], [TFA + BP] and [MFA + BP]. However, the [FFA + BP] structure does not contain any known fragments of the crystal forms of the pure

compound. Therefore, the increase in the crystal lattice energy of the cocrystal compared to initial components may be caused by the **API-BP**, **BP-BP** interactions as well as additional interactions between the API molecules.

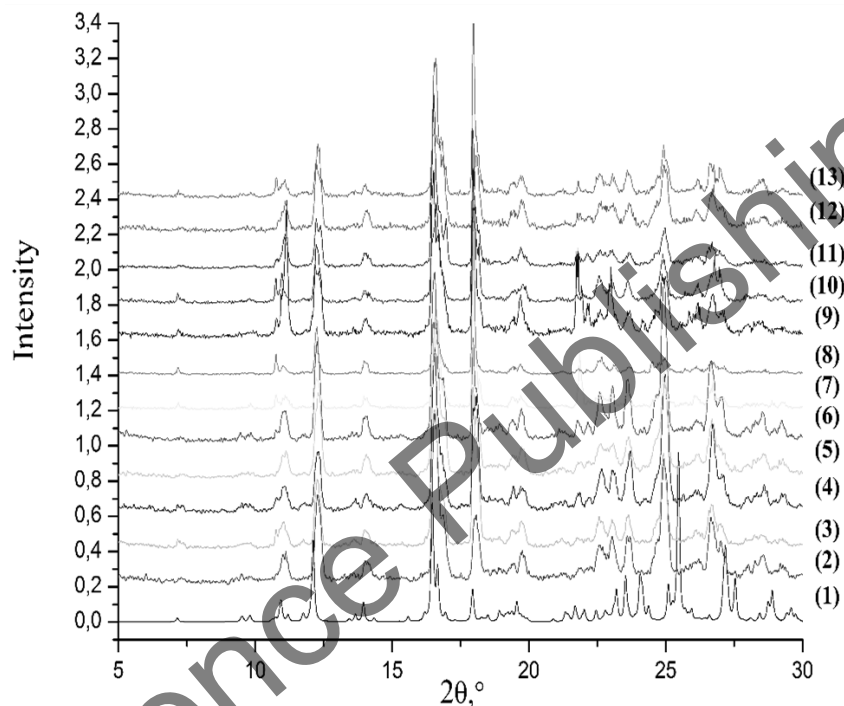


Figure 21. PXRD patterns of the [FFA + BP] co-crystals obtained from 12 different solvents: (1) calculated from single crystal structure data; (2) acetone; (3) acetonitrile; (4) chloroform; (5) dioxane; (6) DMSO; (7) ethyl formate; (8) ethyl acetate; (9) ethanol; (10) isopropyl alcohol; (11) methanol; (12) tetrahydrofuran; (13) toluene.

3.6. Screening for [FFA + BP] Polymorphs

Considering the high propensity of **FFA** to polymorphism, it might be possible to assume that the [**FFA** + **BP**] cocrystal may also be polymorphic [73, 74]. Polymorphism of 4,4'-bipyridine cocrystals with a (1:1) and (2:1) molar ratio has been reported previously [52,75-77]. Screening for [**FFA** +

BP] polymorphs was performed by a solution cocrystallization of **FFA** and **BP** in (2:1) molar ratio using 12 different solvents at room temperature. For the experiment, a wide range of the most frequently used organic solvents for polymorph screening was taken [78]: acetone, acetonitrile, chloroform, dioxane, DMSO, ethyl formate, ethyl acetate, ethanol, isopropyl alcohol, methanol, tetrahydrofuran, toluene. All dry samples were analyzed by XRPD. The results indicate clearly that in all cases cocrystallization of **FFA** and **BP** leads to formation of only one structure (Figure 21). Therefore, the previously unseen packing arrangement of **FFA** molecules in the cocrystal is found to be quite stable. A considerable role in the structure stabilization is probably played by weak van der Waals interactions between the **FFA** and **BP** molecules.

ACKNOWLEDGMENTS

This work was supported by Fellowship of President of Russian Federation (SP- 678.2016.4).

REFERENCES

- [1] Pascucci, R. A. (2002). *The Journal of the American Osteopathic Association*, 102(9): 487-489.
- [2] Flower, R. J. (1974). *Pharmacological Reviews*, 26(1): 33-67.
- [3] Blobaum, A. L., & Marnett, L. J. (2007). *Journal of medicinal chemistry*, 50(7): 1425-1441.
- [4] Rao, P. & Knaus, E. E. (2008). *J. Pharm. Pharm. Sci.*, 11: 81-110.
- [5] Guinamard, R., Simard, C., & Del Negro, C. (2013). *Pharmacology & therapeutics*, 138(2): 272-284.
- [6] Jiang, H., Zeng, B., Chen, G. L., Bot, D., Eastmond, S., Elsenussi, S. E., & Xu, S. Z. (2012). *Biochemical pharmacology*, 83(7): 923-931.

- [7] Klose, C., Straub, I., Riehle, M., Ranta, F., Krautwurst, D., Ullrich, S., & Harteneck, C. (2011). *British journal of pharmacology*, 162(8): 1757-1769.
- [8] Asanuma, M., Miyazaki, I., & Ogawa, N. (2004). *Current pharmaceutical design*, 10(6): 695-700.
- [9] Subaiea, G. M., Adwan, L. I., Ahmed, A. H., Stevens, K. E., & Zawia, N. H. (2013). *Neurobiology of aging*, 34(10): 2421-2430.
- [10] Daniels, M. J., Rivers-Auty, J., Schilling, T., Spencer, N. G., Watremez, W., Fasolino, V., & Wong, R. (2016). *Nature Communications*, 7.
- [11] Eslin, D., Lee, C., Sankpal, U. T., Maliakal, P., Sutphin, R. M., Abraham, L., & Basha, R. (2013). *Tumor Biology*, 34(5): 2781-2789.
- [12] Soriano-Hernandez, A. D., Madrigal-Pérez, D., Galvan-Salazar, H. R., Martinez-Fierro, M. L., Valdez-Velazquez, L. L., Espinoza-Gómez, F., & Lara-Esqueda, A. (2015). *Oncology letters*, 10(4): 2574-2578.
- [13] Bernstein, J. *Polymorphism in Molecular Crystals*; Clarendon Press: Oxford, U.K., 2002.
- [14] Lutker, K. M., Tolstyka, Z. P., & Matzger, A. J. (2007). *Crystal Growth and Design*, 8(1): 136-139.
- [15] López-Mejías, V., Kampf, J. W., & Matzger, A. J. (2009). *Journal of the American Chemical Society*, 131(13): 4554-4555.
- [16] López-Mejías, V., Kampf, J. W., & Matzger, A. J. (2012). *Journal of the American Chemical Society*, 134(24): 9872-9875.
- [17] Fábian, L., Hamill, N., Eccles, K. S., Moynihan, H. A., Maguire, A. R., McCausland, L., & Lawrence, S. E. (2011). *Crystal Growth & Design*, 11(8): 3522-3528.
- [18] Seetha Lekshmi, S., & Guru Row, T. N. (2012). *Crystal Growth & Design*, 12(8): 4283-4289.
- [19] Fonari, M. S., Ganin, E. V., Vologzhanina, A. V., Antipin, M. Y., & Kravtsov, V. C. (2010). *Crystal Growth & Design*, 10(8): 3647-3656.
- [20] Aitipamula, S., Wong, A. B., Chow, P. S., & Tan, R. B. (2014). *CrystEngComm*, 16(26): 5793-5801.

- [21] Surov, A. O., Simagina, A. A., Manin, N. G., Kuzmina, L. G., Churakov, A. V., & Perlovich, G. L. (2014). *Crystal Growth & Design*, 15(1): 228-238.
- [22] Zhou, T., Li, F., Fan, Y., Song, W., Mu, X., Zhang, H., & Wang, Y. (2009). *Chemical Communications*, 22: 3199-3201.
- [23] Uzoh, O. G., Cruz-Cabeza, A. J., & Price, S. L. (2012). *Crystal Growth & Design*, 12(8): 4230-4239.
- [24] Krishna Murthy, H. M., & Vijayan, M. (1979). *Acta Crystallographica Section B: Structural Crystallography and Crystal Chemistry*, 35(1): 262-263.
- [25] Bag, P. P., & Reddy, C. M. (2012). *Crystal Growth & Design*, 12(6): 2740-2743.
- [26] Long, S., Parkin, S., Siegler, M. A., Cammers, A., & Li, T. (2008). *Crystal Growth & Design*, 8(11): 4006-4013.
- [27] McConnell J. F. (1973). *Crystal structure communications*, 3: 459 – 461.
- [28] Krishna Murthy, H. M., Bhat, T. N., & Vijayan, M. (1982). *Acta Crystallographica Section B: Structural Crystallography and Crystal Chemistry*, 38(1): 315-317.
- [29] Krc, J. (1977). *Microscope*, 25(1): 31-45.
- [30] Andersen, K. V., Larsen, S., Alhede, B., Gelting, N., & Buchardt, O. (1989). *Journal of the Chemical Society, Perkin Transactions 2*, (10): 1443-1447.
- [31] Surov, A. O., Szterner, P., Zielenkiewicz, W., & Perlovich, G. L. (2009). *Journal of pharmaceutical and biomedical analysis*, 50(5): 831-840.
- [32] McConnell J. F., Company F. Z. (1976) *Crystal structure communications*. 5: 861 – 864.
- [33] Lee, E. H., Byrn, S. R., & Carvajal, M. T. (2006). *Pharmaceutical research*, 23(10): 2375-2380.
- [34] Yang, X., Sarma, B., & Myerson, A. S. (2012). *Crystal Growth & Design*, 12(11): 5521-5528.

- [35] T. Umeda, N. Ohnishi, T. Yokoyama, T. Kuroda, Y. Kita, K. Kuroda, E. Tatsumi, Y. Matsuda (1985). *Chemical and pharmaceutical bulletin*, 33(5): 2073-2078.
- [36] Gilpin, R. K., & Zhou, W. (2005). *Vibrational spectroscopy*, 37(1): 53-59.
- [37] Kato, F., Otsuka, M., & Matsuda, Y. (2006). *International Journal of pharmaceuticals*, 321(1): 18-26.
- [38] Otsuka, M., Kato, F., & Matsuda, Y. (2004). *Solid State Ionics*, 172(1): 451-453.
- [39] Romero, S., Escalera, B., & Bustamante, P. (1999). *International journal of pharmaceuticals*, 178(2): 193-202.
- [40] Park, K., Evans, J. M., & Myerson, A. S. (2003). *Crystal growth & design*, 3(6): 991-995.
- [41] Urakami, K., Shono, Y., Higashi, A., Umemoto, K., & Godo, M. (2002). *Bulletin of the Chemical Society of Japan*, 75(6): 1241-1245.
- [42] Aguiar, A. J., & Zelmer, J. E. (1969). *Journal of pharmaceutical sciences*, 58(8): 983-987.
- [43] Surov, A. O., Terekhova, I. V., Bauer-Brandl, A., & Perlovich, G. L. (2009). *Crystal Growth and Design*, 9(7): 3265-3272.
- [44] Hu, Y., Liang, J. K., Myerson, A. S., & Taylor, L. S. (2005). *Industrial & engineering chemistry research*, 44(5): 1233-1240.
- [45] Mao, C., Pinal, R., & Morris, K. R. (2005). *Pharmaceutical research*, 22(7): 1149-1157.
- [46] Mattei, A., & Li, T. (2012). *Pharmaceutical research*, 29(2): 460-470.
- [47] Filippini, G., & Gavezzotti, A. (1993). *Acta Crystallographica Section B: Structural Science*, 49(5): 868-880.
- [48] Acree Jr, W., & Chickos, J. S. (2016). *Journal of Physical and Chemical Reference Data*, 45(3): 033101.
- [49] Surov, A. O., Perlovich, G. L., Emel'yanenko, V. N., & Verevkin, S. P. (2011). *Journal of Chemical & Engineering Data*, 56(12): 4325-4332.
- [50] López-Mejías, V., & Matzger, A. J. (2015). *Crystal Growth & Design*, 15(8): 3955-3962.

- [51] MJ Frisch, et al., Gaussian 09, Revision B.01, Gaussian Inc., Wallingford, CT, 2010.
- [52] Surov, A. O., Solanko, K.A., Bond, A.D., Bauer-Brandl, A., Perlovich, G.L. (2014). *CrystEngComm*, 16: 6603-6611.
- [53] Macrae, C. F., Edgington, P. R., McCabe, P., Pidcock, E., Shields, G. P., Taylor, R., Towler, M., van de Streek, J. (2006). *Journal of Applied Crystallography*, 39: 453-457.
- [54] Cruz-Cabeza, A. J., Bernstein, J. (2014). *Chemical Reviews*, 114: 2170-2191.
- [55] López-Mejías, V., Kampf J. W., Matzger, A. J. (2012). *Journal of the American Chemical Society*, 134: 9872-9875.
- [56] Chisholm, J. A., Motherwell, S. J. (2005). *Journal of Applied Crystallography*, 38: 228-231.
- [57] Gavezzotti, A. (2011). *New Journal of Chemistry*, 35: 1360-1368.
- [58] Fleischman, S. G., Kuduva, S. S., McMahon, J. A., Moulton, B., Walsh, R. D. B., Rodriguez-Hornedo, N., Zaworotko, M. J. (2003). *Crystal Growth & Design*, 3: 909-919;
- [59] Johnston, A., Johnston, B. F., Kennedy, A. R., Florence, A. J. (2008). *CrystEngComm*, 10: 23-25;
- [60] Cruz-Cabeza, A. J., Day, G. M., Jones, W. (2011). *Physical Chemistry Chemical Physics*, 13: 12808-12816;
- [61] Delori, A., Galek, P. T. A., Pidcock, E., Patni, M., Jones, W. (2013). *CrystEngComm*, 15: 2916-2928.
- [62] McMahon, J. A., Bis, J. A., Vishweshwar, P., Shattock, T. R., McLaughlin, O. L., Zaworotko, M. J. Z. (2005). *Zeitschrift für Kristallographie*, 220: 340-350;
- [63] McMahon, J. A., Oliveira, M., Peterson, M. L., Zaworotko, M. J. (2005). *Journal of the American Chemical Society*, 125: 16802-16803;
- [64] Seefeldt, K., Miller, J., Alvarez-Nunez, F., Rodriguez-Hornedo, N. (2007). *Journal of Pharmaceutical Sciences*, 96: 1147-1158;
- [65] ter Horst, J.H., Cains, P.W. (2008). *Crystal Growth & Design*, 8: 2537-2542;

- [66] Childs, S. L., Wood, P. A., Rodriguez-Hornedo, N., Reddy, L.S., Hardcastle, K.I. (2009). *Crystal Growth & Design*, 9: 1869–1888;
- [67] Habgood, M., Deij, M.A., Mazurek, J., Price, S.L., ter Horst, J.H. (2010). *Crystal Growth & Design*, 10: 903–912.
- [68] Lowes, M. M. J., Cairo, M. R., Lotter, A. P., van der Watt, J. G. (1987). *Journal of Pharmaceutical Sciences*, 76: 744–752;
- [69] Lang, M., Kampf, J. W., Matzger, A. J. (2002). *Journal of Pharmaceutical Sciences*, 91: 1186–1190;
- [70] Fernandes, P., Shankland, K., Florence, A. J., Shankland, N., Johnston, A. (2007). *Journal of Pharmaceutical Sciences*, 96: 1192–1202;
- [71] Arlin, J.-B., Price, L. S., Price, S. L., Florence, A. J. (2011). *Chemical Communications*, 47: 7074–7076.
- [72] Oliveira, M. A., Peterson, M. L., Davey, R. J. (2011). *Crystal Growth & Design*, 11: 449–457.
- [73] Lemmerer, A., Adsmund, D. A., Esterhuysen, C., Bernstein, J. (2013). *Crystal Growth & Design*, 13: 3935–3952;
- [74] Aitipamula, S., Chow, P. S., Tan, R. B. H. (2014). *CrystEngComm*, 16: 3451–3465.
- [75] Braga, D., Palladino, G., Polito, M., Rubini, K., Grepioni, R., Chierotti, M. R., Gobetto, R. (2008). *Chemistry - A European Journal*, 14: 10149–10159;
- [76] Halasz, I., Rubčić, M., Užarević, K., Đilović I., Meštrović E. (2011). *New Journal of Chemistry*, 35: 24–27;
- [77] Mukherjee, A., Desiraju, G. R. (2011). *Chemical Communications*, 47: 4090–4092.
- [78] Miller, J. M., Blackburn, A. C., Macikenas, D., Collman, B. M., Rodríguez-Hornedo, N. Solvent Systems for Crystallization and Polymorph Selection, in *Solvent Systems and Their Selection in Pharmaceuticals and Biopharmaceuticals*; ed. Augustijns, P. and Brewster, M. E., AAPS Press: New York, 2007.

Nova Science Publishing, Inc.

ABOUT THE EDITORS

Jinjin Li, PhD

Present Position: Professor

Academic Affiliation: Department of Micro/Nano-Electronics, Shanghai Jiao Tong University, 800 Dong Chuan Road, Shanghai 200240, P. R. China

Email: lijinjin.physics@gmail.com

Jinjin Li received her BS degree from Tianjin University of Technology, Tianjin, China, in 2007; PhD degree from Shanghai Jiao Tong University, China, in 2012. He was a post-doc at the University of Illinois at Urbana-Champaign, USA from 2012 to 2014, a post-doc at the University of California, Santa Barbara, USA from 2014 to 2016. She is currently a professor at department of Micro/Nano-electronics, Shanghai Jiao Tong University, China. Her research interests include crystal growth design & calculation; quantum optical properties in nanostructured materials, and first principle calculation for solid state system.

Jianwei Li, PhD**Present Position:** Senior Researcher**Academic Affiliation:** Department of Chemistry, University of Turku, Vatselankatu 2, 20014 Turku, Finland**Email:** Jianwei.li@utu.fi

Jianwei Li received his Bachelor degree from Huazhong Agriculture University in 2006. Inspired by the lock-and-key principle, he then started his Master study in supramolecular chemistry in Prof. Huakuan Lin's lab at Nankai University. In 2009, he moved to the University of Groningen in Netherlands for his PhD study with Prof. Sijbren Otto, investigating self-assembly in complex chemical systems. In March 2014, he obtained his doctorate degree and then joined the group of Prof. Hagan Bayley in Oxford University, UK as a postdoctoral researcher, where he explored reversible chemical reaction and catalysis in protein nanopores at single-molecule level. From September 2016, he started his independent career funded by Turku Collegium for Science and Medicine (TCSM) as a principle investigator in the department of chemistry, University of Turku. In the following years, he will be leading a group to push the frontier of systems chemistry by extending its application in biomedicine and bioenergy.

Yanhui Chu, PhD**Present Position:** Associate Professor**Academic Affiliation:** School of Materials Science and Engineering, South China University of Technology, Guangzhou, China**Email:** chuyh@scut.edu.cn

Yanhui Chu received the BS degree from University of Jinan, Jinan, China, in 2009, and PhD degree in materials science and engineering from Northwestern Polytechnical University, Xian, China, in 2016. He was a visiting scholar at Harvard University, Boston, USA from 2014 to 2015. He is currently an associate professor at the School of Materials Science and Engineering, South China University of Technology, Guangzhou, China. His research interests include high-temperature structure ceramics, sensors and related nanomaterials.

Nova Science Publishing, Inc.

Nova Science Publishing, Inc.

INDEX

#	B
4,4'-bipyridine, 318, 320, 339, 340, 342, 354, 357	base function, 287 basic state, 204, 212 basis set, 127, 146, 286, 287, 288, 289, 300, 307, 308, 312 Bi-Bi bonds, 85 Bi-Bi pairings, 83, 84, 85, 102, 104, 105 binary alloy, vi, viii, 199, 200, 201, 220, 221, 222 birefringence, 252, 258, 266, 267, 269, 270, 272, 273, 274, 279, 280, 282, 283 Bragg's law, 43 modified, 43 Bridgman technique, 11, 12
A	C
alignment crystallographic, 40, 59, 61, 71, 77 alloy, 35, 48, 50, 51, 56, 62, 90, 92, 93, 94, 95, 99, 101, 102, 104, 108, 110, 158, 200, 201, 220, 221, 222 amorphous, 5, 9, 35, 46, 48, 50, 52, 54, 56, 57, 59, 62, 108, 112, 117 alloy, 35, 48, 50, 51, 56, 62 intermediate, 35, 52, 56, 57, 59, 62 anti-phase boundaries, 41 aragonite, viii, 165, 167, 168, 170, 175, 176, 178, 179, 180, 182, 183, 184, 185, 186, 187, 188, 189, 190, 191, 192, 193, 194, 195, 196, 197 arc fusion technique, 14	calcite, viii, 160, 165, 167, 168, 169, 170, 175, 176, 177, 178, 180, 181, 183, 184, 185, 186, 187, 188, 189, 190, 191, 192, 193, 194, 195, 196, 197, 198 calcium carbonate, 165, 170, 196, 197, 198 charge transfer, 75, 83, 85, 97, 103, 104, 113, 117, 235, 300, 310 Chevrel phase, 57

cluster- transformation mechanism, 166, 178

cocrystal formation enthalpies, 320

cocrystals, vi, 317, 318, 319, 320, 339, 340, 341, 342, 343, 344, 345, 346, 347, 349, 352, 353, 354, 355, 356, 357

complex, ix, 2, 4, 7, 17, 36, 62, 103, 104, 105, 106, 120, 124, 125, 126, 140, 151, 158, 230, 265, 268, 276, 286, 287, 288, 290, 291, 293, 297, 299, 300, 309, 312, 352, 366

complex metallic oxides, 120

constant-composition technique, viii, 165, 171, 193

convective, vi, viii, 199, 200, 201, 202, 220, 222

copper (II), 286, 312

critical thickness, 46, 50, 52, 62

crystal growth, ii, viii, ix, 2, 3, 7, 9, 10, 11, 15, 16, 17, 19, 20, 21, 22, 23, 24, 30, 31, 32, 33, 123, 125, 152, 158, 163, 166, 167, 168, 172, 173, 174, 181, 184, 185, 186, 188, 190, 191, 193, 195, 196, 197, 198, 199, 323, 359, 360, 361, 362, 363, 365

crystal lattice energies, 327, 333

crystal orbital overlap population (COOP), 84

crystal structure, ix, 1, 3, 27, 37, 53, 85, 92, 98, 106, 110, 121, 161, 249, 286, 293, 320, 321, 323, 324, 339, 340, 347, 349, 350, 352, 356, 357

crystal system, 28, 286, 293

crystallization, viii, 2, 3, 5, 6, 7, 17, 20, 21, 23, 24, 30, 32, 33, 50, 51, 58, 167, 168, 178, 197, 198, 229, 230, 231, 244, 339, 363

crystallographic, 8, 12, 28, 29, 40, 59, 61, 71, 72, 77, 123, 125, 134, 291, 295, 340, 341

crystallographic data, 28, 29, 291

CuCr₂Se₄, 40, 58, 59, 60, 61, 62, 111

Czochralski techniques, 12

D

density functional theory (DFT), 125, 127, 141, 143, 148, 157, 159, 164, 244, 286, 287, 288, 289, 292, 296, 298, 299, 300, 302, 307, 308, 309, 312

designed materials, 36

differential scanning calorimetry, 45

diffusion, 11, 16, 21, 35, 38, 39, 40, 41, 42, 46, 49, 51, 55, 56, 57, 58, 59, 62, 95, 96, 105, 107, 116, 229, 230, 237, 242, 243

dimer, 265, 266, 271, 272, 273, 281, 320, 321, 322

dipole moment, 299

direct vapor transport, 16

disorder, 61, 72, 73, 77, 79, 104, 142, 324, 352

E

electronegativity, 286, 287, 308, 312

energy landscape, 37, 106, 144

enthalpy, 325, 327, 333, 355, 356

formation, 355, 356

solution, 325

sublimation, 327, 332

experimental, viii, 1, 2, 80, 120, 122, 124, 125, 126, 129, 130, 131, 132, 133, 134, 140, 143, 144, 146, 150, 151, 152, 154, 156, 159, 166, 168, 170, 171, 173, 176, 178, 184, 185, 188, 190, 194, 195, 201, 202, 212, 220, 221, 234, 249, 266, 269, 271, 273, 274, 276, 277, 281, 288, 292, 293, 296, 297, 298, 300, 301, 311, 312, 323, 326, 327, 334, 339, 356

F

fenamates, ix, 317, 318, 319, 320, 324, 327, 330, 332, 333, 334, 335, 338, 339, 340, 341, 344, 345, 353, 354
ferrecrystals, 61, 63, 72, 73, 74, 76, 77, 79, 80, 82, 83, 84, 85, 87, 89, 90, 91, 92, 93, 94, 95, 96, 97, 99, 100, 101, 102, 103, 104, 105, 112, 115, 117
flame fusion technique, 11, 14
flufenamic acid, 318, 322, 323, 333, 339
flux growth, 20
FT-IR spectra, 287

G

GAUSSIAN-09, 289, 290
grain growth, 8, 9, 31

H

heterojunction, 94, 95, 96, 97, 98, 99, 117, 153
heterostructures, viii, 36, 61, 62, 63, 104, 115, 117, 118, 155
hexagonal, 31, 63, 78, 92, 199, 212, 220, 234, 249, 272
highest occupied molecular orbital (HOMO), 286, 289, 299, 300, 302, 303, 304, 305, 306, 308, 310, 312
hydrazone, 287
hydrogen bonds, ix, 294, 317, 332, 342, 356
hydrothermal growth, 19
hyperpolarizability, 286, 287, 289, 290, 307, 310

I

in-plane structure, 77, 79, 81, 85, 100, 104
ionization potential, 286, 287, 308, 312

IR spectra, 287, 288, 297, 301
iron silicides, 108
isomers, 85, 87, 88, 89, 105, 116

K

kinetic control, viii, 35, 36, 39, 41, 47, 54, 62, 65, 85, 124

L

layered structure(s), 63, 71, 98
layering sequence(s), 58, 72, 73, 76, 85, 88, 94, 99
ligand, 228, 232, 235, 236, 237, 243, 249, 250, 286, 293, 297, 299, 300, 302, 303
liquid crystal, vi, viii, 251, 252, 253, 254, 255, 258, 259, 261, 262, 263, 265, 266, 267, 268, 269, 270, 271, 272, 273, 274, 275, 276, 277, 278, 279, 280, 281, 282, 283, 284
lowest unoccupied molecular orbitals (LUMO), 236, 286, 289, 299, 300, 302, 304, 305, 306, 308, 310, 312

M

melting, 11, 12, 13, 14, 15, 21, 25, 32, 48, 263, 318, 320, 327, 330, 332, 333, 334, 335, 353, 354
mesogen, 252, 283
metal, vi, viii, 12, 15, 19, 41, 53, 54, 57, 60, 62, 63, 73, 77, 81, 82, 83, 84, 85, 90, 91, 92, 93, 94, 99, 100, 101, 104, 105, 108, 109, 110, 111, 122, 124, 126, 127, 129, 142, 146, 147, 149, 150, 151, 157, 160, 162, 163, 227, 228, 229, 232, 234, 235, 236, 237, 238, 239, 241, 242, 243, 244, 245, 246, 247, 248, 249, 250, 286, 287, 293, 299, 300, 302, 303

metal–organic frameworks (MOFs), vi, viii, 151, 227, 228, 231, 232, 233, 234, 235, 236, 237, 238, 239, 242, 243, 244, 246, 247, 248, 249, 250

metastability, 36

metastable compounds, v, viii, 35, 36, 40, 51, 52, 62

modulated elemental reactants, viii, 35, 40, 41, 62, 65, 107, 110, 112

molecular conformational, 320, 331

molecular electrostatic potential (MEP), 286, 299, 308, 312

monomer, 266

morphology, v, viii, 2, 22, 33, 119, 120, 121, 122, 125, 126, 129, 130, 131, 132, 133, 134, 135, 136, 139, 140, 143, 145, 146, 147, 149, 150, 152, 155, 156, 157, 158, 161, 164, 168, 244, 323

mushy layer, 200, 201, 202, 203, 212, 220, 221, 222

N

nanoarchitecture, 36, 116

designed, viii, 36, 63, 117

nematic, 252, 253, 254, 256, 258, 262, 269, 272, 279, 280, 281, 283

niflumic acid, 318, 321, 322, 333

nonlinear, vi, viii, 199, 200, 201, 202, 203, 204, 205, 207, 209, 211, 212, 213, 214, 215, 216, 217, 218, 219, 220, 221, 222, 223, 225, 286, 287, 309

nonlinear optical (NLO) parameters, 286, 287, 309, 312

nonlinear optics, 286

N-phenylanthranilic acid, 317, 318, 321, 322, 332, 336, 339

nucleation, 2, 6, 8, 11, 12, 17, 20, 24, 35, 45, 46, 47, 48, 51, 52, 54, 55, 57, 59, 62, 108, 110, 111, 167, 169, 170, 171, 190, 191, 195, 197, 198, 320

nucleation energy, 48, 51, 54, 108, 110

O

order parameter, 252, 260, 261, 267, 272, 274, 280, 281, 283

P

physical vapor deposition, 40, 42, 62, 73

polarizability, 258, 259, 260, 266, 267, 268, 270, 272, 274, 283, 286, 287, 289, 307, 309, 310

polymorphism, 168, 196, 269, 319, 320, 321, 323, 325, 333, 357, 359

porous functional materials, 227

precursor, 40, 41, 42, 43, 44, 45, 46, 47, 48, 49, 50, 51, 52, 53, 54, 55, 56, 57, 58, 62, 65, 67, 68, 69, 71, 72, 90, 94, 96, 99, 105, 111, 121, 148, 169, 333

amorphous, 54, 112, 117

R

Rayleigh number, 203, 212, 220

reaction pathway, 35, 37, 38, 39, 41, 46, 48, 49, 108

repeating unit, 41, 42, 45, 56, 64, 65

Rietveld refinement, 71, 73, 74, 80, 95, 103, 156

rock salt, 69, 73, 79, 85

S

Schiff base, 286, 287, 297, 300

single crystal, v, viii, 1, 2, 3, 5, 7, 8, 9, 10, 11, 12, 13, 19, 20, 21, 22, 26, 27, 29, 30, 31, 33, 111, 154, 163, 230, 286, 287, 293, 321, 339, 357

skull-melting technique, 15

skutterudite, 52, 53, 54, 55, 58, 62, 108, 109, 110
slow evaporation technique, v, 1, 2, 21, 29
smectic, 252, 254, 255, 262, 269, 272, 281, 282, 283
solid-state phase transformation, 10
solvent phases, 299
space group, 77, 79, 81, 129, 135, 137, 286, 293, 321
spin transitions, 287, 300, 304
spinel, 12, 58, 145, 150
Stefan number, 201, 203
strain-annealing technique, 9
structure factor, 79
sublimation, 16, 21, 317, 320, 327, 330, 331, 332, 333, 334, 335
sulfonohydrazide, 286, 287, 294
sulfonylhydrazide, 293
surface energy, 48, 59, 120, 121, 122, 123, 124, 128, 130, 131, 132, 133, 135, 138, 139, 141, 164, 188
synthesis, v, viii, 19, 27, 29, 32, 35, 36, 37, 38, 39, 40, 41, 45, 53, 54, 55, 56, 57, 60, 62, 63, 65, 104, 105, 106, 107, 108, 109, 110, 111, 112, 113, 114, 116, 117, 120, 121, 122, 123, 124, 126, 136, 140, 142, 144, 145, 147, 148, 152, 153, 154, 155, 156, 157, 158, 159, 160, 161, 162, 163, 227, 229, 230, 231, 232, 238, 241, 242, 243, 244, 249, 290
synthetic strategies, viii, 227

T

theoretical, ix, 124, 125, 126, 129, 130, 132, 133, 135, 143, 144, 146, 147, 150, 151, 152, 154, 156, 157, 159, 201, 242, 271, 288, 296, 297, 298, 300, 301, 311, 312, 327

thin films, 7, 36, 59, 111, 125, 153, 236, 248
tolfenamic and mefenamic acids, 318
transition metal dichalcogenide, 41, 60, 62, 63, 77, 81, 82, 83, 84, 85, 90, 91, 92, 93, 94, 98, 99, 100, 104, 105

U

UV-Vis spectra, 287, 299

V

vaterite, 167
vibrational frequencies, 289, 298, 336

W

weakly, viii, 199, 200, 201, 202, 203, 205, 207, 209, 211, 213, 215, 217, 219, 221, 222, 223, 225
Wulff construction, 120, 124, 126, 128, 129, 131, 132, 134, 135, 136, 139, 141, 143, 155

X

X-ray, 28, 29, 30, 242, 288, 292, 293, 296, 336, 339
X-ray diffraction (XRD), ix, 1, 2, 3, 5, 43, 45, 46, 50, 55, 60, 61, 71, 77, 80, 81, 88, 91, 94, 95, 99, 100, 103, 116, 142, 175, 230, 286, 287, 290, 331

Z

zone-melting techniques, 13